



Ricerca di Sistema elettrico

Supporto alla progettazione del combustibile nucleare per il reattore LFR

A. Aly, D. Rozzia, A. Del Nevo
L. Luzzi, D. Pizzocri



SUPPORTO ALLA PROGETTAZIONE DEL COMBUSTIBILE NUCLEARE PER IL REATTORE LFR

A. Aly, D. Rozzia, A. Del Nevo - ENEA, L. Luzzi, D. Pizzocri - POLIMI-CIRTEN

Settembre 2015

Report Ricerca di Sistema Elettrico

Accordo di Programma Ministero dello Sviluppo Economico - ENEA

Piano Annuale di Realizzazione 2014

Area: Produzione di energia elettrica e protezione dell'ambiente

Progetto: Sviluppo competenze scientifiche nel campo della sicurezza nucleare e collaborazione ai programmi internazionali per il nucleare di IV Generazione

Linea: Collaborazione internazionale per il nucleare di IV Generazione

Obiettivo: Progettazione di sistema e analisi di sicurezza

Responsabile del Progetto: Mariano Tarantino, ENEA

Il presente documento descrive le attività di ricerca svolte all'interno dell'Accordo di collaborazione Sviluppo competenze scientifiche nel campo della sicurezza nucleare e collaborazione ai programmi internazionali per il nucleare di IV Generazione

Responsabile scientifico ENEA: Mariano Tarantino

Responsabile scientifico CIRTEN: Giuseppe Forasassi

Titolo

Supporto alla progettazione del combustibile nucleare per il reattore LFR

Descrittori

Tipologia del documento: Rapporto Tecnico
Collocazione contrattuale: Accordo di programma ENEA-MSE su sicurezza nucleare e reattori di IV generazione
Argomenti trattati: Reattori Nucleari Veloci,
 Sicurezza nucleare,
 Analisi incidentale

Sommario

L'attività di ricerca a supporto alla progettazione del combustibile nucleare per reattori veloci di IV generazione, in ambito PAR-2014 LP2, ha riguardato attività di modellistica e simulazione con il codice TRANSURANUS. Il lavoro svolto da ENEA e CIRTEN ha riguardato:

- una revisione critica e di aggiornamento di alcuni modelli fenomenologici del combustibile, per quanto riguarda la redistribuzione del plutonio e il rilascio dei gas di fissione in condizioni di transitori di potenza (*burst release*);
- un'analisi di *performance* delle barrette di combustibile del reattore di riferimento, in condizioni nominali, basata sulla versione del codice aggiornata;
- la validazione del codice sulla base di barrette selezionate da database sperimentali sia per LWR (2 barrette da IFA-597) che FBR (2 barrette da HEDL-P-19)
- un'indagine e comparazione tra le correlazioni MOX del codice, correlazioni disponibili in letteratura e dati sperimentali, l'introduzione nel codice del modello suggerito da Baron-Hervé.

Note: CERSE-POLIMI RL 1501/2015

Autori:


A. Aly, D. Rozzia, A. Del Nevo - ENEA

L. Luzzi, D. Pizzocri – POLIMI-CIRTEN


Copia n.
In carico a:

2			NOME			
			FIRMA			
1			NOME			
			FIRMA			
0	EMISSIONE	25/09/15	NOME	A. Del Nevo	M. Tarantino	M. Tarantino
			FIRMA	<i>A. Del Nevo</i>	<i>M. Tarantino</i>	<i>M. Tarantino</i>
REV.	DESCRIZIONE	DATA	REDAZIONE	CONVALIDA	APPROVAZIONE	

 Ricerca Sistema Elettrico	Sigla di identificazione ADPFISS – LP2 – 087	Rev. 0	Distrib. L	Pag. 2	di 229
--	--	------------------	----------------------	------------------	------------------

 Ricerca Sistema Elettrico	Sigla di identificazione	Rev.	Distrib.	Pag.	di
	ADPFISS – LP2 – 087	0	L	3	229

Parte A. *Supporto alla progettazione del combustibile nucleare per il reattore LFR*
– Contributo ENEA.....5

Parte B. *Supporto alla progettazione del combustibile nucleare per il reattore LFR*
– Contributo POLIMI-CIRTEN.....121

 Ricerca Sistema Elettrico	Sigla di identificazione ADPFISS – LP2 – 087	Rev. 0	Distrib. L	Pag. 4	di 229
--	--	------------------	----------------------	------------------	------------------

 Ricerca Sistema Elettrico	Sigla di identificazione	Rev.	Distrib.	Pag.	di
	ADPFISS – LP2 – 087	0	L	5	229

Abstract

Among the parameters that governs the myriad of processes that occurs during irradiation of fuels rods, the fuel temperature is by far the most important one. The correct prediction of the fuel temperature profile is the basis for the simulation of integral fuel rods by means of fuel performance codes. It is therefore of critical importance to any computer code used for simulation of integral fuel rod behavior to be able to predict the thermal conductivity of the fuel correctly since it directly affects the temperature.

The present activity is conducted in the framework of the PELGRIMM EC Project and deals with the assessment of MOX fuel conductivity correlations used in TRANSURANUS code and comparing them to open literature correlations and experimental data then verifying the code against selected integral fuel rod experiments done for both thermal and fast reactors. In order to assess the thermal conductivity correlations of MOX fuel into an integral simulation, other phenomena that would affect the prediction of temperature have been investigated as well in order to capture the integral behavior of MOX for thermal and fast reactor. This step helped in assessing the ability of thermal conductivity correlations to predict fuel temperature while excluding the effects of other phenomena meanwhile giving a general information about the ability of different models to predict the phenomenon they predict.

It was shown during this work that TU is able to predict temperature, hence the thermal conductivity of thermal reactor MOX with high accuracy. On the other hand, the work revealed a potential field of improvement to predict the thermal conductivity of FR grade MOX, especially if not of stoichiometric grade and if in fresh conditions. However, the code seems to be on the conservative size when modeling FR MOX. A first step in this improvement was taken in this work and targeted the modification of the high temperature thermal conductivity term in order to be able to obtain a better, less conservative prediction of the melting of FR fuel rods early in life in the reactor core.

 Ricerca Sistema Elettrico	Sigla di identificazione ADPFISS – LP2 – 087	Rev. 0	Distrib. L	Pag. 6	di 229
--	--	------------------	----------------------	------------------	------------------

LIST OF CONTENTS

ABSTRACT	5
ABBREVIATIONS.....	11
LIST OF FIGURES	13
LIST OF TABLES.....	17
1 INTRODUCTION.....	19
1.1 Objective of the activity	19
2 THEORETICAL BACKGROUND	21
2.1 Thermal conductivity of ceramic fuel.....	21
2.2 Effect of temperature	22
2.3 Effect of stoichiometry.....	23
2.4 Effect of burn-up.....	24
2.5 Effect of fuel porosity	25
2.6 Effect of Plutonium content	26
2.7 Summary of parameters affecting thermal conductivity.....	26
3 MOX FUEL CONDUCTIVITY CORRELATIONS.....	27
3.1 TRANSURANUS correlations	27
3.1.1 Correlation by Van Uffelen and Schubert.....	27
3.1.2 Correlation by Carbajo	28
3.1.3 Correlation by Lanning and Beyer	29
3.1.4 Correlation by Wiesenack.	30
3.2 Open Literature correlations	31
3.2.1 Martin review 1982	31
3.2.2 FTHCON subcode-MATPRO	32
3.2.3 The COMETHE formulation-1982	33
3.2.4 Baron Hervè 1995 Model.....	34
3.3 Experimental data and correlations.....	34
3.4 Conclusive remarks.....	40

 Ricerca Sistema Elettrico	Sigla di identificazione	Rev.	Distrib.	Pag.	di
	ADPFISS – LP2 – 087	0	L	8	229

4	TRANSURANUS CODE	43
5	ANALYSIS OF LWR MOX: IFA-597 EXPERIMENT	45
5.1	Description of the experiment.....	45
5.1.1	Background and objective of the experiment.....	45
5.1.2	Halden Boiling Water Reactor (HBWR)	45
5.1.3	Design of the rig and rods	48
5.1.4	Linear Heat rating (LHR).....	49
5.2	Modelling IFA597.4/.5 with TU	50
5.2.1	Development of TU input file	50
5.2.2	Boundary conditions	52
5.2.3	Burn-up investigation.....	53
5.3	Reference analysis of IFA597.4/.5.....	54
5.3.1	Fuel temperature.....	54
5.3.2	FGR and pin pressurization.....	54
5.4	Sensitivity analysis.....	58
5.4.1	Effect of linear heat rating uncertainty.....	60
5.4.2	Effect of thermal conductivity correlations.....	64
5.4.3	Relocation models analysis	66
5.4.4	Swelling correlations.....	68
5.4.5	FGR models.....	69
5.4.6	Gap conductance models.....	71
5.4.7	Other parameters	72
5.5	Radial analysis	73
5.5.1	IFA597.4 Radial analysis (5 MWD/KgU)	74
5.5.2	IFA597.5 Radial analysis (24 MWD/KgHM).....	76
6	ANALYSIS OF FR MOX: HEDL P-19 EXPERIMENT	79
6.1	Description of the experiment.....	79
6.1.1	Background and objective of the experiment.....	79
6.1.2	Experimental Breeder Reactor #2 (EBR-II).....	82
6.2	Modelling HEDL P-19 with TU	83
6.2.1	Development of TU input file	83
6.2.2	Boundary conditions	85
6.3	Reference analysis of HEDL P-19 rods	87
6.3.1	Temperature prediction	87
6.3.2	Gap width	87
6.3.3	Central void.....	87
6.3.4	Columnar grains	88
6.3.5	Melting radius	88

 Ricerca Sistema Elettrico	Sigla di identificazione	Rev.	Distrib.	Pag.	di
	ADPFISS – LP2 – 087	0	L	9	229

6.3.6	Melting elevation.....	88
6.4	Sensitivity analysis.....	96
6.4.1	Thermal conductivity correlations	98
6.4.2	Relocation models analysis	100
6.4.3	Solidus-Liquidus melting models.....	101
6.4.4	Fuel restructuring models.....	102
6.4.5	Initial gap width	102
6.5	Radial analysis	104
7	REVIEW OF THERMAL CONDUCTIVITY CORRELATIONS.....	108
8	CONCLUSION	115
	REFERENCES.....	118

 Ricerca Sistema Elettrico	Sigla di identificazione ADPFISS – LP2 – 087	Rev. 0	Distrib. L	Pag. 10	di 229
--	--	------------------	----------------------	-------------------	------------------

Abbreviations

ANL	Argon National Laboratory
at.%	Atomic percentage
BOL	Beginning Of Life
BU	BurnUp
BWR	Boiling Water Reactor
Cs	Cesium
EBR-II	Experimental Breeder Reactor #2
EI	Electronic
EOL	End Of Life
FBR	Fast Breeder Reactor
FD	Dissolved Fission products
FFTF	Fast Flux Test Facility
FGR	Fission Gas Release
FP	Precipitated Fission products
FR	Radiation Factor/ Fast Reactor
Gd ₂ O ₃	Gadolinia
HBWR	Heavy Boiling Water Reactor
HEDL	Hanford Engineering Development Laboratory
HPG	Halden Project Group
HRP	Halden Reactor Project
IFA	Instrumental Fuel Assembly
ITU	Institute for TransUranium elements
Kr	Krypton
Latt	Lattice
LHR	Linear Heat Rate
LMFBR	Liquid Metal Fast Breeder Reactor
LWR	Light Water Reactor
MA	Minor Actinides
MIMAS	Micronized MAster blend
MOX	Mixed Oxide fuel
Nd	Neodymium
OL	Open Literature
O/M	Oxygen to Metal ratio
P	Porosity
PCMI	Pellet Cladding Mechanical Interaction
PuO ₂	Plutonium dioxide
PWR	Pressurized Water Reactor
Rad	Radiation
RADAR	RAting Depressing Analysis routine
TD	Theoretical Density
TU	TRANSURANUS
UO ₂	Uranium dioxide
wt.%	Weight percentage
X	Deviation from stoichiometry

 Ricerca Sistema Elettrico	Sigla di identificazione	Rev.	Distrib.	Pag.	di
	ADPFISS – LP2 – 087	0	L	12	229

Xe
Zr

Xenon
Zirconium

List of figures

<i>Figure 2-1 (U-Pu)_y-O_x fuel total thermal conductivity along with its different constituting components.</i>	23
<i>Figure 2-2 (U-Pu)_y-O_x conductivity: effect of deviation from stoichiometry on the thermal conductivity.</i>	24
<i>Figure 2-3 (U-Pu)_y-O_x conductivity: effect of burn-up on the thermal conductivity.</i>	25
<i>Figure 3-1 MOX thermal conductivity: comparison between correlations and experimental data for 100%TD, O/M=2, PU=20 wt. %.</i>	36
<i>Figure 3-2 MOX thermal conductivity: comparison between correlations and experimental data for 95%TD, O/M=2, PU=20 wt. %.</i>	37
<i>Figure 3-3 MOX thermal conductivity: comparison between Wiesenack correlation and experimental data for 95%TD, O/M=2, PU=20 wt. %.</i>	37
<i>Figure 3-4 MOX thermal conductivity: comparison between correlations and experimental data for 95%TD, O/M=1.98, PU=20 wt. %.</i>	38
<i>Figure 3-5 MOX thermal conductivity: comparison between correlations and experimental data for 95%TD, O/M=1.93, PU=20 wt. %.</i>	39
<i>Figure 3-6 MOX thermal conductivity: comparison between correlations and experimental data for 95%TD, O/M=2, PU=6 wt. %.</i>	40
<i>Figure 5-1 HBWR, schematic diagram and main operation parameters. ^[21]</i>	47
<i>Figure 5-2 HBWR, plan view of the reactor top lid and main parameters. ^[21]</i>	47
<i>Figure 5-3 IFA-597 experiment, schematic radial view of the test rig. ^[2]</i>	49
<i>Figure 5-4 Linear heat rating of solid and hollow rods.</i>	50
<i>Figure 5-5 Simulation of IFA-597, preliminary results: burn-up analysis.</i>	53
<i>Figure 5-6 Simulation of IFA-597, reference results: fuel temperature evolution in rod 10.</i>	55
<i>Figure 5-7 Simulation of IFA-597, reference results: fuel temperature evolution in rod 11.</i>	56
<i>Figure 5-8 Simulation of IFA-597, reference results: FGR evolution in rod 10.</i>	56
<i>Figure 5-9 Simulation of IFA-597, reference results: FGR evolution in rod 11.</i>	57
<i>Figure 5-10 Simulation of IFA-597, reference results: pin pressure evolution in rod 10.</i>	57
<i>Figure 5-11 Simulation of IFA-597, reference results: pin pressure evolution in rod 11.</i>	58
<i>Figure 5-12 Simulation of IFA-597, sensitivity analysis on LHR, fuel temperature.</i>	62
<i>Figure 5-13 Simulation of IFA-597, sensitivity analysis on LHR, FGR.</i>	62
<i>Figure 5-14 Simulation of IFA-597, sensitivity analysis on LHR, rod pressure.</i>	62
<i>Figure 5-15 Simulation of IFA-597, sensitivity analysis on LHR, variation on fuel centreline prediction of rod-10.</i>	63
<i>Figure 5-16 Simulation of IFA-597, sensitivity analysis on LHR, variation on rod pressure prediction of rod-10.</i>	63
<i>Figure 5-17 Simulation of IFA-597, sensitivity analysis on fuel conductivity correlations, temperature prediction.</i>	65

 Ricerca Sistema Elettrico	Sigla di identificazione	Rev.	Distrib.	Pag.	di
	ADPFISS – LP2 – 087	0	L	14	229

<i>Figure 5-18 Simulation of IFA-597, sensitivity analysis on fuel conductivity correlations, rod pressure and FGR prediction.</i>	<i>65</i>
<i>Figure 5-19 Simulation of IFA-597, sensitivity analysis on relocation models, temperature prediction.</i>	<i>67</i>
<i>Figure 5-20 Simulation of IFA-597, sensitivity analysis on relocation models, Pressure & FGR prediction.</i>	<i>67</i>
<i>Figure 5-21 Simulation of IFA-597, sensitivity analysis on swelling correlations, temperature prediction.</i>	<i>69</i>
<i>Figure 5-22 Simulation of IFA-597, sensitivity analysis on swelling correlations, rod pressure and FGR prediction.</i>	<i>69</i>
<i>Figure 5-23 Simulation of IFA-597, sensitivity analysis on FGR: Intra-granular model coupled with inter-granular model IGRBDM=3, temperature and FGR predictions.</i>	<i>70</i>
<i>Figure 5-24 Simulation of IFA-597, sensitivity analysis on FGR: Inter-granular models coupled with intra-granular model FGRMOD=6, temperature and FGR predictions.</i>	<i>71</i>
<i>Figure 5-25 Simulation of IFA-597, sensitivity analysis on gap conductance, temperature prediction.</i>	<i>72</i>
<i>Figure 5-26 IFA-597, temperature radial profile at 5MWd/kgHM as function of the conductivity correlation adopted.</i>	<i>75</i>
<i>Figure 5-27 IFA-597 at 5 MWd/kgHM, thermal conductivity profiles when applied to rod-10, comparison with open literature correlations and experimental data.</i>	<i>75</i>
<i>Figure 5-28 IFA-597 at 5MWd/kgHM, thermal conductivity profiles when applied to rod-11, comparison with open literature correlations and experimental data.</i>	<i>76</i>
<i>Figure 5-29 IFA-597, temperature radial profile at 24MWd/kgHM as function of the conductivity correlation adopted.</i>	<i>77</i>
<i>Figure 5-30 IFA-597 at 24 MWd/kgHM, thermal conductivity profiles when applied to rod-10, comparison with open literature correlations and experimental data.</i>	<i>77</i>
<i>Figure 5-31 IFA-597 at 24 MWd/kgHM, thermal conductivity profiles when applied to rod-11, comparison with open literature correlations and experimental data.</i>	<i>78</i>
<i>Figure 6-1 HEDL P-19, pin power axial profile.^[3]</i>	<i>81</i>
<i>Figure 6-2 HEDL P-19, EBR-II power history during the experiment.^[3]</i>	<i>81</i>
<i>Figure 6-3 Schematic diagram of EBR-II plant.^[29]</i>	<i>83</i>
<i>Figure 6-4 Simulation of HEDL P-19, rod P19-2, LHR at 17 axial elevations.</i>	<i>86</i>
<i>Figure 6-5 Simulation of HEDL P-19, rod P19-2, coolant temperature at 17 axial elevations.</i>	<i>86</i>
<i>Figure 6-6 Simulation of HEDL P-19, rod P19-2, centreline temperature.</i>	<i>89</i>
<i>Figure 6-7 Simulation of HEDL P-19, rod P19-5, reference analysis, centreline temperature.</i>	<i>89</i>
<i>Figure 6-8 Simulation of HEDL P-19, rod P19-2, reference analysis, radial temperature profile at the end of the ramp.</i>	<i>90</i>
<i>Figure 6-9 Simulation of HEDL P-19, rod P19-5, reference analysis, radial temperature profile at the end of the ramp.</i>	<i>90</i>
<i>Figure 6-10 Simulation of HEDL P-19, rod P19-2, reference analysis, prediction of gap width at the end of the experiment.</i>	<i>91</i>

 Ricerca Sistema Elettrico	Sigla di identificazione	Rev.	Distrib.	Pag.	di
	ADPFISS – LP2 – 087	0	L	15	229

<i>Figure 6-11 Simulation of HEDL P-19, rod P19-5, reference analysis, prediction of gap width at the end of the experiment.</i>	91
<i>Figure 6-12 Simulation of HEDL P-19, rod P19-2, reference analysis, prediction of the central void at the end of the experiment.</i>	92
<i>Figure 6-13 Simulation of HEDL P-19, rod P19-5, reference analysis, prediction of the central void at the end of the experiment.</i>	92
<i>Figure 6-14 Simulation of HEDL P-19, rod P19-2, reference analysis, prediction of the columnar grain radii at the end of the experiment.</i>	93
<i>Figure 6-15 Simulation of HEDL P-19, rod P19-5, reference analysis, prediction of the columnar grain radii at the end of the experiment.</i>	93
<i>Figure 6-16 Simulation of HEDL P-19, rod P19-2, reference analysis, prediction of the melting radius.</i>	94
<i>Figure 6-17 Simulation of HEDL P-19, rod P19-5, reference analysis, prediction of the melting radius.</i>	94
<i>Figure 6-18 Simulation of HEDL P-19, rod P19-2, reference analysis, prediction of melting height.</i>	95
<i>Figure 6-19 Simulation of HEDL P-19, rod P19-5, reference analysis, prediction of melting height.</i>	95
<i>Figure 6-20 Simulation of HEDL-P19, sensitivity analysis on thermal conductivity correlations, prediction of melting height.</i>	98
<i>Figure 6-21 Simulation of HEDL-P19, sensitivity analysis on thermal conductivity correlations, prediction of gap width at the end of the experiment.</i>	99
<i>Figure 6-22 Simulation of HEDL-P19, sensitivity analysis on thermal conductivity correlations, prediction of central void at the end of the experiment.</i>	99
<i>Figure 6-23 Simulation of HEDL-P19, sensitivity analysis on thermal conductivity correlations, prediction of columnar grain radius at the end of the experiment.</i>	99
<i>Figure 6-24 Simulation of HEDL-P19, sensitivity analysis on thermal conductivity correlations, prediction of melting radii.</i>	100
<i>Figure 6-25 Simulation of HEDL-P19, sensitivity analysis on relocation models, prediction of gap width at the end of the experiment.</i>	100
<i>Figure 6-26 Simulation of HEDL-P19, sensitivity analysis on relocation models, prediction of melting height.</i>	101
<i>Figure 6-27 Simulation of HEDL-P19, sensitivity analysis on melting models, prediction of central void at the end of the experiment.</i>	101
<i>Figure 6-28 Simulation of HEDL-P19, sensitivity analysis on melting models, prediction of melting height.</i>	102
<i>Figure 6-29 Simulation of HEDL-P19, sensitivity analysis on restructuring models, columnar grain radii prediction.</i>	102
<i>Figure 6-30 Simulation of HEDL-P19, sensitivity analysis on initial gap size, prediction of melting height.</i>	103
<i>Figure 6-31 Simulation of HEDL-P19, sensitivity analysis on, prediction of gap width at the end of the experiment.</i>	103
<i>Figure 6-32 Radial profile of thermal conductivity for rod P-19-2.</i>	106


 Ricerca Sistema Elettrico	Sigla di identificazione	Rev.	Distrib.	Pag.	di
	ADPFISS – LP2 – 087	0	L	16	229

<i>Figure 6-33 Radial profile of thermal conductivity for rod P-19-5.</i>	<i>107</i>
<i>Figure 7-1 lattice and electronic conductivities comparison.</i>	<i>111</i>
<i>Figure 7-2 Rod P-19-2, Comparison between the melting heights and fraction according to the original and modified correlations.</i>	<i>111</i>
<i>Figure 7-3 Rod P-19-2, Comparison between the predicted gap width at the end of the experiment by the original and modified correlations.</i>	<i>112</i>
<i>Figure 7-4 Rod P-19-2, Prediction of centreline temperature by the original and modified correlations.</i>	<i>112</i>
<i>Figure 7-5 Rod P-19-5, Comparison between the melting heights and fraction according to the original and modified correlations.</i>	<i>113</i>
<i>Figure 7-6 Rod P-19-2, Comparison between the predicted gap width at the end of the experiment by the original and modified correlations.</i>	<i>113</i>
<i>Figure 7-7 Rod P-19-5, Prediction of centreline temperature by the original and modified correlations.</i>	<i>114</i>
<i>Figure 7-8 Radial comparison of thermal conductivity for rod P-19-2 predicted by the original and the modified correlations.</i>	<i>114</i>

List of tables

<i>Table 2-1 Factors affecting thermal conductivity of MOX fuel.</i>	26
<i>Table.3-1 Summary of thermal conductivity correlations for MOX.....</i>	35
<i>Table.3-2 List of experimental data on MOX used for comparison with correlations.....</i>	35
<i>Table 5-1 HBWR, summary of the driver fuel main data.</i>	46
<i>Table 5-2 IFA-597 experiment, rod characteristics.</i>	48
<i>Table 5-3 IFA-597 experiment, summary of models and correlations that might affect the prediction of thermal conductivity of the rods.</i>	51
<i>Table 5-4 IFA-597 experiment, local heat rate measurement positions.</i>	53
<i>Table 5-5 Simulation of IFA-597, list of correlations, models and design parameters considered in the sensitivity studies.</i>	60
<i>Table 5-6 IFA-597, summary of radial analysis main data.</i>	74
<i>Table 6-1 HEDL P-19, design data. ^[3].....</i>	80
<i>Table 6-2 HEDL P-19, axial extension of fuel melting at the end of the experiment. ^[3].....</i>	80
<i>Table 6-3 HEDL P-19, measurements of central void, columnar grain radius and TD at pellet center at the end of the experiment. ^[3].....</i>	80
<i>Table 6-4 Simulation of HEDL P-19, summary of models and correlations that might affect the prediction of thermal conductivity of the rods.</i>	84
<i>Table 6-5 Simulation of HEDL P-19, axial discretization of the fuel rods.</i>	85
<i>Table 6-6 Simulation of HEDL-P19, list of correlations, models and design parameters considered in the sensitivity studies.....</i>	97

 Ricerca Sistema Elettrico	Sigla di identificazione ADPFISS – LP2 – 087	Rev. 0	Distrib. L	Pag. 18	di 229
--	--	------------------	----------------------	-------------------	------------------

 Ricerca Sistema Elettrico	Sigla di identificazione	Rev.	Distrib.	Pag.	di
	ADPFISS – LP2 – 087	0	L	19	229

1 Introduction

1.1 Objective of the activity


The development of mixed oxide fuel (MOX) is a strategic option for current and new generation of nuclear reactors. Therefore, it is important to confirm that it can be implemented safely within a reactor system and that its characteristics fits with the type of reactor it will be used in. One of the issues to be investigated, is the assessment of the thermal performance of MOX during irradiation in order to ensure that the fuel element can endure the heat conditions of the reactor core in normal operation and have a safe margin within transient conditions during its in reactor life.

Among the parameters that governs the myriad of processes that occurs during irradiation of fuels rods, the fuel temperature, is by far the most important one (i.e. it dominates the FGR and swelling mechanisms)^[1]. The correct prediction of the fuel temperature profile is therefore the basis for the simulation of integral fuel rods by means of fuel performance codes. The objective of this work is to assess the ability of a computer code TRANSURANUS (TU) to predict the performance of MOX fuel rods within thermal and fast reactors with main focus drawn on thermal conductivity. Thorough investigation is given to the thermal conductivity prediction since it is the direct parameter used in determining the temperature profile and the prediction of melting in the investigated fuel rods. Various phenomena occurring in MOX fuel (Densification, Swelling, Relocation, etc.) during irradiation were investigated to assess the integral capability of the code to model the thermal performance of the rods.

The study involves the analysis of four MOX rods. Two of them were irradiated in Halden heavy Boiling Water Reactor (HBWR) within IFA-597 experiment. The other two were irradiated in Experimental Breeder Reactor #2 (EBR-II) for Hanford Engineering Development Laboratory HEDL P-19 experiment.

IFA-597.4/5/6 experiment was done within the framework of the Halden Reactor Project (HRP) to investigate the thermal performance and FGR characteristics of MOX fuel. The main objective was to gather in-pile measurements of two MOX rods (Solid and hollow) that can be used for further analysis and give more insight about the behavior of MOX within thermal, water cooled reactors. Another objective was the investigation of the difference between the behavior of MOX in solid rods and the hollow rods.^[2]

HEDL P-19 experiment took place in 1971 in EBR-II reactor to investigate the effect of initial fuel-to-cladding diametral gap sizes on the linear-heat-rate needed to cause incipient fuel melting (power-to-melt), Q'_m , at beginning-of-life. Six-teen fresh MOX fueled rods representative of the Fast Flux Test Facility (FFTF) driver fuel were irradiated in this test. The results can also be projected on FBR fuel as well. The rods were subjected to power ramps at a specific designed linear power to induce melting.

 Ricerca Sistema Elettrico	Sigla di identificazione ADPFISS – LP2 – 087	Rev. 0	Distrib. L	Pag. 20	di 229
--	--	------------------	----------------------	-------------------	------------------

Some of the rods experienced melting and some did not. In this work, two rods P-19-2 (experienced melting) and P-19-5 (did not experience melting) were investigated.^[3]

 Ricerca Sistema Elettrico	Sigla di identificazione	Rev.	Distrib.	Pag.	di
	ADPFISS – LP2 – 087	0	L	21	229

2 Theoretical background

2.1 Thermal conductivity of ceramic fuel

Thermal conductivity is a property representing the ability of a solid material to transfer heat. There are three phenomena considered when modelling thermal conductivity. Lattice vibrations, Radiation Heat Transfer and electronic conductivity^[4].

Lattice vibration thermal conductivity (k_{latt}) is modelled by assuming the solid to be an ideal gas consisting of phonons. Phonons are quasi particles representing the wave nature of the vibrating solid in the lattice. They tend to collide with each other and with defects in the crystal with a certain mean free path. They transport their energy as they translate in the medium from the hot side to the cold one. Thermal conductivity depends on the amount of energy a phonon can carry and the mean free path of the phonon^[5]. Phonon's mean free path should be inversely proportional to the temperature. Due to the presence of point defects in the crystal solid that acts as a barrier to phonon's mobility, the mean free path cannot keep monotonically increasing as the temperatures gets lower^[5]. This requires that the mean free path is inversely proportional to temperature plus an extra constant term representing phonon scattering with defects. Being proportional to the mean free path of the phonon, k_{latt} would be written as:

$$k_{latt} = \frac{1}{A + BT} \quad \text{Eq. 2-1}$$

Where A, and B are constants, and T is the temperature in (K).

Heat is conducted as well with radiation on the form of electromagnetic waves. Energy is transported due to the movement of charged particles (protons and electrons) which emit some of their energy on the form of electromagnetic radiation^{[5][6]}. Radiation term of thermal conductivity (K_{rad}) is written on the form of a constant times the cube of temperature:

$$k_{rad} = CT^3 \quad \text{Eq. 2-2}$$

At temperatures high enough, energy is sufficient to generate an amount of electron-hole pairs that contribute to thermal conductivity (K_{el})^[7].

$$k_{el} = 2 \left(\frac{K_b}{e} \right)^2 T \left[\sigma + \frac{2\sigma_e \sigma_h}{\sigma} \left(\frac{E_g}{2K_b T} + 2 \right) \right] \quad \text{Eq. 2-3}$$

Where:

k_{el} = electronic contribution to thermal conductivity.

 Ricerca Sistema Elettrico	Sigla di identificazione	Rev.	Distrib.	Pag.	di
	ADPFISS – LP2 – 087	0	L	22	229

K_b = Boltzmann constant, 1.38×10^{23} (J/K)

e = electron charge, 1.6×10^{-19} (Coul)

$\sigma_{e/h}$ = electron/hole contribution to electrical conductivity ($\frac{1}{\Omega m}$)

$\sigma = \sigma_e + \sigma_h (\frac{1}{\Omega m})$

E_g = energy gap between conduction and valence bands (J)

The first term on the right hand side of Eq. 2-3 is the conductivity effect of holes and electrons separately. The second term represents the ambipolar effect, which is the release of the kinetic energy of both the electron and the hole when they recombine together plus the release of their generation energy at areas of lower temperature leading to the transfer of heat electronically.

This equation can be simplified using some experimental data and assumptions to be written on the form:^[4]

$$k_{el} = D \frac{e^{-\frac{E}{T}}}{T^n} \quad \text{Eq. 2-4}$$

Where D, E and n are constants. It should be noted that n differs from one model to another.

These physical principles of heat conduction and their equation forms are generally taken into account in the models even if they can be implemented in different ways. In general, all the thermal conductivity models implemented in fuel pin mechanic codes take the lattice vibration term into account and most of them will include one of the other two principle. Few models take all three principles into account.

2.2 Effect of temperature

Thermal conductivity of UOx and MOX is a property that depends on temperature. It has been noted experimentally that the thermal conductivity decreases with temperature until a minimum is reached in the range between (1500 to 2000) K as shown in *Figure 2-1*. This decrease is due to the lattice vibration term, which is inversely proportional to the temperature. At temperatures above the plateau range, the thermal conductivity begins to rise again due to the radiation and electronic term. Radiation heat conduction takes place above the plateau temperature even though it is not that much significant^[5]. Electronic term of the thermal conductivity is the second term that is responsible for the increase of thermal conductivity.

As usual, the lattice vibration is implemented including other factors that affect the heat conductivity other than temperature (e.g. burn-up rate, deviation from stoichiometry, etc). Some models, take the radiation conduction term into consideration to explain the increase of thermal conductivity at higher temperatures, while others relate that increase to the electronic conduction term.

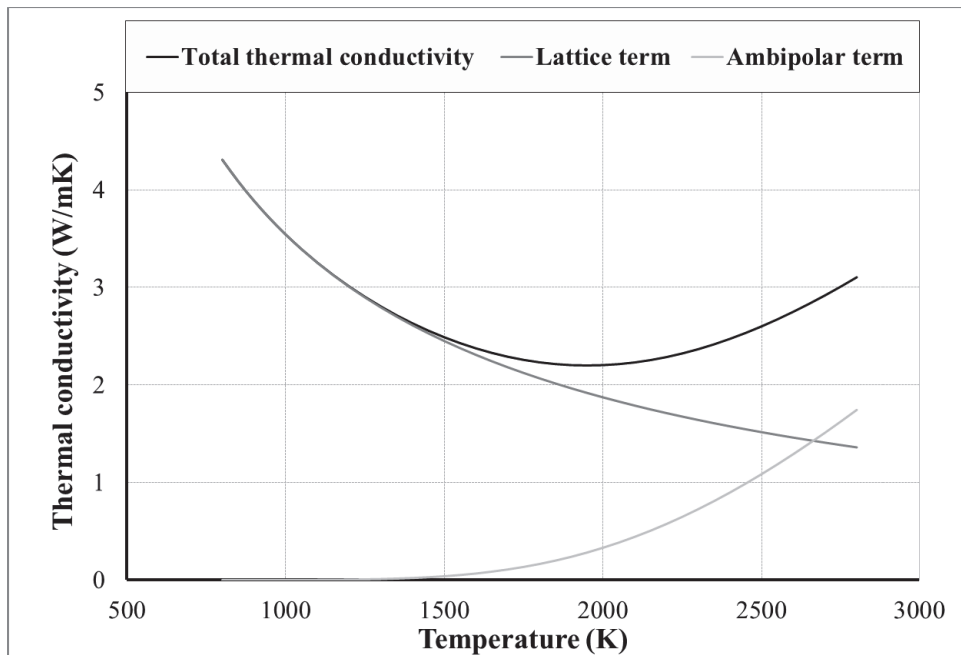


Figure 2-1 $(U-Pu)_y-O_x$ fuel total thermal conductivity along with its different constituting components.

2.3 Effect of stoichiometry

The theoretical oxygen to metal ratio (O/M) between Uranium or Plutonium oxide $(U-Pu)O_2$ is two. Deviation from this value is generally adopted by design and is induced in the nuclear fuel as effect of irradiation. The deviation can lead to hyper (>2) or hypo (<2) stoichiometric state of the fuel^[8].

The effect of deviation from stoichiometry is generally modeled by assuming that this deviation causes more defects in the lattice. This perturbation is included in the constant A in Eq. 2-1 which represents the phonon-defect interaction in the lattice and determined originally for stoichiometric fuel conditions.

The modification of Eq. 2-1 due to deviation from stoichiometry can be written as:

$$k_{latt} = \frac{1}{A_0 + Cx + BT} \quad \text{Eq. 2-5}$$

Where A_0 is the constant A for stoichiometric fuel and C is a constant multiplied by x which is the deviation from stoichiometry $(O/M-2)$. Therefore, the higher the deviation from stoichiometry, the lower the thermal conductivity becomes (Figure 2-2). Deviation from stoichiometry also affects the behavior of thermal conductivity with temperature. In fact, as the fuel deviates from stoichiometry the lower the temperature at which the thermal conductivity reaches its minimum. It can be noticed as well that the effect of deviation from stoichiometry is important at lower temperatures while at higher temperature where the ambipolar term is more important, the effect of deviation from stoichiometry is less significant.

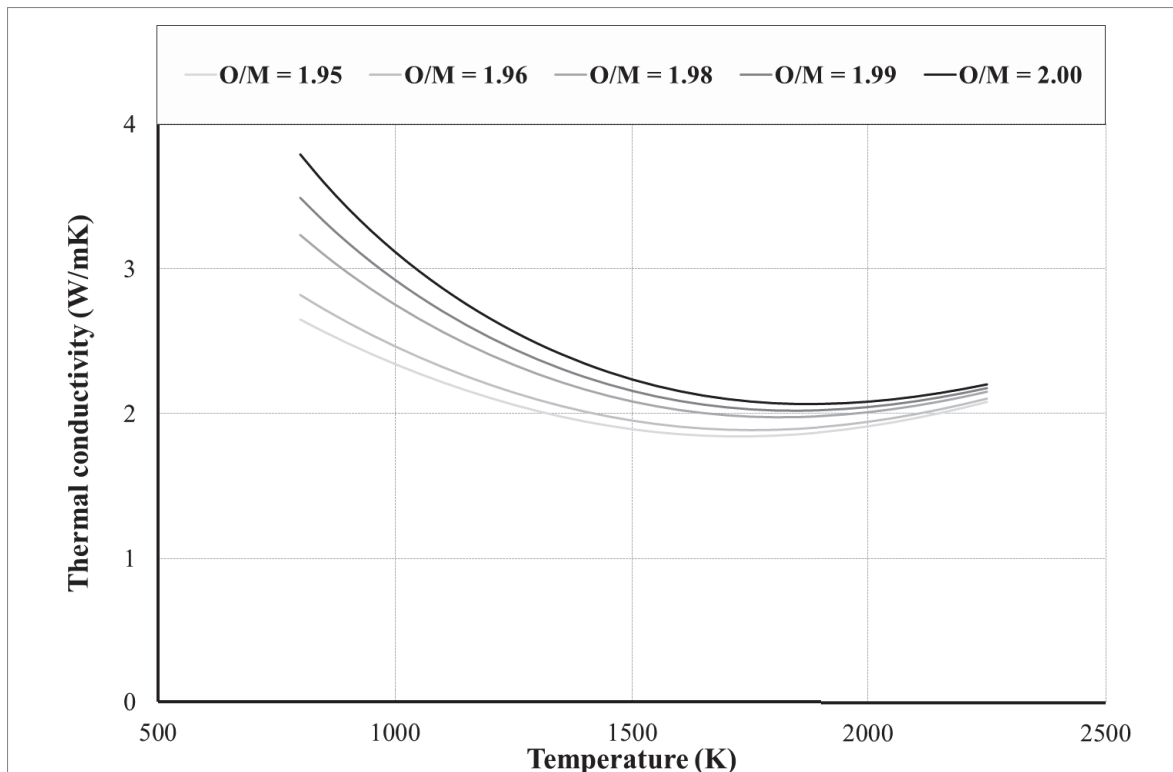


Figure 2-2 $(U-Pu)_yO_x$ conductivity: effect of deviation from stoichiometry on the thermal conductivity.

2.4 Effect of burn-up

The irradiation process that takes place in a nuclear reactor leads to various changes in the properties of the fuel pellet. Defects in the lattice, porosity increase, deviation from stoichiometry and fuel cracking with irradiation leads to degradation of the thermal conductivity. This effect is important in fast reactors (FR) since burn-up can reach to more than 10% of the original weight content of the uranium and plutonium^[8]. Solid fission products have different effects on thermal conductivity. In general, those that are dissolved tend to decrease the thermal conductivity, while those that are precipitated tends to increase it. Fission gases results in thermal conductivity degradation. The integral effect is however a degradation of conductivity with increasing burn-ups.

It is noticed as well that the higher the burn-up, the lower the rate of change of thermal conductivity with temperature *Figure 2-3*. Also as the burn-up increases, the lower the temperature for which the thermal conductivity reaches its minimum becomes before it increases again. At burn-up of $100 \frac{MWd}{kgHM}$, the thermal conductivity is slightly changing with temperature until the temperature is above 1500 K where the effect of the ambipolar term of thermal conductivity starts to rise. This behavior is explained by the increase of the defects in the solid due to irradiation. As a consequence of this, the phonon-defect interaction in the fuel dominates with respect to the temperature dependent phonon-phonon interaction term.

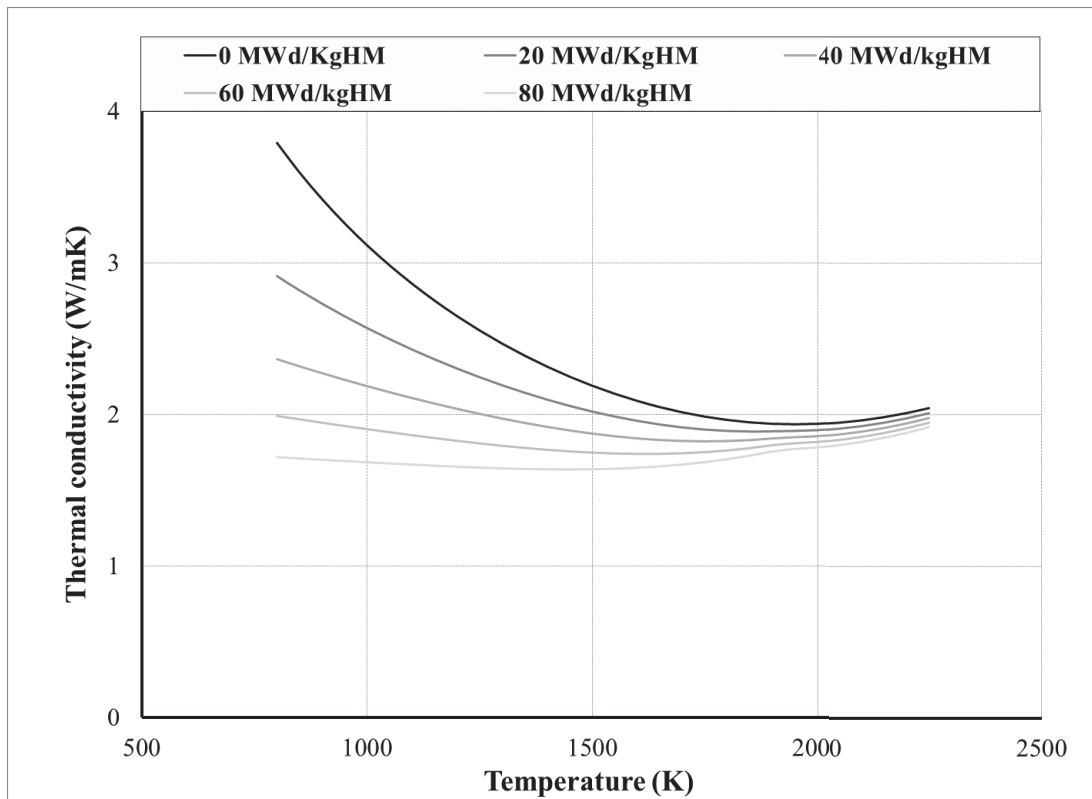


Figure 2-3 (U-Pu)_y-O_x conductivity: effect of burn-up on the thermal conductivity.

2.5 Effect of fuel porosity

The presence of voids in the solid fuel pin leads to degradation of its thermal conductivity. A poreless fuel is required to obtain the maximum thermal conductivity. On the other side, the presence of pores in the fuel pin is important to accommodate the release of fission gases that are formed during irradiation. Fission gases can cause internal pressure of the fuel pin to increase leading to deformation and swelling of the fuel. This effect is more important for fast reactors than thermal reactors because the higher power density leads to more generation of fission gases [8].

The porosity (P) is defined as the volume of the pores inside the fuel divided by the total volume of the fuel this can be written as:

$$P = 1 - \frac{\rho}{\rho_{TD}} \tag{Eq. 2-6}$$

Where ρ is the smeared density of the fuel, and ρ_{TD} is the theoretical density of the fuel's material without pores. The effect of porosity on thermal conductivity is considered by using a correction factor of the thermal conductivity. This factor has many formulations but the most used are the modified Loeb formula:

$$k = k_{TD}(1 - \alpha P) \tag{Eq. 2-7}$$

or the Maxwell-Eucken formula:

$$k = k_{TD} \frac{1-P}{1+\beta P} \quad \text{Eq. 2-8}$$

Where k_{TD} is the thermal conductivity of the poreless fuel, α and β are constants. Theoretically, the values of α is 1 and β is 0.5. Experimentally, the noticed values of these factors are higher than what the theory predicts. This is due to the fact that the pores are not randomly distributed in the lattice^[9]. The wide range of values used for the constants α and β shows that they are in fact variables that depend on the pore shape. The values assigned to them represents an average of the porosity effect.

2.6 Effect of Plutonium content

The effect of Plutonium on the constants A and B in the lattice vibration thermal conductivity term has been carefully studied. Evidence does not show any systematic trend for the variation of the constant A, while it shows a systematic increase of the constant B in Eq. 2-1. Overall the effect of increasing Plutonium's content in the fuel is a decrease of the thermal conductivity of MOX fuel^[5]. This decrease reaches up to 15% for a plutonium content of around 25 wt.%.

2.7 Summary of parameters affecting thermal conductivity

Table 2-1 summarizes the main factors affecting thermal conductivity of MOX fuel and the type of effect they have. The weight of the effect of each factor varies between different models as illustrated in later sections in the report for a variety of models.

Factor	Effect
Temperature	The main factor that is included in all the models and correlations. Thermal conductivity decreases with Temperature upto (1500-1800 K) due to phonon-phonon interaction then increases again due to radiation and electronic conduction.
Deviation from stoichiometry	Decrease or increase of stoichiometry (2±X) leads to a decrease in thermal conductivity.
Burnup	Thermal conductivity degrades with burnup
Porosity	The more decrease of the smeared density of the fuel from the theoretical density value, the lower the thermal conductivity becomes.
Plutonium content	Increase the plutonium content of the fuel results in a degradation of the thermal conductivity of the fuel.

Table 2-1 Factors affecting thermal conductivity of MOX fuel.

 Ricerca Sistema Elettrico	Sigla di identificazione	Rev.	Distrib.	Pag.	di
	ADPFISS – LP2 – 087	0	L	27	229

3 MOX fuel conductivity correlations

In this section, the Thermal conductivity correlations adopted in TRANSURANUS code to simulate MOX fuel conductivity^[11], per literature correlations and experimental data are from various open literature sources are compared with each other. More details about the studied correlations can be found in reference

3.1 TRANSURANUS correlations

3.1.1 Correlation by Van Uffelen and Schubert

This correlation is the standard recommended correlation by TU code. It is based on the data obtained experimentally by Duriez et.al where the laser flash technique was used to measure the thermal diffusivity of MOX fuel. The Pu content of the fuel was between 3-15wt.%, O/M ratio between 1.95 and 2.0 and in the temperature range between 700-2300K. The thermal conductivity was modeled by using values of the heat capacity calculated from Kopp's law^[10]. The ambipolar electronic thermal conductivity term is based on the work of Ronchi et.al in which they measured the thermal diffusivity and the heat capacity of UO₂ for a temperature range between 500 and 1900°C using an advanced laser-flash technique that gave better results than conventional laser flash methods at high temperatures^[15]. The correlation gives the thermal conductivity of MOX as a function of temperature and burn-up:

$$k_{100} = \frac{1}{a + a_1 bu + bT + b_1 bu T_p} + \frac{c}{T^2} e^{-\frac{d}{T}} \quad \text{Eq. 3-1}$$

Where

$$a=0.0308$$

$$a_1 = 5.498 \times 10^{-3}$$

$$b = 2.515 \times 10^{-4}$$

$$b_1 = -2.498 \times 10^{-6}$$

$$c = 4.715 \times 10^9$$

$$d = 16361$$

T is in K and $T_p = \min(1923, T)$, bu is the local burn-up in $\frac{MWd}{kgHM}$

The porosity effect can be taken into account using the following correction formula:

$$k_p = k_{100} (1 - P)^{2.5} \quad \text{Eq. 3-2}$$

This correlation has been assessed assuming different conditions. Due to the lattice vibration term, the correlation predicts a decrease of thermal conductivity for 0 $\frac{MWd}{kgHM}$ fuel with temperature until it reaches a minimum around 2000 K and then begins to rise again due to the electronic heat conduction. The effect of burnup on the thermal conductivity is more important at lower temperature. At 800 K the thermal

 Ricerca Sistema Elettrico	Sigla di identificazione	Rev.	Distrib.	Pag.	di
	ADPFISS – LP2 – 087	0	L	28	229

conductivity decreased by 60% of its original value for un-irradiated fuel when the burnup reached $100 \frac{MWd}{kgHM}$. For 2000 K, the thermal conductivity for the same range of burnup decreases only by 10%.

3.1.2 Correlation by Carbajo

This correlation is based on the work of Carbajo et.al. that takes basis for best value estimation of data available from open literature available recommendations given in other works. The physically based correlation by Lucuta et.al was recommended. It gives the thermal conductivity as a function of temperature, burn-up, and deviation from stoichiometry along with a porosity correction. The correlation takes the fuel irradiation into account as well as the effect of dissolved and precipitated solid fission fragments as a separate function from the un-irradiated fully dense fuel element^[16].

The thermal conductivity for a 100%TD MOX fuel is given by

$$k_{100} = 1.158x \left(\frac{1}{a_0 + a_1X + (b_0 + b_1X)t_k} + \frac{c}{t_k^{2.5}} e^{-\frac{d}{t_k}} \right) x FD(bu, T) x FP(bu, T) x FR(T) \frac{W}{mK} \quad \text{Eq. 3-3}$$

Where

$a_0=0.035$, $a_1=2.85$, $b_0=0.286$, $b_1=-0.715$, $c=6400$ and $d=16.35$

X is the deviation from stoichiometry,

$t_k = \frac{T}{1000}$ and T is the temperature in [K]

The factor FD represents the negative effect of dissolved fission fragments on the thermal conductivity and is defined as:

$$FD(bu_{at}, T) = \omega \left[\arctan\left(\frac{1}{\omega}\right) \right] \quad \text{Eq. 3-4}$$

For $bu_{at} > 0$ and

$$FD(0, T) = 1 \quad \text{Eq. 3-5}$$

where

$$\omega = \frac{1.09}{bu_{at}^{3.265}} + 0.0643 \left(\frac{T}{bu_{at}} \right)^{1/2} \quad \text{Eq. 3-6}$$

bu_{at} is the burnup in at.%

The factor FP represents the increase in thermal conductivity due to the precipitated solid fission products:

$$FP(bu_{at}, T) = 1 + \frac{0.019bu_{at}}{(3 - 0.019 bu_{at}) \left[1 + \exp\left(-\frac{T - 1200}{100}\right) \right]} \quad \text{Eq. 3-7}$$

 Ricerca Sistema Elettrico	Sigla di identificazione	Rev.	Distrib.	Pag.	di
	ADPFISS – LP2 – 087	0	L	29	229

The factor FR accounts for radiation effects. It is important below 900 K and reaches near unity rapidly above 900K and does not play a significant role above that temperature.

$$FR(T) = 1 - \frac{0.2}{1 + \exp\left(\frac{T - 900}{80}\right)} \quad \text{Eq.3-8}$$

The porosity effect is modelled using the Maxwell-Eucken correction formula

$$k_p = k_{100} \left(\frac{1 - P}{1 + 2P} \right) \quad \text{Eq.3-9}$$

The correlation predicts a decrease of thermal conductivity with temperature due to lattice vibration until it reaches a minimum around 2000 K. Then, it begins to rise again due to the electronic heat conduction. It can be noticed as well the decrease of thermal conductivity with burnup. The effect of burnup on the thermal conductivity is more important at lower temperature. At 800 K, the thermal conductivity decreased by 40% of its original value for un-irradiated fuel when the burnup reached 10 at.%. For 2000 K, the thermal conductivity for the same range of burnup decreases by 15%.

It can be noticed that the lower the temperature, the higher the degradation of thermal conductivity with deviation from stoichiometry. For 800 K the thermal conductivity decreases by 30% for a deviation from stoichiometry of 0.05. At 2000 K for the same range of deviations, the decrease of thermal conductivity is around 8% and decreases more as the temperature goes higher.

3.1.3 Correlation by Lanning and Beyer

This correlation gives the thermal conductivity for 95%TD MOX according to Lanning and Beyer. The correlation is based on the work of Duriez et al.^[10] It gives the thermal conductivity as a function of temperature, burnup and deviation from stoichiometry included in the lattice vibration term and another term for ambipolar thermal conductivity that is a function of temperature only.

The thermal conductivity for MOX 95%TD is given by:

$$k_{95} = \frac{1}{(A(X) + B(X)T + f(bu) + (1 - 0.9e^{-0.04bu})xg(bu)xh(T))} + \frac{C_{mod}}{T^2} e^{-\frac{D}{T}} \quad \text{Eq.3-10}$$

Where:

X is the deviation from stoichiometry and

$$A(x) = 0.035 + 2.85X$$

$$B(X) = (2.86 - 7.15X)x10^{-4}$$

$$f(bu) = 1.87x10^{-3}xbu$$

$$g(bu) = 0.038xbu^{0.28}$$

$$h(T) = \frac{1}{1 + 396e^{\frac{-6380}{T}}}$$

$$C_{mod} = 1.5 \times 10^9$$

$$D = 13520$$

T is in K and the burnup is in $\frac{MWd}{kgHM}$.

A porosity correction term according to Lucuta applies to obtain the thermal conductivity at different real densities. The porosity correction is on the form of Maxwell-Eucken formula:

$$k_p = k_{95} \times 1.0789 \times \left(\frac{(1-P)}{1+0.5P} \right) \quad \text{Eq.3-11}$$

The correlation predicts decrease of thermal conductivity with temperature until it reaches a minimum between 1850 and 1900 K then begins to rise again due to the electronic heat conduction. for a 95%TD of the fuel at different burnups. The effect of burnup on the thermal conductivity is more important at lower temperature The degradation of conductivity in the order of 40% at 800K (in the range 0 – 100MWd/kgHM). At 2000 K, the thermal conductivity for the same range of burnup decreases by 18%.

The more hypostoichiometric the fuel is, the higher the decrease of the thermal conductivity becomes. For a change of O/M from 2 to 1.95, the decrease in thermal conductivity can reach upto 30% at 800 K. This effect gets lower as the temperature goes high. At 2000 K and the reduction in thermal conductivity on the same range of change of O/M ratio is about 8%.

3.1.4 Correlation by Wiesenack.

Correlation 34 is the original Wiesenack's correlation that is developed for UO₂ fuel. In order to apply it for MOX, the correlation is multiplied by a correction factor of 0.92. The original correlation gives the thermal conductivity of MOX as a function of temperature and burnup on the form:

$$k_{95} = \frac{1}{A_0 + A_1 bu + Bx \min\{1650, \vartheta\} + B_2 bu x \min\{1650, \vartheta\}} + C e^{D\vartheta} \left[\frac{W}{mK} \right] \quad \text{Eq.3-12}$$

Where:

$$A_0 = 0.1148$$

$$A_1 = 0.0035$$

$$B = 2.475 \times 10^{-4}$$

$$B_2 = -8.24175 \times 10^{-7}$$

$$C = 0.0132$$

$$D = 0.00188$$

And ϑ is the temperature in [$^{\circ}$ C] and bu is the burn-up in $\frac{MWd}{kgUO2}$

 Ricerca Sistema Elettrico	Sigla di identificazione	Rev.	Distrib.	Pag.	di
	ADPFISS – LP2 – 087	0	L	31	229

There is no specific equation for porosity correction given for this model so the original MATPRO-11 porosity correction is used:

$$k_p = k_{95} \frac{1 - \beta P}{1 - 0.05\beta} \quad \text{Eq.3-13}$$

Where P is the porosity and $\beta = 2.58 - 0.58 \times 10^{-3} \theta$

The correlation predicts a decrease of thermal conductivity with temperature until it reaches a minimum between 1700 and 1900 K. For un-irradiated fuel, the minimum of thermal conductivity is reached at 1900. The correlation indicates that as the burnup of the fuel increases, that minimum in thermal conductivity is reached at a lower temperature. The minimum in thermal conductivity at burnup of $100 \frac{MWd}{kgUO_2}$ is reached at a temperature range between 1500 to 1600.

The effect of burnup on the thermal conductivity is higher at lower temperature. At 800 K the thermal conductivity decreased by 55% of its original value for un-irradiated fuel when the burnup reached $100 \frac{MWd}{kgHM}$. For 2000 K, the thermal conductivity for the same range of burnup decreases by 25%. The burn-up at temperatures higher than 2000K seems to have a constant effect. The amount of thermal conductivity decrease is the same regardless of the initial level of thermal conductivity.

3.2 Open Literature correlations

Several open literature correlations are described along with the variables that are considered.

3.2.1 Martin review 1982

In this work, Martin did a re-appraisal of four thermal conductivity correlations by (Washington, Aniscough, Killeen and Brandt) and chose one of them to do some amendments on. The correlation chosen was that based on Washington's review in 1973. Even though the correlation by Killeen was the most physically based correlation for stoichiometric fuel, That of Washington was selected since there were no theoretical knowledge to apply the first one to non-stoichiometric fuel. The two correlations are close to each other at low and high temperature range, and even in the intermediate one, the deviation of Washington's correlation from that of Killeen should not cause great errors^[9]. The data available were reappraised and the few new data that appeared since the work of Washington were added to the review. The correlation seemed to be giving satisfactory results for UO₂ and MOX as a function of temperature and O/M ratio.

The amended correlation can be written for hypostoichiometric MOX as:

$$K_{100} = \frac{1}{0.037 + 3.33X + 2.37 \cdot 10^{-4}T} + 78.9 \cdot 10^{-12}T^3 \quad \text{Eq.3-14}$$

 Ricerca Sistema Elettrico	Sigla di identificazione	Rev.	Distrib.	Pag.	di
	ADPFISS – LP2 – 087	0	L	32	229

The original correlations were tailored for UO₂ and were adapted to MOX by assuming a correction factor of 0.95. The new correlation neglected the effect of irradiation in the temperature range of (500-2800 °C) and the effect of plutonium content. It took the O/M ratio into account in the lattice vibration term. The porosity correction was based on a modified Loeb formula for porosity level between (0 < P < 0.1) and based on Maxwell-Eucken formula in the range of (0.1 < P < 0.2).

The effect of deviation from stoichiometry is a degradation of the thermal conductivity. This effect is predicted from this correlation to be from 42% (at temperature of 800 K) to a value of 18% (at 2000K, it decreases with temperature) for a stoichiometry change between (2 and 1.95). The effect of stoichiometry keeps decreasing with temperature but it can be considered important on the whole range of normal operation of a thermal and fast reactor fueled with MOX.

3.2.2 FTHCON subscode-MATPRO

The correlation used by the FTHCON subroutine determines the thermal conductivity of un-cracked UO₂ and MOX fuels as a function of temperature, O/M ratio and plutonium content of a solid fuel. It uses a porosity correction based on the Maxwell-Eucken relation. The burnup is used only to calculate the melting temperature of the fuel. Interpolation is used to remedy the discontinuity of the slope in the temperature range between (1364-2300 K) [7].

The correlation is on the following form:

$$= \left[\frac{D}{1 + (6.5 - 0.00469T'(1 - D))} \right] \left[\frac{C_v}{(A + BT'')(1 + 3e_{th})} + 5.2997 \times 10^{-3} T e^{\left[\frac{-13358}{T} \right]} \left\{ 1 + 0.169 \left[\frac{13358}{T} + 2 \right]^2 \right\} \right] \quad \text{Eq.3-15}$$

Where:

K = Thermal conductivity (W/m.K)

D = fractional theoretical density

C_v = Phonon contribution to the specific heat at constant volume (J/kg.K). MATPRO correlation for specific heat is used to calculate this factor.

e_{th} = Linear strain caused by thermal expansion for temperatures above 300 K.

MATPRO correlation for linear strain is used to calculate this factor for uranium and plutonium then the value is weighted according to the percentage of Plutonium in the fuel.

A = represents the point defect contribution to the phonon's mfp. = 0.339 + 12.6X where X is the absolute value of the deviation from stoichiometry

B = a factor representing the phonon-phonon scattering contribution to the thermal conductivity. = 0.06867(1 + 0.6238 PU) where PU is the weight fraction of the plutonium content of the fuel.

T = Fuel temperature in (K)

 Ricerca Sistema Elettrico	Sigla di identificazione	Rev.	Distrib.	Pag.	di
	ADPFISS – LP2 – 087	0	L	33	229

T' = Fuel temperature if <1364 .

For temperature higher than 1834 then $D\{1 + [6.5 - 0.00469T']\} = -1$

For intermediate range ($1364 < T < 1834$), linear interpolation is used to obtain the value of T'

T'' = Fuel temperature if $T < 1800$

2050 if $T > 2300$

Between ($1800 < T < 2300$) Linear interpolation is used to obtain the value of T''

Even though the deviation from stoichiometry is included in the model as a parameter determining thermal conductivity, it is slightly sensible with respect to deviation from stoichiometry (compared to the other models). The maximum change of thermal conductivity at temperature of 500 K is less than 2% and decreases more with temperature to reach less than 0.3% at 3000 K.

The correlation predicts a change of thermal conductivity between (12 to 9)% with the plutonium content (0 to 30 wt.%) between 500K and 2250 K respectively. This shows a rate of decrease of (0.4 to 0.3%) for every unit wt.% increase in Plutonium content. The results shows that the thermal conductivity is more dependent on Plutonium content than on deviation from stoichiometry.

3.2.3 The COMETHE formulation-1982

This formula is used for UO_2 and MOX fuels. It gives thermal conductivity of 95%TD fuel. A porosity correction is used to give the thermal conductivity at different porosities. It was enhanced to take the plutonium weight percentage into account based on the data from Gibby, Van Crynest and Weilbacher^[17]. The formula is written as follows:

$$K_{95TD} = \frac{A_0}{A_1 + A_2X + (1 + B_0q)T} + CT^3 \quad \text{Eq.3-16}$$

Where:

K_{95TD} is given in (W/cm.K)

T = temperature (K)

X = absolute value of deviation from stoichiometry

q = Plutonium content

$A_0 = 40.05$

$A_1 = 129.4$

$A_2 = 16020$

$B_0 = 0.8$

$C = 0.6416 \times 10^{-12}$

The model predicts a decrease in thermal conductivity at lower temperature of about 0.5% for every 1wt.% increase in the Plutonium content for stoichiometric fuel. The rate of decrease slightly decreases above 2000 K. The decrease of thermal conductivity with hypostoichiometry can reach up to 42% decrease in thermal conductivity at lower temperatures (800 K). This effect decreases with temperature to reach around 18% decrease with stoichiometric decrease from 2 to 1.95 at 2000 K.

 Ricerca Sistema Elettrico	Sigla di identificazione	Rev.	Distrib.	Pag.	di
	ADPFISS – LP2 – 087	0	L	34	229

For the whole range of temperatures of interest, the change of thermal conductivity with deviation from stoichiometry is higher than that due to increase of plutonium content of the fuel.

3.2.4 Baron Hervé 1995 Model

The model is a modification of the same model that originated in 1994. The modification concerns the high temperature term. It included originally a term relating high temperature conductivity to radiation. The modification substituted this term by another one that considers electronic thermal conductivity instead. This was done based on the work by Delette and Charles^[17]. The model takes the temperature, deviation from stoichiometry, plutonium and Gadolinium content as variables. In order to apply this model to MOX fuel, the Gadolinium content should be set to zero in Eq.3-17.

$$K(T) = \frac{1}{A_0 + A_1x + A_2g + A_3g^2 + (B_0(1 + B_1q) + B_2g + B_3g^2)T} + \frac{C + Dg}{T^2} \exp\left(-\frac{W}{kT}\right) \quad Eq.3-17$$

Where:

k =Boltzmann constant ($1.38 \cdot 10^{-23}$ J/K)

$W = (1.41 \cdot 1.6) \cdot 10^{-19}$ J

$A_0 = 4.4819 \cdot 10^{-2}$ (m.K/W), $A_1 = 4$, $A_2 = 0.611$ (m.K/W), $A_3 = 11.081$ (m.K/W)

$B_0 = 2.4544 \cdot 10^{-4}$ (m/W), $B_1 = 0.8$, $B_2 = 9.603 \cdot 10^{-4}$ (m/W), $B_3 = -1.768 \cdot 10^{-2}$ (m/W)

$C = 5.516 \cdot 10^9$ (W.K/m)

$D = -4.302 \cdot 10^{10}$ (W.K/m)

T is temperature in K up to 2600 K,

x is the absolute value of deviation from stoichiometry,

q is the plutonium weight content, and g is the Gadolinium weight content.

The model predicts the same effect of Plutonium as in the COMETHE formulation. Similar to the COMETHE formulation, the decrease of thermal conductivity with hypostoichiometry can reach up to 42% decrease in thermal conductivity at lower temperatures (800 K). This effect decreases with temperature to reach around 18% decrease with O/M ratio decrease from 2 to 1.95 (2000 K). For the whole range of temperatures of interest, the change of thermal conductivity with deviation from stoichiometry is higher than that due to the increase of plutonium content of the fuel.

3.3 Experimental data and correlations

The correlations presented in the previous sections are compared with experimental data from a variety of sources.^{[10][18][19]}

The comparison is done at different states of the modeling parameters used in the different correlations to be able to understand how sensitive the models are to those parametric changes and how much do they agree with the experimental data at the different levels of the modeling parameters. All the comparisons with experimental data are done at zero burn-up since there were no other data possessed at higher burn-up values. In order to distinguish the TRANSURANUS models from the open

literature correlations, the figures mentioned hereafter are plotted with this logic: solid lines will represent TU correlations while the open literature correlations are in dotted lines.

Table.3-1 summarizes the difference between all the studied models in terms of the parameters they take into account. *Table.3-2* summarizes the data sources used in each subsection and their details.

Name of the correlation	Temperature	Deviation from stoichiometry	Burn up	Plutonium content	Porosity	Source
Van Uffelen and Schubert	×		×		×	Standard TU
Carbajo	×	×	×		×	TU
Lanning and Beyer	×	×	×		×	TU
Wiesenack	×		×		×	TU
Martin	×	×		×	×	OL
Matpro	×	×		×	×	OL
COMETHE	×	×		×	×	OL
Baron Hervè	×	×		×	×	OL

Table.3-1 Summary of thermal conductivity correlations for MOX.

Data source	Year	Temperature range	Number of points	Levels of parameters
Van Crynest	1968	813-2188	22	100% TD, O/M=2, Pu= 20 wt.%
Fukushima	1983	826-1817	29	
Hetzler	1987	1066-2143	20	
Van crynest & Weilbacher	N/A	813-2175	26	95%TD, O/M=2, Pu= 20 wt.%
Gibby	1969	825-1882	46	
Schemidt		900-16445	9	
Gibby	1969	917-2244	13	95%TD, O/M=1.98, Pu= 20 wt.%
Weilbacher	1972	893-2685	9	
Bonnolet	1988	1163-2291	20	
Gibby	1969	770-1423	13	95%TD, O/M=1.93, Pu= 20 wt.%
Schemidt	N/A	1110-2054	9	
Van crynest & Weilbacher	N/A	785-2026	6	
Weibacher	1972	778-2370	8	96%TD, O/M=2, Pu= 6 wt.%
Duriez	2000	817-2089	32	
Industrial MIMAS Sample	N/A	812-2083	43	

Table.3-2 List of experimental data on MOX used for comparison with correlations.

1-Comparison at 100% TD, O/M=2, Pu= 20 wt.%

The correlations are compared with experimental data from three sources, *Figure 3-1*. It can be noticed that the data from Van crynst and Hetzler have a large spread that almost covers the whole range of variation between the studied correlations. The data from Fukushima are more precise and it can be seen that Martin’s correlation matches it in a quite good manner but in general, no decision with sufficient accuracy can be made from these data.

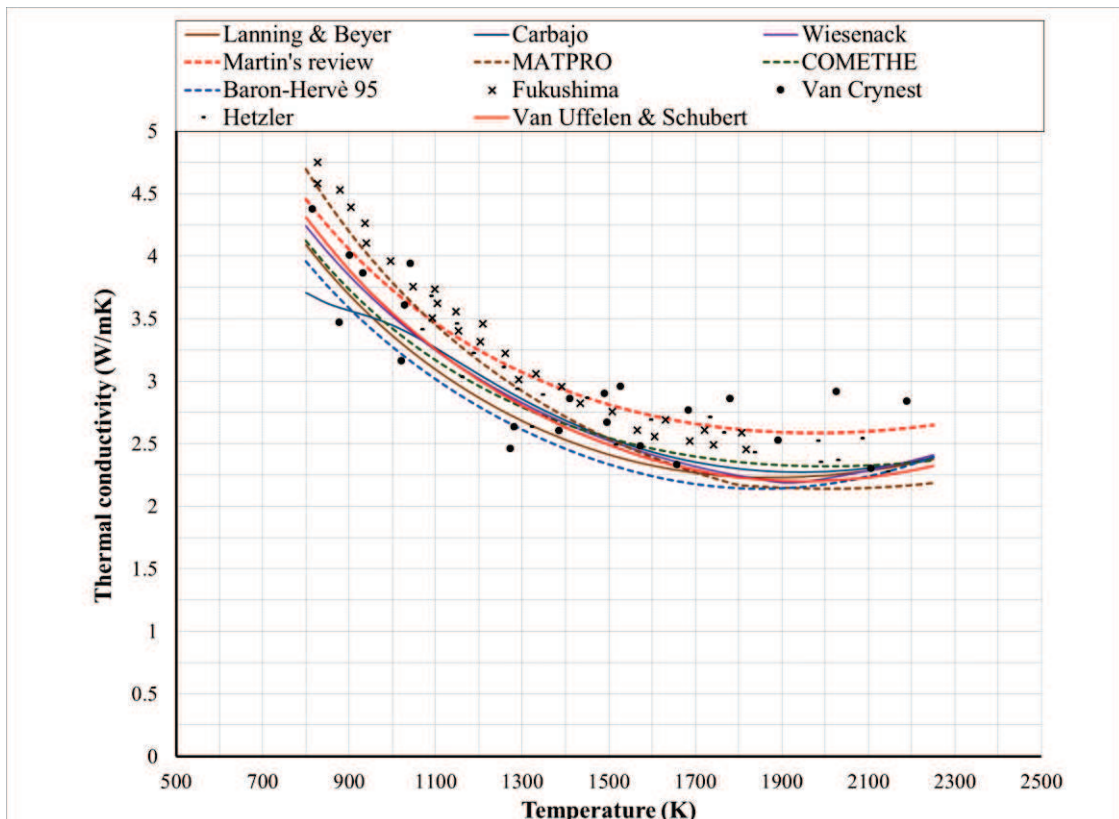


Figure 3-1 MOX thermal conductivity: comparison between correlations and experimental data for 100%TD, O/M=2, PU=20 wt.%.

2- Comparison at 95%TD, O/M=2, Pu= 20 wt.%

The correlations are compared with experimental data from three sources in *Figure 3-2*. The data from Van Crynest and Weilbacher have a large spread and spans the whole range of experimental data. A conclusion cannot be made base on their uncertainty. The data from Schemidt and Gibby are more accurate but are in opposite directions from each other’s. While Schemidt’s data are higher than all the studied correlations, Gibby’s data are lower than all of them. There is a preference given to Gibby’s data for two reasons: the first is the larger number of data points and the wider range of temperature covered. The second comes from the fact that Wiesenack’s correlation was designed for UO₂ fuel then multiplied by a factor of 0.92 to fit it to MOX. The data from Schemidt then would predict a thermal conductivity of MOX that is equal to or even higher than UO₂ (*Figure 3-3*) which contradicts the fact that the conductivity of MOX is lower than that of UO₂.

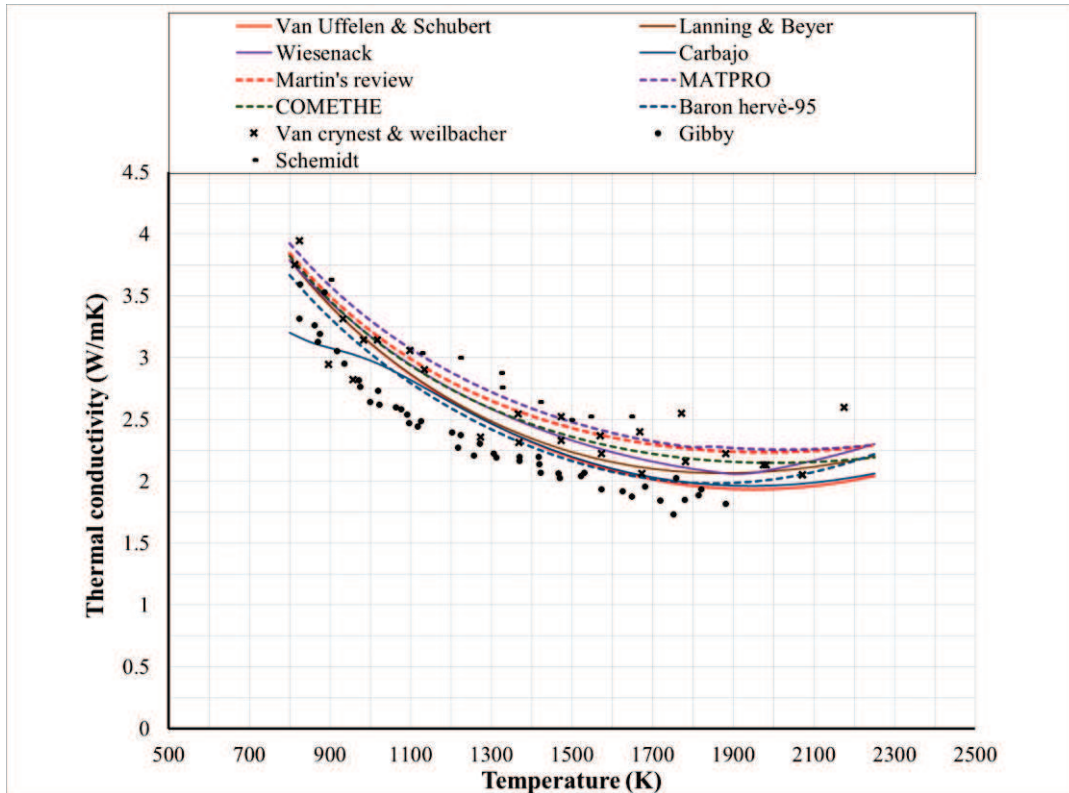


Figure 3-2 MOX thermal conductivity: comparison between correlations and experimental data for 95%TD, O/M=2, PU=20 wt.%.

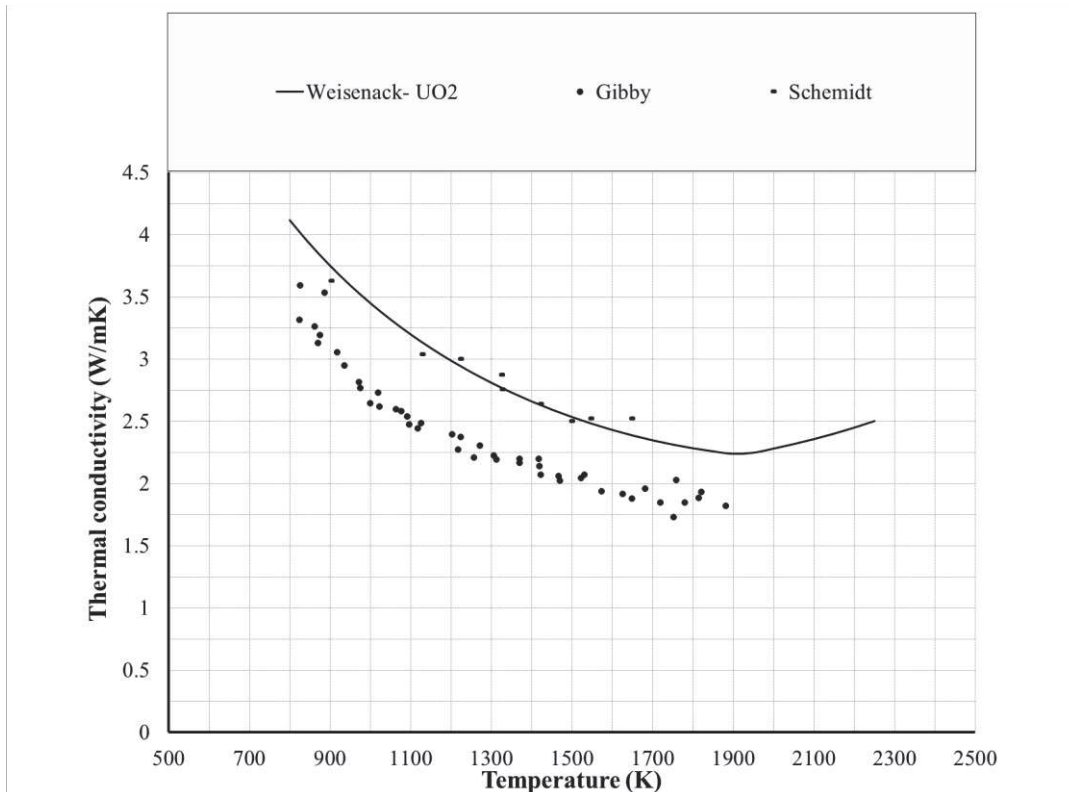


Figure 3-3 MOX thermal conductivity: comparison between Wiesenack correlation and experimental data for 95%TD, O/M=2, PU=20 wt.%.

3-Comparison at 95%TD, O/M=1.98, Pu= 20 wt.%

The correlations are compared with experimental data from three sources *Figure 3-4*. The included data are more precise than the previous cases and it can be noticed that the Baron-Hervè correlation has a good match with the data from Weilbacher and Gibby. Other correlations have a good match with the data from Bonnoret and weibacher data at higher temperatures. The TU correlations that do not take deviation from stoichiometry into account and Matpro correlation are higher than all the experimental data except for Van Uffelen and Schubert that matches the experimental data above 2000 K.

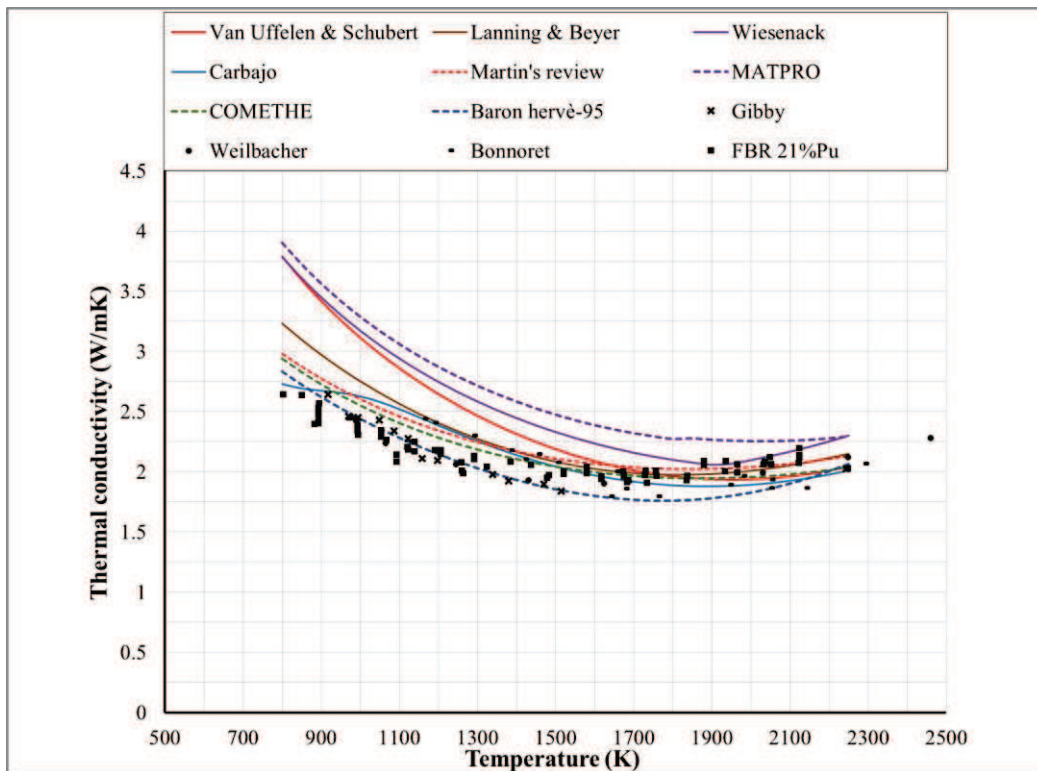


Figure 3-4 MOX thermal conductivity: comparison between correlations and experimental data for 95%TD, O/M=1.98, PU=20 wt.%.

4-Comparison at 95%TD, O/M=1.93, Pu= 20 wt.%

This is an extreme case and is reported here for clarifying the dependence of thermal conductivity on O/M ratio. A large deviation from stoichiometry leads to a drastic decrease in thermal conductivity as shown in *Figure 3-5*. It is clear that the correlations that do not take deviation from stoichiometry into account will fail to match the thermal conductivity measurements experimentally. The rest of the correlations that takes deviation from stoichiometry into account will generate a better prediction of the thermal conductivity. It is therefore visible that deviation from stoichiometry is an important factor that should be taken into account in any thermal conductivity correlation that aims to simulate non-stoichiometric fuel.

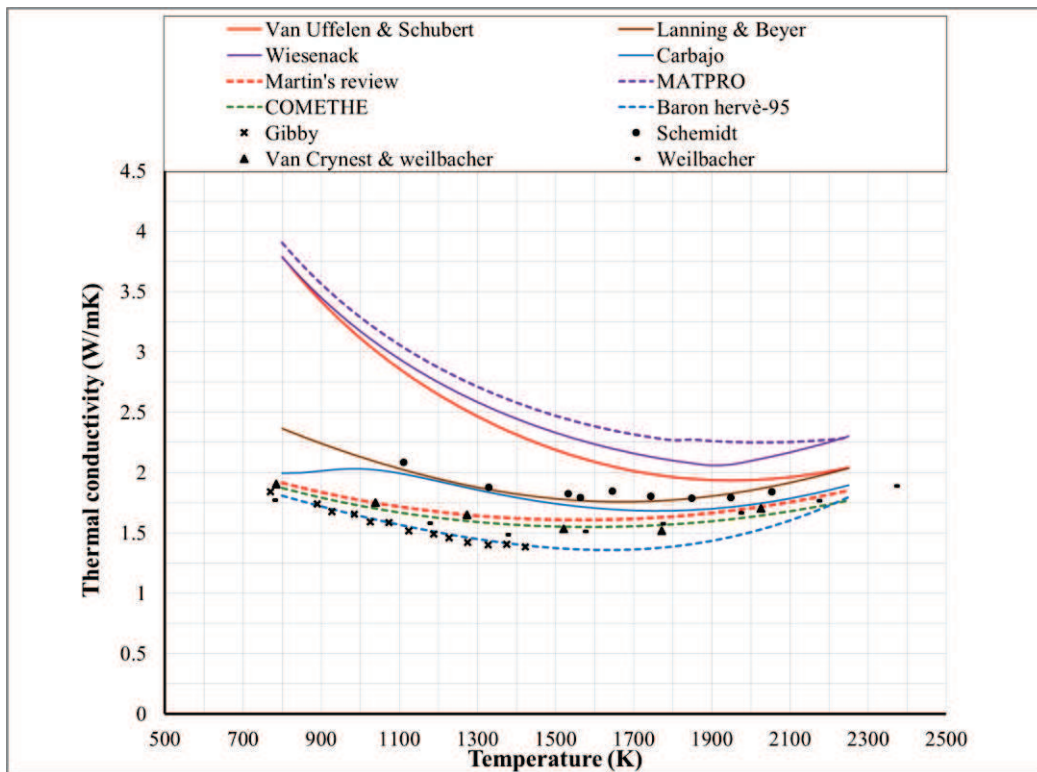


Figure 3-5 MOX thermal conductivity: comparison between correlations and experimental data for 95%TD, O/M=1.93, PU=20 wt. %.

5-Comparison at 95%TD, O/M=2, Pu= 6 wt. %

A comparison is made between the correlations and experimental data from Duriez and an industrial sample prepared used the MIMAS process (Micronized Master blend). The process aims to producing soluble fuel that would be reprocessed to a final product that fulfills the requirements for LWR MOX fuel.^[20] It can be seen (Figure 3-6) that TU thermal conductivity correlations fits well both the laboratory prepared sample of Duriez and the sample from industry. This gives an evidence of the ability of these correlations to predict the behavior of stoichiometric LWR MOX with low plutonium content. Open literature correlations seems to over-predict the thermal conductivity at lower plutonium contents except for Baron-Hervè correlation that is comparable to the samples data.

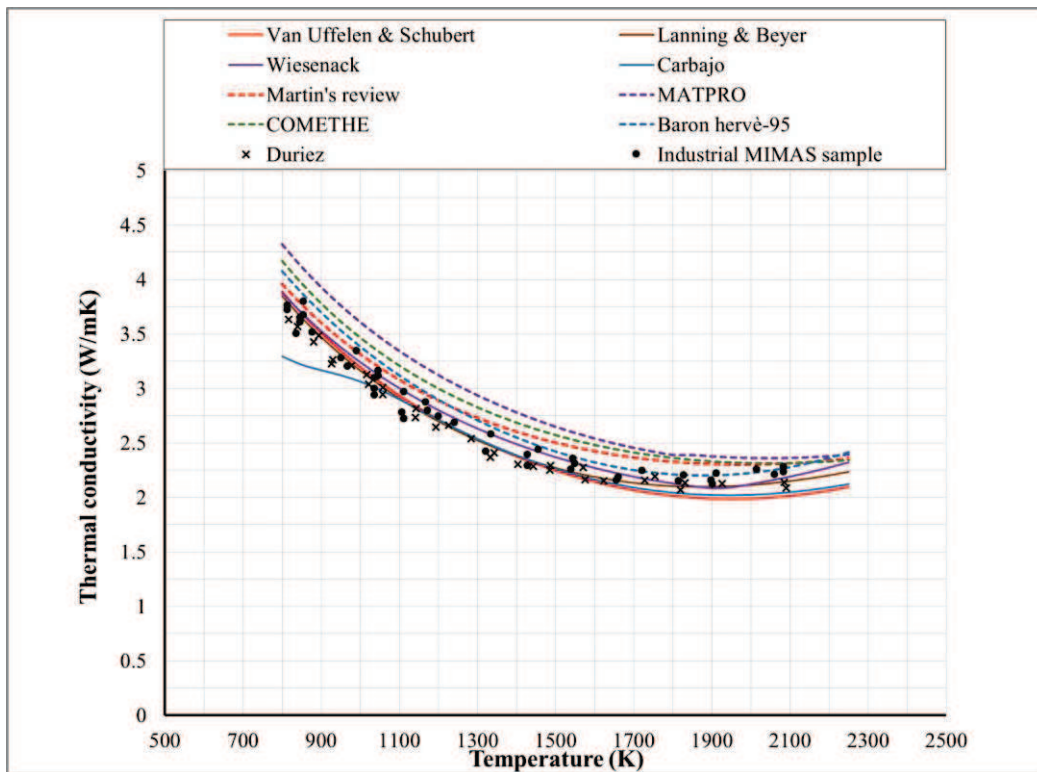


Figure 3-6 MOX thermal conductivity: comparison between correlations and experimental data for 95%TD, O/M=2, PU=6 wt. %.


3.4 Conclusive remarks

Thermal conductivity of MOX fuel is one of the parameters that govern the prediction of fuel temperature whose prediction is of great relevance to any integral fuel pin simulation. There are three mechanisms of heat conduction relevant to MOX; Lattice, Radiation and electronic conduction. Correlations used to predict thermal conductivity always consider Lattice conduction and combine it with one of the two other mechanisms to predict the conduction at higher temperatures.

There are several parameters that govern the thermal conductivity. The main parameter is the temperature that is included in all the correlations. In particular, thermal conductivity decreases with increasing the temperature up to (1500-1800 K) then starts to increase again due to enhancement of conduction due to radiation or electronic conduction phenomena.

Other parameters such as (Burnup, deviation from stoichiometry, Pu content) may or may not be included in a correlation and they vary in their importance. Therefore, it is important to investigate how critical is it not to include a certain parameter and how the correlations with different parameters deviate from each other's:

- Porosity obviously degrades the thermal conductivity
- Thermal conductivity always decreases with deviation from stoichiometry
- Thermal conductivity degrades with burnup.
- Increasing Pu content leads to a decrease in thermal conductivity.

 Ricerca Sistema Elettrico	Sigla di identificazione	Rev.	Distrib.	Pag.	di
	ADPFISS – LP2 – 087	0	L	41	229

It is important to note that thermal conductivity is more sensitive to all the investigated parameters at lower temperatures. As the temperature increases, the degradation of thermal conductivity is less sensitive to the variation of the studied parameters.

TU code includes four correlations that are used to predict the MOX fuel conductivity. They all account for temperature, porosity and burn-up as parameters. Two of them include deviation from stoichiometry. The correlations of TU do not include Plutonium content.

Four other open literature correlations were investigated and compared with the ones from TU. They do not include burnup as a factor but they include the plutonium content parameter. All of the open literature correlations include the deviation from stoichiometry, porosity and temperature as factors.


Comparing the correlations from both sources together gives some inferences related their sensitivity to various parameters. At stoichiometric conditions the correlations deviate from each other, especially in the low temperature zone. This is due to the different data on which the correlations are based and the different parameters and their weighted effect in total.

As the deviation from stoichiometry increases, the variation increases between the two TU correlations that do not include deviation from stoichiometry and all the other correlations. The thermal conductivity is much less sensitivity to variation in Pu content.

In order to confirm the results of the comparison between the correlations, experimental data were collected at different levels for each of the parameters. The role of experimental data is to judge which correlation predicts the variability with a certain parameter accurately. This was done for all the parameters except for burn-up due to non-possession of thermal conductivity data for MOX fuel at higher burn-up than zero.

The comparison confirmed the importance of deviation from stoichiometry. The correlations that do not include it will introduce a significant error if used for hypostoichiometric fuel. To sum up, A thermal conductivity correlation should include Burnup and deviation from stoichiometry which are important parameters to be included. Pu content is not that significant and could be neglected without critical errors. Porosity is taken into account as a correction factor with many formulas. Thermal conductivity at higher temperature is preferred to be modelled by electronic conduction mechanism but there is not enough data to prove it experimentally.

 Ricerca Sistema Elettrico	Sigla di identificazione ADPFISS – LP2 – 087	Rev. 0	Distrib. L	Pag. 42	di 229
--	--	------------------	----------------------	-------------------	------------------

 Ricerca Sistema Elettrico	Sigla di identificazione	Rev.	Distrib.	Pag.	di
	ADPFISS – LP2 – 087	0	L	43	229

4 TRANSURANUS code

TRANSURANUS is a code developed by the institute of Transuranium elements to be used for the thermal and mechanical analysis of nuclear fuel rods.^{[11][13]} The code includes a lot of physical models and numerical algorithms to predict the thermal and mechanical properties of the fuel rods and their effects on each other. In the next subsections, some details related to thermal, mechanical, and burn-up modelling by the code are extracted from the code's manual for illustration purpose.^[11] The code is a quasi 2D model which relays basically on the concept of superposition of 1D radial and axial analysis. The physical phenomena modelled are covered by many available models for different materials used in fuel, cladding and structure material of the rod that are valid over the various operation conditions of the rods and different time range of the states in which the rod exists from milliseconds to years. The code can be used for both deterministic and probabilistic analysis.


The choice of the desired models of the different materials is free to the code by the usage of an input file that dictates to the code the kind of analysis to be done (Deterministic or probabilistic), The reactor type, fuel and cladding types and the details of their construction parameters on the macro and micro scales. It also informs the code whether structure materials are modelled or not, the numerical algorithms to be used and the time steps and the boundary conditions of the modelled situation etc. The results of the analysis are then stored in output subroutines that can be summoned both numerically and visually using a plotting tool as a function of time for discrete axial locations in the rod or as integral values, a function of axial position of the rod, or as a function of radius at different axial positions.

The *capabilities* of the TRANSURANUS code can be summarised as follows:

- Analysis of all fuel rod types under normal, off-normal and accident conditions (deterministic and probabilistic) is in principle possible.
- Consistent steady-state and transient analysis.
- Clearly defined mechanical-mathematical framework into which physical models can easily be incorporated.
- Fast and reliable.
- Database, models and code extensively verified.
- Applied by different groups and different licensing authorities.

More details are available in Refs. [11][13]

 Ricerca Sistema Elettrico	Sigla di identificazione ADPFISS – LP2 – 087	Rev. 0	Distrib. L	Pag. 44	di 229
--	--	------------------	----------------------	-------------------	------------------

 Ricerca Sistema Elettrico	Sigla di identificazione	Rev.	Distrib.	Pag.	di
	ADPFISS – LP2 – 087	0	L	45	229

5 Analysis of LWR MOX: IFA-597 experiment

5.1 Description of the experiment

5.1.1 Background and objective of the experiment

Within the scope of the current work, it is important to give a brief description of IFA-597.4/.5/.6/.7. There were different stages of irradiation that were done in Halden reactor between July 1997 to January 2002. The experiment involved the irradiation of two MOX rods. One is a solid rod with four annular pellets on top to allow the accommodation of fuel center thermocouples. The other rod was a complete hollow pellets rod. Along with the thermocouples used to measure the centerline temperature, pressure bellows transducers were instrumented to provide data of the pressure along the time span of the experiment.^[2]

The main purpose of IFA-597.4/.6 was to study the thermal behavior of MOX including fission gas release mechanisms (FGR) when subjected to normal operation. This was done in a single cluster rig that contained both rods. Subjecting them to the same conditions allowed the investigation of the different behavior of FGR of both kinds of rods. Deliberate power uprating was done in order to cause opening in the interlinkage at the grain boundaries of the fuel lattice. That would lead to significant gas release through these interlinked tunnels. This was done at 10 MWD/KgMOX for IFA-597.4 and at 22.27 MWD/KgMOX for IFA-597.6.

In IFA-597./5./7, the objective was to accumulate Fission gases in the matrix; Hence FGR was to be avoided. In order to avoid FGR, The rig was shifted outwards in the core to reduce the power. Several UO₂ rods that were irradiated up to 13 MWD/KgUO₂ in IFA-597.1 were added to the rig along with the MOX rods. Four UO₂ rods were added in IFA-597.5. Three rods were used in IFA-597.7 to restrict FGRs. During IFA-597.5/.7 the power level was maintained low in the MOX rods and no significant FGR was noticed.

Since the FGR during IFA-597./6 was higher than expected and could not be explained, IFA-597.7 was decided to be unloaded. The experiment stopped in January 2002. The focus in this report is on IFA-495.4./5 because of the unexpected behavior in IFA-597.6 and the termination of IFA-597.7

5.1.2 Halden Boiling Water Reactor (HBWR)

HBWR is a reactor located in Halden in the south of Norway near its borders with Sweden.^[21] The reactor is a natural circulation heavy boiling water reactor. The maximum power of the reactor is 25 MW (thermal). Water temperature is 240°C pressurized to 33.3 bar. The reactor vessel primary circuit system dwells inside a rock cavern that is 30-60 m thick with a net volume of 4500 m³. The reactor pressure vessel is made of carbon steel and is cylindrically shaped. The round shaped bottom and the cylindrical portion are clad with stainless steel. A schematic diagram of the reactor, pressure vessel and operation data can be seen in *Figure 5-1*.

The reactor facilities have then been subjected to a huge development until it became one of the most versatile in the world. Through these developments, around 300 in-pile experiment took place on different levels of complexities and purposes.

The facility has high pressure loops with light water provided for testing under prototypic BWR and PWR conditions. In order to provide experimental variation of void fraction in the assemblies an external sub cooler loop is installed. The central location of the core is occupied by the emergency core cooling tubes.^[23]

The source of the fuel charge is test fuel from participant organizations in member countries of the reactor project and a driver fuel assemblies used for providing reactivity needed for operation purpose. The core consist of 110-120 fuel assemblies. The test fuel is located in an open hexagonal lattice of a pitch 130 mm (Figure 5-2). The maximum height of the fuel section is 1710 mm. Currently, driver fuel assemblies consist of eight to nine fuel rods with 6% enrichment. The standards and specifications and main parameters of the facility are included in Table 5-1

Assembly	Unit	Quantity
Shroud material	--	Zr-2
Shroud ID	mm	71
Shroud thickness	mm	1
Number of rods per assembly	--	8
Pitch circle diameter	mm	50
Length from lowest pellet in lower rod to highest pellet in upper rod	mm	810
Fuel material	--	UO2
Fuel enrichment	%	6
Pellet density	g/cm3	10.52
Pellet OD	mm	10.49
Pellet height	mm	8.6-10.8
Length of natural fuel per rod	mm	12
Active length	mm	748-811
Cladding material	--	Zr-2, Zr-4
Cladding ID	mm	10.67
Cladding wall thickness	mm	0.8
Nominal gap	mm	0.16-0.18

Table 5-1 HBWR, summary of the driver fuel main data.

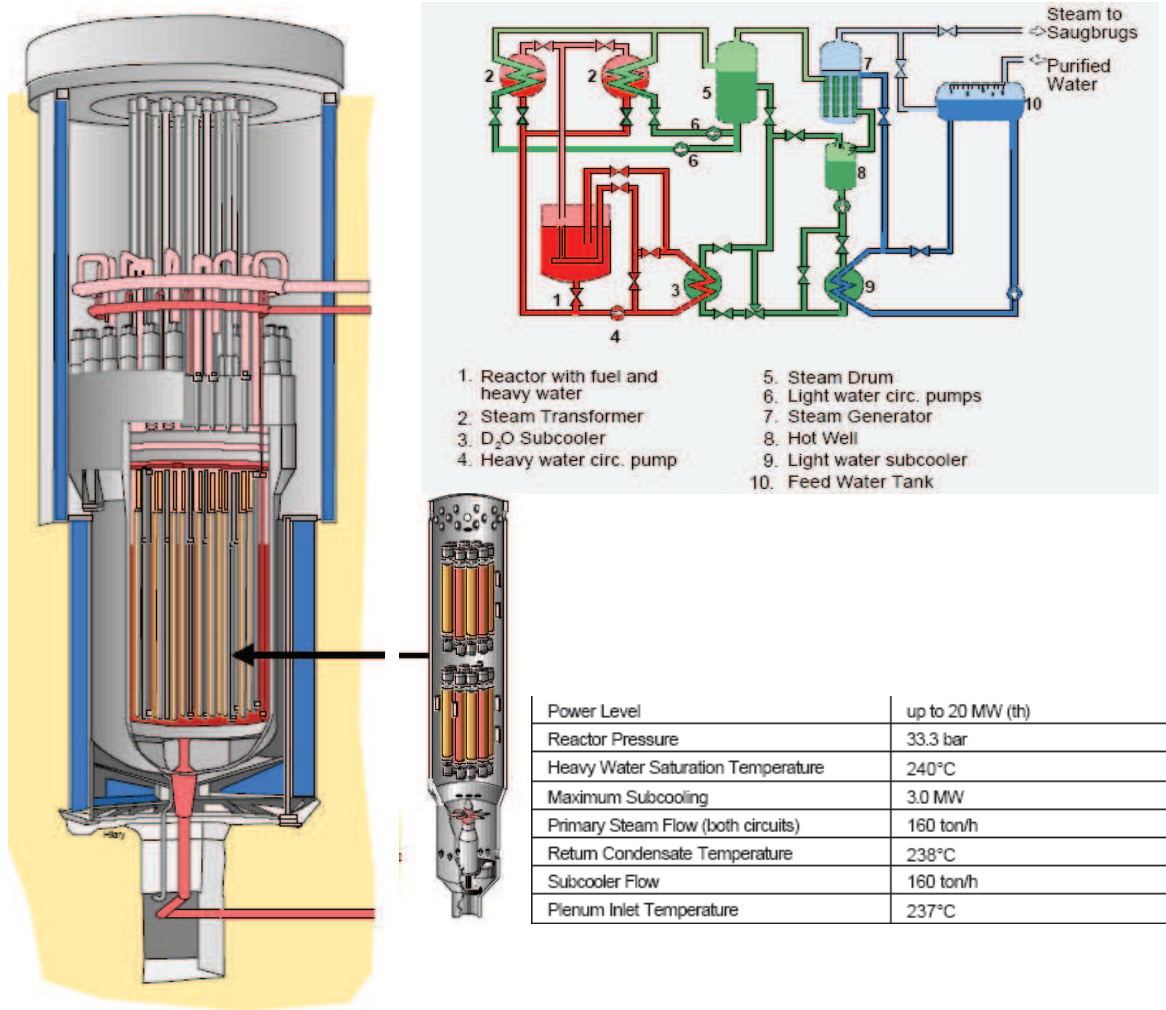


Figure 5-1 HBWR, schematic diagram and main operation parameters. [21]

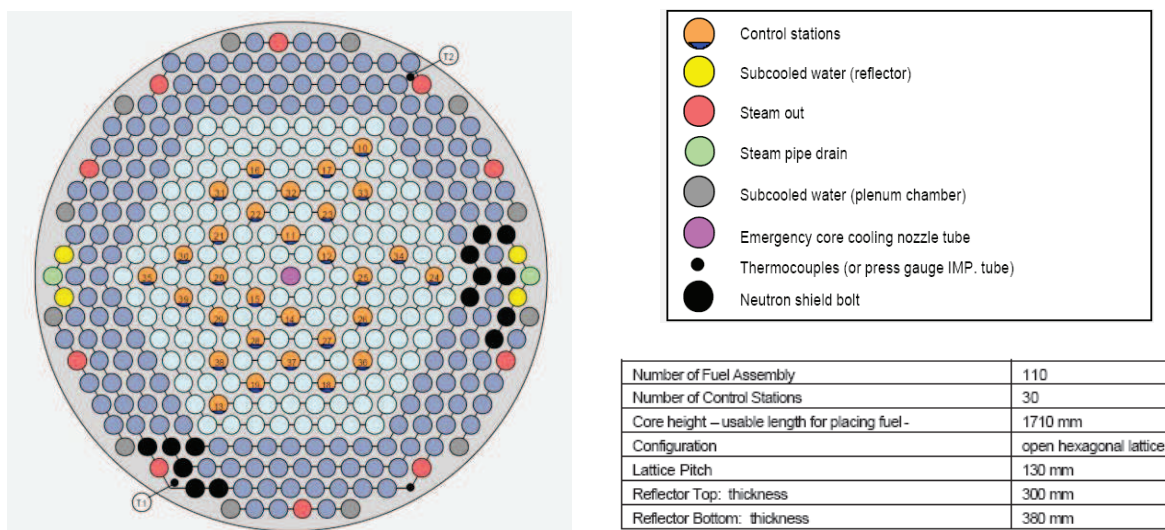


Figure 5-2 HBWR, plan view of the reactor top lid and main parameters. [21]

5.1.3 Design of the rig and rods

In *Figure 5-3*, a schematic of the testing rig can be seen. The rig had one cluster that contained the MOX fuel and the power suppressing UO₂ when needed. The rig contained four Vanadium neutron detector and three water coolant thermocouples. Two of those thermocouples were located at the outlet and one at the inlet. In core connectors for the instrument cables are placed at the top and bottom of each rod position.^[2]

The Rig operated in IFA-597.4 in power level between 20-35 kW/m to release fission gases. It was relocated to an outer position later in IFA-597.5 to assure lower LHR and avoiding FGR. Then in IFA-597.6 it was relocated inwards again for the same reason as in IFA-597.4

The solid and hollow MOX rods named as rod 10 and rod 11 respectively were irradiated in IFA-597.4 as fresh rods with initial total Pu content of 8.44%, and 6.07% fissile Plutonium content. Manufacturing parameters of the rods are summarized in *Table 5-2* along with data of the UO₂ that were used in the experiment. Rod 10 is 224 mm height consisting of 17 solid fuel pellet and on top of them 4 hollow pellets in which the centerline thermocouple was accommodated. Rod 11 is 220 mm height consisting of 21 pellets all of them are hollow. The initial outer diameter of the pellets is 8.04 mm and the hollow pellets had an initial center hole diameter of 1.8 mm. Cladding outer diameter is 9.5 mm with a gap of 180 μm of width. The pressure bellow transducers were located at the bottom. The bellows were initially pressurized to 4 bar. The rods were pressurized with Helium to 5 bar at 20°C.

	Rod 10	Rod 11	Rod 1	Rod 2	Rod 3	Rod 5
Fuel						
Fuel type	MIMAS-MOX	MIMAS-MOX	UO ₂	UO ₂	UO ₂	UO ₂
Active fuel length (mm)	224	220	503	502	499	502
Fuel mass (Kg)	0.1179	0.1106	0.404	0.415	0.419	0.432
Instrumentation upper end	TF1	TF2	-	-	-	-
Instrumentation lower end	PF2	PF5	-	EC3	EC4	-
Fuel density (g/cc)	10.54	←	10.55	←	←	←
Initial fuel enrichment (wt%)	6.07 Pu(f)	←	4.95 ²³⁵ U	←	←	←
Initial fuel diameter (mm)	8.04	←	10.25	←	10.45	100.58
Diam clearance (mm)	0.18	←	0.4		0.2	0.07
Pellet length (mm)	10.7	10.5	8.2	8.4	8.5	8.4
Pellet form (not including end pellets)	17 solid, 4 hollow	21 hollow	61 hollow	50 solid, 10 hollow	59 hollow	60 hollow
Drilled center hole diameter (mm)	1.8	←	1.9	←	←	←
Dishing	Both ends	←	Top end	←	←	←
Dishing depth (mm)	0.26	←	0.75	←	←	←
Rod						
Cladding material	Zr-4	←	Zr-2	←	←	←
Filler gas pressure (bar)	5 (He)	←	←	←	←	←
Cladding OD (mm)	9.5	←	12.25	←	←	←
Cladding thickness (mm)	0.64	←	0.8	←	←	←
Free volume (cc)	4.5	4.9	9.6	9.8	8.2	8.9

Table 5-2 IFA-597 experiment, rod characteristics.

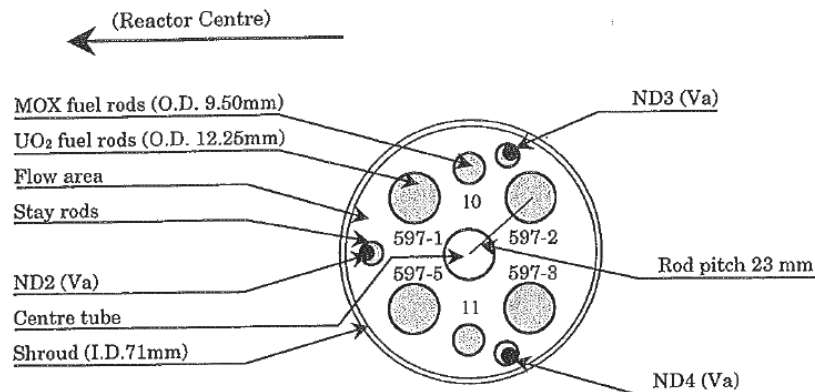


Figure 5-3 IFA-597 experiment, schematic radial view of the test rig. ^[2]

5.1.4 Linear Heat rating (LHR)

The location of the rig in the reactor and the small height of the rods led to an almost unity maximum to average heat rating in the rods. Therefore the local LHR at the thermocouple position was almost the same as the average LHR in both rods. The LHR is more uniform for rod 11 with a variation less than 2%. Relative to 7% variation from average for rod 10. The plan of the experiment was to have power uprating every 10 MWD/KgMOX to study FGRs.

The linear heat rating began in the first half of IFA-597.4 in the range of 30-35 kW/m and in the range of 27-30 kW/m in the second half of the experiment. During the experiment several occasional gas release occurred. For IFA-597.5 the rods were relocated to a lower LHR location with the addition of four UO₂ rods to suppress the LHR of the MOX rods. No FGR was noticed because of that decrease of LHR to a range between 8-17 kW/m. In IFA-597.6 the heat rating was increased again to a level in the range of 20-24 kW/m. The average LHR in rod 10 was higher than rod 11. The maximum LHR was always located almost in the middle of the rods. There is an uncertainty level of 5% in the power level. This is generated from the calorimetric power calibration done at the beginning of each experiment done in HBWR for IFA rods. The uncertainty of this process is 5%. After the experiment begins, repeating this process is not always possible. The determination of the thermal power level of the rods is then determined by neutronic simulations using HELIOS code. The estimated error is expected to increase from 5% to 10% at the end of the experiment. In this study, the uncertainty in LHR will be considered only to be the initial 5% as shown in Figure 5-4.

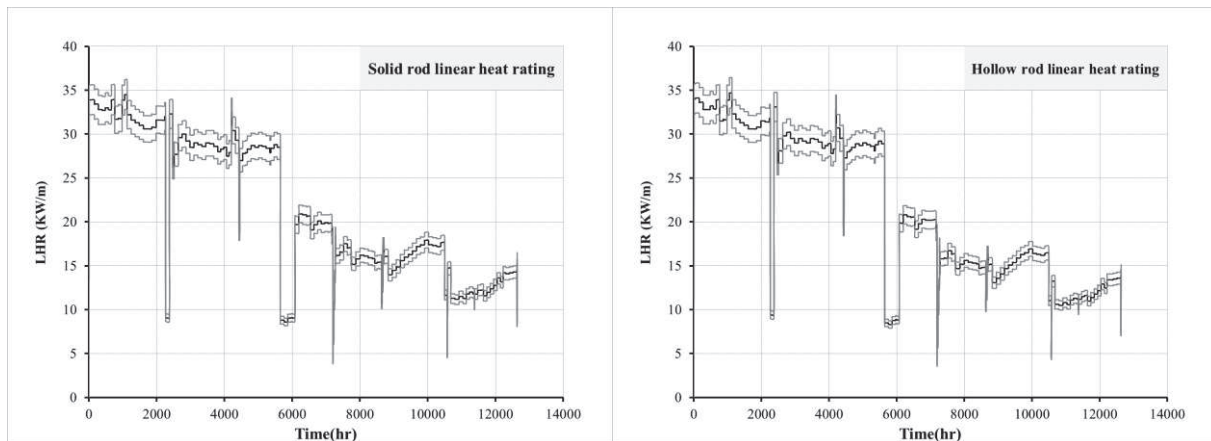


Figure 5-4 Linear heat rating of solid and hollow rods.

5.2 Modelling IFA597.4/.5 with TU


5.2.1 Development of TU input file

The fuel rods are modelled using TRANSURANUS code, version “v1m1j12”, with the deterministic option, steady state thermal and mechanical analysis. The version of the manual is “v1m1j12”^[11]. The boundary conditions were prepared using a Fortran-90 program prepared by the author.

The input decks are prepared according to the information available in the manual of the code. Most of the models used in the reference analysis were the standard recommended models by the code developers. Some deviations occurred when needed e.g. the usage of UO_2 models for the MOX fuel swelling because the MOX models available in the code are still under investigation and not totally validated. *Table 5-3* summarizes the options that have been selected and that are expected to affect the prediction of the fuel temperature.

IFA-597 Reference input decks			
Parameter	Reference Option	Description	Other options
Fuel conductivity	Correlation 31 (recommended)	Standard correlation of the thermal conductivity of MOX fuel (best estimate) according to Van Uffelen and Schubert. based on experimental data obtained by Duriez et al for fresh MOX fuel and laser flash measurements of irradiated MOX fuel at ITU. It is extended by an ambipolar term recommended by Ronchi et al.	32,33,34,35
Fuel swelling	Correlation 20	Developed by K. Lassmann from correlation 19. The gaseous swelling contribute was modified and integrated from this steady state equation considering the local contribute of the burn-up, the temperature, the stress and the diffusion coefficient.	18, 19, 21,25, 3, 11, 12, 13
Pellet fragment relocation	Model ireloc 8	Modified FRAPCON-3 model. It considers the as fabricated gap size, the burn-up and the linear heat rate.	2, 3, 4, 5, 6
Fuel grain growth	Model igrnsz 1 (recommended)	Grain growth model of Ainscough and Olsen. It computes the grain radius increase as function of the fuel local temperature assuming a maximum grain radius for each temperature.	--
Fuel densification	Model idensi 2 (recommended)	Empirical model for LWR and FBR. This model needs the input of the minimum porosity DENPOR at the end of thermal and irradiation induced densification and the time constant DENBUP (burn-up in MWd/tU, at which irradiation induced densification is terminated).	3, 7
Gap conductivity	Model ihgap 0 (recommended)	Standard Option: gas Bonding thermal conductivity of mixture according to Lindsay and Bromley. Accommodation coefficients are taken into account	1, 3, 4, 5
Fission gas release	Models: fgrmod6 (recommended), igrbdm3, Idifsolv0	FGRMOD 6: URGAS algorithm with the diffusion coefficients of Hj. Matzke (thermal) and a constant athermal diffusion coefficient. IGRBDM 3: New model developed according to modified Koo model for ramps IDIFSOLV 0: Diffusion equation is solved by the URGAS-algorithm	Fgrmod: 4,9 Igrbdm: 0, 1, 2 Idifsov: 1, 2, 3 4,5,6

Table 5-3 IFA-597 experiment, summary of models and correlations that might affect the prediction of thermal conductivity of the rods.

 Ricerca Sistema Elettrico	Sigla di identificazione	Rev.	Distrib.	Pag.	di
	ADPFISS – LP2 – 087	0	L	52	229

5.2.2 Boundary conditions

The boundary conditions used are:

- Linear heat rate at 4 axial position;
- Fast neutron flux (>1 MeV);
- Coolant temperature
- Coolant pressure.

Linear heat rate (LHR) is considered constant over the time step in which it applies. The heat rate increase/decrease with a rate of 6 (Kw/m.h) for any change between different values of LHR. This transition rate and the time needed for the LHR to be changed is calculated based on the LHR in the peak position. The linear heat rate was measured and calculated at four position of the rods. One of them is at the position of the thermocouples and the rest are in the bottom, middle and top of the rods. The axial positions of the measurements can be seen in *Table 5-4*.

The active part of the fuel was considered in this study. It was divided into 4 slices at the positions of LHR measurement given in *Table 5-4*. The rods are divided into a number of m_3 slices that are determined by the number of boundary condition points given in the experiment data. In TU, there are two different methods of dealing with the discretized slices; Slice option or Sectional option. In both cases, the fuel is analyzed slice per slice, starting from slice 1 up to slice m_3 . The difference is that with the slice option, a slice is analyzed at the middle, i.e. at the axial position $\frac{z_i + z_{i+1}}{2}$, whereas with the sectional option a slice is analysed at the bottom and the top, i.e. at the coordinates z_i and z_{i+1} . Thus, the total number of axial analyses is m_3 for the slice option and $m_3 + 1$ for the sectional option. In addition, there is another difference: in the slice option, it is assumed that all axial quantities, e.g. the linear rating, are constant along the slice, whereas in the sectional option these quantities may vary linearly along the slice.^[11]

In this work, the rod is treated using the sectional option of the discretization since it showed more accuracy of capturing the experimental values of burn-up which is a crucial step in the beginning of the specific analysis of the code performance. The nodalization of the fuel rods is based on the positions of the locations on which the LHR is measured. A 5% uncertainty of LHR is taken into consideration in the analysis as a factor that might affect the results.

The fast flux is calculated from the LHR according to the following equation.

$$\text{Fast flux level} = 1.6 \cdot 10^{11} * LHR$$

As for the coolant temperature and pressure they are taken as constant values for the cold and hot conditions. They are taken to be the standard values of operation of HBWR (240°C, 33.3 bar).

Name	Position-Rod10 [mm]	Name	Position-Rod11 [mm]	Location
LHRB1	0.0	LHRB2	0.0	Bottom
LHRM1	112	LHRM2	110	Mid
LHRT1	224	LHRT2	220	Top
LHRTF1	184	LHRTF2	180	TF tip position

Table 5-4 IFA-597 experiment, local heat rate measurement positions.

5.2.3 Burn-up investigation

A first and important step to be done before any further analysis takes place is Burn-up investigation. This is important to demonstrate the validity of any calculation done. In fact, it helps in assuring that the rod being analyzed is actually modeled in the exact state that it should be on when the test ends. In TU code, burn-up was calculated according to TU-LWR burn up models^[11]. As usual, due to uncertainty of experimental data (which is $\pm 5\%$) and simplification of the model adopted, the calculations are retained in agreement up to around $\pm 10\%$ of the experimental data.

In *Figure 5-5*, the experimental data are plotted taking into consideration 5% uncertainty. It can be seen that the burn-up for the solid rod is slightly under-predicted but lays within the 5% uncertainty of the experimental calculations. For the hollow rod, a general over-prediction of the burn-up is noticed that exceeds in the mid-section of the experiment the 5% uncertainty level but it is still acceptable since it did not exceed 10% range of uncertainty. At the end of the experiment, the burn-up predicted by TU is within the 5% uncertainty again. To conclude, the calculations capture the burn-up of these rods and are therefore representative of their status.

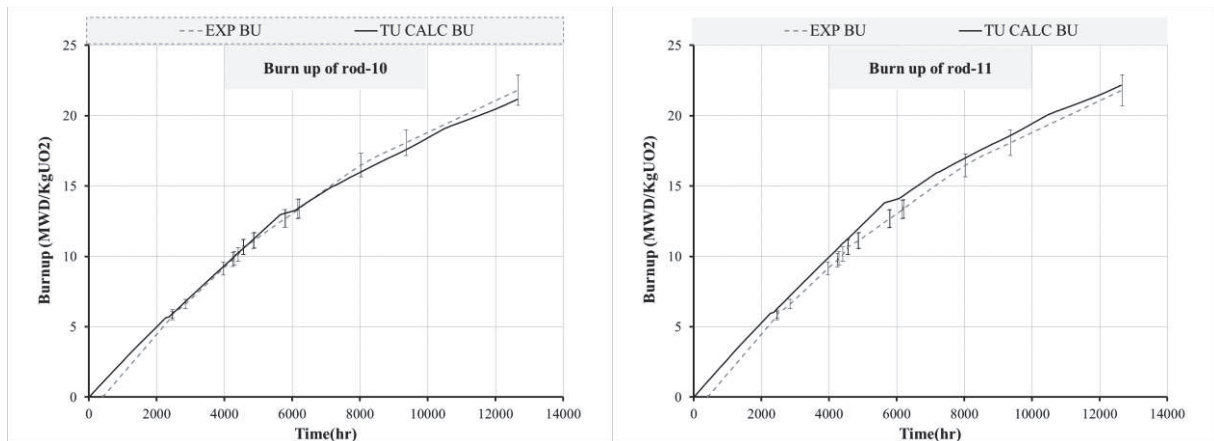


Figure 5-5 Simulation of IFA-597, preliminary results: burn-up analysis.

 Ricerca Sistema Elettrico	Sigla di identificazione	Rev.	Distrib.	Pag.	di
	ADPFISS – LP2 – 087	0	L	54	229

5.3 Reference analysis of IFA597.4/5

5.3.1 Fuel temperature

The fuel temperature is analyzed in *Figure 5-6* and *Figure 5-7*. These figures report the measured centerline temperature, the simulated temperature at the corresponding axial position (which is slice 4) and the evolution of the fuel to cladding gap (simulated only) in the peak axial position (slice 2).

Solid rod (rod-10, *Figure 5-6*): matches well the experimental data. It can be noticed as well that at the end of each cycle, that the code tends to slightly over-predict the temperature, this could be connected to uncertainties in the LHR. The fuel to cladding gap is predicted to remain opened.

The hollow rod (rod-11, *Figure 5-7*), is slightly under-predicted at the beginning of the first cycle. This could be connected to parameters that affect densification; in fact these parameters are modeled based on an average grain size and porosity whose local deviations may affect densification phenomena and consequently fuel temperature. The second cycle is less dependent upon densification and it follows the same trend as with the solid rod: the code begins with a good fit with experimental data then over-predicts the temperature later in the cycle.

During the whole simulated experiment, the predicted temperature did not deviate from the experiment measurement more than ± 35 °C. This should lay within the $\pm 5\%$ uncertainty level of the LHR as later illustrated in the sensitivity analysis (section 0). The code can generally predict the temperature of the irradiated MOX appropriately. It can be seen as well the dependency of the gap width on the temperature. As the temperature increases, the gap width tends to decrease and vice versa. Gap width size would affect the prediction of the gap conductivity which is a source of feed-back to the prediction of the centerline temperature.

5.3.2 FGR and pin pressurization

The Fission Gas Release (FGR) is analyzed in *Figure 5-8* and *Figure 5-9*. These figures report the measured centerline temperature, the simulated integral FGR and the calculated FGR (which has been given in the experimental report based on on-line pressure measurements and burn-up calculations).

The code under-estimated FGR for the solid rod, *Figure 5-8*. The maximum FGR predicted by the code was 4% while the experimental reached up-to 7%. It should be mentioned that, in fuel pin mechanic code simulations, for these relatively low values of FGR it is generally retained acceptable even with deviations in the range -50%, +100%. When the code was able to predict releases, it predicted them at the right onset and LHR, this confirms the selection of the burst release model (typically adopted for power ramps) which causes grain boundary venting when a given power variation and local temperature are met.

For the hollow rod, TU failed to predict FGRs, the maximum that was was 1% while the experiment reached up to 10.4%. The failure of the code with the hollow rod

could not be explained but it might be due to the failure of predicting micro-cracking of the fuel which generates pathways for the fission gases to be released through.

The pin pressurization is depicted in *Figure 5-10* and *Figure 5-11*. These figures report the measured pin pressure, the simulated pin pressure and the simulated total and upper plenum free volumes.

For the solid rod (*Figure 5-10*), the pressure was slightly over-predicted in IFA-597.4 (first cycle) and slightly under-predicted in IFA-597.5 (second cycle). In the first cycle, the over prediction can be related to under estimation of densification or relocation by the code which means predicting a smaller free volume which leads to over prediction of the pressure. In the second cycle, the under-prediction of the pressure can be related to the under-prediction of FGR. The same is true for the hollow rod (*Figure 5-11*), and we can notice that the over prediction in the first cycle is higher than that of the solid rod and the pressure is highly under-predicted in the second cycle which is consistent with the very low FGRs predicted by the code.

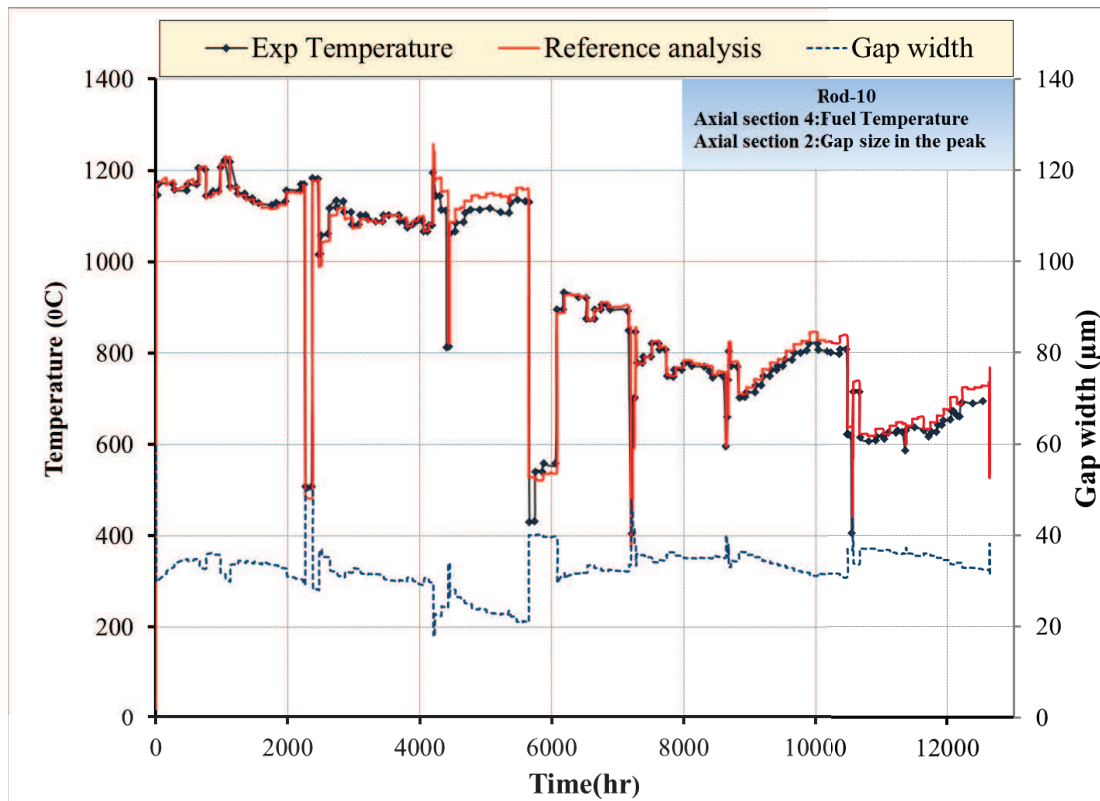


Figure 5-6 Simulation of IFA-597, reference results: fuel temperature evolution in rod 10.

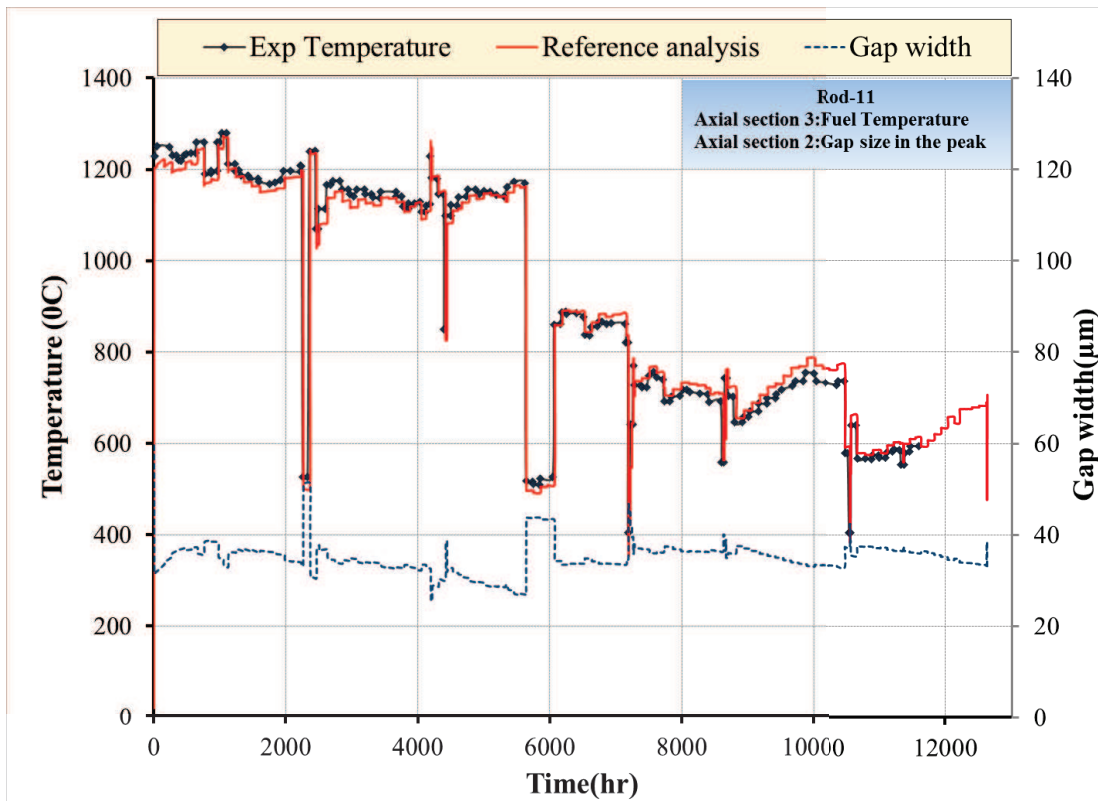


Figure 5-7 Simulation of IFA-597, reference results: fuel temperature evolution in rod 11.

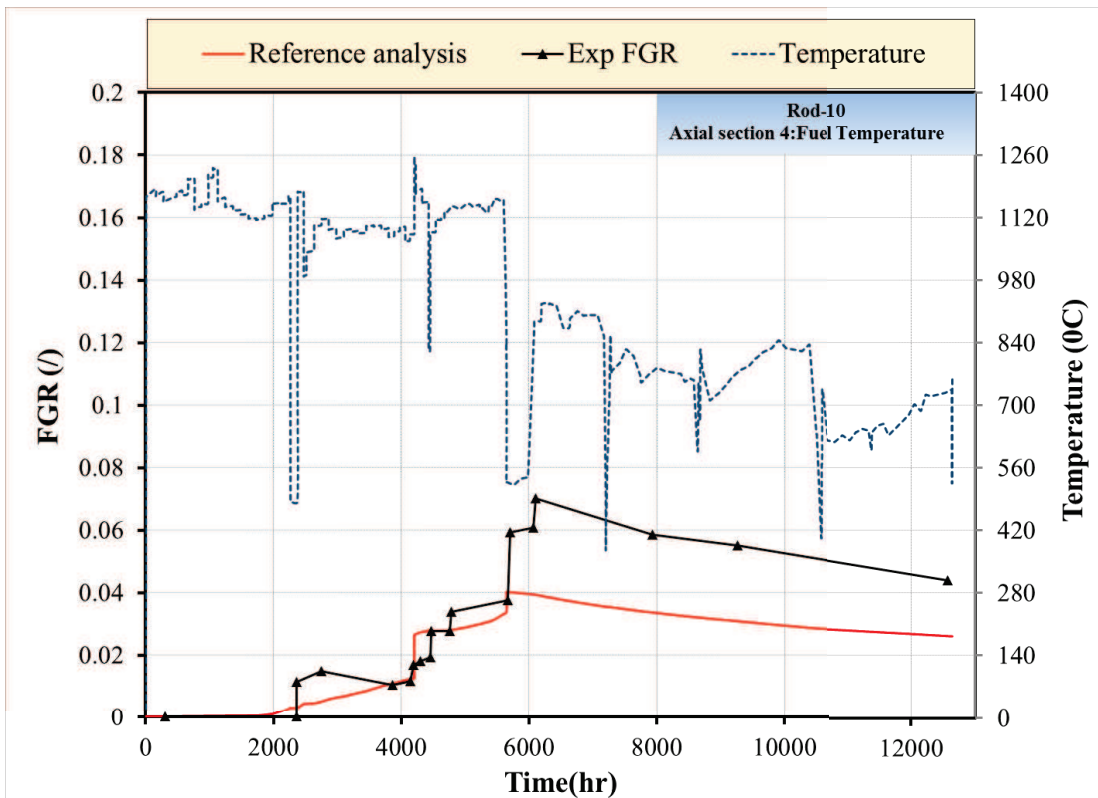


Figure 5-8 Simulation of IFA-597, reference results: FGR evolution in rod 10.

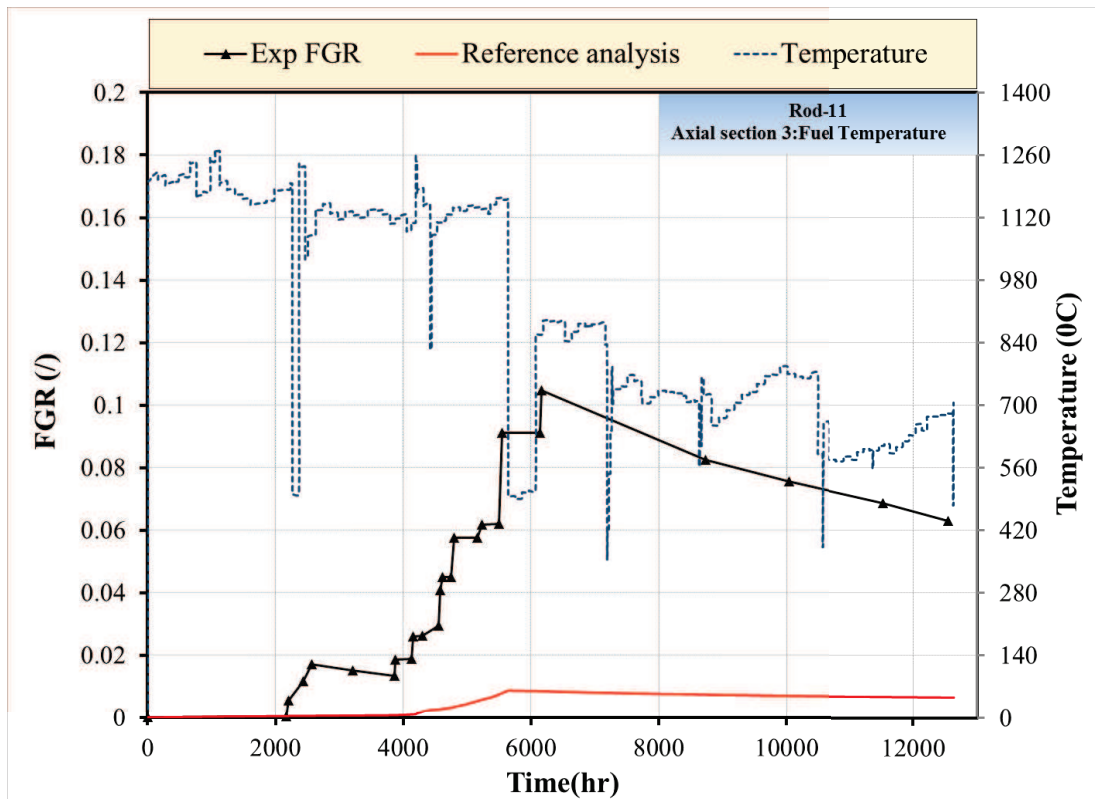


Figure 5-9 Simulation of IFA-597, reference results: FGR evolution in rod 11.

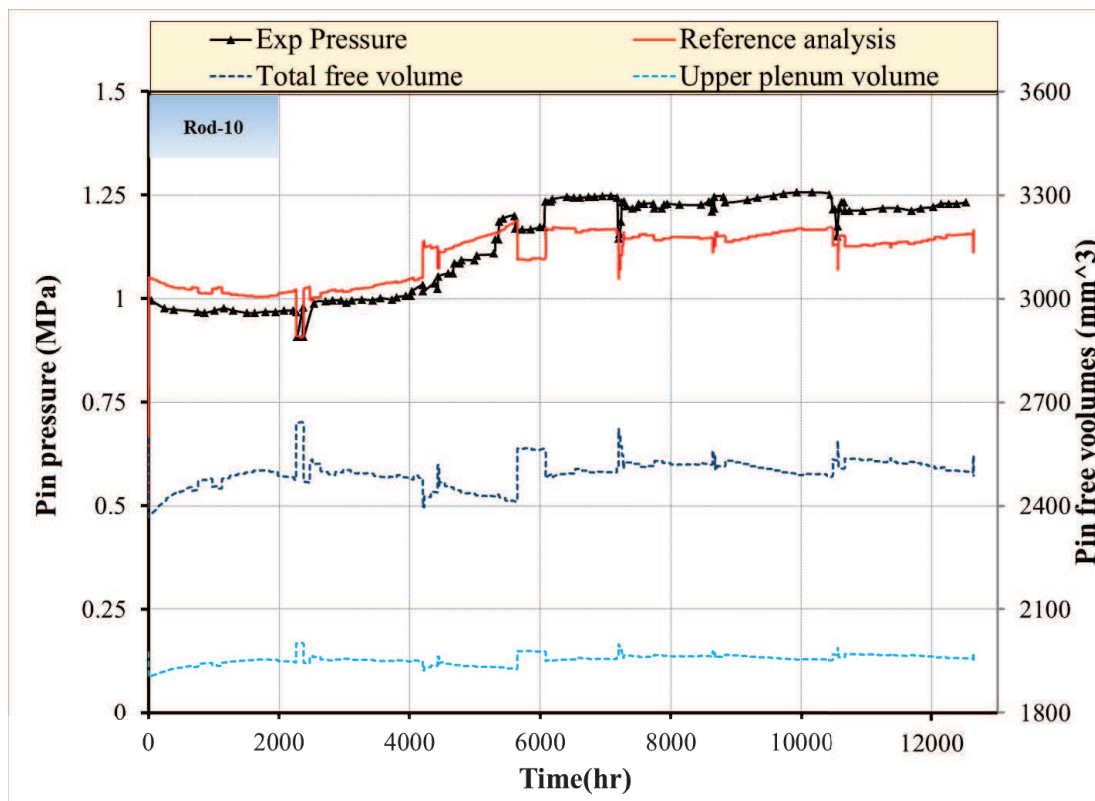


Figure 5-10 Simulation of IFA-597, reference results: pin pressure evolution in rod 10.

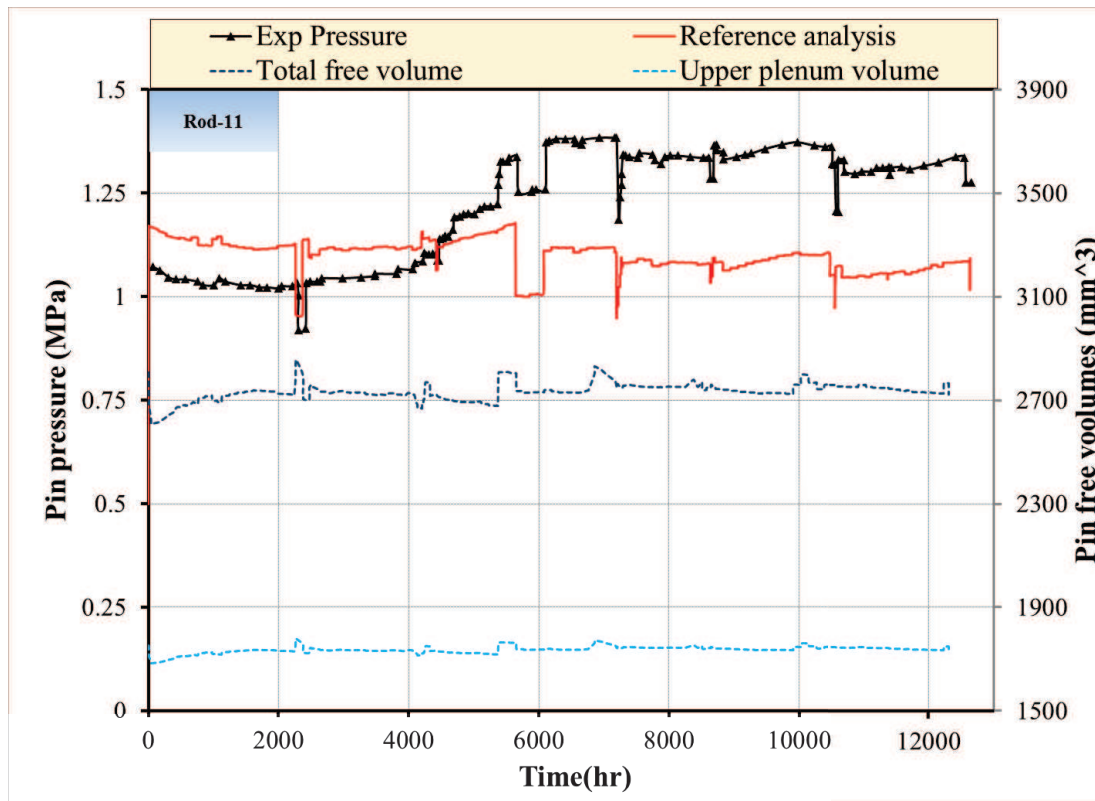


Figure 5-11 Simulation of IFA-597, reference results: pin pressure evolution in rod 11.

5.4 Sensitivity analysis

It is important to conduct sensitivity analysis of the code to the various conditions, correlations and models that are provided as options in the code. This step is helpful in the demonstration of robustness of the calculations, detecting possible reasons for discrepancies between calculations and measurements, and identifying parameters that requires higher accuracy in their values in order to be able to get results that are more accurate by the code.

In *Table 5-5*, A list of all sensitivity analysis that were performed during this study could be found and the motivation behind them. The analysis was performed on either parametric design values given by the experiment data, correlations and models provided by the code. Design parameters are labeled by **(D)**, while correlations are labeled by **(C)** and Models labeled **(M)**.

In the next subsections, separate sensitivity analysis of the factors stated in *Table 5-5* is illustrated.


Case	Run	Modification	Objective
Fuel conductivity	C1.1	Modfuel(j=6)=31	Investigate the impact of fuel conductivity on fuel temperature, pin pressure and FGR. <i>Correlation of Van Uffelen & Schubert.</i>
	C1.2	Modfuel(j=6)=32	Investigate the impact of fuel conductivity on fuel temperature, pin pressure and FGR. <i>Correlationo of Carbajo..</i>
	C1.3	Modfuel(j=6)=33	Investigate the impact of fuel conductivity on fuel temperature, pin pressure and FGR. <i>Correlation of Lanning & Beyer.</i>
	C1.4	Modfuel(j=6)=24	Investigate the impact of fuel conductivity on fuel temperature, pin pressure and FGR. <i>According to Wiesenack multiplied by a MOX correction factor.</i>
Pellet fragment relocation	M1.1	Ireloc 2	Investigate the impact of fuel relocation on fuel temperature, pin pressure gap size and FGR. <i>Original KWU-LWR model based on initial gap size only.</i>
	M1.2	Ireloc 3	Investigate the impact of fuel relocation on fuel temperature, pin pressure, gap size and FGR. <i>GAPCON-THERMAL-3 based on initial gap size, LHR and burn-up.</i>
	M1.3	Ireloc 5	Investigate the impact of fuel relocation on fuel temperature, pin pressure, gap size and FGR. <i>Modified KWU-LWR model, own calibration 1997</i>
	M1.4	Ireloc 8	Investigate the impact of fuel relocation on fuel temperature, pin pressure, gap size and FGR. <i>Modified FRACPON-3 model based on the as fabricated gap, the burn-up and the linear heat rate.</i>
Fuel swelling	C2.1	Modfuel(j=4)=18	Investigate the impact of fuel swelling on fuel temperature, gap size, fuel elongation and FGR. <i>Simple correlation applied: swelling proportional to burn-up.</i>
	C2.2	Modfuel(j=4)=19	Investigate the impact of fuel swelling on fuel temperature, pin pressure and FGR. <i>Original MATPRO swelling model considering separate contributions of the solid and gaseous fission products</i>
	C2.3	Modfuel(j=4)=20	Investigate the impact of fuel swelling on fuel temperature, pin pressure, gap size and FGR. <i>Implicit formulation of the reference correlation.</i>
Fission gas release	M2.1	Igrbdm 3 FGRmod 4	Investigate the impact of intra-granular and inter-granular models on fuel temperature, pin pressure and FGR. <i>Inter-granular model according to the modified Koo model and intra-granular model of Matzke and White Tucker.</i>
	M2.2	Igrbdm 3 FGRmod 6	Investigate the impact of intra-granular and inter-granular models on fuel temperature, pin pressure and FGR. <i>Inter-granular model according to the modified Koo model and intra-granular diffusion coefficient according to Matzke (thermal) and a constant athermal diffusion coefficient.</i>
	M2.3	Igrbdm 3 FGRmod 9	Investigate the impact of intra-granular and inter-granular models on fuel temperature, pin pressure and FGR. <i>Inter-granular model according to the modified Koo model and intra-granular model of Turnbull.</i>
	M2.4	Igrbdm 1 FGRmod 6	Investigate the impact of intra-granular and inter-granular models on fuel temperature, pin pressure and FGR. <i>Inter-granular model according to the standard model</i>

Case	Run	Modification	Objective
			<i>and intra-granular diffusion coefficient according to Matzke (thermal) and a constant athermal diffusion coefficient.</i>
	M2.5	Igrbdm 2 FGRmod 6	Investigate the impact of intra-granular and inter-granular models on fuel temperature, pin pressure and FGR. <i>Inter-granular model according to the temperature dependent model and intra-granular diffusion coefficient according to Matzke (thermal) and a constant athermal diffusion coefficient.</i>
Gap conductance	M3.1	lhgap 0	Investigate the impact of gap conductance models on fuel temperature, pin pressure and FGR. <i>Gap conductance model according to the standard model.</i>
	M3.2	lhgap 3	Investigate the impact of gap conductance models on fuel temperature, pin pressure and FGR. <i>Gap conductance model according to the Lindsay & Bromley. Accommodation coefficients not taken into account.</i>
	M3.3	lhgap 4	Investigate the impact of gap conductance models on fuel temperature, pin pressure and FGR. <i>Gap conductance model according to Tondon & Saxena. Accommodation coefficients are taken into account.</i>
Gap size	D3.1	Gap size (+12µm)	Test the impact of increased gap width at the beginning of irradiation on fuel temperature and FGR. Initial value obtained assuming maximum cladding and minimum fuel radii according to design uncertainties.
	D3.2	Gap size (-12µm)	Test the impact of decreased gap width at the beginning of irradiation on fuel temperature and FGR. Initial value obtained assuming minimum cladding and maximum fuel radii according to design uncertainties
Grain size	D1.1	4.4µm	Assess the impact of decreasing grain size to the lower limit defined by the experiment data on FGR and fuel centerline temperature
	D1.2	6.6µm	Assess the impact of increasing grain size to the upper limit defined by the experiment data on FGR and fuel centerline temperature
Sintering porosity DENPOR	D2.1	+50%	Assess the impact of increasing the sintering porosity on the prediction.
		-50%	Assess the impact of decreasing the sintering porosity on the prediction.
DENBUP	D3.1	0 MWD/tHM	Assess the impact of not considering fuel densification on the prediction of CLT
	D3.2	3000 MWD/tHM	Assess the impact of considering fuel densification lower cutoff burnup on the prediction of CLT
	D3.3	10000 MWD/tHM	Assess the impact of considering fuel densification higher cutoff burnup on the prediction of CLT

Table 5-5 Simulation of IFA-597, list of correlations, models and design parameters considered in the sensitivity studies.

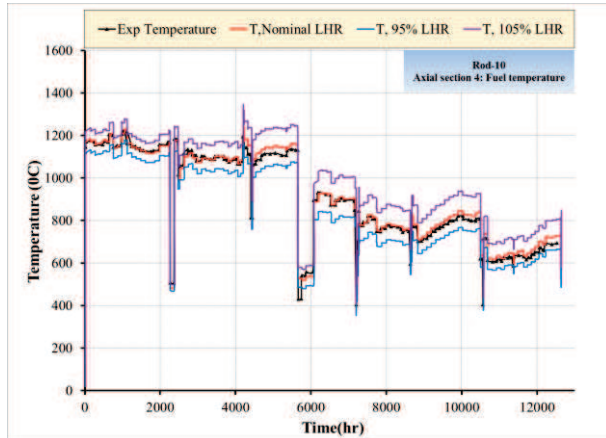
5.4.1 Effect of linear heat rating uncertainty

Uncertainty in linear heat rating should be investigated to determine its effect on fuel centerline temperature prediction. In this experiment the uncertainty ranged between 5% at the BOL and reached around 10% at the end of cycle. In this study only the

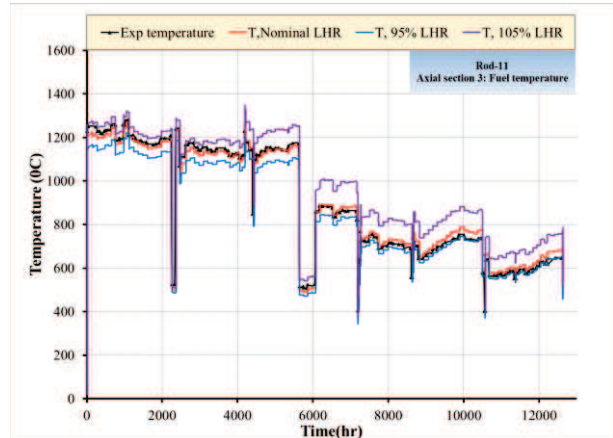
 Ricerca Sistema Elettrico	Sigla di identificazione	Rev.	Distrib.	Pag.	di
	ADPFISS – LP2 – 087	0	L	61	229

initial 5% uncertainty is taken into account. In *Figure 5-12*, *Figure 5-13* and *Figure 5-14*, the uncertainty limits are tested against the measured temperature, the measured pin pressure and the calculated FGR.

In *Figure 5-15* it can be seen in the beginning of IFA-597.4 and before FGR take place, that increasing/decreasing the LHR with $\pm 5\%$ leads to uncertainty of temperature of less than 5%. FGR results in feedbacks that affected the pin pressure. At higher LHR By releasing more fission gases the gap conductivity degrades which leads to even higher temperatures and the increase of temperature increases by more than 5% in the rest of the experiment and can reach up to 10 or 15%.^[24] The opposite is true at 95% LHR. With the lower temperature, lower FGR is predicted which means that the gap conductance suffers less degradation than in the nominal case. Then the better conduction, the lower the temperature becomes and the feedback of FGR results in a temperature decrease of between 5-10%. FGR does not vary linearly with LHR. Increasing the LHR results in more increase in FGR than the rate of the decrease when the LHR is decreased by the same ratio. The FGR uncertainty affects the pressure in the gap as well. In fact the gap pressure (*Figure 5-16*) is more sensitive to FGR than temperature and can vary between 20 to 30% at IFA-597.5. An over-all effect of this LHR uncertainty is that the code predicts temperatures and pressures that includes the experimental measurements within their upper and lower limits.

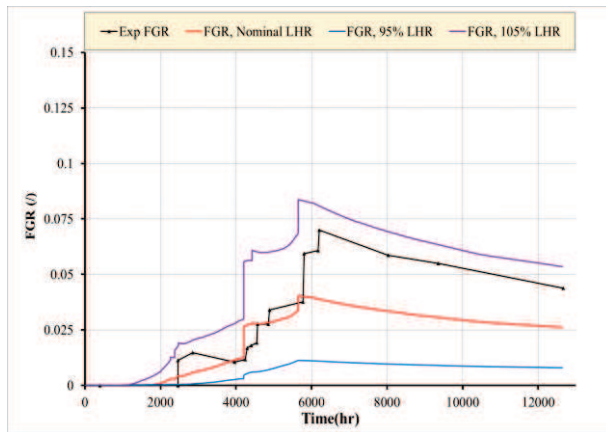


Solid rod (rod-10)

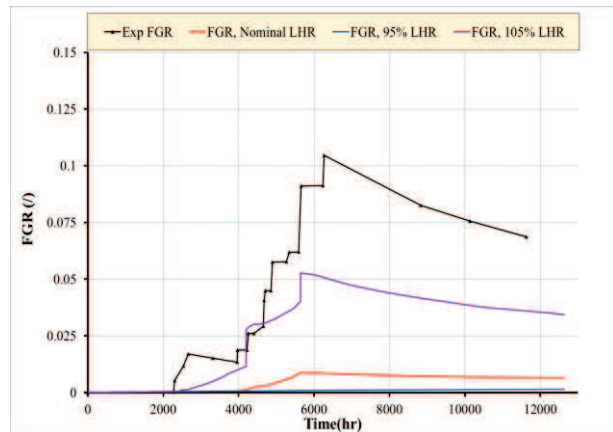


Hollow rod (rod-11)

Figure 5-12 Simulation of IFA-597, sensitivity analysis on LHR, fuel temperature.

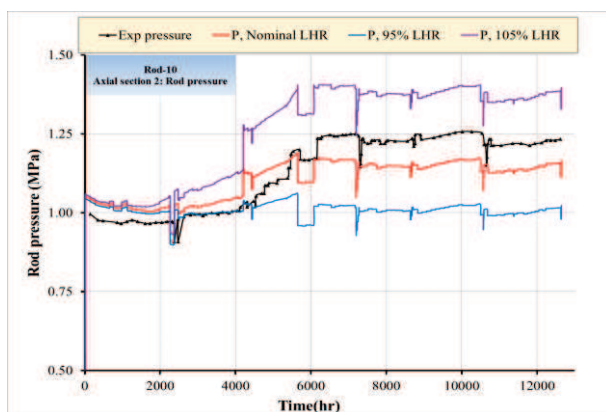


Solid rod (rod-10)

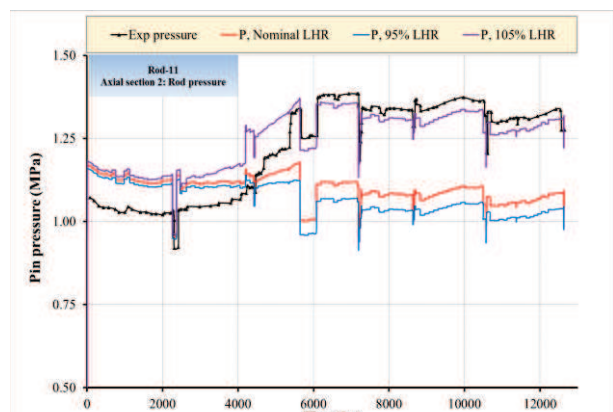


Hollow rod (rod-11)

Figure 5-13 Simulation of IFA-597, sensitivity analysis on LHR, FGR.



Solid rod (rod-10)



Hollow rod (rod-11)

Figure 5-14 Simulation of IFA-597, sensitivity analysis on LHR, rod pressure.

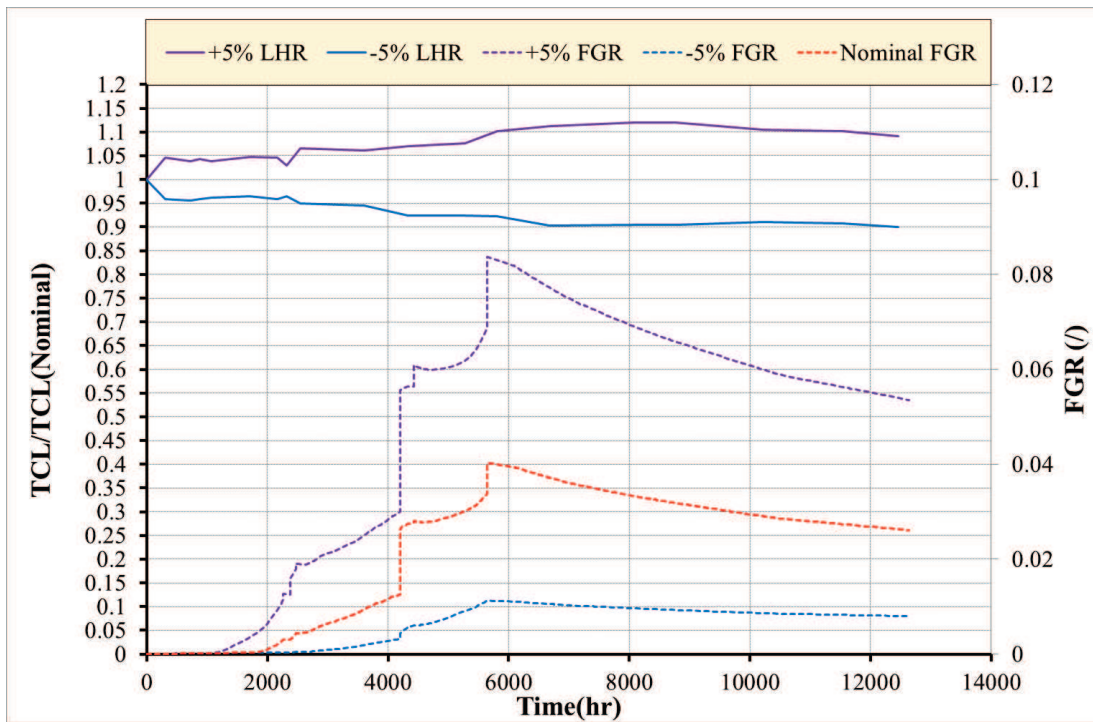


Figure 5-15 Simulation of IFA-597, sensitivity analysis on LHR, variation on fuel centreline prediction of rod-10.

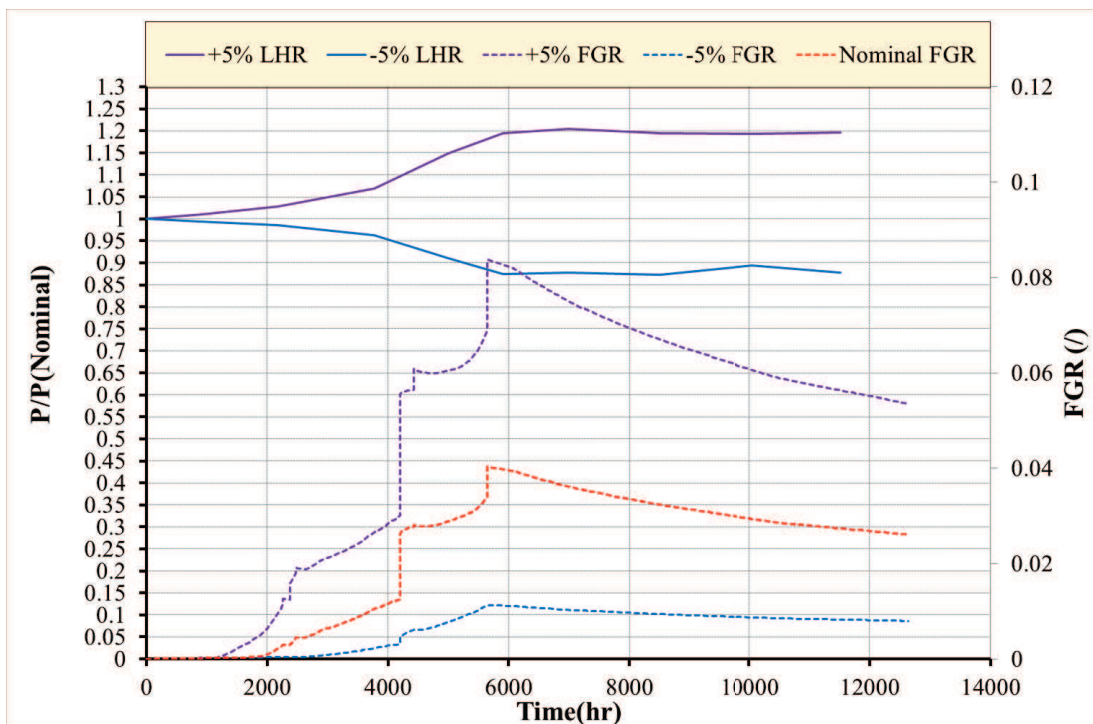



Figure 5-16 Simulation of IFA-597, sensitivity analysis on LHR, variation on rod pressure prediction of rod-10.

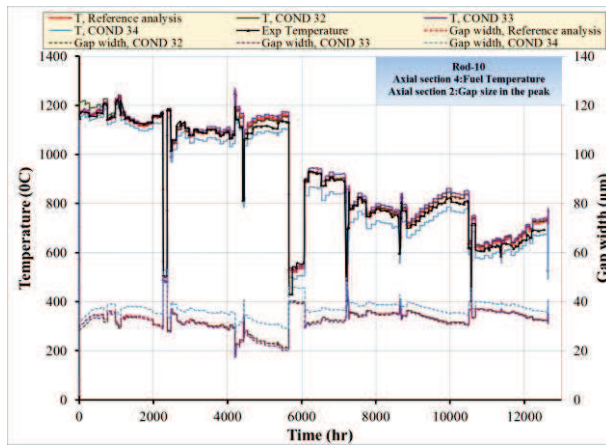
 Ricerca Sistema Elettrico	Sigla di identificazione	Rev.	Distrib.	Pag.	di
	ADPFISS – LP2 – 087	0	L	64	229

5.4.2 Effect of thermal conductivity correlations

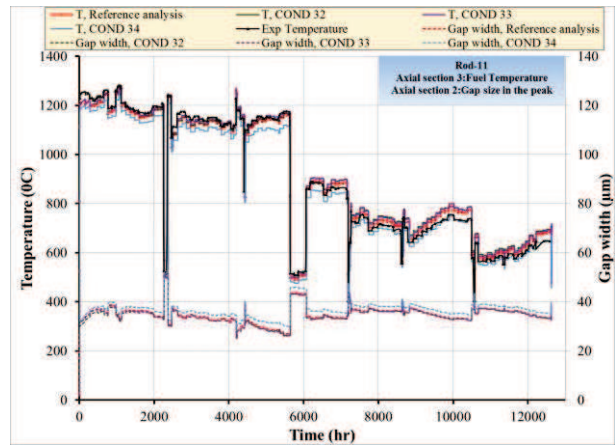
The correlations described in section 3.1 are tested in this analysis. *Figure 5-17* and *Figure 5-18* report the influence of the conductivity correlations on the prediction of the fuel temperature and FGR-pin pressurization, respectively.

There is a close match in the predicted temperature by the MOX correlations of Lanning&Beyer (Cond-33) and Carbajo (Cond-32) and the standard correlation of TU of Van Uffelen&Schubert (Cond-31), *Figure 5-17*. Cond-32 predicted temperatures approximately of the same values of the standard correlations except in the beginning of irradiation up-to 975hr where the temperature predicted is higher than the standard correlation. Cond-33 predicted temperature is slightly higher than that of the standard correlation over most of the time span of irradiation. The temperature over-prediction by Cond-33 does not become higher than 20⁰C. The correlation of Wiesenack (Cond-34) under-predicted the temperature during the whole range of irradiation. This under-prediction can reach up to 65⁰C at some points of time in IFA597.5. This correlation is originally designed for UO₂ fuel and multiplied by a factor of 0.92 as an approximation for MOX fuel. The conductivity of UO₂ is higher than that of MOX fuel. Therefore, the factor taken is not low enough to reduce the thermal conductivity to a value comparable to the rest of the correlations originally designed for MOX. The result of this higher thermal conductivity by Cond-34 is that the prediction of temperature is lower than the standard correlations and experimental data. To conclude, the standard correlation of TU is the one that best captures the experimental measurements. The previous analysis applies for both rods.

For both the rods, the correlations predicts similar FGR and pin pressures in the first two thirds of IFA597.4. Then the correlations deviates from each other. The values predicted by Cond-34 is the earliest to deviate from the others. The rest begin to show different prediction of the pin pressure and FGR in a later stage. It can be noticed comparing *Figure 5-17* and *Figure 5-18* that the prediction of higher temperature results in a higher prediction of FGR and consequently the pin pressure. This is obviously connected to the thermal activated mechanisms that take place in the diffusion of fission gases into the grain and accumulation and release of gases from the grain boundaries to the pin free volume.

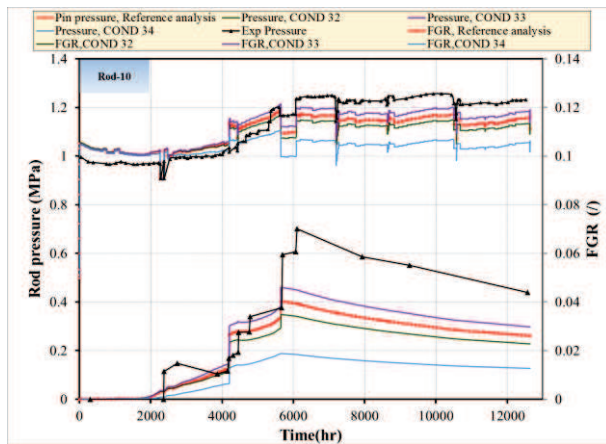


Solid rod (rod-10)

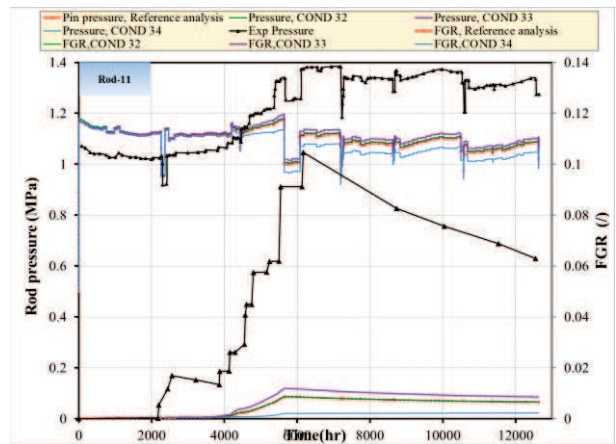


Hollow rod (rod-11)

Figure 5-17 Simulation of IFA-597, sensitivity analysis on fuel conductivity correlations, temperature prediction.




Solid rod (rod-10)



Hollow rod (rod-11)

Figure 5-18 Simulation of IFA-597, sensitivity analysis on fuel conductivity correlations, rod pressure and FGR prediction.

 Ricerca Sistema Elettrico	Sigla di identificazione	Rev.	Distrib.	Pag.	di
	ADPFISS – LP2 – 087	0	L	66	229

5.4.3 Relocation models analysis

The direct effect of the pellet fragment relocation models is on the gap width between fuel and cladding. Variations of the size of the gap will result in a variation of the gap conductivity and variation of the prediction of temperature. The reference relocation model is the modified FRAPCON-3 model (RELOC-8). The model depends on the as fabricated gap, the burn-up and LHR. It neither consider axial strain nor apply when the gap is closed^[11]. The other models are:

- The original KWU-LWR model (RELOC-2) accounts for the as fabricated gap, for tangential and axial relocation and it applies also when gap is closed. ^[23]
- The GAPCON-THERMAL-3 (RELOC-3) accounts for the tangential strain due to relocation depending on the as fabricated gap, the burn-up (exponential function that saturates at 5MWd/kgU), the linear heat rate (a simple function). It does not consider the axial strain and it applies also when gap is closed. ^[23]
- The modified KWU-LWR (RELOC-5) accounts for the tangential and axial strain due to relocation depending only on the as fabricated gap. It applies also when gap is closed.

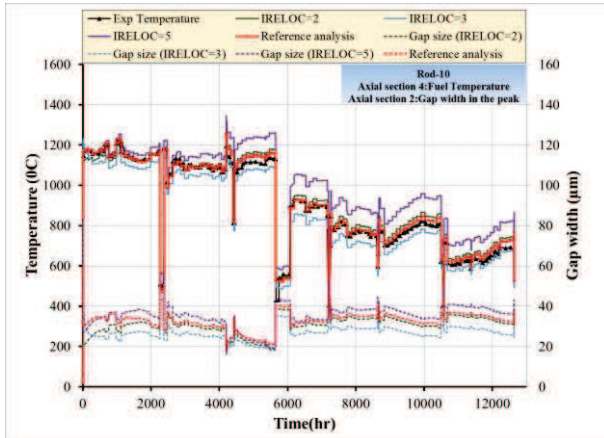
Although the models have impact directly on the gap width, this parameter was not measured in the experiment. Therefore, one can compare how much the predicted gap results in an accurate prediction of temperature.

In *Figure 5-19* analyzes the effect of the relocation models on the fuel temperature, the variation of the gap widths between the various relocation models studied is plotted. For rod-10, IRELOC-8 and IRELOC-2 are consistent with each other and closer to the experimental data IRELOC-8 gives a closer prediction to the experimental temperature than IRELOC-2. Overall, IRELOC-2 does not predict a temperature higher than 25°C on the whole range of irradiation. The wider gap predicted by IRELOC-5 results in a higher prediction of temperature while the opposite is true for IRELOC-3; the code is more sensitive to the increase of the predicted gap size than the decrease of the gap size. Therefore, IRELOC-5 highlights an increase of temperature that can reach up-to 115 °C more than the reference case. IRELOC-3 predicts a decrease that reaches a maximum of 75 °C (compared to the reference case).

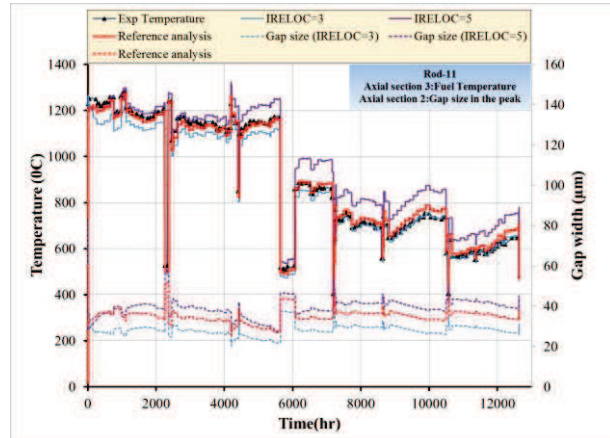
For rod-11, highlights similar trends excepts in the final part of the irradiation in which IRELOC-3 had the best match with the experimental temperature. Based on the results of rod-10, IRELOC-2 was not taken into consideration in the analysis of Rod-11.

To conclude, IRELOC-8 is the model that was the most closer to the experimental temperatures over the whole range of irradiation for both rods. IRELOC-3 was only better for IFA597.5 for the hollow rod only.

The rod pressure and FGR are analyzed in *Figure 5-20*: they reflect the prediction of temperature. In fact, due the over-prediction of temperature, IRELOC-5 overestimate the FGR and pin pressure with respect to the experimental data (rod-10).

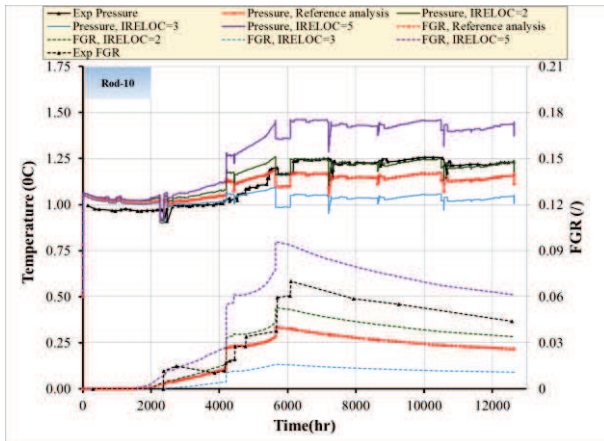


Solid rod (rod-10)

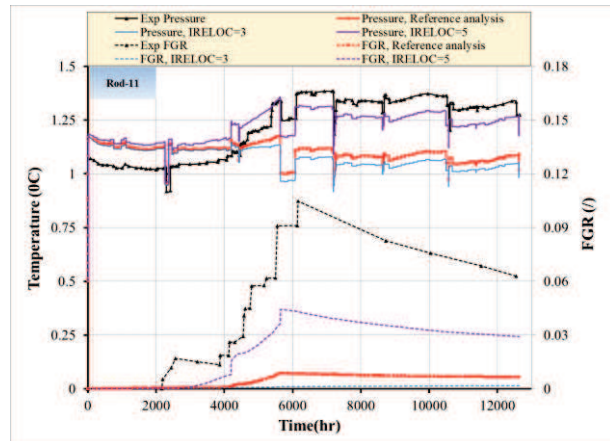


Hollow rod (rod-11)

Figure 5-19 Simulation of IFA-597, sensitivity analysis on relocation models, temperature prediction.




Solid rod (rod-10)



Hollow rod (rod-11)

Figure 5-20 Simulation of IFA-597, sensitivity analysis on relocation models, Pressure & FGR prediction.

 Ricerca Sistema Elettrico	Sigla di identificazione	Rev.	Distrib.	Pag.	di
	ADPFISS – LP2 – 087	0	L	68	229

5.4.4 Swelling correlations

Swelling occurs in nuclear fuel due to the accumulation of fission products generated during irradiation. The contributions of Solid and gases FPs to fuel swelling are different from each other. For the gases in solid solution and the small intra-granular gas bubbles, it is estimated that they furnish about 0.056% per MWd/kgU to matrix swelling rate.^[23] The contribution of gases to swelling is mainly due to the formation of Xenon and Krypton gases. The formation of bubbles of gases leads to the increase in the volume of the solid. Inter-granular gas bubbles can make the largest contribution to swelling depending on the amount of gas formed and the temperature range of operation. At temperatures high enough, those bubbles can interlink together and form a tunnel path for gases to be released. Therefore, fuel swelling will affect FGR, gap width between fuel and cladding and thermal conductivity of the fuel. Different correlations modelling fuel swelling will result in variation of thermal conductivity of the fuel element hence temperature prediction and FGR and the sensitivity of those predictions to fuel swelling should be investigated. In this analysis the correlations used are based on oxide fuel since the correlations used for MOX fuel are still under development.

The reference standard model (SWE-20) considers solid swelling as a linear function of burn-up and applies an exponential term that depends on fitting constants, local temperature and local stress to account for gaseous swelling. The remaining models are^{[13][11]}.

- SWE-18: is the simplest model that accounts for solid swelling only
- SWE-19 is the MATPRO swelling model and accounts for both solid swelling and gaseous swelling. This last contribution is linearly dependent on temperature and exponentially dependent on local burn-up.

The results are given in *Figure 5-21* and *Figure 5-22*, It can be seen that the prediction of the standard SWE-20 and SWE-19 of the temperature, pressure and FGR is the same for rod-10. In IFA597.4, the gap width predicted by both correlations is similar. In IFA597.5, the models did not predict the same gap width and there is a wide variation between the gap sizes of both correlations. The discrepancy between the predicted gaps should have affected the other predicted parameters (Temperature, FGR and pressure). This was not the case here, and a higher temperature was associated to a smaller gap width.

SWE-18 correlation is a simple one that takes only the volume change as a simple function of burn-up and does not consider swelling due to fission gases. SWE-18 resulted in a higher prediction of the temperature. It predicted higher FGRs which was comparable to the experimental data and was a consequence of the higher temperature predicted.

The hollow rod was insensitive to the swelling correlations and no significant difference was detected.

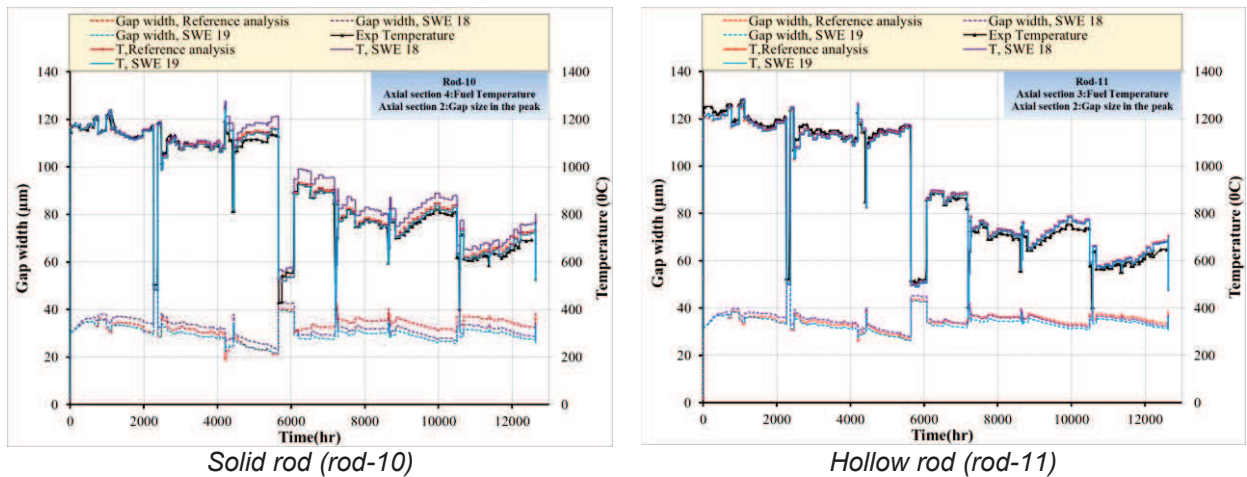


Figure 5-21 Simulation of IFA-597, sensitivity analysis on swelling correlations, temperature prediction.

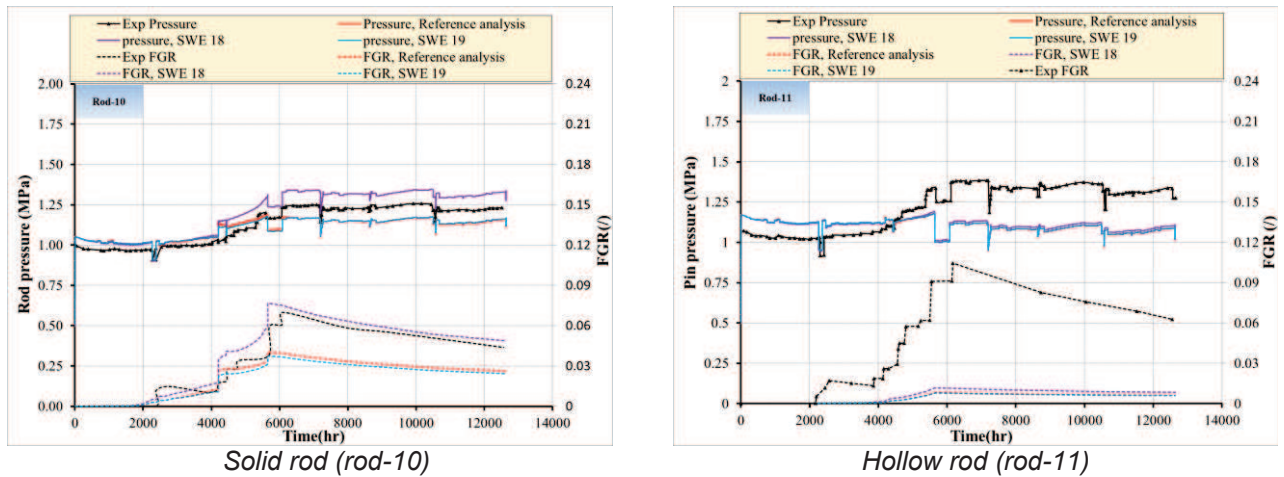


Figure 5-22 Simulation of IFA-597, sensitivity analysis on swelling correlations, rod pressure and FGR prediction.

5.4.5 FGR models

Three Intra-granular FGR models were investigated in this study along with three other inter-granular diffusion models. The reference case FGRMOD=6 is based on a model of Matzke for thermal intra-granular diffusion. For athermal diffusion, a model based on ITU data is used. The rest of the models can be found in *Table 5-5*. This model was combined with an inter-granular diffusion model derived from Koo model for a power ramp conditions (it assumes a constant standard value of gas concentration at grain boundaries and it releases the extra part of gas that reaches the boundaries if no ramp conditions are met. If the power variation exceeds 3.5kW/m and local temperature exceeds a burn-up dependent threshold the grain boundaries are completely vented to simulate micro-cracking of grain boundaries).

The intra-granular models analyzed are^[11]:

- FGRMOD4 is based on the thermal diffusion coefficient of Matzke and athermal diffusion by White and Tucker.

- FRGMOD9 based on the atomic diffusional coefficient of Turnbull.

In *Figure 5-23*, for IFA597.4, there was no difference in temperature prediction between the models until the last stages of the cycle. This is expected since early in the experiment there were no FGR to cause differences. For rod-10, it can be seen that FGRMOD=4 gave the highest FGR but still not close to the experimental prediction. In IFA597.5, The temperature predicted by that model was slightly higher than the reference case within 15 °C. Model FGRMOD=9 gave the lowest of the three models. For rod-11, the FGR was not captured at all by all the models and the temperature predicted by them is almost equal and no preference can be made base on that rod.

For the IGRDM analysis the reference intra-granular model FGRMOD=6 was fixed and the various IGRDM models were analyzed. They are:

- IGRDM1 which is the same of the reference option excepts the condition of venting in case of power ramps that is not accounted for.
- IGRDM2 that assumes the saturation concentration at grain boundaries to achieve the release of the extra gas as a function of the local temperature.

Again, for rod-11, the models did not predict FGR (*Figure 5-24*). The temperature predicted by IGRDM=2 had the best fit of temperature prediction with the experimental data. Still it had a worst under prediction of FGR. For rod-10, It can be seen that the prediction of temperature that best fits the experimental data is that for IGRDM=1. The FGR is more under predicted than for the reference case but still comparable to each other.

To conclude, the reference selection of models (that consider FGR due to micro-cracking) highlights the higher capability to capture both temperature and FGR even if this last parameter remains under-estimated.

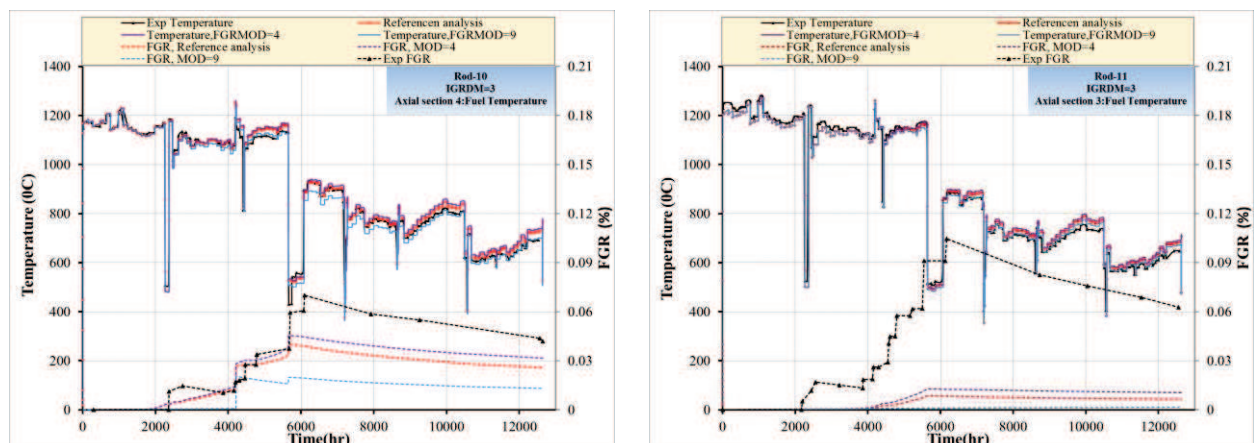


Figure 5-23 Simulation of IFA-597, sensitivity analysis on FGR: Intra-granular model coupled with inter-granular model IGRBDM=3, temperature and FGR predictions.

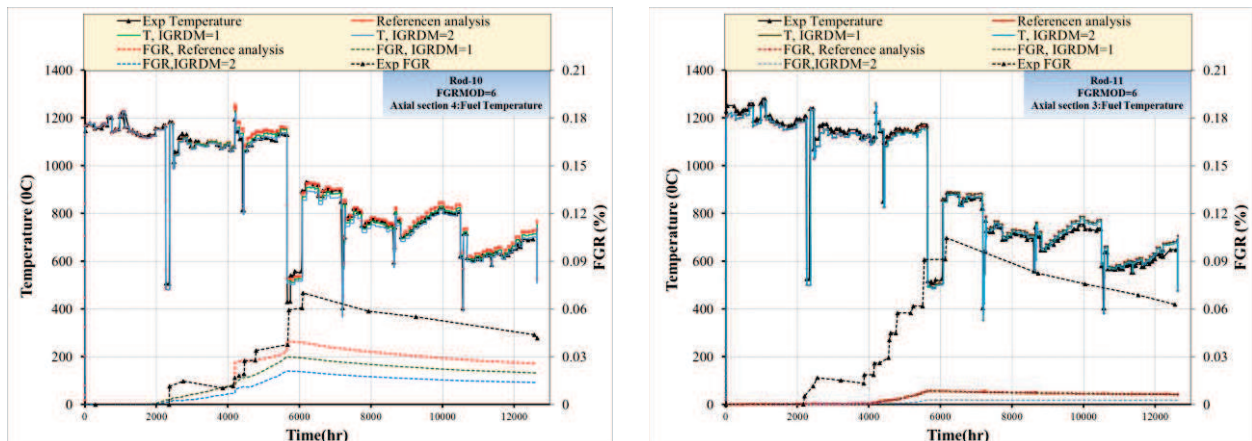


Figure 5-24 Simulation of IFA-597, sensitivity analysis on FGR: Inter-granular models coupled with intra-granular model FGRMOD=6, temperature and FGR predictions.

5.4.6 Gap conductance models

The ability to predict the gap conductance will affect the whole thermal resistivity of the fuel rod. IHGAP=0 is the standard model based on thermal conductivity of mixture according to Lindsay and Bromley with accommodation coefficients are taken into account.^[11] The remaining models are:

- IHGAP 3: as standard option but without considers accommodation coefficients
- IHGAP 4: thermal conductivity of mixture according to Tondon and Saxena. Accommodation coefficients are taken into account.

Taking accommodation coefficients into account does not result in significant difference from the case when it was neglected, Figure 5-25. The difference in temperatures between both cases does not exceed 5 °C. Based on IFA597, No preference can be made between IHGAP=3 and IHGAP=4 at some parts of the experiment IHGAP=3 fits well with experimental data and at other points IHGAP=4 is better. At some points both models predict the same value. A general conclusion is that the temperature prediction is not significantly sensitive to the different models implemented in TU.

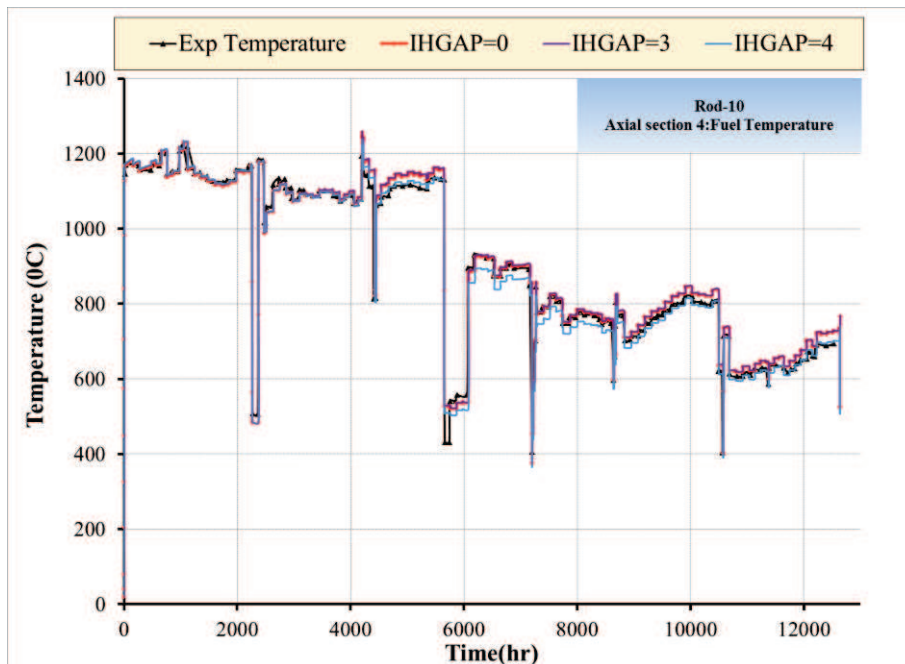


Figure 5-25 Simulation of IFA-597, sensitivity analysis on gap conductance, temperature prediction.


5.4.7 Other parameters

Initial gap width

Initial gap width is a parameter provided by the experiment data. In this study, the nominal initial gap width was assumed to have around 15% uncertainty. 80% percent of this uncertainty was due to uncertainty in the outer fuel radius and 20% is related to the inner cladding radius. The results of the conducted analysis is that the nominal gap width provided by the experiment data lead to a good prediction of the temperature. The temperature prediction is more sensitive to increasing the initial gap width, which leads to higher temperature prediction. A decrease in the initial gap size will lead to a lower prediction of the temperature but the sensitivity of the prediction to that decrease is lower than its sensitivity to the increase in the gap. In general, the initial gap size measurements will affect the whole results of the simulations and it is important to accurately consider it as parametric analysis.

Grain size DKORN

The grain size of the fuel material is given in the experiment data between a lower and an upper limit. The Grain size parameter (DKORN) was taken as an average value between those two limits. The result of the conducted analysis show shows that the nominal average grain size taken in the reference case gave a good estimate of the temperature and it can be concluded that the average experimental data given by the experiment are not a cause of any deviation of the code prediction from the experimental data. The temperature prediction is more sensitive to decreasing the grain size than to increasing it. Smaller grains means as well more probability of fission gases reaching the grain boundary and with the higher temperature leading to

 Ricerca Sistema Elettrico	Sigla di identificazione	Rev.	Distrib.	Pag.	di
	ADPFISS – LP2 – 087	0	L	73	229

interlinking between fission gas bubbles which leads to a higher FGR predicted by the code for the lower limit of the grain size.

DENBUP

Is the cut off burn up above which the densification halts. Fuel densification is important to consider and if it was not, the temperature will be seriously under-predicted to more than 200⁰C. If no densification is considered, the gap size will be smaller than when it is considered at the same LHR conditions. This will enhance the conduction through the gap and will lead to the significant under prediction. The reference case used here was DENBUP=10000 MWD/tHM. As a sort of sensitivity study, DENBUP was decreased to 3000 MWD/tHM. The densification overall effect was no different from the case when higher value was taken. Therefore being conservative and taking higher value of densification cutoff will not result in severe effect on the temperature temporal profile evolution.

DENPOR

Is a parameter representing the porosity of the fuel rod at the end of sintering. Uncertainties related the prediction of this parameter should be investigated. There is an uncertainty of around 50% of the data used to fit an equation for this parameter was validated using TU. The nominal data obtained by the equation predicted the best fit of the temperature. The sensitivity to DENPOR parameter is higher with the increase of the parameter while it is less sensitive to its decrease which is consistent with the experimental data upon which DENPOR correlation was fitted.

5.5 Radial analysis

In order to investigate the radial profile of the thermal conductivity during IFA597.4/.5, two points in time were taken at approximately 5 MWD/kgU and 24 MWD/KgU. These points were chosen based on the average burn-up value. The points in time at which these values of burn-ups were reached varied between rod-10 and rod-11 due to the different locations they held in the rig. The exact values of the burn-ups and times can be found in *Table 5-6*.

Those were chosen to result in a broad analysis that captures relatively low and medium values of burn-up hence, to capture the influence of this parameter.

The thermal conductivities in both cases were plotted as functions of the temperature profile of the rods at these specific moments taking into consideration the radial variation of the rod conditions (temperature, local burn-up, porosity). O/M ratio did not vary during the experiment and during modelling when a test flight was made to investigate if the code will detect sensible variation of that parameter by choosing the option IOXIRE=1 which allows modelling changes of O/M ratio.

A radial sensitivity analysis was performed to investigate variation between thermal conductivity values and how would that affect the temperature profile of the rods. Not only TU correlations were investigated in this study, also open literature correlations were investigated as well. The values of thermal conductivities based on TU correlations were captured directly from the code. The open literature correlations were calculated on the discretized radial nodes based on the temperature, Plutonium

content and porosity radial profiles. Performing this analysis would not result in obtaining a temperature profile by open literature correlations but can give a qualitative idea about how would they predict or deviate from TU correlations if they were applied in TU code. After that, those correlations were compared to experimental data (They were available at Zero burn-up only but should still be comparable with the results at this low burn-up) to check their compatibility with them. The results of these investigations are summarized in the next subsections.

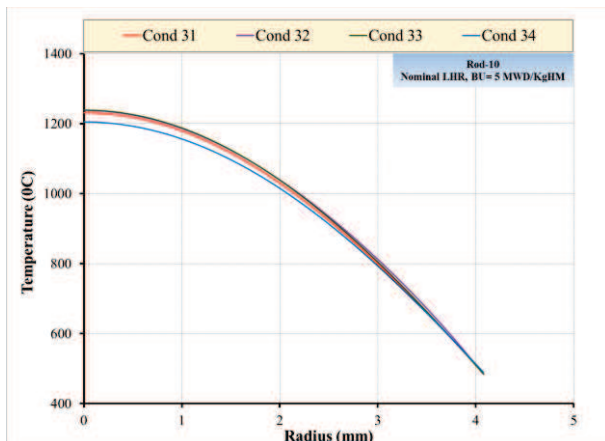
	Rod-10 (Solid pellets)	Rod-11 (Hollow pellets)
Axial position	Peak position (section 3)	Peak position (section 2)
Time-1 (hr)	1757.44	1692.6
Burn up (MWD/KgU)	5.0	5.11
Time-2 (hr)	12633	11647
Burn-up (MWD/KgU)	23.99	23.986

Table 5-6 IFA-597, summary of radial analysis main data.

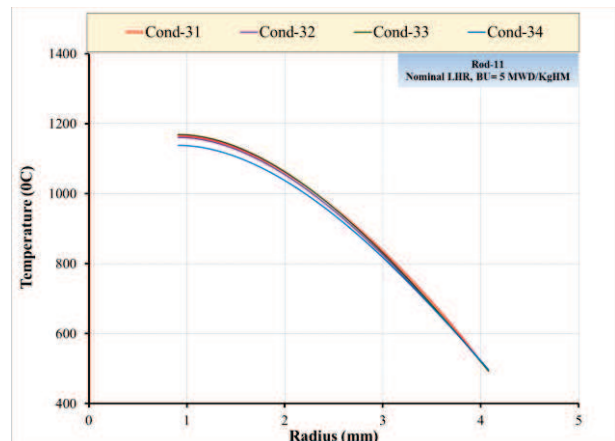
5.5.1 IFA597.4 Radial analysis (5 MWD/KgU)

The temperature profile at an average burn-up of 5 MWD/KgU at the peak power location in the rods was plotted as function of fuel pin radius, *Figure 5-26*. The temperature varies between 1238 °C at the center and 490 °C at the periphery of the rod. Only Wiesenack's correlations (COND-34) deviated from the rest of the correlations and tended to predict an obvious lower temperature profile in most radial regions of the rod that is under-predicted relative to the experimental data as well.

The thermal conductivities as function of temperature are given in *Figure 5-27* and *Figure 5-28*. The figures include the correlations given in 3.2 and experimental data obtained for un-irradiated MOX of similar design (to IFA-597 rods). Regarding open literature correlations, it can be seen that MATPRO and MARTIN's correlations resulted in a highly over predicted thermal conductivities that would predict a lower temperature profile. Comethè correlation predicted thermal conductivity slightly higher than Wiesenck. Baron-Hervè-95 correlation predicts thermal conductivity similar to COND34 at the peripheries and center of the rod. In the mid-section of the rod the profile is similar to COND32. In general, it is expected to predict a temperature profile higher than COND34 but lower than the others. The experimental data-points fits the TU correlations, the Baron-Hervè and the Comethè correlations.



Rod - 10



Rod - 11

Figure 5-26 IFA-597, temperature radial profile at 5MWd/kgHM as function of the conductivity correlation adopted.

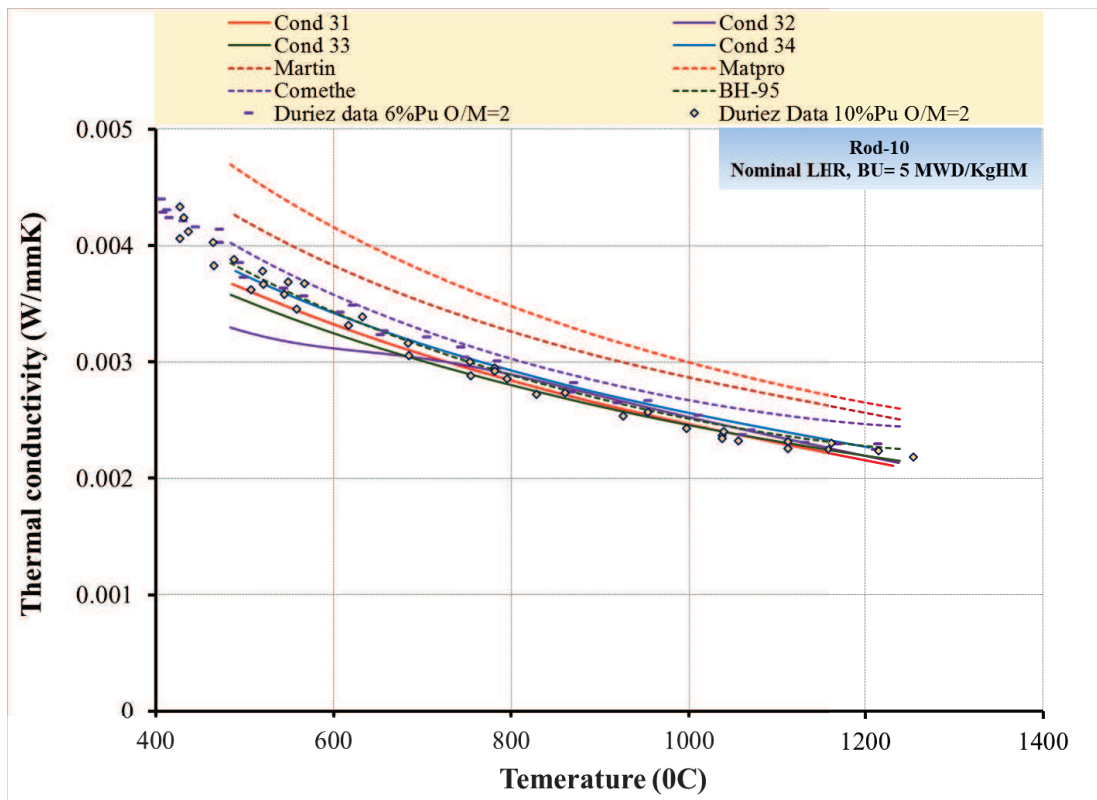


Figure 5-27 IFA-597 at 5 MWd/kgHM, thermal conductivity profiles when applied to rod-10, comparison with open literature correlations and experimental data.

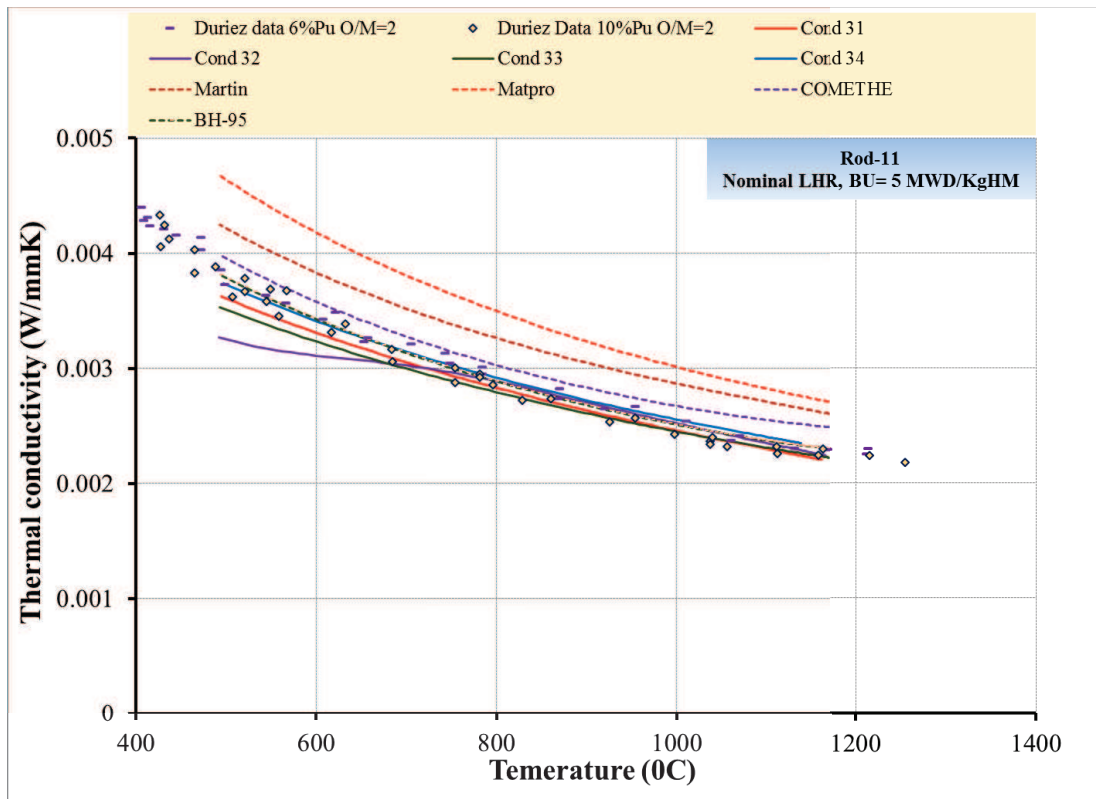


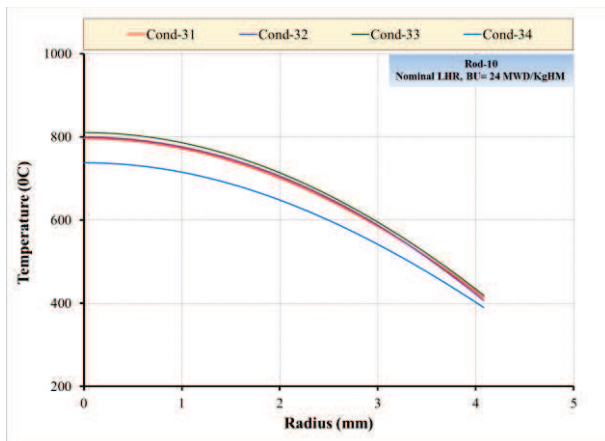
Figure 5-28 IFA-597 at 5MWd/kgHM, thermal conductivity profiles when applied to rod-11, comparison with open literature correlations and experimental data.

5.5.2 IFA597.5 Radial analysis (24 MWD/KgHM)

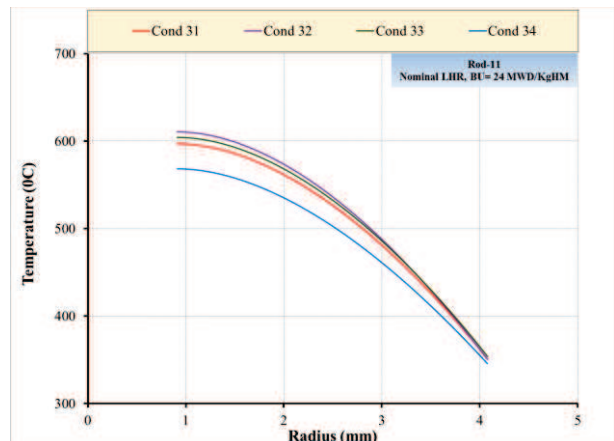
The temperature profile of the solid rod lays between around 800 °C at the center and around 420 °C at the peripheries of the rod (*Figure 5-29*). The correlation of Wiesenack (COND 34) predicted a temperature that is around 65 °C lower than the others. The temperature profile predicted by the other correlations have more variability than the previous case but they are still compatible with each other.

The thermal conductivities as function of temperature are given in *Figure 5-30* and *Figure 5-31*. The figures include the correlations given in 3.2.

Comparing the thermal conductivities, it can be seen that the studied correlations shows great variability than at 5 MWd/kgHM. TU correlations consider burn-up as a factor that the thermal conductivity will degrade with burn-up. It can be seen that TU predicts the lowest thermal conductivity compared to open literature due to the burn-up effect. Open literature correlations are higher and will definitely predict a lower temperature profile. The centerline temperature predicted by TU correlations matches the experimental measurement during IFA597. Therefore, it is an indication that burn-up is an important factor that cannot be neglected when modelling thermal conductivities of MOX, since from medium values.



Rod - 10



Rod - 11

Figure 5-29 IFA-597, temperature radial profile at 24MWd/kgHM as function of the conductivity correlation adopted.

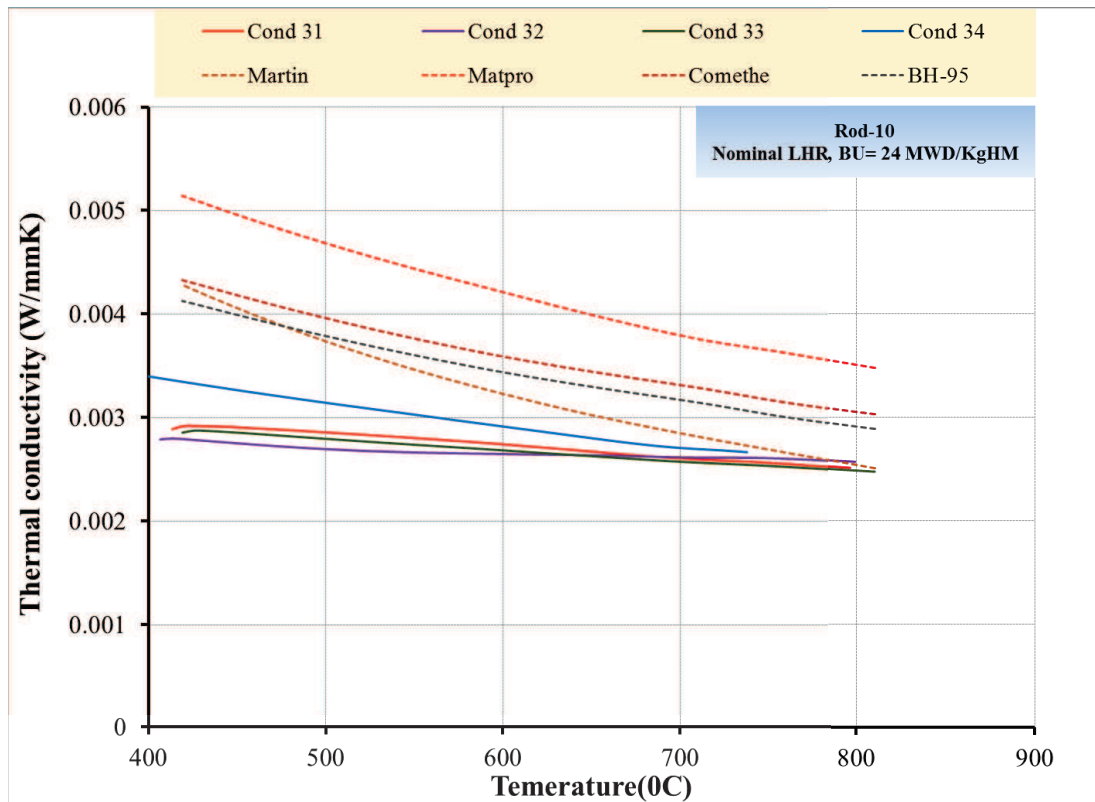


Figure 5-30 IFA-597 at 24 MWd/kgHM, thermal conductivity profiles when applied to rod-10, comparison with open literature correlations and experimental data.

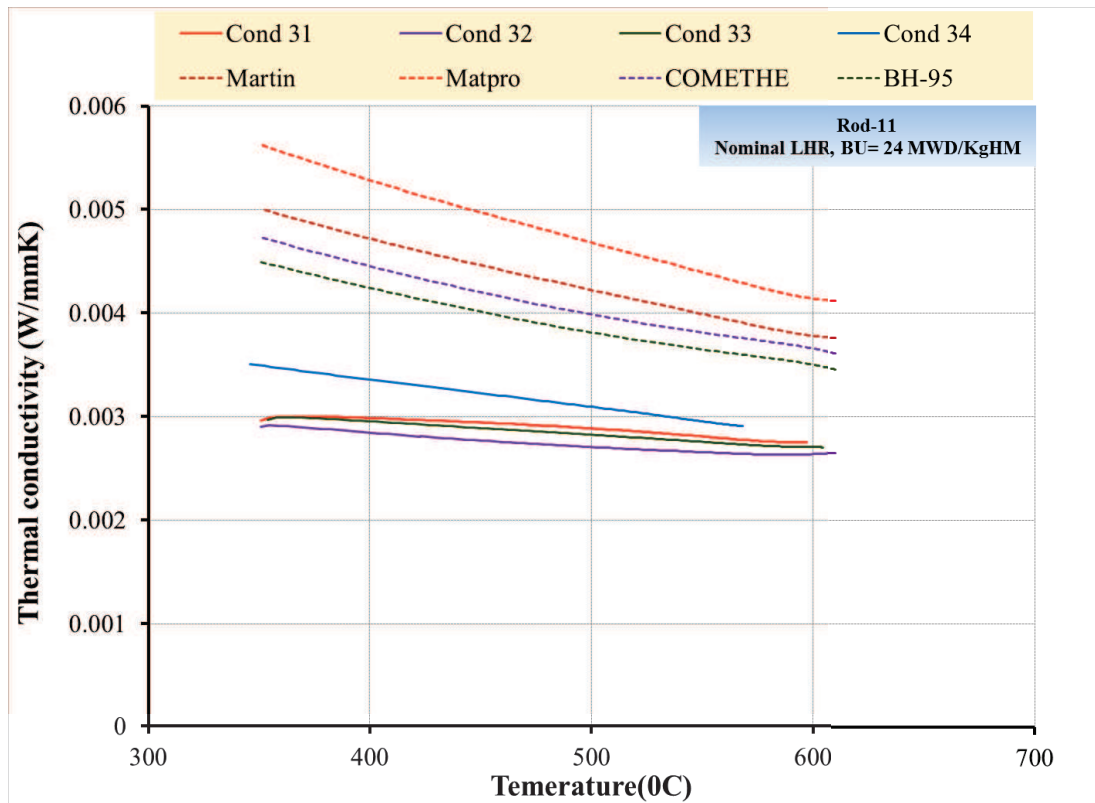



Figure 5-31 IFA-597 at 24 MWD/kgHM, thermal conductivity profiles when applied to rod-11, comparison with open literature correlations and experimental data.

 Ricerca Sistema Elettrico	Sigla di identificazione	Rev.	Distrib.	Pag.	di
	ADPFISS – LP2 – 087	0	L	79	229

6 Analysis of FR MOX: HEDL P-19 experiment

6.1 Description of the experiment


6.1.1 Background and objective of the experiment

The purpose of the HEDL P-19 experiment was to investigate the effect of as-fabricated fuel to cladding gap from (0.086 to 0.25 mm) on the linear power needed to cause incipient melting $Q'm$.^[3] The normalized linear power to the peak is plotted in *Figure 6-1*. The MOX fuel used was (25% PuO₂-75%UO₂) rods. The experiment consisted of a subassembly containing 19 encapsulated pin representative of the Fast Flux Test Facility (FFTF) fuel design. Sixteen of them were fresh fuelled pins, three pins were pre-irradiated before the experiment. The cladding outer diameter of half of the fresh pins is 5.84 mm. The other half was of 6.35 mm. The pins were filled with pure helium and clad with 316 stainless steel (20% cold worked). Main design data can be found in Table 6-1.

The experiment aimed to simulate fast start-up situations of FBR. The power history of the P-19 experiment is plotted in *Figure 6-2*. Steady state power was then kept for an hour after which the power was rapidly ramped with a 15% increase. This higher power was kept for 10 minutes to test the power resulting in fuel melting. The reactor was then scrammed to quench the fuel structure so that further neutron radiographical analysis will be informative. This radio-graphical investigation was to determine if melting occurred inside the rods and the melting heights in the rods that propagated melting. The radio-graphical analysis confirmed no partial melting of all the pins with cladding outer diameter of (5.84 mm) with gap width of less than 0.14 mm. The rest of the pins developed melting regions with different extents.

Transverse fuel ceramographic samples were used to measure fuel restructuring radii, residual gap widths and radial extent of melting at the peak power position. There is uncertainty regarding the power to melt due to the uncertainty of the effect of the relocated molten fuel on the local power. Also, the central void formation is uncertain due to melting that obliterated the formed central void.

Since most of these peak power regions operated at much higher powers than $Q'm$, melting is extensive even in adjacent fuel.^[26] The axial extents of melting, as determined from longitudinal ceramographic sections, offered the best data for determining $Q'm$ since these sections were actually located where incipient melting occurred and experienced the least power variation due to molten fuel relocation. The main data for the two rods of interest in this analysis (P-19-2 & P-19-5) from PIE are given in *Table 6-2* and *Table 6-3*.

 Ricerca Sistema Elettrico	Sigla di identificazione		Rev.	Distrib.	Pag.	di
	ADPFISS – LP2 – 087		0	L	80	229

Rod N°	1	2	3	4	5	6	7	8	9	10	11	12	13	14	15	16
Rod Id.	P 19 2	P 19 3R	P 19 5	P 19 6	P 19 7R	P 19 8	P 19 13	P 19 20	P 19 24R	P 19 25R	P 19 26R	P 19 27R	P 19 28	P 19 30	P 19 33	P 19 35
Gap μm	99	127	72.5	49.5	79	122	99	123	127	101.5	76	51	43	89	62.5	91.5
%TD	90.75 92.40	X	X	X	X	X	X	X	X	X	X	X	X	X	X	X
Clad OD mm	5.84	X	X	X	X	X	X	X	X	X	X	X	X	X	X	X
Fuel	25% PUO ₂ - 75% UO ₂															
Cladding	316 stainless steel (20% cold worked)															
Filling gas	98% He at 1 bar															
O/M	1.96															
Active length	343 mm															
Na inlet temp.	371 °C															
Max LHR kW/m	54.5	64	56.1	56.1	66.6	53.8	54.5	54.1	64.6	66	66.9	66.9	67.9	65.6	55.1	54.1

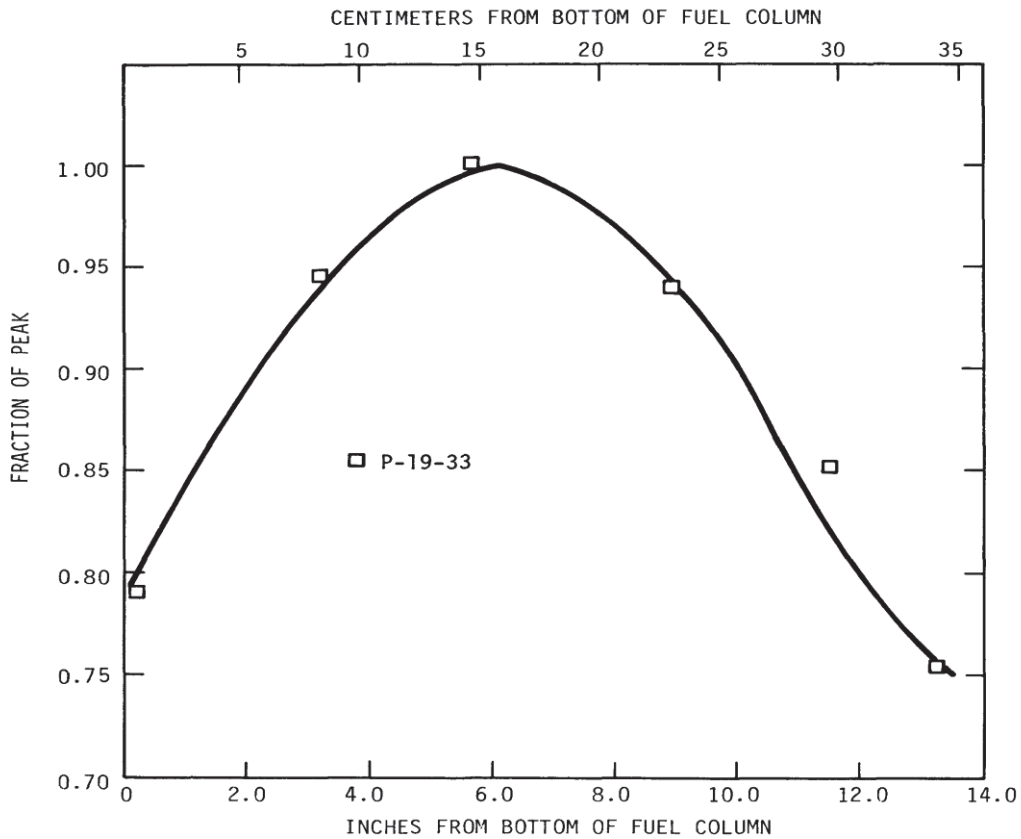
Table 6-1 HEDL P-19, design data. ^[3]

Rod Id	Peak Power [kW/m]	EXP Bottom axial Melting extent			EXP Top axial Melting extent		
		Location [cm]	Local power [kW/m]	Coolant Temp [°C]	Location [cm]	Local power [kW/m]	Coolant Temp [°C]
P-19-2	54.5	72.1	51.8	386	248.4	50.5	426
P-19-5	56.1	--	--	--	--	--	--

Table 6-2 HEDL P-19, axial extension of fuel melting at the end of the experiment. ^[3]

Rod Id	Id	Location [cm]	Central void radii [mm]	Molten radii [mm]	Columnar radii [mm]	grain	Diametric gap [mm]
P-19-2	1	15.5	0.64	0.94	1.80		0.142
	2	19.1	0.58	0.79	1.73		0.142
P-19-5	1	15.5	0.46	0.00	1.68		0.102
	2	18.5	0.48	0.00	1.65		0.147
	3	20.3	0.43	0.00	1.55		0.102
	4	21.6	0.46	0.00	1.60		0.122

Table 6-3 HEDL P-19, measurements of central void, columnar grain radius and TD at pellet center at the end of the experiment. ^[3]



HEDL 7611-54.13

Figure 6-1 HEDL P-19, pin power axial profile.^[3]

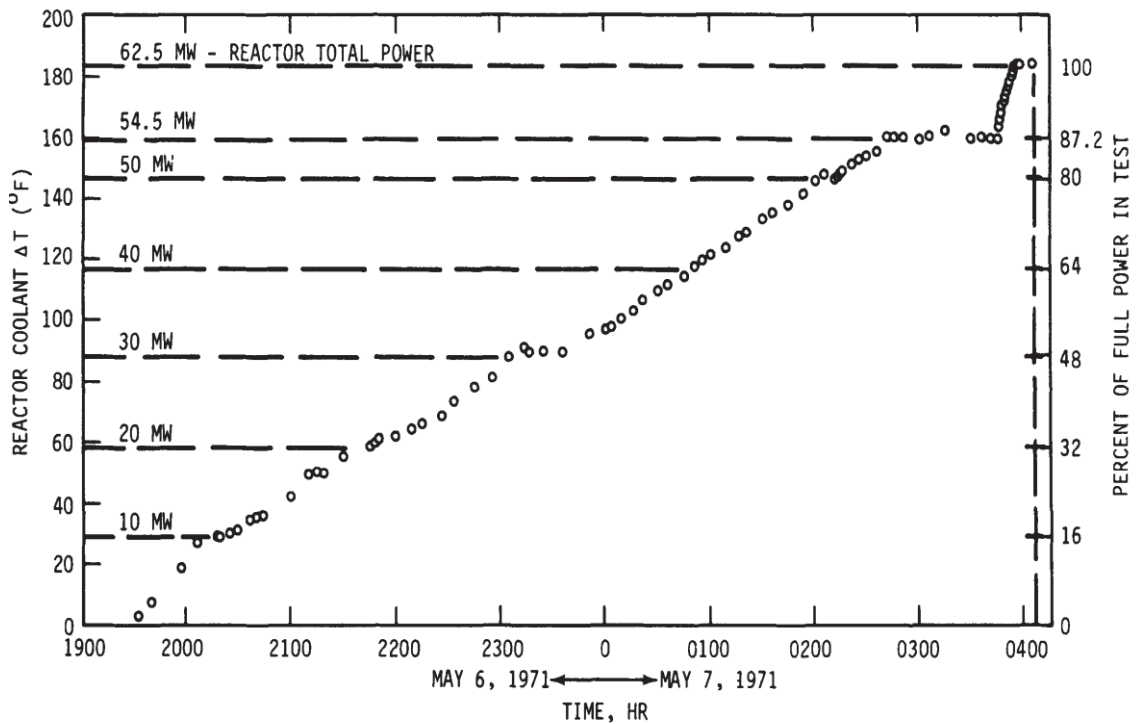



Figure 6-2 HEDL P-19, EBR-II power history during the experiment.^[3]

 Ricerca Sistema Elettrico	Sigla di identificazione	Rev.	Distrib.	Pag.	di
	ADPFISS – LP2 – 087	0	L	82	229

6.1.2 Experimental Breeder Reactor #2 (EBR-II)

EBR-II is a sodium cooled reactor that was designed and operated by Argonne National Laboratory. It was shut down in 1994. The reactor was operated with thermal power of 62.5 MW_t (20 MWe). The reactor was intended as a FBR accompanied with an on-site reprocessing facility. During the first five years of the reactor life, (1964-1969), 35000 fuel element were reprocessed. The reactor was then transformed to a burner and its aim was shifted to testing fuel materials for future sustainable LMFBR. The reactor operated as an integral fast reactor prototype that cost more than US\$32 millions starting from 1964 to 1994. 30000 irradiation tests took place in the reactor during its 30 years lifetime. Two billion KWh_e were generated from the reactor that were used as electricity and heat source for ANL facilities.^[27]

The pool type design of the reactor assured the passively safe reactor concept. In case of failure of scrambling the reactor by the operator, the reactor will shut down spontaneously without external assistance. That helped developing many safety tests that involved loss of flow accidents. The accidents were simulated with normal shutdown systems disabled and no excessive temperatures were reached.^[28]

A schematic diagram of the plant system is sketched in *Figure 6-3*. The primary system contains the reactor system, the sodium coolant primary cycle, and the heat removal systems. They dwell in the containment building designed to accommodate any release during transient or accident situations. The fuel handling system was submerged in Sodium contained in the primary tank. The sodium is withdrawn from the bulk sodium and pumped into the reactor to flow upwards in the reactor through the subassemblies cooling the fuel and the blanket. Two lines are used to cool the reactor. One high-pressure line for the subassemblies and the inner blanket side. Another low-pressure line is used to cool the outer side of the blanket. Afterwards, Sodium is driven to a heat exchanger to be cooled and returned back to the Sodium bulk. The reactor is geometrically close-packed due to the existence of single size of the subassemblies. The hexagonal subassembly tube was 2.290 inches across external flats of 0.040-inch wall thickness. The subassemblies were spaced on a triangular pitch of 2.320-inch center distance.^[29]

The secondary system consists of four main components, Sodium circulating pump, heat exchanger, steam super-heater and steam evaporator. It is used as a mediator containing non-radioactive Sodium that transfers heat from radioactive Sodium on the primary side to a steam system. Flow rate on the secondary side is 2.5 x 10⁶ pounds per hour. Super-heated steam is driven to a turbine at 850 °F with a rate of 1250 pounds per inch².

The Power Plant contained the turbine generator and associated equipment and the control room for the reactor and power cycle. It was interconnected to the Reactor Plant by means of one air lock to permit personnel access to the Reactor Plant. The building was of conventional construction. The Fuel Cycle Facility contained two shielded cells for disassembly, processing, and manufacture of fuel elements and subassemblies, and supporting facilities for these operations. It also contained the inert-gas storage facilities, the sodium equipment cleanup cell, and exhaust

ventilation system and the stack for the exhaust from the Fuel Cycle Facility and Reactor Plant.

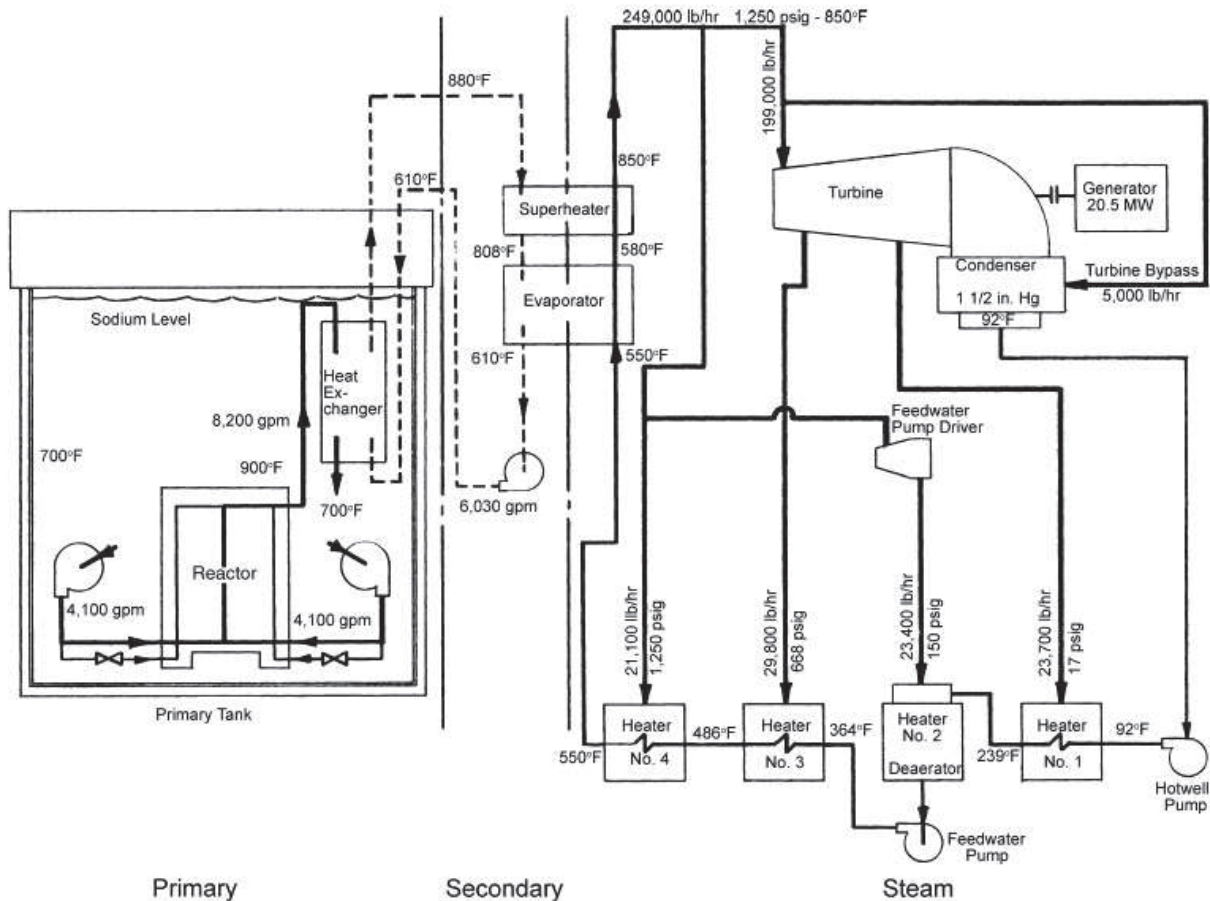


Figure 6-3 Schematic diagram of EBR-II plant. [29]

6.2 Modelling HEDL P-19 with TU

6.2.1 Development of TU input file

The documented work was modelled using TRANSURANUS code, version “v1m1j12”, with the deterministic option, steady state thermal and mechanical analysis. The version of the manual is “v1m1j12”. The boundary conditions were prepared using a program prepared using PERL language.

An input deck was prepared according to the information available in the manual of the code. Most of the models used in the reference analysis were the standard recommended models by the code developers. Some deviations occur when needed. For EBR-II the melting model used is the one used for Uranium nitride fuel MODFUEL(16)=15. This is due to the fact that this model gives the melting temperature as a constant value (2760°C) which fits better with the conditions of P-19 experiment. Other melting temperature models that use the plutonium content, O/M and burn-up will be later investigated as a sort of sensitivity analysis in section 6.4.3. The average grain diameter was assumed to be 22 μm while the upper plenum was

taken to be 300 mm (comparable to the active length of the rod). The main models that were expected to affect the measured parameters of the rods and the prediction of fuel temperature are summarized in *Table 6-4*. Most of the models used in this analysis are the ones recommended by TU. For various reasons other models were chosen. In section 6.4, sensitivity analysis of the results to some of the models or correlations that were not chosen in the reference case will be done.

HEDL P-19 Reference input decks			
Parameter	Reference Option	Description	Other options
Fuel conductivity	Correlation 31 (recommended)	Standard correlation of the thermal conductivity of MOX fuel (best estimate) according to Van Uffelen and Schubert. based on experimental data obtained by Duriez et al for fresh MOX fuel and laser flash measurements of irradiated MOX fuel at ITU. It is extended by an ambipolar term recommended by Ronchi et al.	32,33,34,35
Pellet fragment relocation	Model ireloc 8	Modified FRAPCON-3 model. It considers the as fabricated gap size, the burn-up and the linear heat rate.	2, 3, 4, 5, 6
Fuel grain growth	Model igrnsz 1 (recommended)	Grain growth model of Ainscough and Olsen. It computes the grain radius increase as function of the fuel local temperature assuming a maximum grain radius for each temperature.	--
Fuel densification	Model idensi 2 (recommended)	Empirical model for LWR and FBR. This model needs the input of the minimum porosity DENPOR at the end of thermal and irradiation induced densification and the time constant DENBUP (burn-up in MWd/tU, at which irradiation induced densification is terminated).	3, 7
Gap conductivity	Model ihgap 0 (recommended)	Standard Option: gas Bonding thermal conductivity of mixture according to Lindsay and Bromley. Accommodation coefficients are taken into account	1, 3, 4, 5
Solidus and Liquidus Melting Temperatures	Correlation 15	The correlation is recommended in the Gmelin handbook. It is used for Nitride and mixed nitride fuel $T_{Liquidus} = 3035 \text{ K} (2762^{\circ}\text{C})$	10,11,13

Table 6-4 Simulation of HEDL P-19, summary of models and correlations that might affect the prediction of thermal conductivity of the rods.

6.2.2 Boundary conditions

The boundary conditions used are:

- Linear heat rate at 17 axial position;
- Fast neutron flux (>1 MeV);
- Sodium bulk Coolant temperature
- Coolant pressure.
- Heat transfer coefficient at the cladding outer surface

Linear heat rate (LHR) increase/decrease with a rate of 6 (KW/m.h) for any change between different values of LHR. This transition rate and the time needed for the LHR to be changed is calculated based on the LHR in the peak position. During the ramp the rate of the change of the power was taken as 500 KW/m.h, this is typically used during power ramp tests. The linear heat rate were calculated at 17 position of the rods. The axial positions of the measurements can be seen in *Table 6-5*. Those positions were chosen based on the power profile that can be seen in *Figure 6-1*.

The fast neutron flux is given as a constant rate of 1×10^{14} n/cm².s. The coolant pressure is given as a constant over the whole period of the experiment with a value of 0.1 MPa (Open pool condition). The coolant temperature is given on the same axial positions of the linear power and its evolution is calculated based on the experimental report.

The trend of the linear power and coolant temperature applied to rod P19-2 can be seen, respectively, in *Figure 6-4* and *Figure 6-5*. The active part of the fuel was considered in this study. The rods are divided into a number of m_3 slices that are determined by the number of boundary condition points given in the experiment data. The sectional option was chosen in this analysis. Thus, the total number of points taken is $m_3 + 1$.

Axial node	Position-Rod (mm)
1	0
2	18.533
3	33.7837
4	54.1279
5	73.9818
6	92.3147
7	110.668
8	126.489
9	145.392
10	163.815
11	180.717
12	211.498
13	238.207
14	255.199
15	275.263
16	296.348
17	335.775

Table 6-5 Simulation of HEDL P-19, axial discretization of the fuel rods.

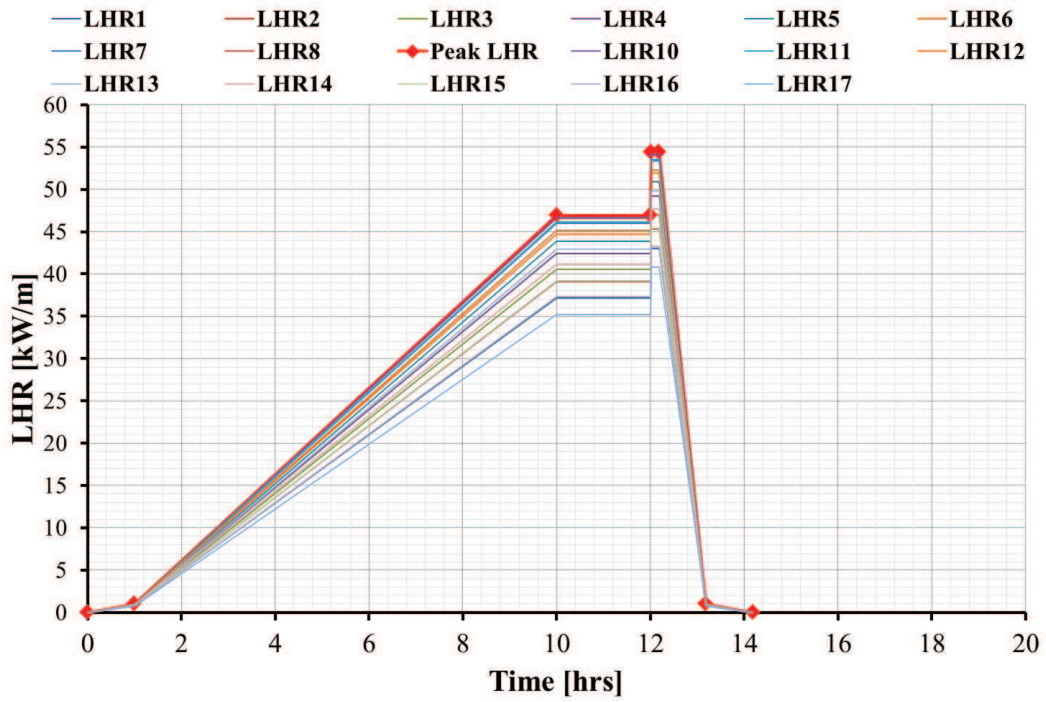


Figure 6-4 Simulation of HEDL P-19, rod P19-2, LHR at 17 axial elevations.

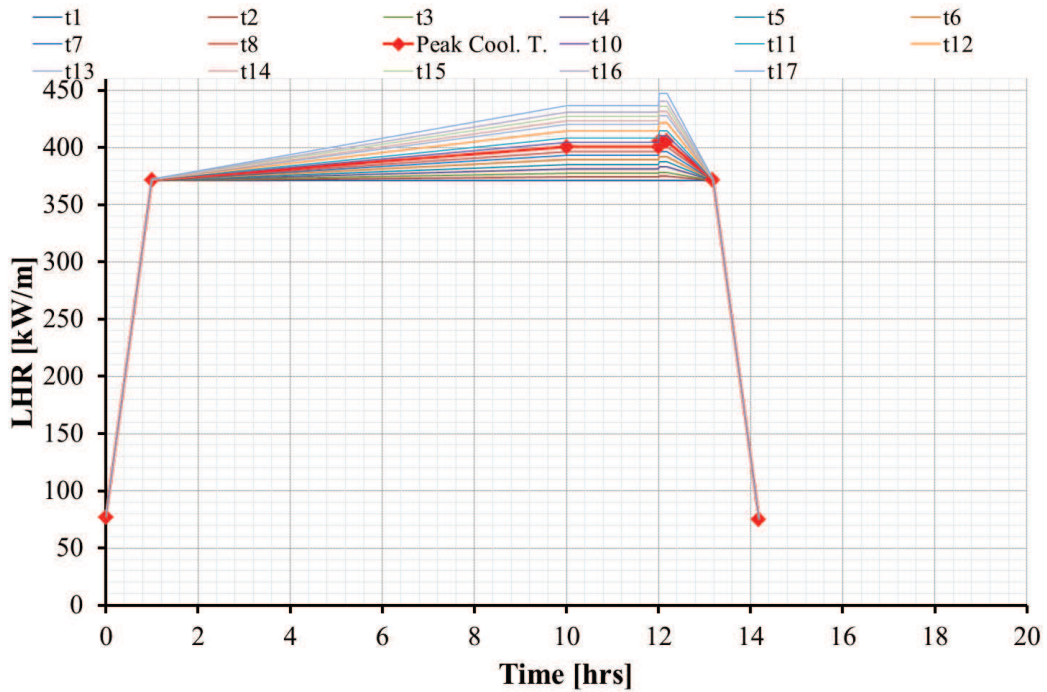


Figure 6-5 Simulation of HEDL P-19, rod P19-2, coolant temperature at 17 axial elevations.

 Ricerca Sistema Elettrico	Sigla di identificazione	Rev.	Distrib.	Pag.	di
	ADPFISS – LP2 – 087	0	L	87	229

6.3 Reference analysis of HEDL P-19 rods

6.3.1 Temperature prediction

The evolution of the fuel temperature at the pellet center in the peak power position is given in *Figure 6-6* and *Figure 6-7*. The temperature profile increases gradually with the LHR up to 10 hours. At that time the LHR and temperature are kept constant for two hours. During that time it can be seen that the code predicted that the maximum temperature in the rods is almost equal to the melting temperature marked by the horizontal line. This means that any slight increase in LHR will lead to the beginning of melting of both rods. That was predicted for both rods by the code as the LHR increase to a level where melting can happen, both rods temperatures increase beyond melting temperatures up to 3220 °C for rod P-12-2 and a slightly lower temperature 3122 °C for rod P-12-5, both temperatures are predicted at the Peak LHR positions. Since this experiment was a melting experiment, there was no temperature measurement attempted. Therefore, there is no direct comparison between temperature predicted by the code and experimental measurements, rather integral comparison of the melting heights is done here. It can be mentioned here that neutron radiography showed that rod P-12-5 did not suffer melting at all. This means that temperature in this rod did not exceed the melting temperature during the ramp phase of the experiment. This leads to a conclusion that the code over-predicted the temperature in that rod even though it cannot be said quantitatively to what extent was the temperature over-predicted but it is not less than 350°C.

The radial temperature profile at a moment prior to the reactor scram is investigated in *Figure 6-8* and *Figure 6-9*. Radial temperature distribution is reported for the fuel and the cladding. It can be seen that for rod P-19-2, at a radius of 0.92 mm the temperature increases beyond the melting temperature. For rod P19-5, the temperature increases beyond melting point at 0.73 mm.


6.3.2 Gap width

The gap width was modelled by TU using standard relocation model (IRELOC-8, briefly introduced in section 5.4.3). The code was able to capture the experimental measurements that were done at the end of the experiment. For P19-2 the code was able to capture the gap width at the two measurement positions, *Figure 6-10*. For P-19-5 the code was able to capture two points out of the four measurements locations, *Figure 6-11*. This correlation resulted in the best prediction of the gap size for the other rods in P-19 experiment with some exceptions.^[26]

Assuring an accurate prediction of the gap width is a first step in assuring that the prediction of the melting height of the rod is related to the prediction of the temperature in the fuel rod itself, which is directly dependent on the MOX thermal conductivity correlations.

6.3.3 Central void

The code under-predicts the central void size at the end of the experiment (*Figure 6-12* and *Figure 6-13*). The predictions were much smaller than the experimental

 Ricerca Sistema Elettrico	Sigla di identificazione	Rev.	Distrib.	Pag.	di
	ADPFISS – LP2 – 087	0	L	88	229

measurement. However, at least for rod P-19-2, only qualitative comparisons is possible since the measured void is uncertain because it is affected by the relocation of the melted fuel that would obliterate the formation of central void.

6.3.4 Columnar grains

The columnar growth of the grains did not start until the power increase of more than 36 KW/m after 8 hours of the beginning of the experiment. The grains kept growing up to the end of melting when the reactor was scrammed. The growth seized then and the radius of the columnar zones remained constant for the last two hours after the scram. The code was able to predict the columnar growth with minor deviations (*Figure 6-14, Figure 6-15*). The predicted radius was lower than experimental measurements at the end of the experiment of about 0.1-0.2 mm in radius.

6.3.5 Melting radius

The melting radius of the fuel is not given directly from TU code. Still, it can be inferred for each axial segment of the rod by checking the radial distribution of the thermal conductivity and considering the maximum radius where the thermal conductivity is constant (1.5 J/m.K) as the molten radius of that segment. That was done for the 17 segments of the fuel and plotted in *Figure 6-16* and *Figure 6-17*. The code was able to accurately capture the molten radius of rod P-19-2. For P-19-5, the code predicted melting while the examination of the rod showed that it did not melt at all. This means that the melting radius should be zero.

6.3.6 Melting elevation

The prediction of the melt front is the main task in this analysis since it is the reference for which an inference about temperature prediction of TU can be made. Rod P-19-2 is analyzed in *Figure 6-18*: the melt front is over predicted when compared to the experimental examination. This longer axial melting leads us to draw a conclusion that there is an overall over prediction of the temperature inside the rod. From the fact that the gap width between the fuel and the cladding is accurately predicted, it corroborates the fact that TU code under-predicts the fuel conductivity (at least in the high temperature regimes). The same conclusion is valid for rod P-19-5 (*Figure 6-19*) which did not propagate melting while the code predicted considerable axial melting in the rod which can be related as well to the under prediction of the heat conduction in the rod. Even if the code behaves in a conservative way, the reasons for this over prediction of the melting heights should be thoroughly investigated by checking its sensitivity to the various phenomena that occurs in the rod and the different ways of modelling them.

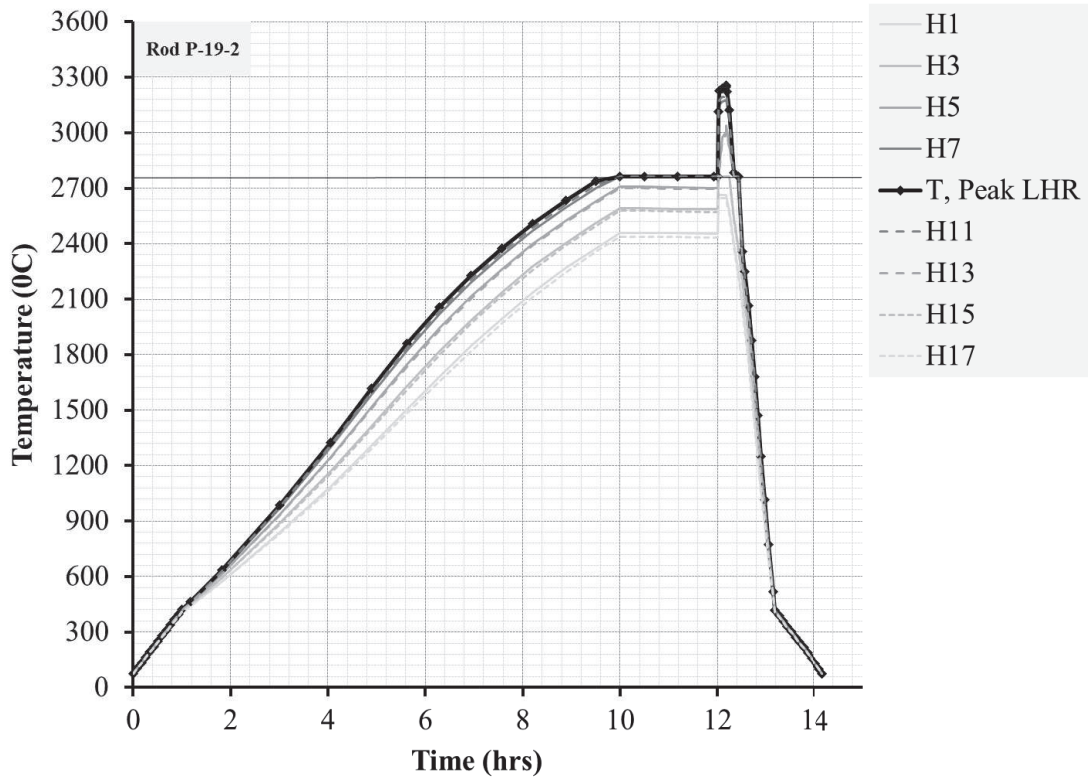


Figure 6-6 Simulation of HEDL P-19, rod P19-2, centreline temperature.

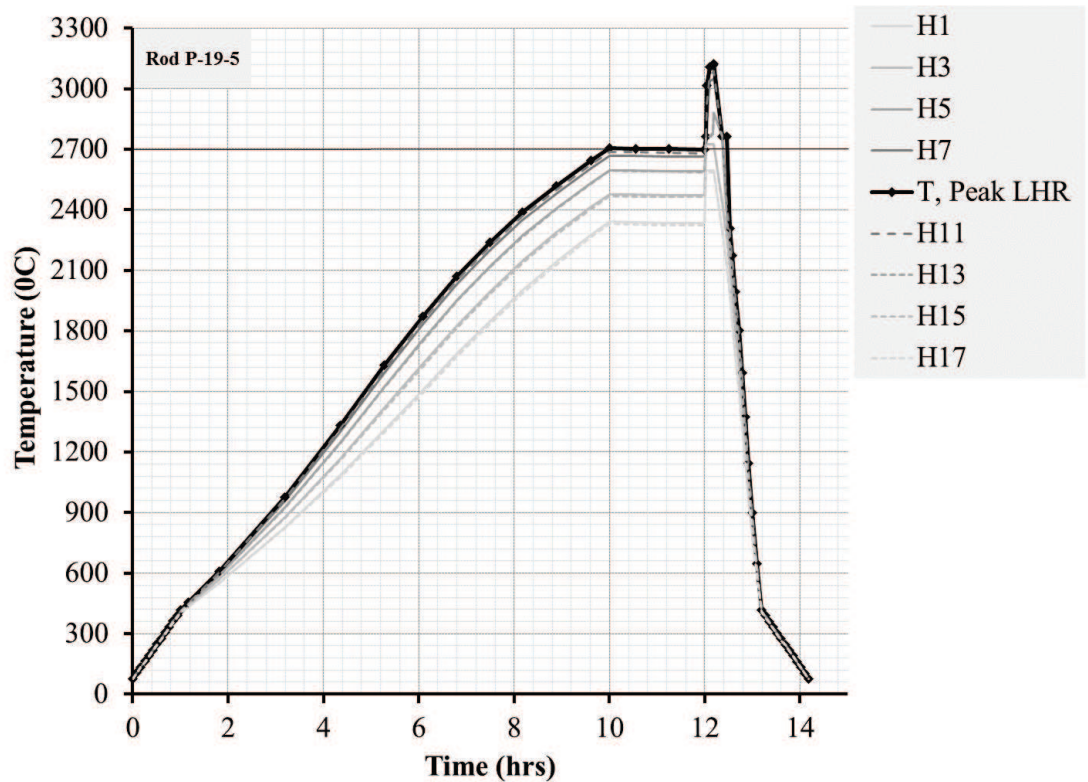


Figure 6-7 Simulation of HEDL P-19, rod P19-5, reference analysis, centreline temperature.

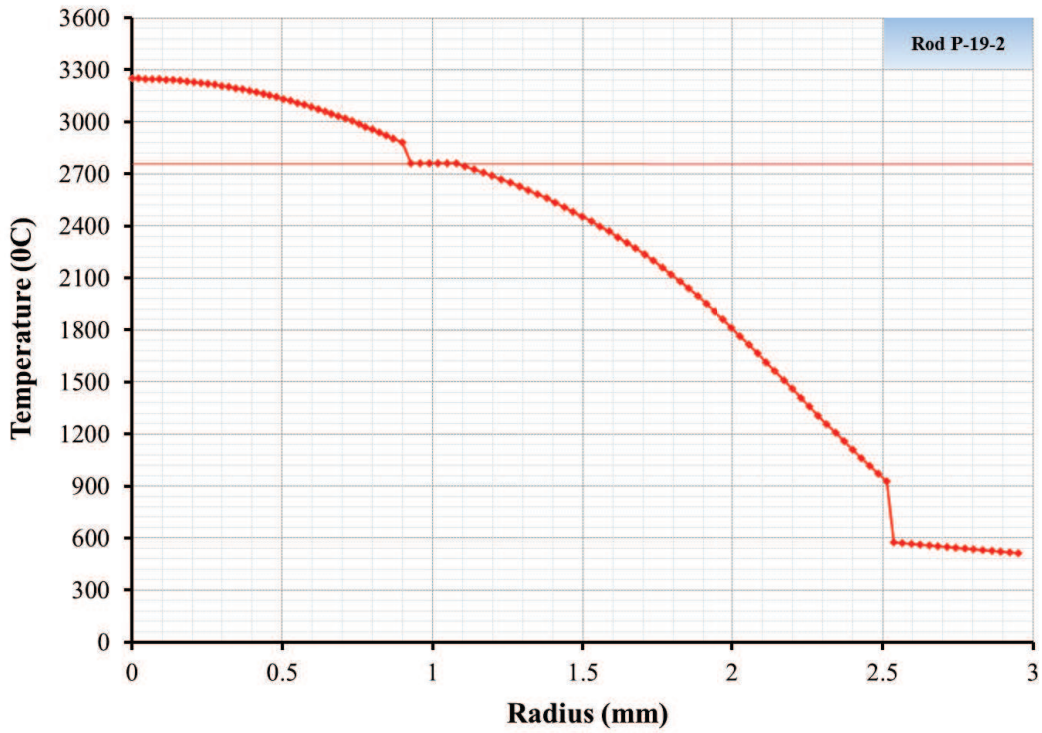


Figure 6-8 Simulation of HEDL P-19, rod P19-2, reference analysis, radial temperature profile at the end of the ramp.

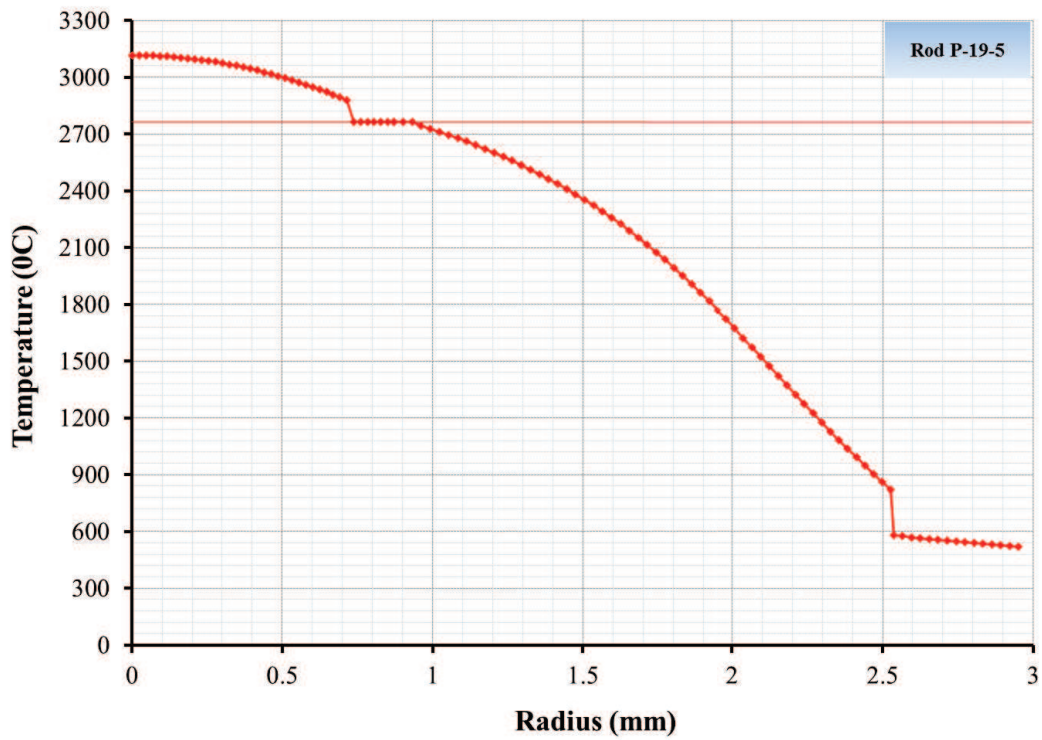


Figure 6-9 Simulation of HEDL P-19, rod P19-5, reference analysis, radial temperature profile at the end of the ramp.

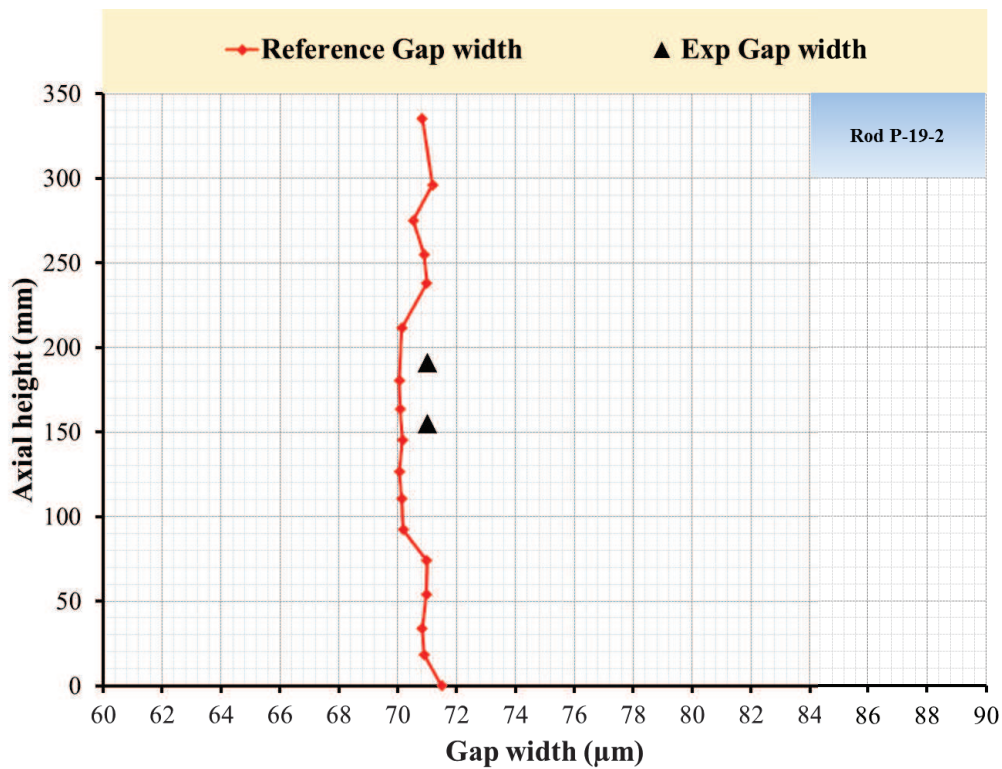


Figure 6-10 Simulation of HEDL P-19, rod P19-2, reference analysis, prediction of gap width at the end of the experiment.

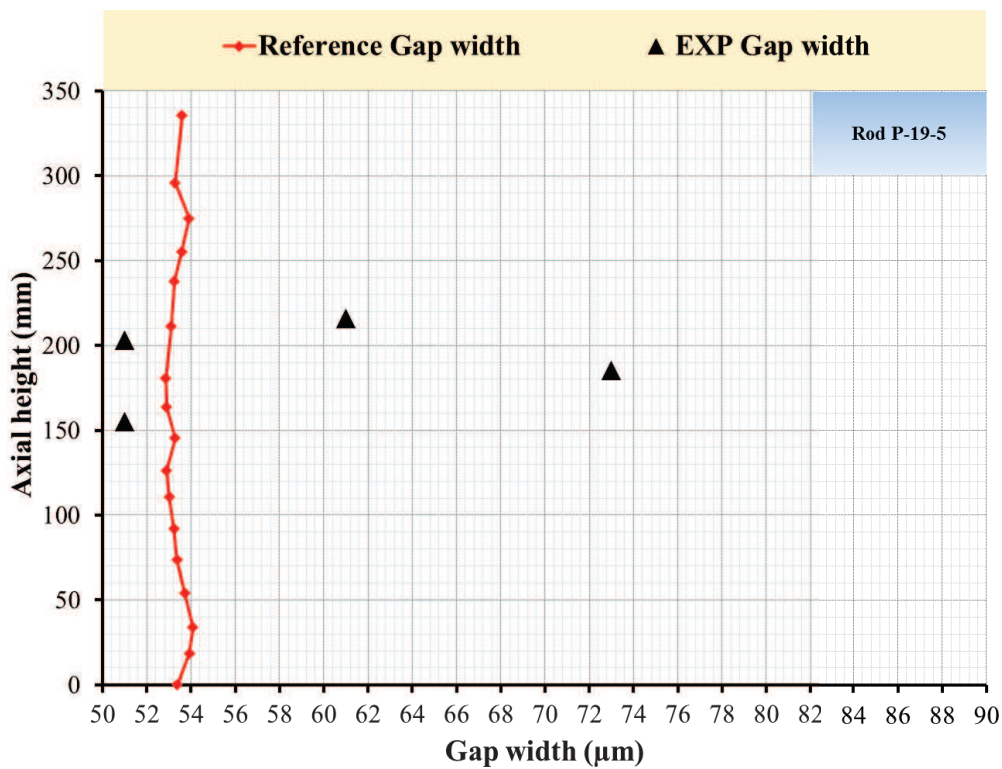


Figure 6-11 Simulation of HEDL P-19, rod P19-5, reference analysis, prediction of gap width at the end of the experiment.

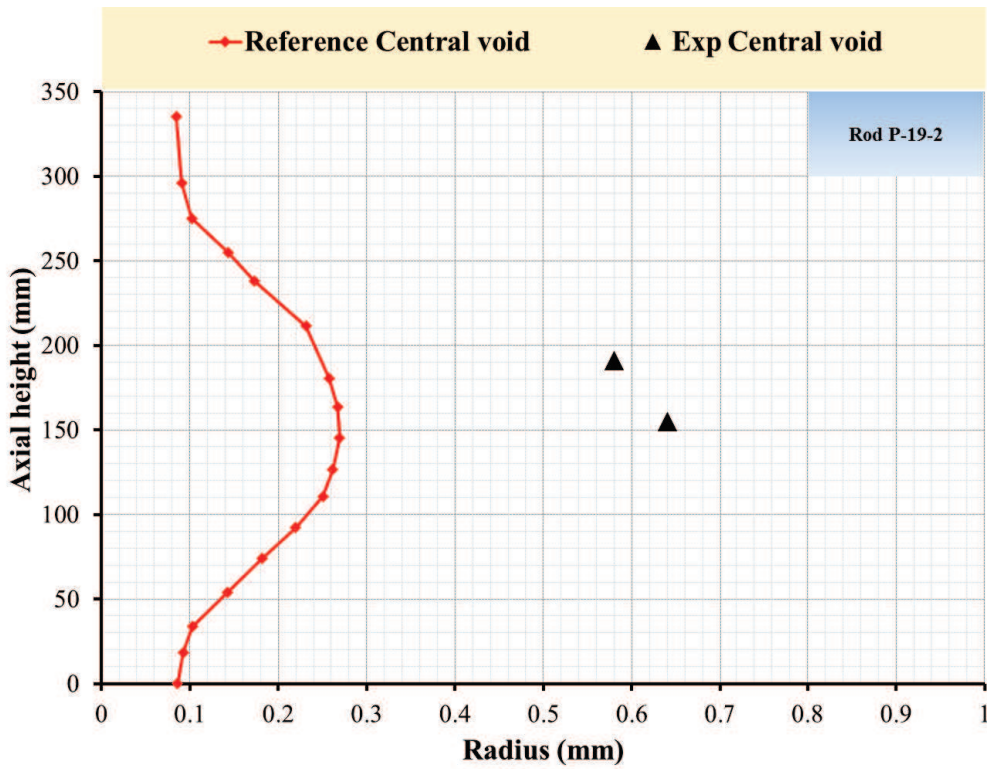


Figure 6-12 Simulation of HEDL P-19, rod P19-2, reference analysis, prediction of the central void at the end of the experiment.

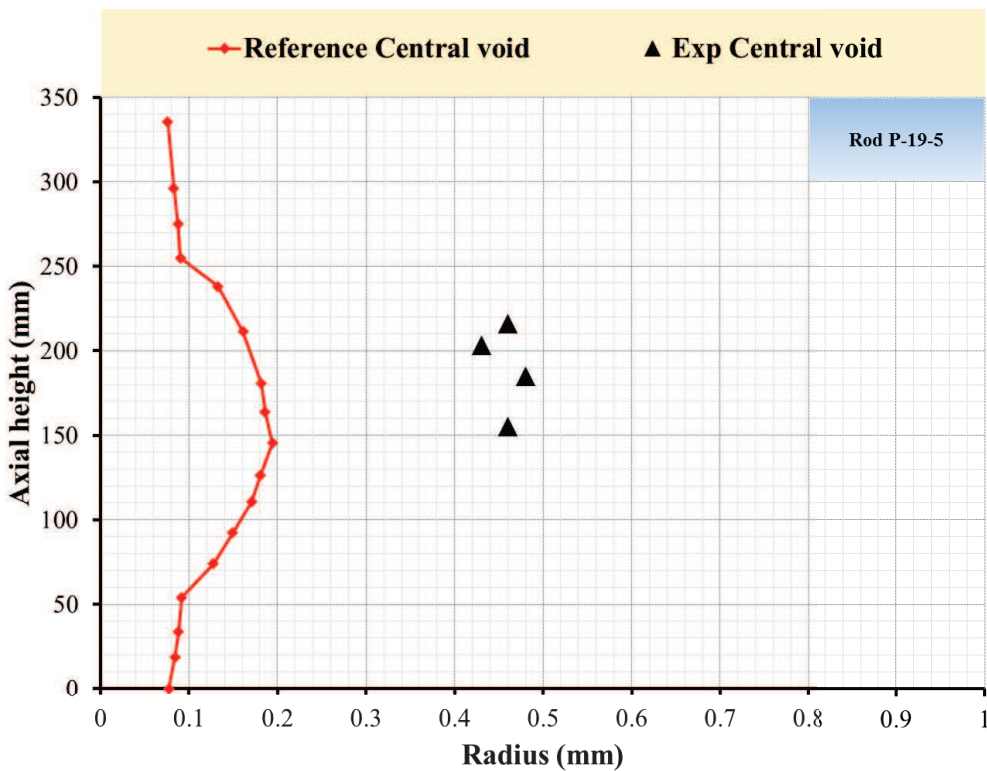


Figure 6-13 Simulation of HEDL P-19, rod P19-5, reference analysis, prediction of the central void at the end of the experiment.

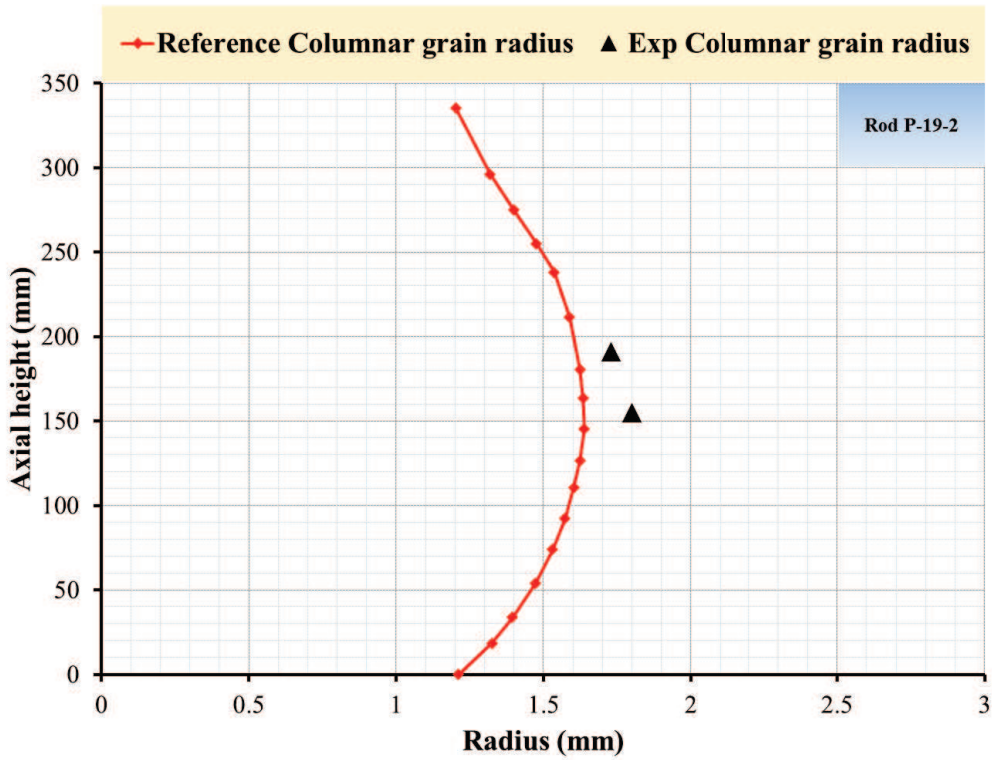


Figure 6-14 Simulation of HEDL P-19, rod P19-2, reference analysis, prediction of the columnar grain radii at the end of the experiment.

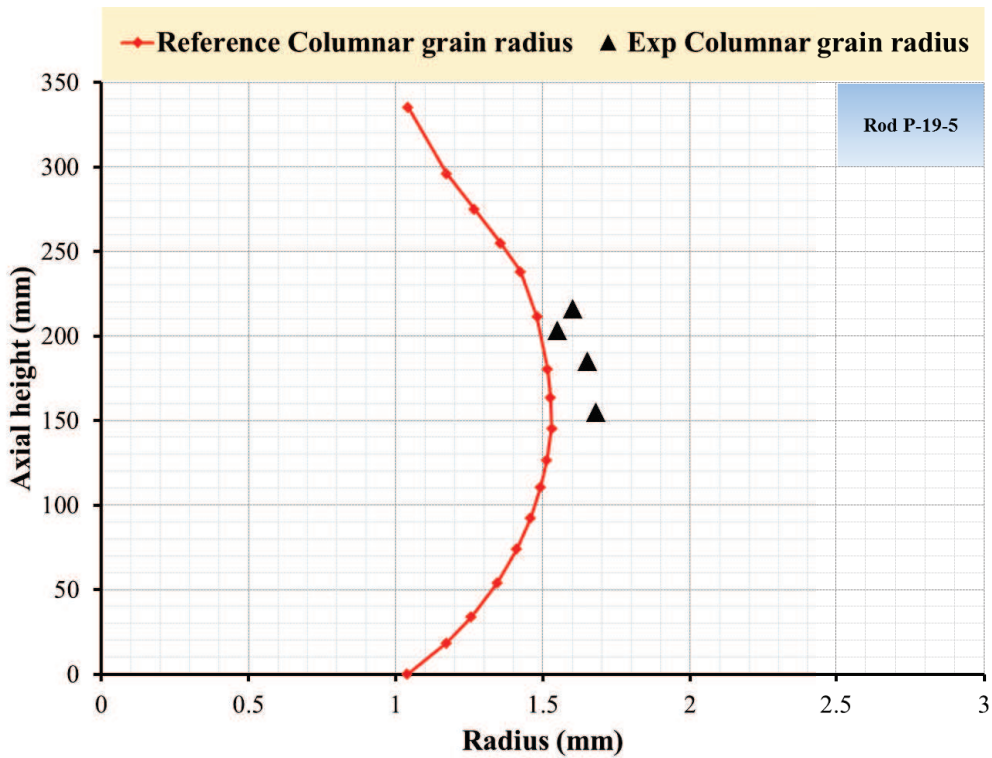


Figure 6-15 Simulation of HEDL P-19, rod P19-5, reference analysis, prediction of the columnar grain radii at the end of the experiment.

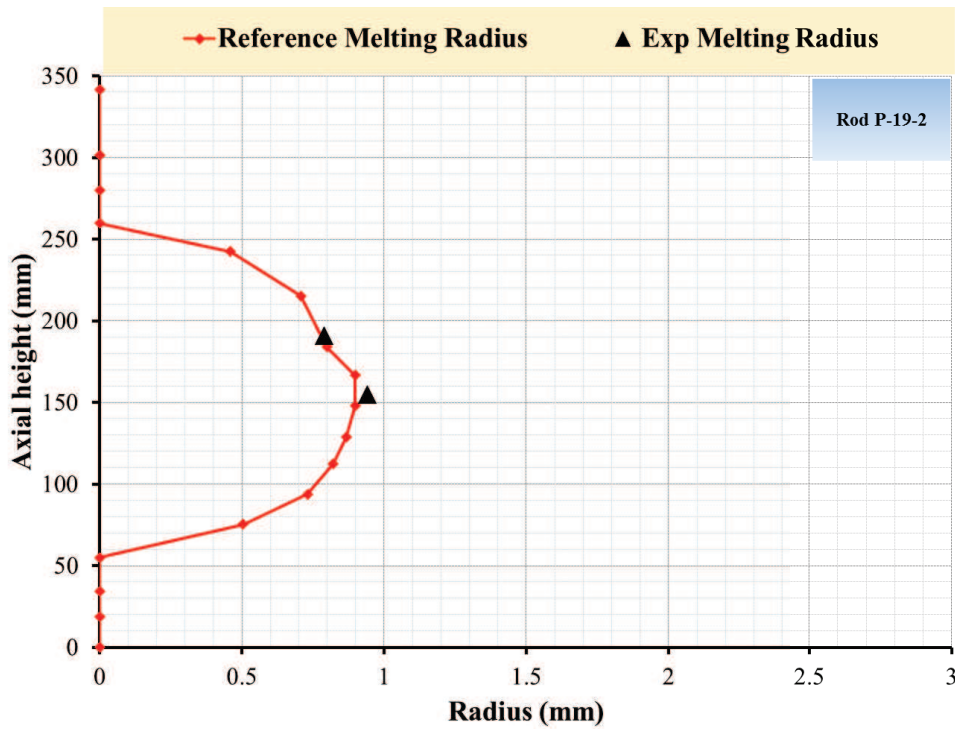


Figure 6-16 Simulation of HEDL P-19, rod P19-2, reference analysis, prediction of the melting radius.

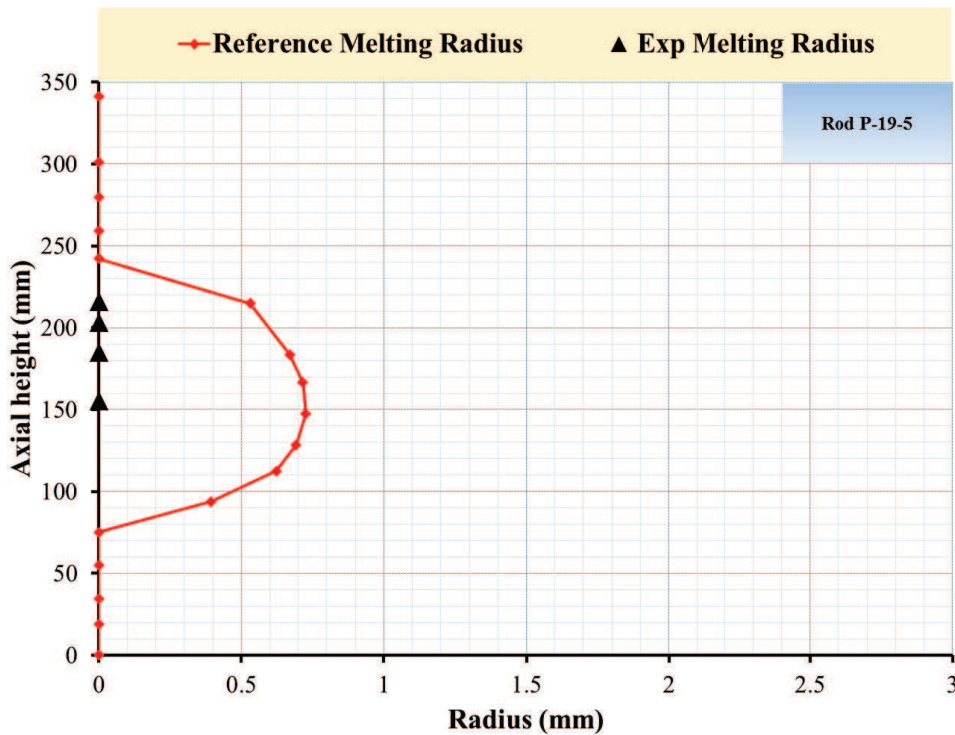


Figure 6-17 Simulation of HEDL P-19, rod P19-5, reference analysis, prediction of the melting radius.

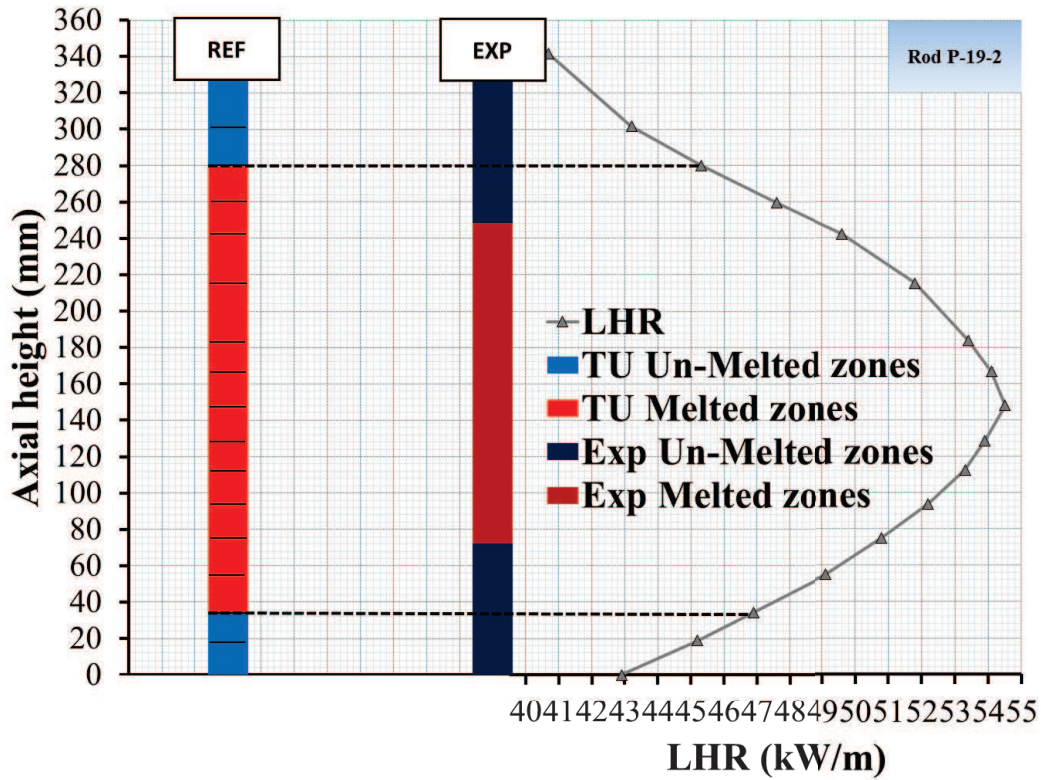


Figure 6-18 Simulation of HEDL P-19, rod P19-2, reference analysis, prediction of melting height.

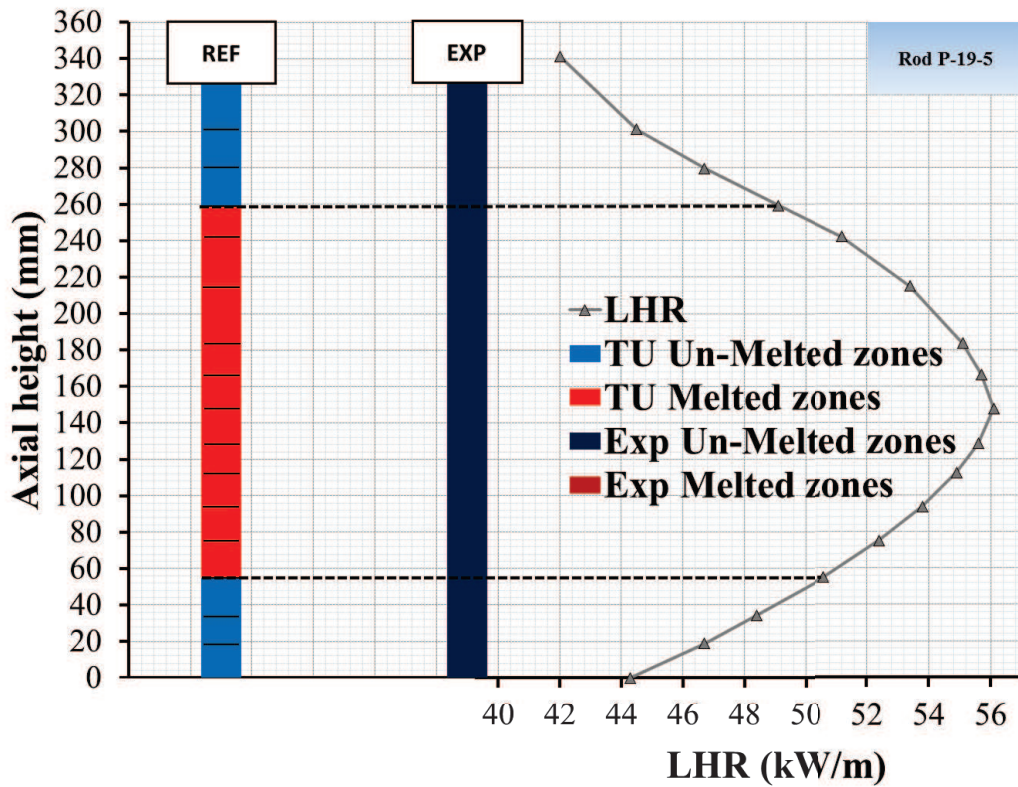


Figure 6-19 Simulation of HEDL P-19, rod P19-5, reference analysis, prediction of melting height.

 Ricerca Sistema Elettrico	Sigla di identificazione	Rev.	Distrib.	Pag.	di
	ADPFISS – LP2 – 087	0	L	96	229

6.4 Sensitivity analysis

The list of the sensitivity analyses that were performed for HEDL P-19 rods during this study could be found in *Table 6-6* and the motivation behind them. The analysis was performed on either parametric design values given by the experiment data, correlations and models provided by the code. Design parameters are labeled by **(D)**, while correlations are labeled by **(C)** and Models labeled **(M)**. In the next subsections, separate sensitivity analysis of the factors stated in *Table 6-6* is going to be illustrated.

Case	Run	Modification	Objective
Fuel conductivity	C1.1	Modfuel(j=6)=31	Investigate the impact of fuel conductivity on melt front, Gap width, Central void and columnar. <i>Correlation of Van Uffelen & Schubert.</i>
	C1.2	Modfuel(j=6)=32	Investigate the impact of fuel conductivity on melt front, Gap width, Central void and columnar. <i>Correlation of Carbajo.</i>
	C1.3	Modfuel(j=6)=33	Investigate the impact of fuel conductivity on melt front, Gap width, Central void and columnar. <i>Correlation of Lanning & Beyer.</i>
	C1.4	Modfuel(j=6)=24	Investigate the impact of fuel conductivity on melt front, Gap width, Central void and columnar. <i>According to Wiesenack multiplied by a MOX correction factor.</i>
Pellet fragment relocation	M1.1	Ireloc 2	Investigate the impact of fuel relocation on gap width and melt front. <i>Original KWU-LWR model based on initial gap size only.</i>
	M1.2	Ireloc 3	Investigate the impact of fuel relocation on gap width and melt front. <i>GAPCON-THERMAL-3 based on initial gap size, LHR and burn-up.</i>
	M1.3	Ireloc 4	Investigate the impact of fuel relocation on gap width and melt front. <i>operational relocation model according to Eberle and Stackmann, own calibration 1997, explicit formulation.</i>
	M1.4	Ireloc 6	Investigate the impact of fuel relocation on gap width and melt front. <i>operational relocation model according to Eberle and Stackmann, own calibration 1997, implicit formulation.</i>
	M1.5	Ireloc 8	Investigate the impact of fuel relocation on gap width and melt front. <i>Modified FRACPON-3 model based on the as fabricated gap, the burn-up and the linear heat rate.</i>
Fuel restructuring models	M2.1	Istzne 2	Investigate the impact of fuel restructuring on melt front, gap size, and columnar growth. <i>Original model of Olander.</i>
	M2.2	Istzne 5	Investigate the impact of fuel restructuring on melt front, gap size, and columnar growth. <i>Fuel restructuring zones are calculated from boundary temperatures.</i>
	M2.3	Istzne 6	Investigate the impact of fuel swelling on fuel temperature, pin pressure and FGR. <i>Fuel restructuring zones are calculated from boundary grain Sizes.</i>
solidus–liquidus melt temperature	C2.1	Modfuel(j=16)=10	Investigate the impact of solidus-Liquidus melt temperature on the development of the melt front and the central void. <i>Correlation of Többe.</i>
	C2.2	Modfuel(j=16)=13	Investigate the impact of solidus-Liquidus melt temperature on the development of the melt front and the central void. <i>Correlation by Pesl et al.</i>
	C2.3	Modfuel(j=16)=15	Investigate the impact of solidus-Liquidus melt temperature on the development of the melt front and the central void. <i>Correlation is recommended in the Gmelin handbook.</i>
Gap size	D1.1	Gap size (+15µm)	Investigate the impact of uncertainty in the initial gap width on the evolution of the gap width and on the melt front formation. Initial value obtained assuming maximum cladding and minimum fuel radii according to design uncertainties.
	D1.2	Gap size (-15µm)	Investigate the impact of uncertainty in the initial gap width on the evolution of the gap width and on the melt front formation. Initial value obtained assuming minimum cladding and maximum fuel radii according to design uncertainties

Table 6-6 Simulation of HEDL-P19, list of correlations, models and design parameters considered in the sensitivity studies.

6.4.1 Thermal conductivity correlations

The conductivity correlations are assessed to highlight their influence on the prediction of the experimental data. The experimental melting height along with the prediction of the available TU correlation are depicted in *Figure 6-20*. TU correlations over-predicted the melting height of the rod except for COND-34 where the melting is under-predicted. This is consistent with the results obtained for the LWR MOX in section 5.4.2 and gives an indication of a trend of this correlation to under predict the temperature. COND-33 (Lanning and Bayer) fit the melting height of Rod P-19-2 in the best way. For rod P-19-5 the TU correlations predicted considerable melting of the rod excepts COND-34 that did not predict melting at all. A general conclusion is the tendency of TU thermal conductivity correlations to under-predict the thermal conductivity. The correlations were verified against LWR rods and in their operational regime. Their ability to predict the FBR rods behavior especially at high temperature close to melting is not completely checked. No major differences are observed when analyzing their influence on the prediction of the gap size, *Figure 6-21*. The correlation of Carbajo (COND32) highlights an improvement in the prediction of the central void (*Figure 6-22*) and on the columnar grain radius (*Figure 6-23*). However, it can be seen that the columnar grain radii are proportional to the prediction of the temperature. Higher predicted temperatures results in higher columnar growth radii. Thus, this correlation further overestimate the melting height and the molten fuel radius, (*Figure 6-24*).

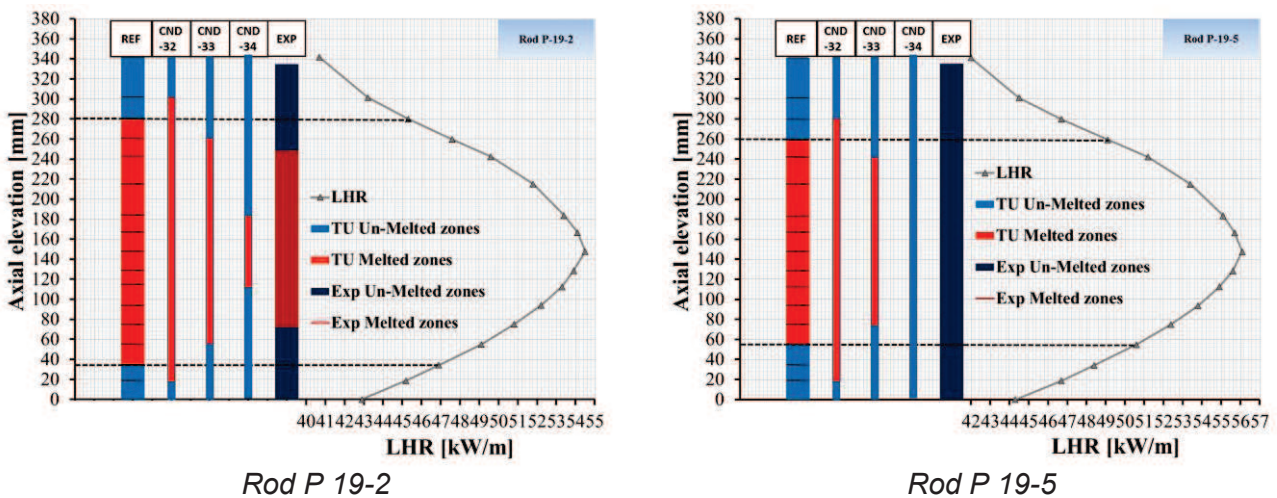
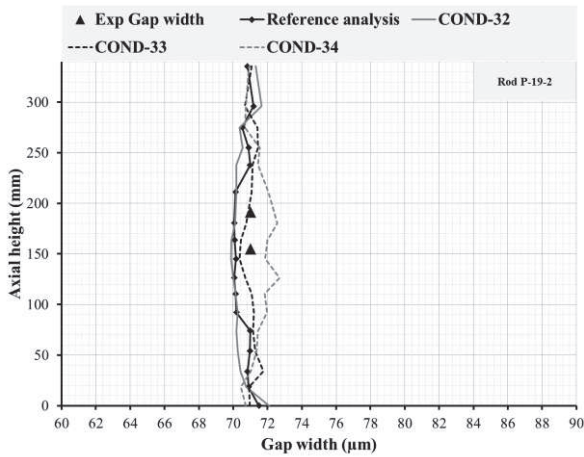
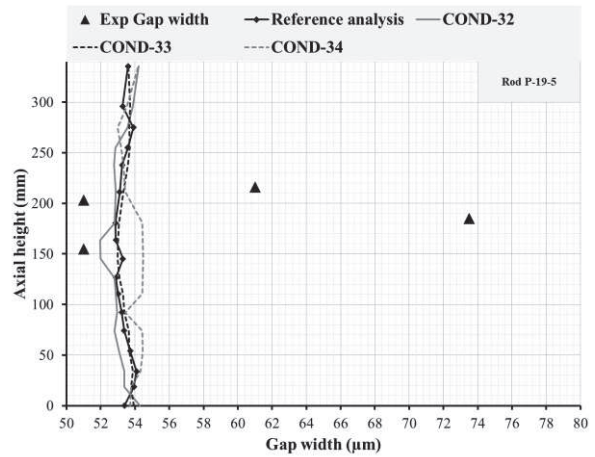


Figure 6-20 Simulation of HEDL-P19, sensitivity analysis on thermal conductivity correlations, prediction of melting height.

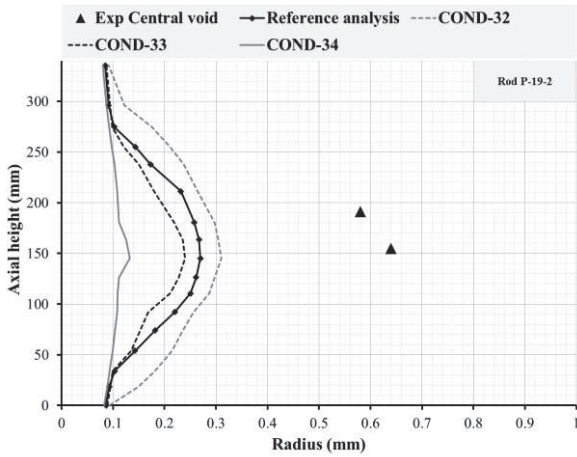


Rod P 19-2

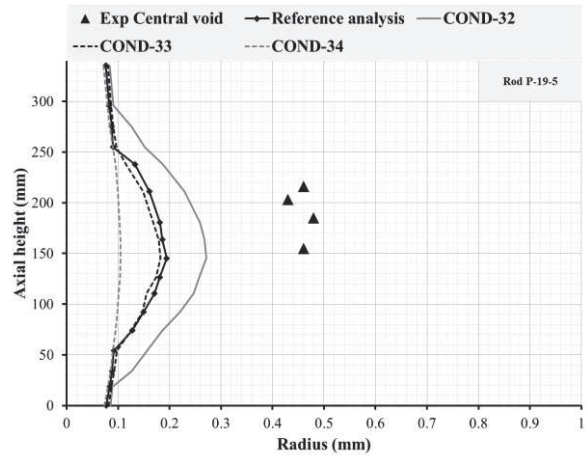


Rod P 19-5

Figure 6-21 Simulation of HEDL-P19, sensitivity analysis on thermal conductivity correlations, prediction of gap width at the end of the experiment.

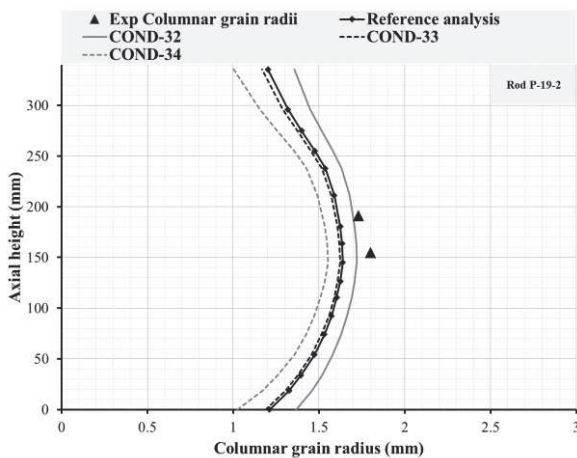


Rod P 19-2

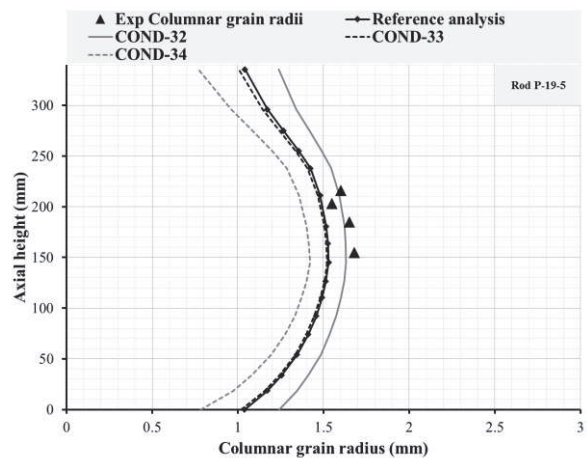


Rod P 19-5

Figure 6-22 Simulation of HEDL-P19, sensitivity analysis on thermal conductivity correlations, prediction of central void at the end of the experiment.



Rod P 19-2



Rod P 19-5

Figure 6-23 Simulation of HEDL-P19, sensitivity analysis on thermal conductivity correlations, prediction of columnar grain radius at the end of the experiment.

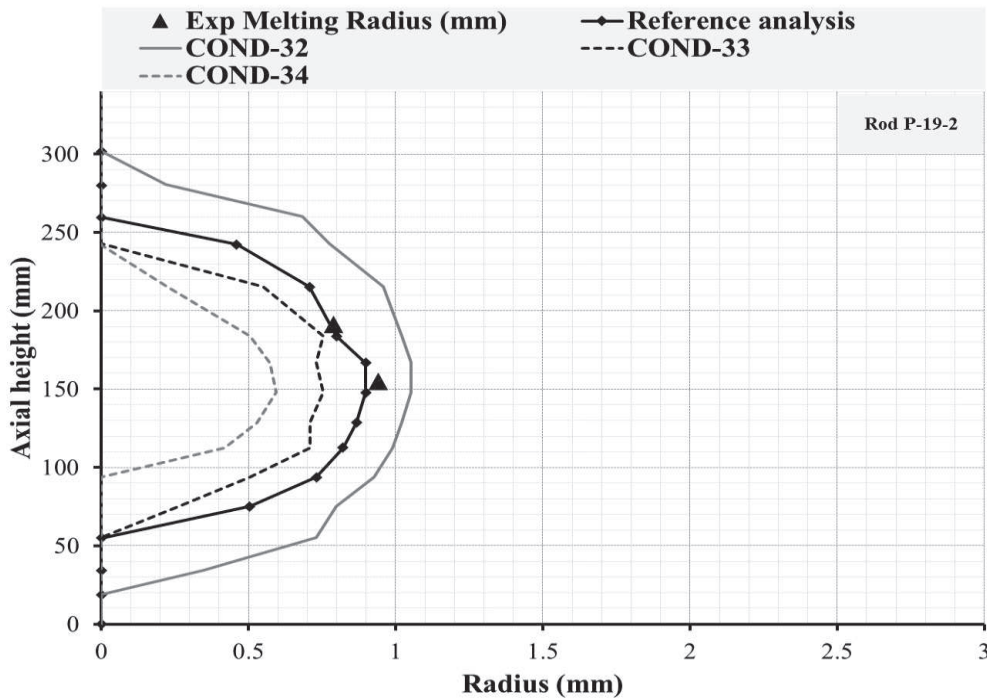


Figure 6-24 Simulation of HEDL-P19, sensitivity analysis on thermal conductivity correlations, prediction of melting radii.

6.4.2 Relocation models analysis

The gap widths predicted by relevant pellet fragment relocation models are plotted in Figure 6-25. It is notice that the variability in gap widths is higher for P-19-2 than P-19-5 that did not experience melting. The reference model IRELOC=8 is the one that is more close to the experimental data. This did not result in different melting heights Figure 6-26. This can be related to the higher mesh in the discretization of the fuel rod. Still, the melting ratio of the fuel is variable between the models even if the melting heights are the same.

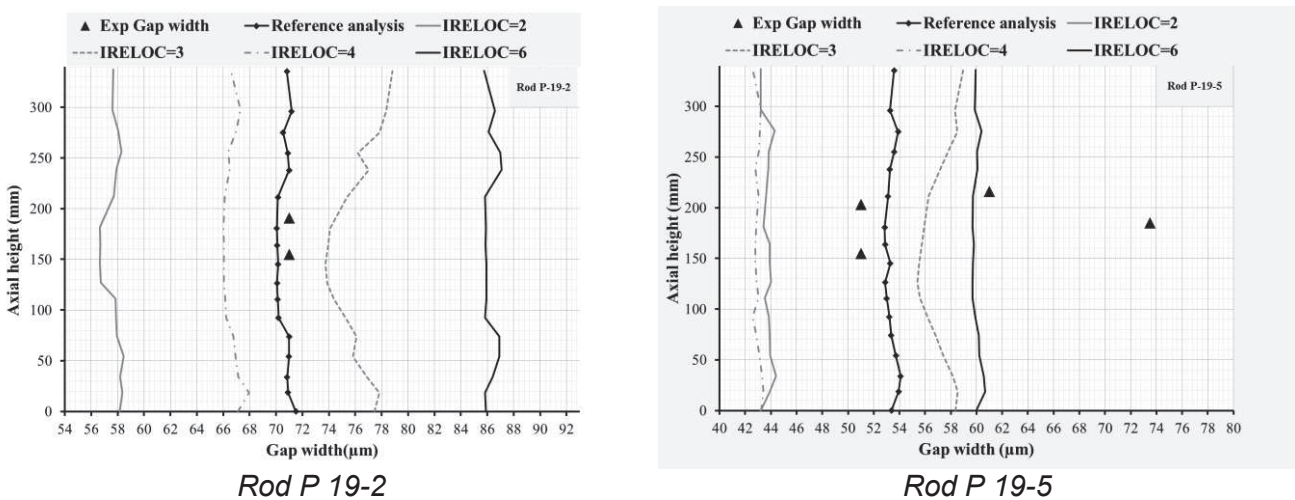
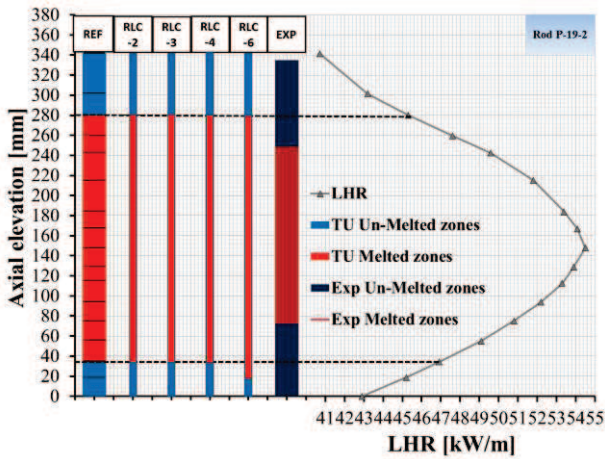
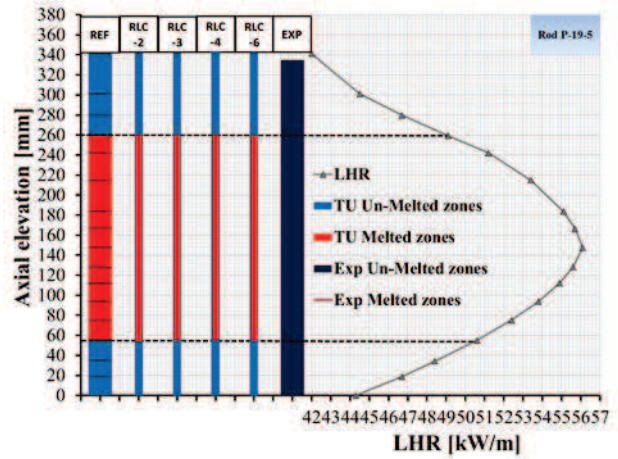


Figure 6-25 Simulation of HEDL-P19, sensitivity analysis on relocation models, prediction of gap width at the end of the experiment.



Rod P 19-2

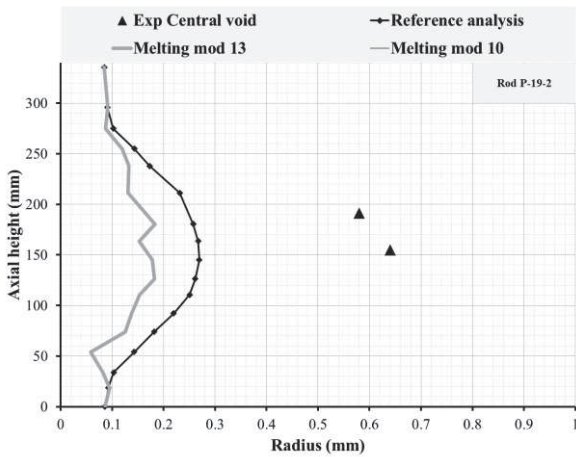


Rod P 19-5

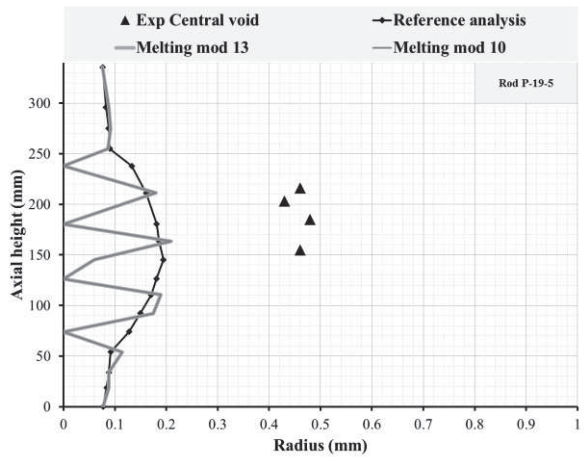
Figure 6-26 Simulation of HEDL-P19, sensitivity analysis on relocation models, prediction of melting height.

6.4.3 Solidus-Liquidus melting models

The models available in the code to simulate MOX fuel melting considers the melting temperature as a function of burn-up O/M ratio and Pu content, the reference model was a constant value (similar to those experimentally measured in HEDL-P19). The models resulted in noticeable variation of the central void prediction and the melting height: *Figure 6-27, Figure 6-28*. The rest of the experimental parameters were not significantly affected. The reference model predicted the highest void formation for both rods.

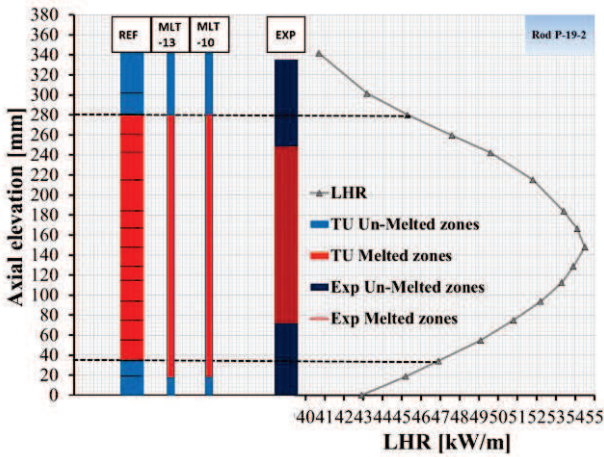


Rod P 19-2

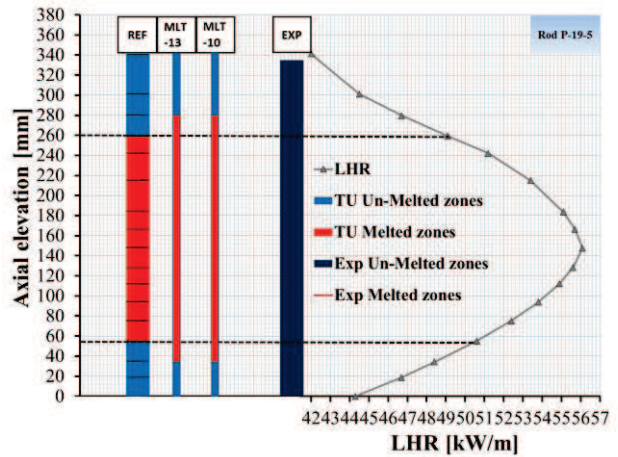


Rod P 19-5

Figure 6-27 Simulation of HEDL-P19, sensitivity analysis on melting models, prediction of central void at the end of the experiment.



Rod P 19-2

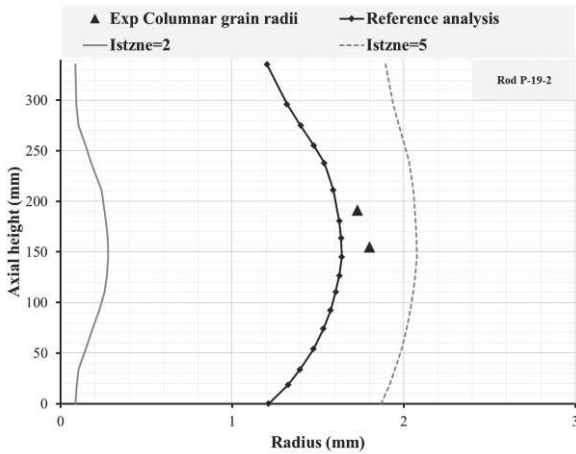


Rod P 19-5

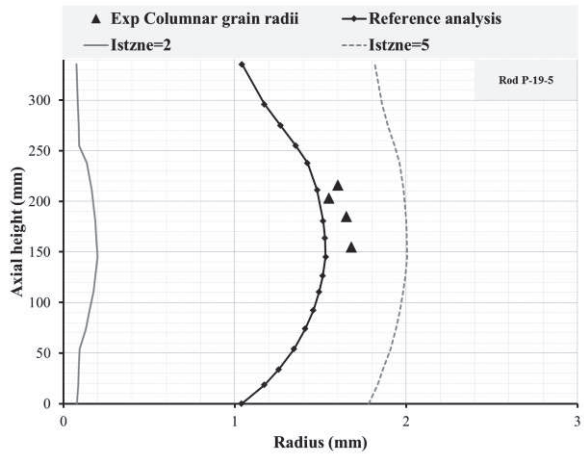
Figure 6-28 Simulation of HEDL-P19, sensitivity analysis on melting models, prediction of melting height.

6.4.4 Fuel restructuring models

The fuel restructuring models did not affect any of the measured parameters in the rod except the outer radius of columnar grain zone *Figure 6-29*. The melting heights predicted by the models were the same. The prediction of the formation of the columnar zone by Istzne-2 was the smallest while the reference case highlight capture the columnar growth in the rod in a good way.



Rod P 19-2



Rod P 19-5

Figure 6-29 Simulation of HEDL-P19, sensitivity analysis on restructuring models, columnar grain radii prediction.

6.4.5 Initial gap width

Initial gap width is a parameter provided by the experiment. In this study, the nominal initial gap width was assumed to have around 15% uncertainty. 80% percent of this

uncertainty was due to uncertainty in the outer fuel radius and 20% is related to the inner cladding radius.

Uncertainty in the initial gap width affects all the measured parameters of the rod. It is a critical factor to be precisely measured. Increasing the initial gap size results in a degradation of thermal conductivity and as a result higher temperatures inside the rod are expected. This affects everything else and results in wider central void and melting radius and more columnar grain growth inside the rod. The final result of that is a longer melting height inside the rod, *Figure 6-30*. The opposite is true when the initial gap size is reduced, better heat transfer will occur inside the rod and the temperature and melting heights will decrease. However, the nominal initial gap width resulted in the best predicted value of the gap width at the end of the experiment, *Figure 6-31*. Therefore the analysis was continued with relief that the initial gap width measurement was not a source of significant error in the results and any bias of the results in the over prediction of the temperature is not related to an error in the initial gap determination by the experimenter.

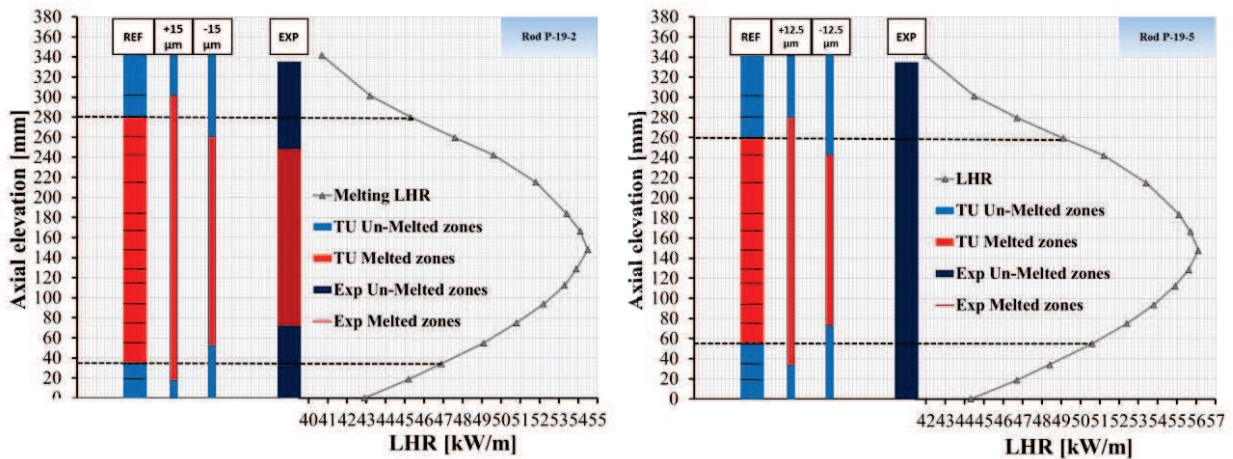


Figure 6-30 Simulation of HEDL-P19, sensitivity analysis on initial gap size, prediction of melting height.

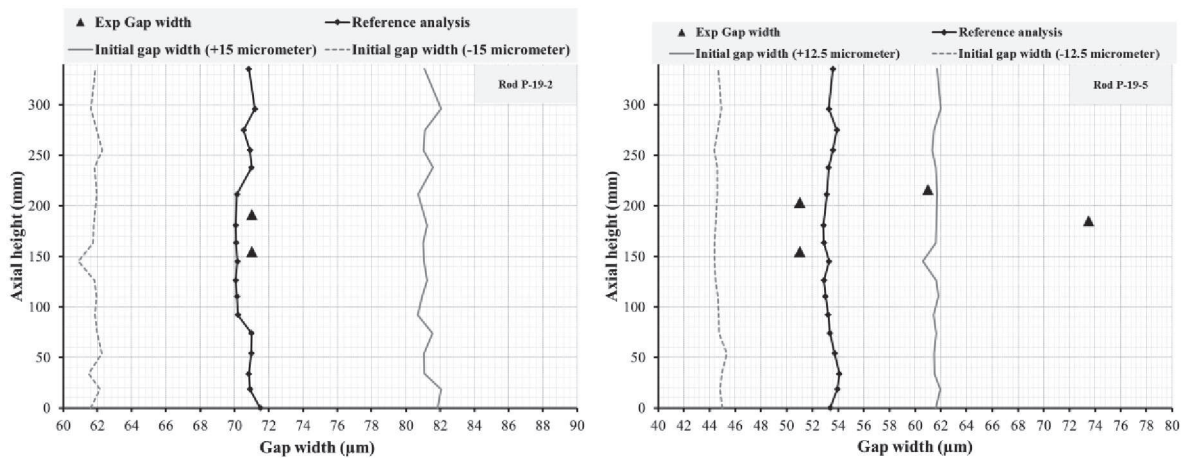



Figure 6-31 Simulation of HEDL-P19, sensitivity analysis on, prediction of gap width at the end of the experiment.

 Ricerca Sistema Elettrico	Sigla di identificazione	Rev.	Distrib.	Pag.	di
	ADPFISS – LP2 – 087	0	L	104	229


6.5 Radial analysis

Two separate approaches were used for each P-19 rod because of the difference in the post-irradiation conditions of them. Radial analysis for rod P-19-2 was done at the end of melting at the moment when the melt fraction and the melting height reached their maximum values. For rod P-19-5, the analysis was done prior to power ramp to induce melting. The reason behind that is that the rod did not experience any melting as confirmed by the radio-graphical investigation. The temperature during the power ramp should be lower than the melting temperature (2762 °C). It is not known how low the real temperature was below the melting value. TU predicted melting inside the rod. Considerable melting heights were predicted by the code which indicates a temperature much higher than the melting temperature. Therefore, the comparison was done before the power ramp where melting did not occur neither experimentally nor by TU prediction. Open literature correlations were plotted as well in the same manner and for the same purposes in section 5.5.

Rod P-19-2 experienced melting heights of values between the upper and lower boundaries mentioned in *Table 6-2*. The thermal conductivity correlations of TU resulted in an over-prediction of the melting heights which can lead to a conclusion of under predicted thermal conductivities. Predicting lower thermal conductivity would result in code prediction of higher melting heights than the actual height except for COND-34 that under-predicted the melting height. During melting the thermal conductivity is assumed to be 1.5 W/mK for COND-31, COND-33, and COND-34. COND-32 assumed a thermal conductivity beyond melting of 2.5 W/mK.

In *Figure 6-32* various TU and OL correlations are plotted together for comparison among themselves and with fitted experimental data. As expected from the previous analysis (section 6.4.1), COND-34 predicted the highest thermal conductivity on the whole range of temperatures in the rod. That range of thermal conductivity resulted in the smallest melting height. This is an indication that the thermal conductivity, especially in the high temperature range should be lower than COND-34 but still should be higher than the rest of the other correlations. COND-32 predicted the lowest thermal conductivity on the whole range of temperatures except in the part where melting is predicted the thermal conductivity is higher since it is modelled as a constant of choice of the developer of 2.5 W/m.K while the rest of the correlations chose a melting thermal conductivity of 1.5 W/mK. COND-33 predicted lower melting height than COND-31 and closer to the experimental measurements. In facts, the thermal conductivity predicted by COND-33 in most of the ranges of temperatures prior to melting is higher than COND-31. Only near the periphery of the rod where ($T < 1400^{\circ}\text{C}$) where the thermal conductivity of COND-31 is slightly higher but at that location it would not cause much difference in the temperature profile.

The open literature correlations are compared only prior to melting since thermal conductivity during melting is modelled as constant. Matpro correlation predicted higher thermal conductivity than the rest of the correlations upto 2270°C where it becomes lower than COND-34 up to melting. Thermal conductivity according to Martin predicted thermal conductivities comparable to the standard correlations COND-31 up to 2000°C where it becomes lower than COND-32. The correlation is expected to result in a higher prediction of temperatures and melting heights similar

 Ricerca Sistema Elettrico	Sigla di identificazione	Rev.	Distrib.	Pag.	di
	ADPFISS – LP2 – 087	0	L	105	229

to COND-32. Comethè correlation predicted thermal conductivity higher than COND-33 up to 2080°C where it becomes lower than it but higher than COND-31 up to 2550°C where it becomes slightly lower than it. Comethè correlation might give similar prediction to COND-31. Baron-Hervè correlation predicted higher thermal conductivity than COND-31 on the whole range prior to melting. It predicts higher thermal conductivity than COND-31 except in the mid section of the rod where (1600°C < T < 2300°C). In general, Baron-Hervè-95 has a potential of predicting better melting heights and is investigated later.

Special preparations were taken to compare the experimental data with the studied correlations. The experimental data available were taken from the work of Duriez et.al^[10]. The sample used in this study was a fresh MOX with homogeneous Pu 21.4wt% and O/M ratio 1.982, and theoretical density 95.6% up to 1850°C. In order to be able to use this sample for comparison with the studied correlations, close examination of the similarities between the sample and the P-19 pins was investigated. The plutonium content in the studied P-19 pins, was around 22wt% and can be considered to be homogeneous. It is a close value to the sample and no modification was done to it. Examining the theoretical densities, the studied pins had a smeared density in the mid-section and peripheries of around 91.4%TD. In order to be able to compare the MOX sample to the P-19 pins, the experimental data were rescaled to the porosity level of the pins using Lucuta's formula. That is the formula used as a porosity correction for COND-33^[11]. Since there is no formula to rescale the O/M ratio, the sample was added for comparison at the original level (1.982) and it was used only for qualitative comparison with the models.

It can be seen that the data are closer and in the same trend as that of COND-33 in the low temperature range up to 1400°C. Above that value, it can be seen that the experimental data of thermal conductivity shows ascending pattern with temperature with a higher rate than that of COND-33 and is going along side with COND-34 up to 1800C. What can be induced from this point up in temperature is that there is a visible trend of the experimental data to increase above all TU correlations except COND-34. At higher temperature, the effect of deviation from stoichiometry decreases. At 2000 K (1727°C) the change of thermal conductivity due to a change of O/M from 2 to 1.95 does not exceed 8%. Therefore, a change of the experimental 1.98 value to 1.96 of the pins is not expected to decrease the scale of the experimental data with more than 3%. Practically this value would be even lower since the temperature exceeds the melting temperature (2762°C) which means much lower effect of deviation from stoichiometry on the thermal conductivity.

What can be concluded from this comparison is that the thermal conductivity of TU correlations is under-predicted relative to the experimental data might say. To what extent this under prediction, it cannot be determined exactly without obtaining more experimental data on high temperature, high Plutonium content MOX fuel since the work of Ronchi which is the basis for the high temperature terms of COND-31 and COND-33 was intended for LWR grade of MOX fuel.

The same analysis applies for rod P-19-5 and can be seen in *Figure 6-33*. As expected there is no much change from the previous comparison for P-19-2 since the

plutonium content, Porosity, O/M ratio are the same for both rods. The figure is similar to that of rod P-19-2 excepts that it is on a lower scale since the analysis was done prior to the ramp conditions and no prediction of melting was done by the code which means a range of comparison up to 2760 (COND-32) and not exceeding it for the rest of the correlations.

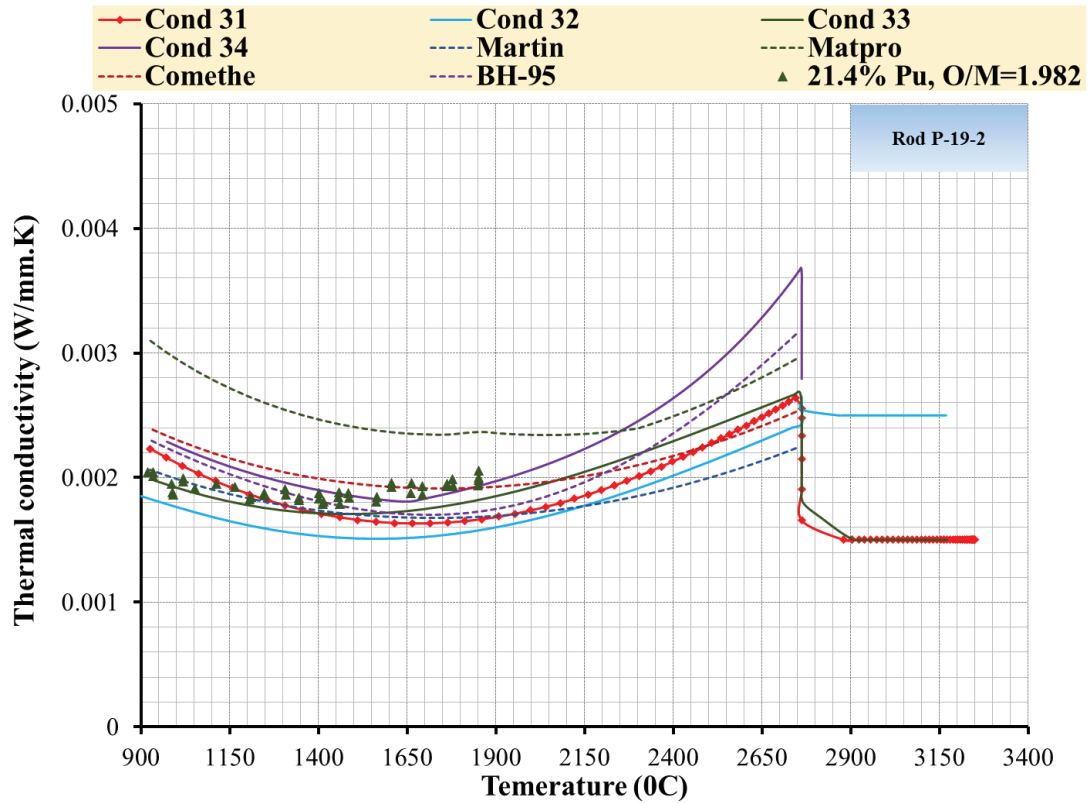


Figure 6-32 Radial profile of thermal conductivity for rod P-19-2.

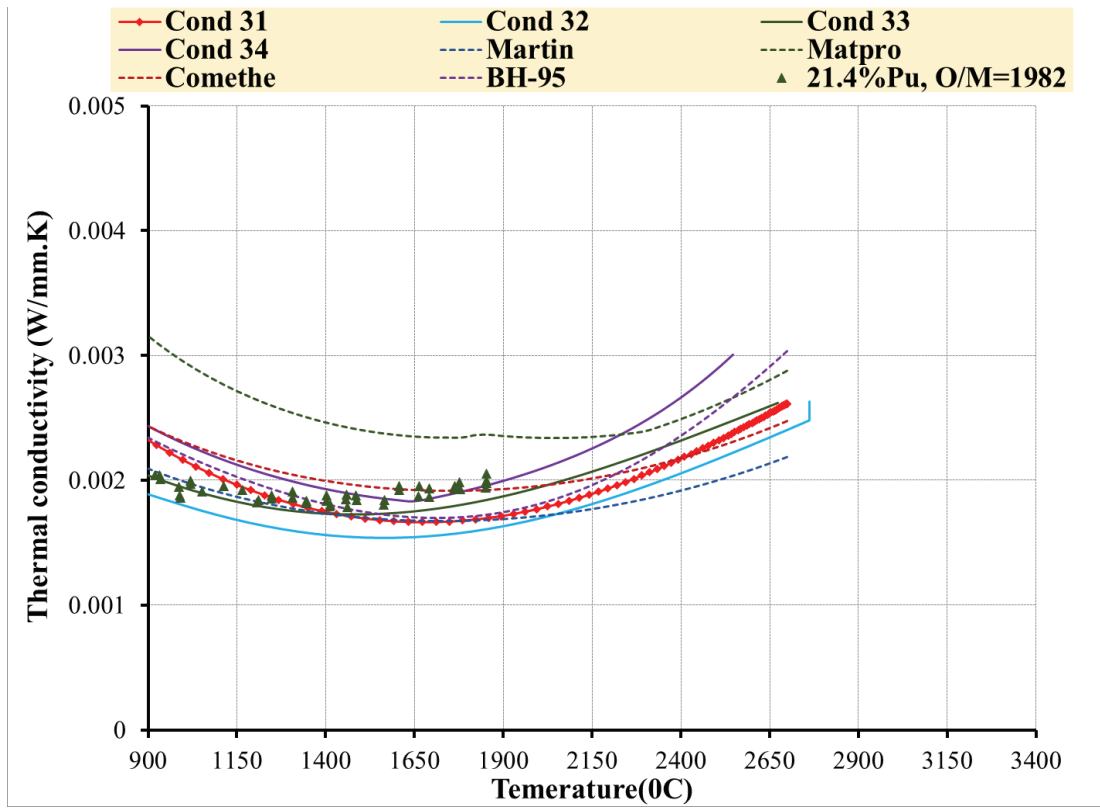


Figure 6-33 Radial profile of thermal conductivity for rod P-19-5.

 Ricerca Sistema Elettrico	Sigla di identificazione	Rev.	Distrib.	Pag.	di
	ADPFISS – LP2 – 087	0	L	108	229

7 Review of thermal conductivity correlations


COND-31 (Van Uffelen & Schubert), COND-33 (Lanning & Beyer), and Baron-Hervé 1995 correlations will be investigated for the potential differences between them. The main goal is to investigate for a correlation that can result in a better prediction of the FR MOX fuel melting height discussed in the previous chapter. The main causes of differences between the correlations are the O/M ratio, the high temperature conduction term and the Plutonium content. The Plutonium content is not expected to be a significant reason for the incapability of the code to predict the fuel melting. The reason for that is that the thermal conductivity decreases with Pu content increase. A decrease in thermal conductivity than what the original correlations predicts would lead to more over prediction of the melting of the investigated fuel rods.

Figure 7-1 represents an analysis of the lattice and electronic terms of the investigated correlations. Several remarks were noticed from the figure. It can be seen that the lattice conduction term is lower for BH-95 correlation than TU correlations. At higher temperatures, it is noticed that the lack of O/M ratio term in COND-31 correlation did not result in any visible deviation from COND-33 correlation. This is expected since at higher temperature the effect of O/M ratio on thermal conductivity decreases. At lower temperatures, the effect of O/M is visible. During high linear power operation of FBR, these temperatures will exist near the periphery of any investigated FR rod where the temperature gradient is more important in heat transfer than the thermal conductivity.

It can be seen also that at the most of the temperature range, COND-31 has a higher lattice thermal conductivity except near the melting temperature. Yet the correlation predicts a higher melting height than the height predicted by COND-33. This gives an indication that the overall higher thermal conductivity predicted by COND-33 is related to the higher electronic conduction term of this correlation.

It is therefore expected that the lower prediction of the melting height by COND-33 is related to the electronic conduction term, rather than the O/M factor that is missing from COND-31. The higher electronic conduction term in BH-95 correlation is the reason of the higher thermal conductivity predicted by it at very high temperature near the melting temperature of the investigated FBR rods in the previous chapter (*Figure 6-32*). In order to properly investigate the melting LHR of FBRs, the conduction due to higher temperature factors should be investigated for fast reactors grade of MOX fuel.

TRANSURANUS code is going to be used as a verification tool of the effect of the high temperature term in BH-95. The functions lamf31.f95 and lamf33.f95 are the TU fortran functions that contains the functions that are used for calculating the thermal conductivity based on COND-31 and COND-33 respectively. They were both edited so that the higher temperature term in the original correlations was changed to that from BH-95 correlation. The code was then re-compiled to create a new version in


 Ricerca Sistema Elettrico	Sigla di identificazione	Rev.	Distrib.	Pag.	di
	ADPFISS – LP2 – 087	0	L	109	229

which the new changes were integrated. The FBR rods were then analyzed using TU to verify the ability of the new version of the correlations to predict the integral behavior of the rods and the ability of the code to predict the melting heights, the centerline temperature and the gap width of the two rods.

Rod P-19-2 was analyzed using the modified correlations COND-31 and COND-33. It can be seen in *Figure 7-2* that the code predicted a shorter melting height of the rod than the original correlations. The lower limit of the predicted melting is comparable to the experimental measurement. The higher limit of melting predicted by the correlations is 242 mm height that is slightly shorter than the experimental measurement (249 mm). This cannot lead to a conclusion of under prediction of the thermal conductivity by the code due to the nature of the discretization of the rod. The next node on the rod where the melting is zero is at 259 mm. As shown in *Figure 7-2*, the melting fraction prediction by the code at the lowest melting position is between (0.5% and 0.9% of the rod by COND-33 and COND-31 respectively). Therefore as shown in the figure, the actual point at which the rod did not suffer melting is somewhere between (242 and 259 mm) which is not determined precisely by the code. The figure also shows how the melting fraction predicted by the code is lower is much lower than that the original correlations which is a consequence of the decrease of the melting height predicted by the code. The similarity between the melting heights of both the modified correlations relative to the difference of melting heights of the original ones strengthen the idea that the electronic conduction term is the key factor in the prediction of the thermal conductivity in HEDL P-19 experiment. When the same high temperature term in both correlation is used, the melting heights predicted became the same.

The Gap width predicted by the new correlation is compared with the experimental data in order to be able to relate the newly predicted heights to the change of thermal conductivity rather than any inaccuracies in the prediction of gap size. In *Figure 7-3* the gap width predicted by the original and modified correlations at the end of the experiment is plotted. It can be seen as the modified correlations predicts lower melting which is associated to lower temperature prediction resulted in a higher gap size. This is expected due to the lower thermal expansion due to the lower temperature predicted. However, the difference between the gap width predicted by all the correlations is within ($\pm 1 \mu\text{m}$). The gap width predicted by the modified COND-31 is the most accurate and comparable to the experimental measurements.

Finally. The centerline temperature temporal evolution during the whole experiment is considered in *Figure 7-4*. It can be seen that the reference correlation (COND-31) and the modified version gives the same prediction of the centerline temperature up to 1800°C. This is expected since at these temperatures the lattice vibration term is more important and is the same for both correlations. Above this temperature, the temperature prediction deviates from each other and the modified correlation predicts lower centerline temperature due to the higher electronic conduction term than the original correlation. The temperature predicted by the modified correlations are comparable to each other with lower difference between them than that between the original TU correlations.

 Ricerca Sistema Elettrico	Sigla di identificazione	Rev.	Distrib.	Pag.	di
	ADPFISS – LP2 – 087	0	L	110	229

The maximum centerline temperature during melting for the modified correlations are (3023 and 2965 °C for COND-31 and COND-33 respectively) which is around 250°C lower than the original COND-31. This high difference is an evidence of the lack of ability of TU to predict the temperature of FR MOX. The original code is too conservative for the HEDL P-experiment. The modified version is less conservative and more able to accurately predict the melting heights inside the rods, which is reflective of its better capability to predict the real unknown temperature during the melting phase of the experiment. The modified COND-31 is more conservative than the modified COND-33 and predicts a maximum temperature that is 58 °C higher. This is the A qualitative conclusion that can be inferred based on the nature of HEDL P-19 experiment, which is a melting experiment in which the actual temperatures of the rods were not measured.

The analysis of rod P-19-5 using the modified correlations showed a lower melting heights than the original code (*Figure 7-5*). The rod did not experience melting during the experiment but the code predicted melting. Still, the prediction of the modified code is lower (better) than the original one for both aspects of the melting; The melting height and fraction. The melting fraction does not exceed 3.8% at peak position in the rod compared to (10-12%) for the original code (*Figure 7-5*). The code is still conservative but on a lower level. The gap predicted by the code using both modified correlations is wider than the original one (*Figure 7-6*). This leads to a difference between the experimental measurement and the code prediction of about (3 μm) This higher gap width predicted by the code increase the temperature prediction making the code more conservative. The centerline temperature (*Figure 7-7*) during the melting phase predicted by the code does not increase above the melting temperature of the fuel (2762°C). The temperature predicted by the original reference correlation COND-31 is 3122°C. Therefore, the original code predicts a temperature that is 360°C higher than the modified code which is still conservative.

The radial profile of the thermal conductivity is analyzed during the melting phase in the same way as in section 6.5. This time all the results are based on values calculated by TU for the exact conditions predicted by the code for the original and modified code. Only the original and modified COND-31 and COND-33 are considered. COND-34 is plotted as a sort of limiting comparison since it is the correlation that resulted in the highest thermal conductivity predicted by the original code and the only correlation that under predicted the melting heights of rod P-19-2.

It can be seen in *Figure 7-8* that for temperatures above 2000°C the modified correlations predicts higher thermal conductivities than the original ones. Modified COND-33 predicts the highest thermal conductivities and at some range of temperature becomes tangential with COND-34. At lower temperatures, the modified COND-31 gives the same results as the original one since at low temperature, the electronic conduction term is negligible. Above 1400°C The modified correlation increases than the original one and keeps increasing to the end of the studied range below melting but does not reach the same level as COND-34. The modified COND-33 predicts the same value for the original one at low temperatures then initially decreases below it. This is due to the slightly lower electronic conduction from BH-95 correlation than that from the original COND-33 as shown in *Figure 7-1*. Above

1900°C, the modified COND-33 is higher than all the other correlations and keeps increasing above the original correlation but stays below COND-34.

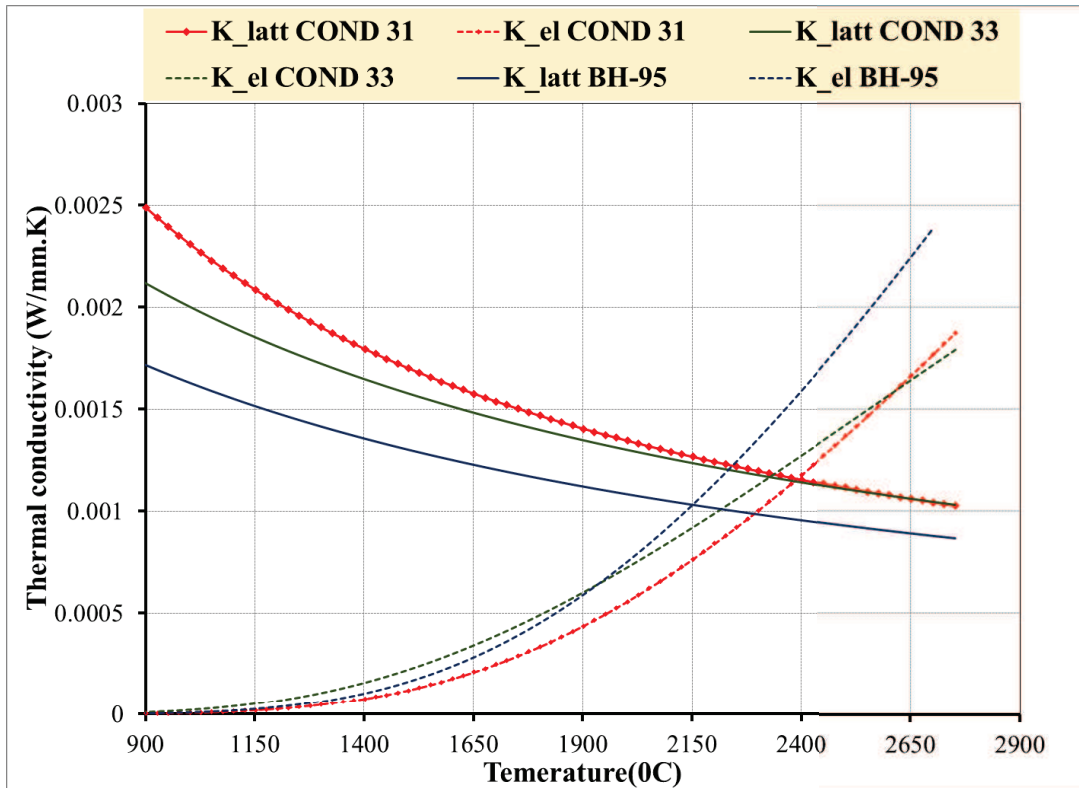


Figure 7-1 lattice and electronic conductivities comparison.

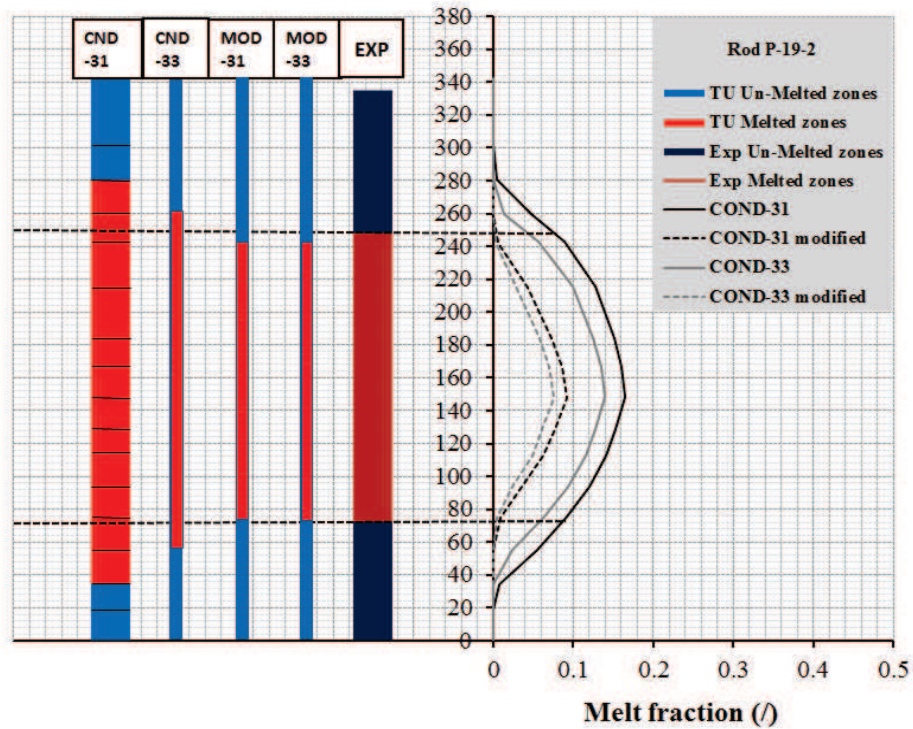


Figure 7-2 Rod P-19-2, Comparison between the melting heights and fraction according to the original and modified correlations.

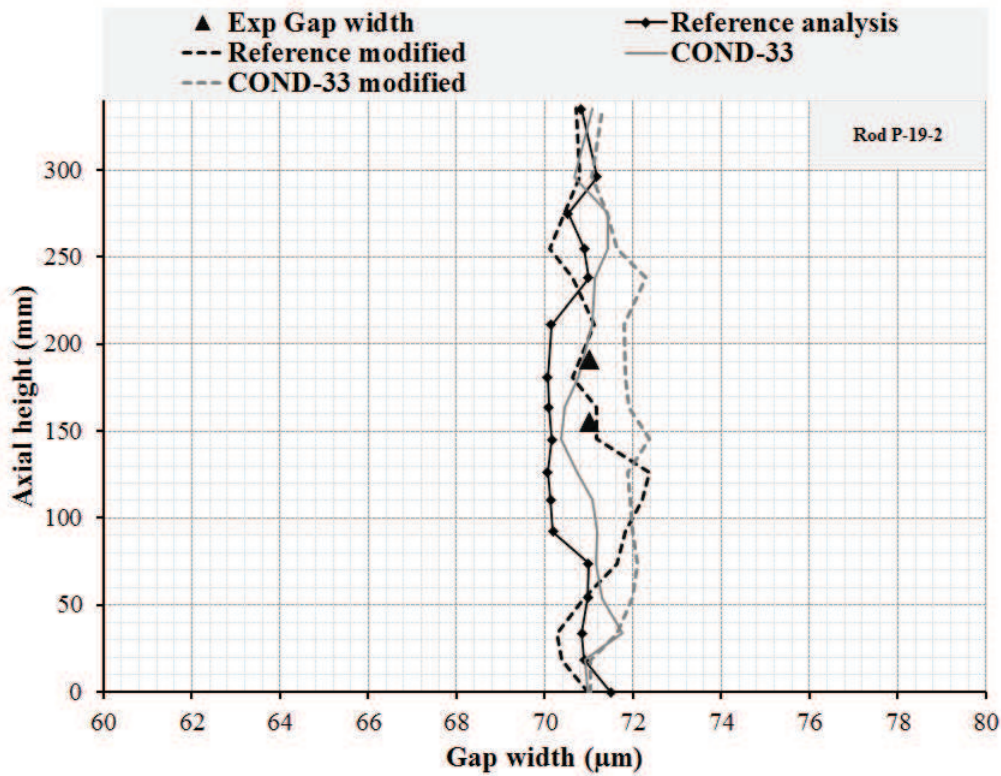


Figure 7-3 Rod P-19-2, Comparison between the predicted gap width at the end of the experiment by the original and modified correlations.

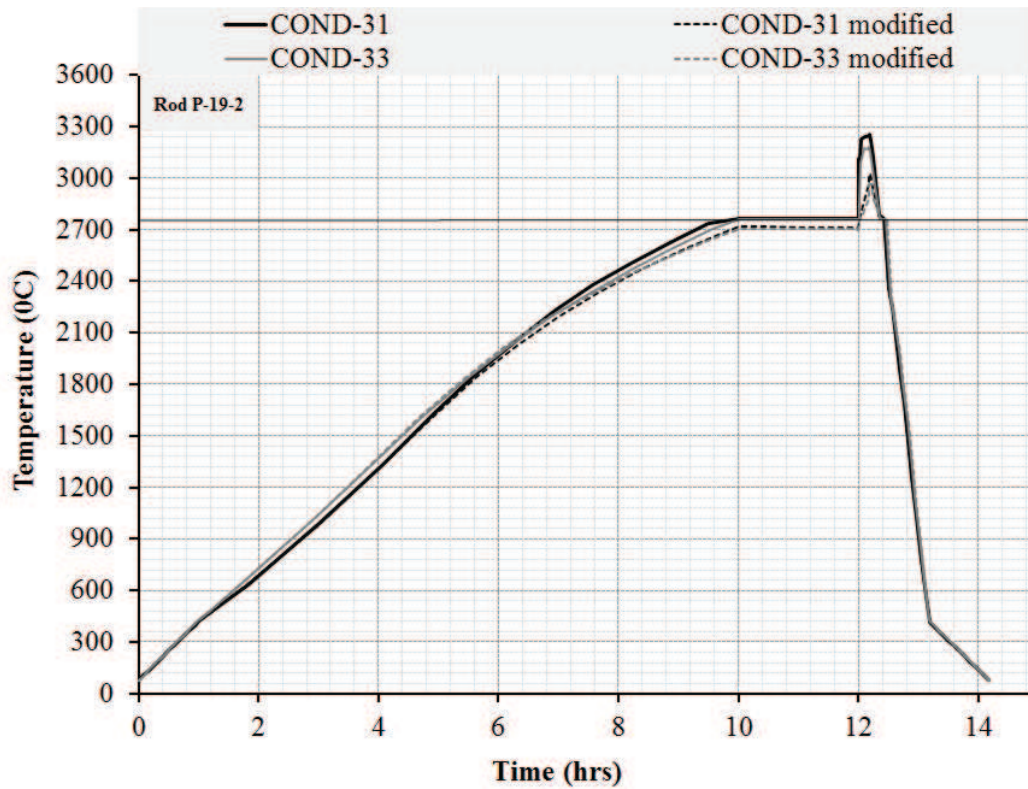


Figure 7-4 Rod P-19-2, Prediction of centreline temperature by the original and modified correlations.

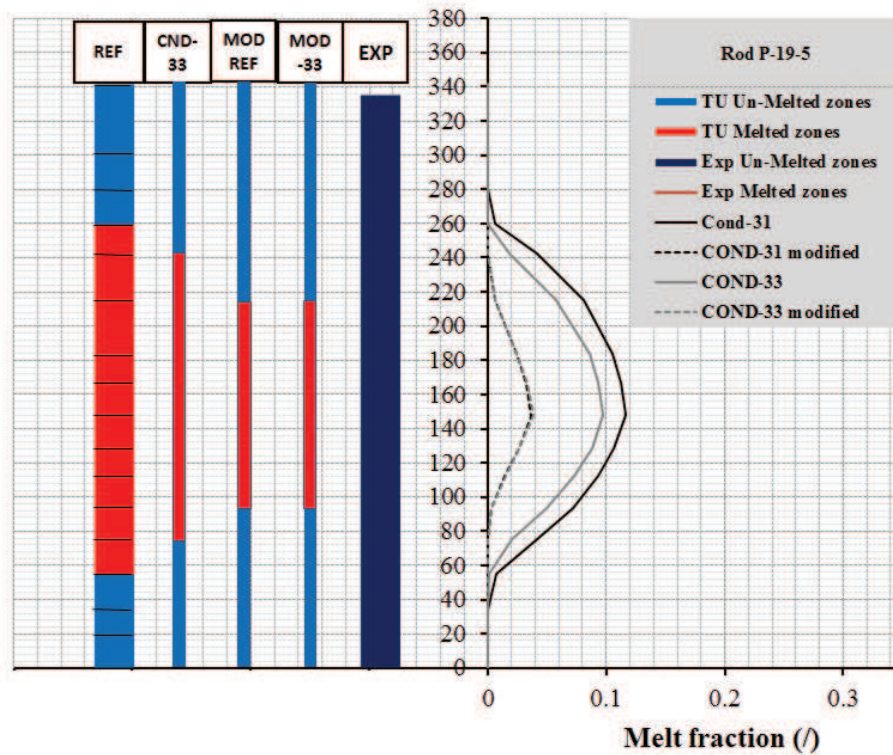


Figure 7-5 Rod P-19-5, Comparison between the melting heights and fraction according to the original and modified correlations.

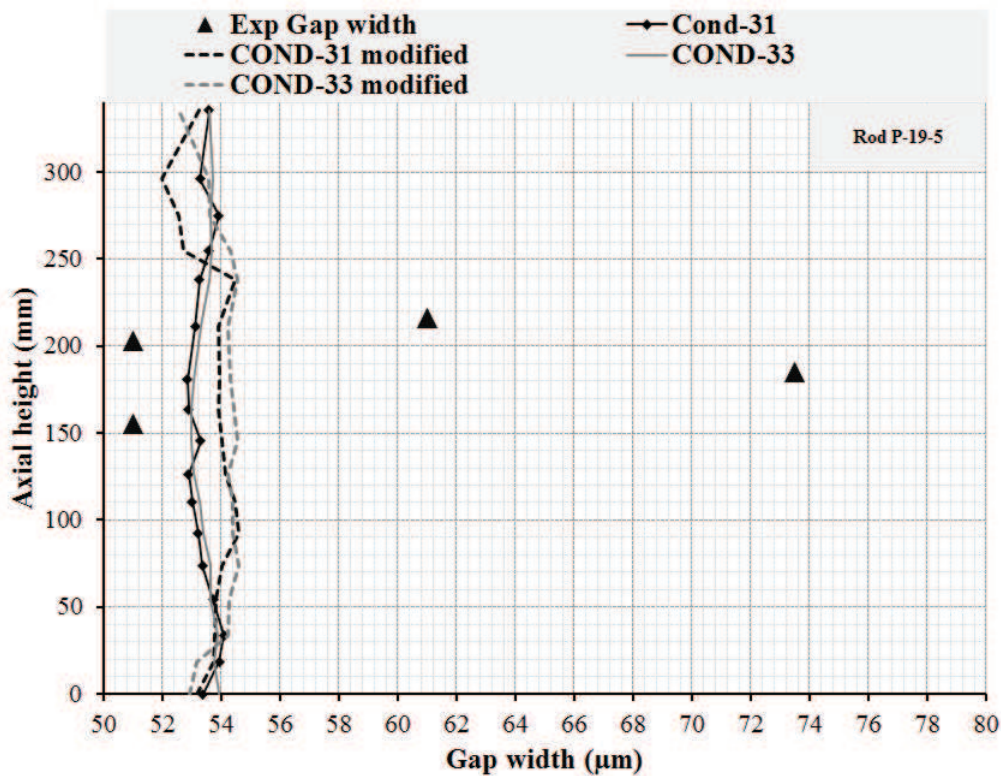


Figure 7-6 Rod P-19-2, Comparison between the predicted gap width at the end of the experiment by the original and modified correlations.

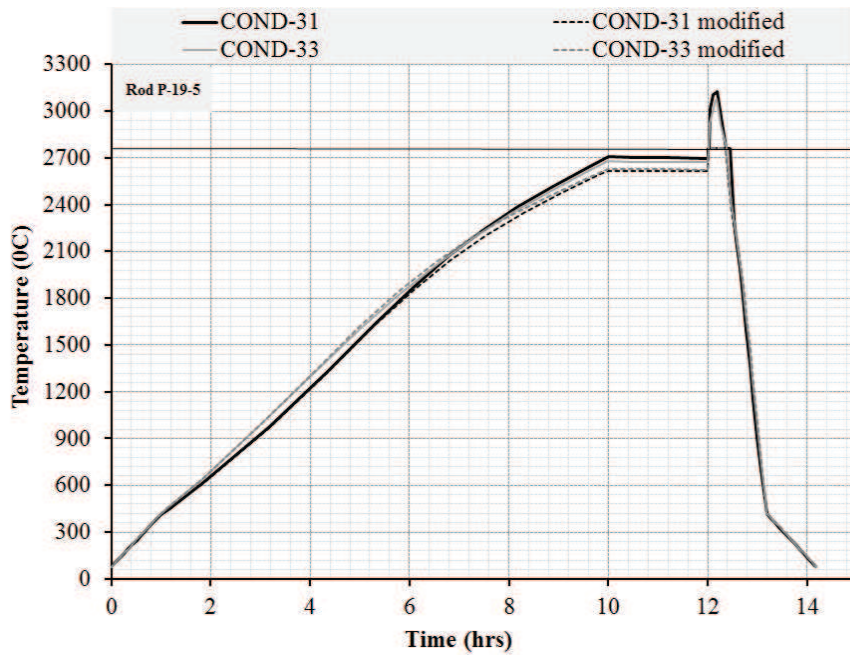


Figure 7-7 Rod P-19-5, Prediction of centreline temperature by the original and modified correlations.

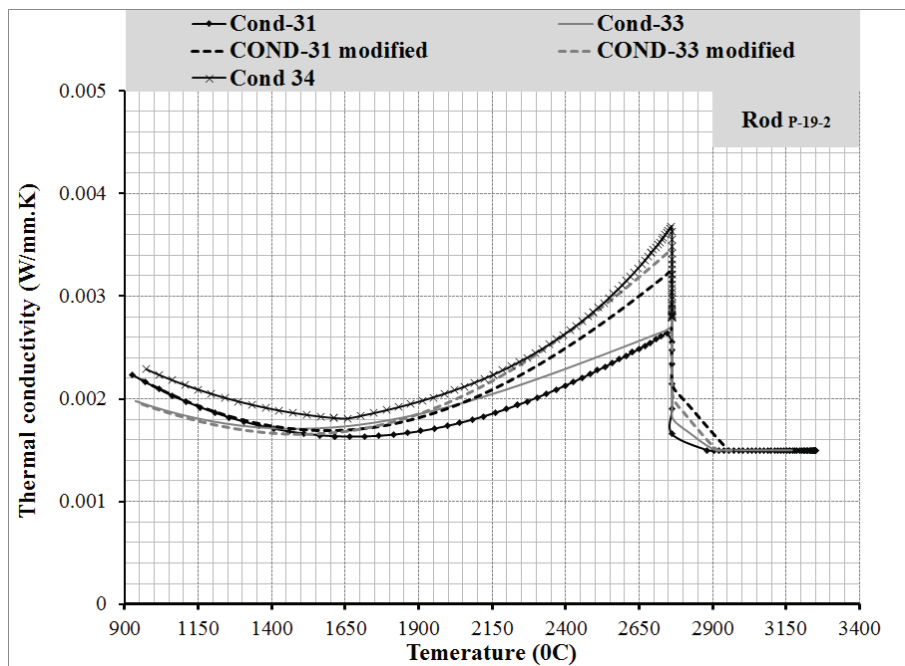



Figure 7-8 Radial comparison of thermal conductivity for rod P-19-2 predicted by the original and the modified correlations.

 Ricerca Sistema Elettrico	Sigla di identificazione	Rev.	Distrib.	Pag.	di
	ADPFISS – LP2 – 087	0	L	115	229


8 Conclusion

There are various factors that affect the thermal conductivity and hence the prediction of the temperature profile in MOX fuel. At different temperature ranges, different concepts of heat conduction applies. At lower temperature lattice vibration term is the main mechanism of heat conduction and results in a general decrease of thermal conductivity with temperature while at higher temperatures, the main mechanism that has an increasing impact with temperature is either modelled as radiation heat transfer or electronic conduction. The way of modelling these parameters and the difference between the two phenomena results in a variation between correlations predicting thermal conductivity. The lattice vibration is affected by several phenomena such as burn-up, deviation from stoichiometry, Plutonium content and fuel porosity. Taking account or disregarding any of these parameters and how they are considered, and the different data upon which a thermal conductivity correlation is based results in a variation between the predictions of thermal conductivity correlations that needed to be assessed.

Deviation from stoichiometry results in a decrease of thermal conductivity and is an important factor to be considered when modelling non-stoichiometric fuel. Burn-up cannot be neglected and its degrading effect on the thermal conductivity is confirmed. Porosity is taken into account by various corrections factors that represents an averaging effect of the pores shapes and sizes. Plutonium content has a minor effect on the thermal conductivity at low Pu content usually used in thermal reactors. However, there is a significant difference in FR fuel behaviour which uses a higher content of plutonium (>20 wt.%) than at low content. This indicates that thermal conductivity correlations based on LWR fuel type can fail to predict the thermal conductivity of FR fuel type. Therefore, Codes that are tailored to predict the thermal performance of the MOX fuel must be validated for both kinds of reactors separately to confirm the range of the applicability of the code to the specified reactor and provide a window for further improvement of the correlations used in the code.

In this work, TRANSURANUS was investigated against thermal and fast reactors rods to assess the ability of the code to predict the integral behaviour MOX fuel rods of both types of reactors. This was done based on two experimental databases IFA597/4./5 and HEDL P-19.

IFA597/4./5 was performed in Halden heavy Boiling Water Reactor and included two LWR MOX fuelled rods (Solid and Hollow). The base irradiation process took place at different levels depending on the purpose of the experiment; Higher level to study FGR in IFA597.4, while in IFA597.5 the purpose was to accumulate fission gases in the lattice itself. Reference models and correlations used to predict various phenomena in the fuel (Densification, Swelling, Pellet fragment relocation, etc.) were combined together in a reference input file to predict the overall behaviour of the fuel rods. The code was able to generally capture the experimental centreline temperature measured online on both rods. There were slight under-prediction of the centreline temperature but it still lays within the 5% uncertainty of the LHR. A general


 Ricerca Sistema Elettrico	Sigla di identificazione	Rev.	Distrib.	Pag.	di
	ADPFISS – LP2 – 087	0	L	116	229

conclusion is that the code is able to capture the centreline temperature temporal profile during the experiment. This is an indication of the ability of thermal conductivity correlations to predict the temperature profile of thermal reactor MOX fuel. An exclusion to that is the correlation by Wiesenack that resulted in a significant under-prediction of the temperature. The correlation was originally designed for UO₂ fuel and projected to MOX fuel using a correction factor of 0.92. The missing burn-up factor in the open literature correlations compared to this case limits their ability to predict thermal conductivity of the fuel to lower burn-up rates. Their prediction deviate from TU significantly at higher burn-up and would result in a significant under-prediction of the centreline temperature. TU under-predicted FGR for both rods. A consequence of that is the under-prediction of the pin pressure.


Behaviour of MOX fuel in FR was verified against HEDL-P-19 experiment. The experiment was conducted in the EBR-II to investigate power to melt of fresh MOX rods representative of the FFTFs driven fuel design. The temperature profile was not measured in this experiment since melting of the fuel was expected. Therefore, the fuel was radiographed as part of post irradiation investigation to determine the extent of melting and calculate the power limit at which the fuel is expected to produce melting. Two rods out of total of sixteen fresh rods irradiated in this experiment were studied in this work. Rod P-19-2 radiography showed that it suffered partial melting during the experiment while rod P-19-5 did not. The prediction of the melting heights by the code was determined by investigating the melting fractions predicted by the code and determining the melting heights based on it. The code results are an over-prediction of the melting heights for rod P-19-2 and prediction of melting of rod P-19-5 that remained solid during the experiment. The code was able to predict the gap width at the end of the experiment and underestimated the central void. However, the later parameter cannot be compared accurately with the simulations (at least for the rod that experiences melting) due to the occurrence of liquid fuel relocation. The over-prediction of the melting heights can be related to the under-prediction of the thermal conductivity of the FR grade of MOX fuel in the high temperature regime (close to melting).

By comparing the radial profile of the thermal conductivity at the melting phase of the experiment, the thermal conductivity at high temperature is expected to be higher that what was predicted by TU. The high temperature thermal conductivity term is expected to be the main reason for this overall under-prediction of the thermal conductivity. The review of the open literature correlations along with TU correlations suggested the usage of the high temperature term from Baron-Hervè correlation along with the standard correlation of TU and the correlation by Lanning and beyer. This term was inserted to TU and the code was recompiled to generate a new testing version of the code.

The insertion of this term resulted in a melting height comparable to what was investigated experimentally for rod P-19-2. The new version predicted some melting inside the rod P-19-5 but did not exceed 4% at peak power position. The maximum temperature predicted by the code was comparable to the melting temperature of MOX. The gap widths predicted by the code is still comparable to the experimental measurements. The equal heights of melting by using the same high temperature

 Ricerca Sistema Elettrico	Sigla di identificazione	Rev.	Distrib.	Pag.	di
	ADPFISS – LP2 – 087	0	L	117	229

term in the correlations mentioned above confirmed the idea that the lower electronic conduction term in the original correlations is the main factor that led to the under-prediction of the code. Using the same electronic conduction term led to the prediction of the same melting heights. There are still differences in the centreline temperature prediction. The standard correlation adopted by TU is more conservative and predicts a higher centreline temperature than that predicted by Lanning & Beyer but it is around 200⁰C lower than the original version. Unfortunately, due to the nature of the experiment, the temperature cannot be compared accurately to determine how much accurate the new versions of the correlations predicts the temperature. The effect of this modification on the prediction of normal operation conditions of FR is unknown but it is expected that the code will predict a lower temperature than before but not as lower as in the case studied in this work. This modification will not affect the ability of the code to predict the centreline temperature of thermal reactors since the temperatures in this type does not exceed values where the high temperature thermal conductivity terms are important. The current modification would be useful in predicting early in life power-to-melting and simulate the conditions of melted fuel. However, the ability of the code to predict normal operation temperatures and the effect of burn-up on the code prediction should be verified against other types of experiments where the temperature is actually measured.


 Ricerca Sistema Elettrico	Sigla di identificazione	Rev.	Distrib.	Pag.	di
	ADPFISS – LP2 – 087	0	L	118	229

REFERENCES

- [1] *Van Uffelen P.*, **Modeling of Nuclear Fuel Behavior**, Publications Office, JRC Publications, Report EUR 22321 EN, European Commission, 2006..
- [2] *Takayuki Nakano*, **OECD-HRP, The MOX fuel behaviour test IFA-597.4/5./6./7; Thermal and gas release data**, Institut of energiteknikk, Halden, June 2003.
- [3] *R.B. Baker*, **Integral heat rate to incipient melting in UO₂-PuO₂ fast reactor fuel**, Hanford Engineering Development Laboratory, May 1978.
- [4] *G.J.Hyland*, **Thermal conductivity of solid uo₂: critique and recommendation 1982**. *J. Nuclear Materials* 113 (1983) 125-132
- [5] *D. R. Olander*, **Fundamental Aspects of Nuclear Reactors Fuel Elements**. Department of Nuclear Engineering University of California, Berkeley, 1976.
- [6] http://en.wikipedia.org/wiki/Heat_transfer#Radiation, Last check 22-09-2014
- [7] **SCDAP/RELAP5/MOD3.1 Code manual volume4: MATPRO—A library of materials properties for light water reactor accident analysis**.
- [8] *Neil E. Todreas, Mujid S. Kazimi*, **Nucleaer Systems I, thermal Hydraulic Fundamentals 1st edition**. Massachusetts Institute of Technology, 1990.
- [9] *D.G. Martin*, **A reappraisal of the thermal conductivity of UO₂ and mixed (U,Pu) oxide fuels**. *Journal of Nuclear Materials* 110 (1982) 73-94.
- [10] *Christian Duriez, Jean-Pierre Alessandri, Thierry Gervais, and Yannick Philipponneau*, **Thermal conductivity of hypostoichiometric low Pu content (U,Pu)O_{2-x} mixed oxide**. *J. Nuclear Materials* 277 (2000) 143-158.
- [11] *K. Lassmann, A. Schubert, P. Van Uffelen, J. Van der Laar*, **TRANSURANUS handbook version v1m1j12**. JRC, ITU 2012.
- [12] *L. Luzzi, S. Lorenzi, D. Pizzocri, D. Rozzia, A .Aly, A. Del Nevo*, **Modelling and analysis of nuclear fuel pin behaviour for innovative Lead cooled FBR**. Technical report September 2014.
- [13] *Lassmann K.*, **TRANSURANUS: a fuel rod analysis code ready for use**, *Journal of Nuclear Material* 188 (1992) 295-302
- [14] *Tolonen P., Pihlatie M., Fujii H.*, **The MOX fuel behavior test IFA597-4/5/6;Thermal and gas release data to a burn-up of 25 MWd/kgMOX, HWR-652**, OECD Halden Reactor Project, February 2001.

 Ricerca Sistema Elettrico	Sigla di identificazione	Rev.	Distrib.	Pag.	di
	ADPFISS – LP2 – 087	0	L	119	229

- [15] *C. Ronchi, M. Sheindlin, M. Musella, and G.J. Hyland, Thermal conductivity of uranium dioxide up to 2900 K from simulations measurement of the heat capacity and thermal diffusivity. J. Applied Physics 85, 776 (1999)*
- [16] Juan J. Carbajo, Gradyon L. Yoder, Sergey G. Popov, and Victor K. Ivanov, **A review of the thermophysical properties of MOX and UO₂ fuels.** J. Nuclear Materials 299 (2001) 181-198
- [17] *Daniel Baron, Fuel thermal conductivity: A review of the modeling available for UO₂, (U-Gd)O₂ and MOX fuel.* Thermal performance of high burn-up LWR fuel, seminar proceedings Cadarache, France 3-6 March, 1998.
- [18] *Y. Philipponneau, Thermal conductivity of (U,Pu)O_{2-x} mixed oxide fuel.* J. Nuclear Materials 188(1992) 194-197
- [19] *S. E. Lemehov, MACROS: Modelling MADF and MABB fuels.* PELGRIMM. 3rd progress meeting. ENEA – Rome, March 27-28, 2014
- [20] **On the analysis of Pu distribution in MIMAS MOX.** EPMA. B. Vos, A. Leenaers and M. Verwerft
- [21] *IFE, OECD-HRP, Halden Boiling Water Reactor,* Institutt for energiteknikk, Halden January 2003.
- [22] *J. a. Turnbull, Fuel Behavior Data Available from IFE-OCDE Halden Project for Development and Validation of Computer Codes.* Review of Nuclear Fuel Experimental Data. OECD-NEA, 1995.
- [23] *D. Rozzia, A. Del Nevo, A. Ardizzone, M. Tarantino, Modeling of FGR in BWR Fuel Rods Based on IFA-409 Database.* ENEA CR Brasimone internal report FM-N-R-046IFA-409, 2013.
- [24] *Compiled by Terje Tverberg, Mixed oxide (MOX) fuel performance benchmark,* OECD 2007
- [25] *J.T. Maki, J.E. Meyer, LWR fuel performance analysis fuel cracking and relocation,* Energy laboratory report No:MIT-EL 78-038. October, 1978
- [26] *D. Rozzia, N. Forgione, A. Ardizzone Analysis of high burn-up MOX fuel behavior under normal operation and DBA conditions,* August 2013
- [27] http://en.wikipedia.org/wiki/Experimental_Breeder_Reactor_II, Last check 19-02-2015
- [28] <http://www.ne.anl.gov/About/reactors/frt.shtml#fragment-1>, Last check 19-02-2015
- [29] *Leonard J. Koch, Experimental breeder Reactor (EBR-II) An integrated experimental fast reactor nuclear power station,* Authorized by Argonne national laboratory

 Ricerca Sistema Elettrico	Sigla di identificazione ADPFISS – LP2 – 087	Rev. 0	Distrib. L	Pag. 120	di 229
--	--	------------------	----------------------	--------------------	------------------

[30] <http://www.pelgrimm.eu>, Last check 29-04-2015



CIRTEN
Consorzio Interuniversitario per la Ricerca TEcnologica Nucleare

POLITECNICO DI MILANO
DIPARTIMENTO DI ENERGIA, Sezione INGEGNERIA NUCLEARE - CeSNEF

Support to the design of the nuclear fuel for the Lead Fast Reactor

Lelio Luzzi, Davide Pizzocri

CERSE-POLIMI RL 1501/2015

Milano, Agosto 2015

*Lavoro svolto in esecuzione dell'Attività LP2.A2_A
AdP MSE-ENEA sulla Ricerca di Sistema Elettrico - Piano Annuale di Realizzazione 2014
Progetto B.3.1 "Sviluppo competenze scientifiche nel campo della sicurezza nucleare
e collaborazione ai programmi internazionali per il nucleare di IV generazione"*



(this page is intentionally left blank)



Index

LIST OF FIGURES	125
LIST OF TABLES	127
LIST OF SYMBOLS	129
LIST OF ACRONYMS	131
INTRODUCTION	133
1. MOX FUEL MODELLING IN TRANSURANUS	137
1.1 PLUTONIUM REDISTRIBUTION MODEL.....	137
1.1.1 Model description.....	137
1.1.2 Status of the implementation in TRANSURANUS.....	139
1.2 BURST RELEASE MODEL.....	140
1.2.1 Model description.....	140
1.2.2 Status of the implementation in TRANSURANUS.....	143
2. APPLICATION OF TRANSURANUS TO ALFRED	145
2.1 DESCRIPTION OF THE ALFRED REACTOR.....	145
2.2 REFERENCE CASE DEFINITION.....	185
2.2.1 Selection of average and hot channel.....	185
2.2.2 Power history and axial profile.....	188
2.2.3 Material properties.....	189
2.3 REFERENCE CASE RESULTS.....	190
2.3.1 Fuel and cladding temperature.....	191
2.3.2 Fission gas release.....	193
2.3.3 Gap dynamics.....	194
2.3.4 Stress and strain in the cladding.....	195
2.4 CLOSING REMARKS.....	197
3. SENSITIVITY ANALYSIS	199



3.1 MODELS CONSIDERED	199
3.1.1 Fuel swelling model	199
3.1.2 Fuel thermal conductivity model.....	200
3.1.3 Cladding swelling model and fast neutron fluence	200
3.2 WORST CASE DEFINITION	201
3.3 WORST CASE RESULTS.....	203
3.4 CLOSING REMARKS	207
4. FEEDBACKS ON ALFRED FUEL PIN DESIGN.....	209
4.1 DESIGN VARIABLES	209
4.2 IMPROVED DESIGN CASE DEFINITION	212
4.3 IMPROVED DESIGN CASE RESULTS	217
4.4 CLOSING REMARKS	219
CONCLUSIONS.....	221
ACKNOWLEDGEMENTS	223
REFERENCES	225
SHORT SCIENTIFIC CURRICULUM.....	229



List of figures

Figure 1: Schematic of the optimization process that can be carried out by means of the LFR-oriented TRANSURANUS version to give feedbacks on the ALFRED conceptual design.....	135
Figure 2: Correction factor for the diffusion coefficient as a function of the oxygen-to-metal ratio.....	139
Figure 3: ALFRED reactor primary system.	182
Figure 4: ALFRED fuel pin axial section (not in scale).	184
Figure 5: Graphical representation of the position of the AC (a) and the HC (b) within ALFRED core.	185
Figure 6: Power histories for ALFRED average and hot channel as a function of EFPD (a) and axial position (b).	188
Figure 7: Inner and outer fuel temperature, and gap conductance evolution versus burn-up for (a) AC and (b) HC reference case.	192
Figure 8: Coolant and cladding temperature evolution for (a) AC and (b) HC reference case.	192
Figure 9: Fission gas release (FGR) and internal pressure as a function of burn-up for (a) AC and (b) HC reference case.	193
Figure 10: Cladding inner and fuel outer radius, and gap width evolution as a function of burn-up for (a) AC and (b) HC reference case.	194
Figure 11: Contact pressure between fuel and cladding along with the radially averaged equivalent stress in the cladding for (a) AC and (b) HC reference case.	196
Figure 12: Graphical structure of the sensitivity analysis performed. The worst case corresponds to the fuel swelling model (option B) from Pesh et al. (1987), the fuel thermal conductivity model (option B) from Carbajo et al. (2001), the cladding swelling, C, model (option A) "AIM1" (Luzzi et al., 2014), and the fast neutron fluence, F, energy threshold (option B) >10 keV.	202
Figure 13: Comparison between ALFRED HC reference case and worst case: fuel temperature evolution.	204



Figure 14: Comparison between ALFRED HC reference case and worst case: radially averaged equivalent stress in the cladding..... 205

Figure 15: Comparison between ALFRED HC reference case and worst case: permanent strain components. 206

Figure 16: Kiviati's diagram comparing configurations with initial gap width of 150 micron. The comparison is based on the limit-normalized figures of merit important for a safety point of view (HC worst case models)..... 214

Figure 17: Kiviati's diagram showing initial gap width influence on ALFRED fuel pin performance, at different levels of initial internal pressure (HC worst case models)..... 215

Figure 18: "Temperature optimum" configuration compared with the basic design configuration (HC worst case models). 216

Figure 19: Inner and outer fuel temperature evolution versus burn-up: comparison between the reference and the optimum case for (a) AC and (b) HC reference case. 218



List of tables

<i>Table 1: ALFRED reactor specifications.....</i>	<i>183</i>
<i>Table 2: ALFRED fuel pin design parameters at Beginning of Life (BoL).</i>	<i>183</i>
<i>Table 3: Main parameters of ALFRED AC and HC modeling.</i>	<i>186</i>
<i>Table 4: Summary of ALFRED main parameters for heat exchange. Every quantity is referred to the average channel AC at BoC.</i>	<i>187</i>
<i>Table 5: Preliminary design limits for ALFRED and LFRs.</i>	<i>190</i>
<i>Table 6: Summary of ALFRED reference case results at EoL.</i>	<i>197</i>
<i>Table 7: Models considered in the sensitivity analysis.....</i>	<i>201</i>
<i>Table 8: Models defining the worst case.</i>	<i>201</i>
<i>Table 9: Summary of worst case and reference case numerical results at EoL.</i>	<i>207</i>
<i>Table 10: ALFRED fuel pin design parameters considered.....</i>	<i>211</i>
<i>Table 11: Limits considered.....</i>	<i>211</i>
<i>Table 12: Limit-normalized figures of merit.....</i>	<i>211</i>
<i>Table 13: Range of variation of ALFRED fuel pin design parameters.</i>	<i>212</i>
<i>Table 14: ALFRED "temperature optimum" design configuration.....</i>	<i>217</i>
<i>Table 15: Comparison between the results of "temperature optimum" and "standard design" configurations at EoL, applying reference models.....</i>	<i>219</i>



(this page is intentionally left blank)



List of symbols

In Section 1. MOX fuel modelling in TRANSURANUS

A	empirical constant
c	concentration of plutonium
d	pore thickness
D_{diff}	diffusion coefficient of plutonium
D_{pore}	diffusion coefficient of pores
l	pore diameter
p_{pore}	pressure inside the pores
Q	effective molar heat of transport for Pu migration
r	radial coordinate
T	temperature (K)
t	time
v	pore velocity
B_{span}	experimental parameter
bu	burn-up
F	fractional coverage
F_{sat}	saturation coverage
f	fraction of active grain faces
G	experimental parameter
m	micro-cracking parameter
s	empirical integer parameter
T_{cent}	central temperature, experimental parameter
u	micro-crack healing parameter
τ	micro-crack healing time constant

In Section 2. Application of TRANSURANUS to ALFRED

CDF	cladding cumulative damage function (/)
CDF_{lim}	cladding cumulative damage function limit (/)
D	cladding diameter (mm)
g_0	initial gap width (μm)
$h_{up,0}$	initial upper plenum height (mm)
Nu	Nusselt number
p	pin pitch (mm)
p_{int}	internal helium filling pressure (MPa)
$p_{int,0}$	initial internal helium filling pressure (MPa)
Pe	Peclet number
Pr	Prandtl number
R	gas constant



Re	Reynolds number
T	temperature (K)
T_{lim}	inner fuel temperature limit (K)
Γ	design configuration
δ	limit-normalized cladding plastic strain (/)
ε_p	cladding plastic strain (%)
$\varepsilon_{p,lim}$	cladding plastic strain limit (%)
ε_{th}	thermal creep cladding hoop strain (%)
$\varepsilon_{th,lim}$	thermal creep cladding hoop strain limit (%)
θ	limit-normalized maximum inner fuel temperature ($K K^{-1}$)
κ	limit-normalized maximum cladding CDF (/)
π	limit-normalized inner maximum internal pressure (/)
τ	limit normalized maximum thermal creep cladding hoop strain (/)



List of acronyms

AC	Average Channel
ALFRED	Advanced Lead-cooled Fast Reactor European Demonstrator
BoC	Beginning of Cycle
BoL	Beginning of Life
CDF	Cumulative Damage Function
EoC	End of Cycle
EoL	End of Life
EFPD(s)	Equivalent Fuel Power Day(s)
FGR	Fission Gas Release
FCMI	Fuel Cladding Mechanical Interaction
HC	Hot Channel
HLM(s)	Heavy Liquid Metal(s)
ITU	Institute for TransUranium elements
JOG	Joint Oxide Gain
LEADER	Lead-cooled European Advanced DEMonstration Reactor
LFR(s)	Lead-cooled Fast Reactor(s)
LWR(s)	Light Water Reactor(s)
MYRRHA	Multipurpose hYbrid Research Reactor for Hightech Applications
MOX	Mixed OXyde
O/M	Oxygen-to-metal-ratio
ULOF	Unprotected Loss Of Flow



(this page is intentionally left blank)



Introduction

The Lead-cooled Fast Reactor (LFR) has been selected by the Generation IV International Forum as one of the candidates for the next generation of nuclear power plants (GIF, 2002). Advanced reactor concepts cooled by Heavy Liquid Metals (HLMs) ensure a great potential for plant simplifications and higher operating efficiencies compared to other coolants, nevertheless introducing additional safety concerns and design challenges (Cacuci, 2010). Reactor conditions of HLM-cooled reactor designs (e.g., extended exposure to neutron irradiation, high temperature, corrosive environment) impose challenges for engineers and designers concerning the selection of structural and cladding materials. Key guidance on material behavior and help to improve the design can be achieved by means of fuel pin performance codes. Since the fuel pin behavior is determined by the synergy of several phenomena (heat transfer to the coolant, creep, swelling and corrosion of the cladding, relocation, densification, creep, and swelling of the fuel, fission gas release, etc.), a fuel pin analysis can be adequately accomplished by means of integral performance codes.

This work is grafted in the research activity of the Nuclear Reactor Group of the Politecnico di Milano on LFRs. The particular features of these innovative reactor concepts attained the attention of the European Commission, and the LEADER Project (LEAd Advanced DEMonstration Reactor) has been introduced in the 7th Framework Program (FP7, <http://wwpw.leader-fp7.eu/>). As a part of the LEADER Project, the preliminary design of a demonstrator reactor has been carried out. This is a small (300 MW_{th}) reactor, called ALFRED (Advanced Lead-cooled Fast Reactor), whose aim is to prove the technical and economic feasibility of the Generation IV lead reactor concept (Alemberti et al., 2013).

In a previous work carried out in the frame of the "MSE-ENEA AdP-2013" (Luzzi et al., 2014), the TRANSURANUS code (Lassmann et al., 2013) developed at JRC-ITU (Karlsruhe) has been extended for the analysis of LFR nuclear fuel pin behavior, employing 15-15Ti austenitic steels as cladding material, and realizing an LFR-oriented version of TRANSURANUS. This represented a necessary step in a more general process of analysis of LFR fuel performance (see Figure 1), aimed at supporting the design and the construction of ALFRED by means of the following actions:



1. Critical analysis of the fuel pin behavior in reactor through the study of a "reference case" (based on "best estimate" models) to verify the respect of design limits.
2. Identification of possible critical issues through an extensive sensitivity analysis on the most significant phenomena affected by a considerable modeling uncertainty, and oriented to the definition of a "worst case scenario" for the fuel pin performance.
3. Improvement of the fuel pin design, in order to enhance the fuel performance and the safety-by-design features of the ALFRED reactor.

This work is focused on these three items. First of all, in continuation of the modelling work started in Luzzi et al. (2014), two new models for MOX fuel are presented (Section 1). Then, analysis of the ALFRED fuel pin behavior is performed by means of the LFR-oriented version of TRANSURANUS. In particular, Sections 2, 3 and 4 represent the three logical steps described above, which effectively lead important feedbacks to ALFRED fuel pin design.

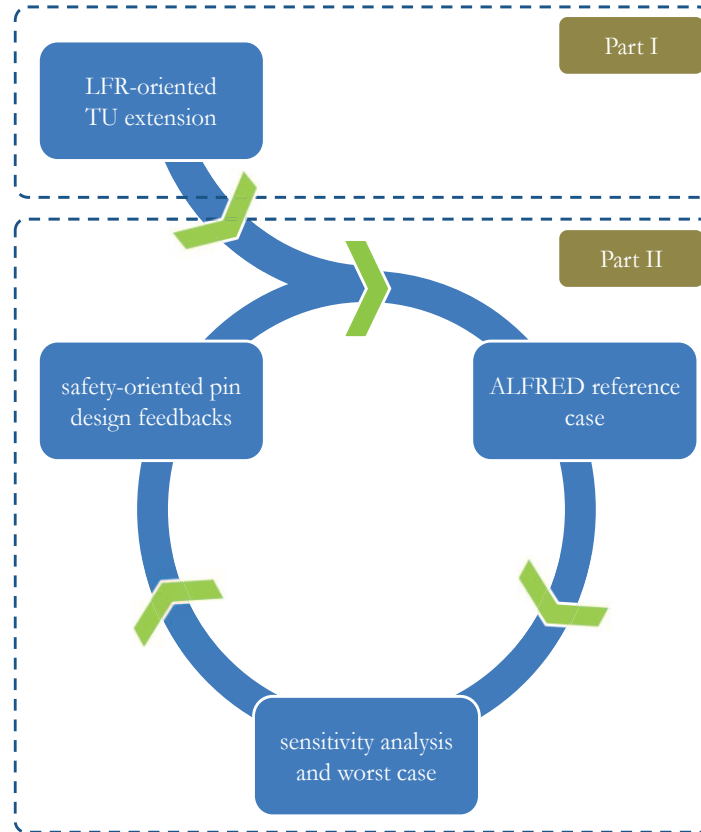


Figure 1: Schematic of the optimization process that can be carried out by means of the LFR-oriented TRANSURANUS version to give feedbacks on the ALFRED conceptual design.



(this page is intentionally left blank)



1. MOX fuel modelling in TRANSURANUS

In this Section, two recently developed models for MOX fuel are described. The first one (Section 1.1) is an improved model for plutonium redistribution, which is present in the v1m1j14 released version of TRANSURANUS (and has been used in the following analysis), while the second (Section 1.2) is a model for burst release, whose implementation in TRANSURANUS is on-going (and has not been used in the following analysis).

1.1 Plutonium redistribution model

In hypo-stoichiometric MOX (Mixed OXides) fuel for Fast Breeder Reactors (FBRs), plutonium, Pu, migrates to the central, high temperature pellet region. As a consequence, fuel thermal properties such as the thermal conductivity and the melting temperature could be strongly affected, resulting in a restriction of the safety margins for power uprating in commercial fast reactors (Olander, 1976). Several post irradiation examinations and out-of-pile experiments indicated that plutonium migration is promoted by two main mechanisms (Bober and Schumacher, 1973): (i) solid-state thermal diffusion; (ii) vapor transport by migrating pores (which contribute to the formation of the central void).

1.1.1 Model description

The TRANSURANUS model for Pu redistribution (PUREDI), described in Lassmann (1992) and Lassmann et al. (2013), has been recently refined in order to include the effects of oxygen-to-metal ratio, burn-up and their feedback (Di Marcello et al., 2012), and further extended to account for the effect of vapor transport (Di Marcello et al., 2014).

Pu migration is modelled considering that thermal diffusion occurs simultaneously with vapor transport via pores in the fuel. Assuming axial symmetry and neglecting axial concentration gradients, actinides can migrate only along the radial coordinate, r , so that the following equation is obtained:



$$\frac{\partial c}{\partial t} = \frac{1}{r} \frac{\partial}{\partial r} \left\{ r \left[D_{Diff} \left(\frac{\partial c}{\partial r} + c(1-c) \frac{\partial T}{\partial r} \frac{Q}{RT^2} \right) - D_{Pore} \left(APc \frac{l}{d} \frac{\partial T}{\partial r} \exp \left(-\frac{D_{Pore}}{lv} \right) \right) \right] \right\} \quad (1)$$

where c is the concentration of plutonium, T (K) is the temperature, and R is the gas constant. The diffusion coefficient of Pu, D_{Diff} ($\text{m}^2 \text{s}^{-1}$), is determined as $D_{Diff} = 3.4 \cdot 10^{-5} \exp(-55891/T)$, while the diffusion coefficient of the pores is assumed as $D_{Pore} = D_{Diff}$. A correction factor according to Glesser-Leme and Matzke (1982) (Figure 2) is applied to the diffusion coefficient, to account for the hypo-stoichiometry of the fuel. The effective molar heat of transport for Pu migration, Q , is set to $-146.5 \text{ kJ mol}^{-1}$. $A = 0.35 \text{ K}^{-1}$ is an experimentally determined constant. l and d are the pore diameter and thickness, respectively, and P is the fuel porosity. The pore velocity, v , is a parameter subject to great uncertainty. According to Di Marcello et al. (2014) the correlation by Lackey et al. (1972) is adopted, which reads

$$v = \frac{3.364}{p_{Pore} T^{1.5}} \frac{\partial T}{\partial r} \exp \left(-212.275 + 65.842 \left(\frac{O}{M} \right) + 8.9453 \cdot 10^{-2} T \right. \\ \left. - 2.55399 \cdot 10^{-2} \left(\frac{O}{M} \right) T + 2.956 \left(\frac{O}{M} \right)^2 - 5.6541 \cdot 10^{-6} T^2 \right) \quad (2)$$

where (O/M) is the oxygen-to-metal-ratio of the fuel, and p_{Pore} (atm) is the total pressure in the pore (assuming ideal gas law, it is calculated from the ratio of the fuel temperature and the sintering temperature). For a detailed discussion about the choice of these parameters, we refer to Di Marcello et al. (2014).

The Neumann boundary conditions imposing zero flux of Pu at both the fuel outer, R_o , and the inner, R_i , radius for Eq. 1 must also ensure that the mass balance of Pu is preserved during migration. The solution of Eq. 1 is obtained by means of the finite difference scheme described in Di Marcello et al. (2012). The model applies for the different Pu isotopes present in the fuel (Pu-238, Pu-239, Pu-240, Pu-241, Pu-242).

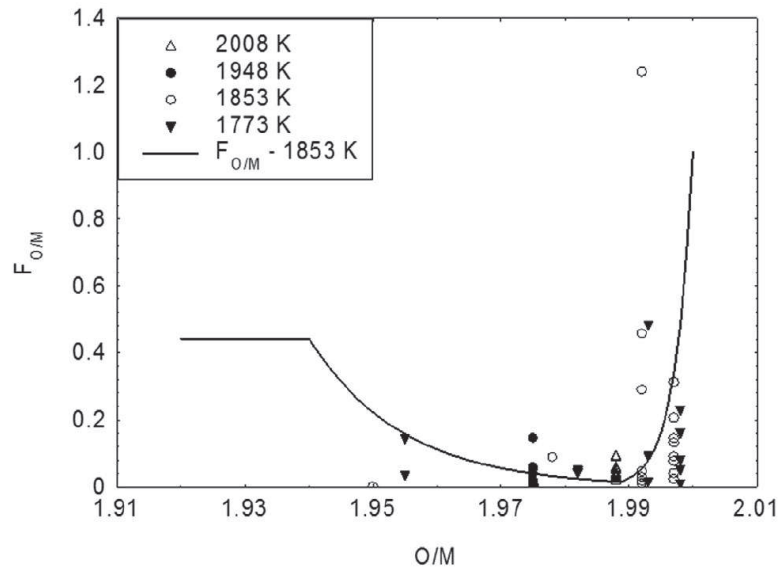


Figure 2: Correction factor for the diffusion coefficient as a function of the oxygen-to-metal ratio.

1.1.2 Status of the implementation in TRANSURANUS

The here described model for plutonium redistribution in MOX fuel is implemented in the LFR-oriented version of TRANSURANUS and has been applied to the analysis of ALFRED fuel pin performance. The model is also available in the v1m1j14 released version of TRANSURANUS.



1.2 Burst release model

In this Section, we discuss a recently developed model for *burst release*, applicable in both oxide and MOX fuel (Pastore et al., 2014; Pizzocri et al., 2015). The validation of this model is on-going, with preliminary encouraging results (Pizzocri et al., 2015). The application of this model to fuel performance analysis of LFRs is foreseen in the future.

1.2.1 Model description

The substantial release of fission gas during temperature transients (*burst release*) can be critical during operational reactor transients and (design-basis) accidents. A purely diffusion-based model cannot explain the rapid kinetics of the process. Avoiding an extensive review of the experimental state-of-the-art (which can be found in Pastore et al. (2014) and in Pizzocri et al. (2015)), there is strong evidence (Rothwell, 1962; Notley and MacEwan, 1966; Carroll et al., 1969; Hasting et al., 1986; Baker and Killeen, 1987; Small, 1988; Walker et al., 1988; Une and Kashibe, 1990; Nakamura et al., 1999; White et al., 2006; and specifically related to MOX fuel, Ducros et al., 2013) supporting the following modelling assumptions:

- Burst release occurs through grain-boundary micro-cracking, which entails gas depletion of a fraction of the grain faces.
- Release bursts are triggered by temperature variations.
- The rate of gas release during bursts is a peaked function of temperature with the maximum at a *central* temperature, which depends on burnup.

The here presented model for burst fission gas release extends a previous purely diffusion-based model for the coupled fission gas release (FGR) and swelling (Pastore et al., 2013; available in the v1m1j14 version of TRANSURANUS). Gas depletion of a fraction of the grain faces is modelled as a reduction of the fractional coverage, F . In particular, F is scaled by a factor, f , corresponding to the fraction of non-cracked (intact) grain faces. The reduction of the fractional coverage effectively leads to a decrease of the amount of gas retained in the fuel (and consequently of fission gas swelling) and to a corresponding increase of FGR. The lost gas-storing capacity of cracked grain



faces is represented by scaling the saturation coverage, F_{sat} , by the factor f . Moreover, the healing process of cracked grain faces is considered as a progressive restoration of the grain-face gas storing capacity. Therefore, the fractional coverage and the saturation coverage obey the following equations:

$$\begin{cases} \frac{dF}{dt} = \left[\frac{dF}{dt} \right]_d + F \left[\frac{df}{dt} \right]_c \\ \frac{dF_{sat}}{dt} = F_{sat} \left(\left[\frac{df}{dt} \right]_c + \left[\frac{df}{dt} \right]_h \right) \end{cases} \quad (3)$$

where the subscript d stands for diffusion-controlled processes (Pastore et al., 2013), c stands for micro-cracking, and h for micro-crack healing. The value for the maximum (initial) saturation coverage (corresponding to all intact grain faces) is $F_{sat,i} = 0.5$.

The micro-cracking process is simplified into a temperature and burnup-dependent behavior, characterized by a micro-cracking parameter, m . Observing that the process can only affect intact grain faces, we can write

$$\left[\frac{df}{dt} \right]_c = -\frac{dm}{dt} f \quad (4)$$

where $[df/dt]_c$ is the reduction rate due to micro-cracking of the fraction of intact grain faces, f . The micro-cracking parameter is taken as a function of temperature and burnup. In particular, the temperature dependence is such that

$$\left[\frac{df}{dt} \right]_c = 0 \quad \text{if} \quad \frac{dT}{dt} = 0 \quad (5)$$

which conforms to the experimentally observed characteristic of burst release as triggered by temperature variations. The time-dependence of the micro-cracking parameter is assumed to be implicit in the temperature-dependence. Moreover, a dependence on local burnup, bu , is included, i.e., $m(T(t), bu)$. Under the condition expressed by Eq. 5, the analytic solution of Eq. 4 with initial conditions $f(t_0) = f_0$ and $m(t_0) = m_0$ is

$$f(t) = f_0 \exp(m(t) - m_0) \quad (6)$$



Based on the available experimental evidence, the functional form of m is chosen as a temperature and burnup-dependent sigmoid function

$$m(T, bu) = 1 - \left[1 + G \exp \left(s \frac{T - T_{cent}(bu)}{B_{span}} \right) \right]^{-\frac{1}{G}} \quad (7)$$

where T_{cent} (K) is the central temperature, B_{span} (K) is a measure of the temperature-domain width of the phenomenon, G (-) is a parameter, and s is set to +1 during heating transients and to -1 during cooling transients, so that m increases during both heating and cooling transients. The following values for the parameters are adopted in this work: $B_{span} = 10$ K, $Q = 33$. These values ensure an almost complete burst when annealing up to high temperatures (≈ 2500 K), in agreement with Ducros et al. (2013), and allowing for the intrinsic asymmetry between heating and cooling transients, in agreement with Rothwell (1962).

The burnup-dependence of the temperature at which burst is more effective (Baker and Killeen, 1987; Small, 1988; Une and Kashibe, 1990) is accounted for defining T_{cent} (K) as

$$T_{cent}(bu) = 1773 + 520 \exp \left(-\frac{bu}{10} \right) \quad (8)$$

where bu (GWd t_U⁻¹) is the average burnup.

Therefore, in a semi-empirical approach, the present model describes micro-cracking as directly affecting the grain-face gas bubble development, nevertheless adopting an empirical formulation (Eq. 7) for the parameters characterizing the process.

From the above features, the developed model inherently allows for burst release (i) to be activated only during temperature transients (Eq. 5), (ii) is significant only in the neighborhood of the central temperature, and (iii) considers the burnup-dependence of bursts. Therefore, the treatment conforms to the experimentally observed peculiarities of transient FGR, without introducing any discrete threshold. It follows that continuity of the coupled fission gas release and swelling in both time and space is guaranteed, in line with a physically sound description of fission gas behavior.



A preliminary treatment of micro-crack healing is also included in the present model. Following Hering (1982), a simplified treatment of the healing process into a purely burnup-dependent behavior is adopted. Analogous to the treatment of micro-cracking, the process is characterized by a healing parameter, u . Observing that the process can only affect cracked grain faces, we can write:

$$\left[\frac{df}{dt} \right]_h = \frac{du}{dt} (1 - f) \quad (9)$$

The healing parameter is taken as a function of the sole burnup, i.e., $u = u(bu(t))$. The analytic solution of Eq. 13 with initial conditions $f(t_0) = f_0$ and $u(t_0) = u_0$ is

$$f(t) = f_0 + (1 - f_0)[1 - \exp(u(t) - u_0)]$$

The expression for the parameter u is chosen as

$$u(bu) = bu/\tau \quad (10)$$

where $\tau = 1 \text{ GWd } t_U^{-1}$ is adopted, corresponding to $\approx 99\%$ restore of the grain-face gas storing capacity after $5 \text{ GWd } t_U^{-1}$ (Hering, 1982).

1.2.2 Status of the implementation in TRANSURANUS

The here presented burst release model is not yet implemented in any TRANSURANUS version, and consequently it is not applied in the following analysis. As the model validation proceeds (preliminary results are described in Pizzocri et al., 2015), the implementation in TRANSURANUS is foreseen.



(this page is intentionally left blank)



2. Application of TRANSURANUS to ALFRED

In this Section, we applied the LFR-oriented version of TRANSURANUS (detailed in Luzzi et al., 2014) to the ALFRED reactor. First of all, ALFRED main features are presented (Section 2.1), and a reference case simulation (i.e., based on best estimate models) of its fuel pin performance is discussed considering the power history of both the average and hot channel (Sections 2.2 and 2.3).

2.1 Description of the ALFRED reactor

ALFRED (Advanced Lead-cooled Fast Reactor European Demonstrator) is a small-size (300 MW_{th}) pool-type LFR. Its current primary system configuration (Alemberti et al., 2013) is depicted in Figure 3.

The ALFRED core is composed by wrapped hexagonal Fuel Assemblies (FAs), each one containing 127 fuel pins arranged on a triangular lattice. The 171 FAs are subdivided into two radial zones (57 inner and 114 outer) with different plutonium fractions, and surrounded by two rows of dummy elements serving as reflector. In particular, the fuel considered for ALFRED is made by annular U-Pu Mixed OXide (MOX) pellets. As far as the cladding is concerned, a steel from the 15-15Ti class has been selected, because already licensed for other fast reactors (Phenix, Superphenix). In this work, the AIM1 is assumed as cladding material (for further details about the modelling of the cladding steel in TRANSURANUS, see Luzzi et al., 2014). In



Table 1: ALFRED reactor specifications.

Reactor specification	
Thermal power (MW)	300
Fuel residence time (years)	5
Coolant inlet temperature (°C)	400
Average coolant outlet temperature (°C)	480
Coolant mass flow rate (kg s ⁻¹)	≈ 25700
Average coolant velocity (m s ⁻¹)	≈ 1.4

Table 2: ALFRED fuel pin design parameters at Beginning of Life (BoL).

Fuel pin design specification	
Fuel type	MOX
Cladding	AIM1
Coolant	Lead
Enrichment as Pu/(Pu+U) (wt. %) (inner zone)	21.7
Enrichment as Pu/(Pu+U) (wt. %) (outer zone)	27.80
Fuel density (% theoretic density)	95
O/M (/)	1.97
Filling gas	He
Initial filling pressure (MPa)	0.1
Upper plenum volume (mm ³)	≈ 30000
Upper plenum length (mm)	120
Active length (mm)	600
Lower plenum length (mm)	550
Cladding outer diameter (mm)	10.5
Cladding inner diameter (mm)	9.3
Fuel pellet outer diameter (mm)	9
Fuel pellet inner diameter (mm)	2
Initial fuel-cladding gap width (μm)	150
Pin pitch (mm)	13.86



2.2 Reference case definition

The in-reactor life of a fuel pin is characterized by the interaction between many different phenomena. The properties of fuel and cladding, the position of the pin in the core, the power and irradiation history, all interact in determining the fuel pin general performance.

2.2.1 Selection of average and hot channel

We considered two different coolant channels of the ALFRED reactor, i.e., the Average Channel (AC) representative of the average conditions among the fuel pins, and the Hot Channel (HC) representative of the most critical conditions achieved in the core in terms of power history. These two channels are graphically represented in Figure 5.

The AC is defined as the triangular channel placed in a generic sub-assembly and it is characterized by a reactor average linear power, constant along the five irradiation years. The HC is a triangular channel as well, being the most close to the core center between the more enriched pins (outer zone). Actually, the corner channel is difficult to be modeled in TRANSURANUS, because the bypass flow between two FAs has not been determined already in the ALFRED design. Therefore, the immediately adjacent channel has been chosen. This channel is characterized by practically the highest linear power, which decreases from the Beginning of Life (BoL) to the End of Life (EoL).

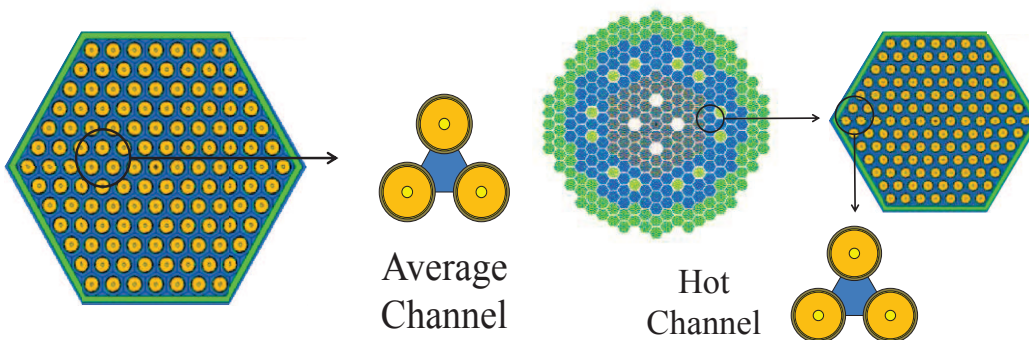


Figure 5: Graphical representation of the position of the AC (a) and the HC (b) within ALFRED core.



In Table 3 and Table 4, the main parameters of the AC and HC modelling are presented. Neutronic analysis of the ALFRED fuel pin has been carried out by means of the SERPENT code (Aufiero, 2013; SERPENT, 2011), which is able to calculate the one-group neutron cross sections and fast fluence to be provided to TRANSURANUS. In particular, the fast fraction of the neutron flux is crucial for the determination of the irradiation damage dose on the materials (e.g., related to swelling and irradiation creep). The flux changes over a batch, leading to different values at Beginning of Cycle (BoC) and at End of Cycle (EoC). These values are also affected by large discrepancies, namely: (i) the threshold above which neutrons are considered fast enough to produce damage; (ii) the conversion factor between fluence and displacement per atoms which is usually adopted in the correlations. These discrepancies will be taken into account in the sensitivity analysis.

Table 3: Main parameters of ALFRED AC and HC modeling.

	AC	HC
Pin power (kW)	12.9	17.7
Lead mass flow rate (kg s ⁻¹)	1.14	1.14
Burn-up (at. %)	7	9.5
Axial peak factor (BoC)	1.16	1.20
Axial peak factor (EoC)	1.13	1.13
Total flux (n cm ⁻² s ⁻¹)	1.53 10 ¹⁵	1.60 10 ¹⁵
Fast Flux (> 100 keV) (n cm ⁻² s ⁻¹)	0.47 10 ¹⁵	0.51 10 ¹⁵
Fast Flux (> 10 keV) (n cm ⁻² s ⁻¹)	0.93 10 ¹⁵	1.00 10 ¹⁵



Table 4: Summary of ALFRED main parameters for heat exchange. Every quantity is referred to the average channel AC at BoC.

ALFRED heat exchange parameters	
Lattice pitch, p (mm)	13.86
Rod outer radius, D/2 (mm)	5.25
p/D (/)	1.32
Mass flow per pin (kg s ⁻¹)	1.15
Linear power (kW m ⁻¹)	21.4
Lead velocity (m s ⁻¹)	1.37
Coolant area (mm ²)	79.77
Re	68269
Pr	0.0175
Pe	1192
Nu	16.72
Heat transfer coefficient (kW m ⁻² K ⁻¹)	29.47



2.2.2 Power history and axial profile

The power history used in this work is based on a calculation performed by means of the deterministic ERANOS code. This power history is calculated simulating a five year cycle with five refueling phases. This leads to a decreasing power of the hot channel from one batch to the other, as is shown in Figure 6. For the average channel, a constant value along the five years is calculated. For both the channels, the shutdown lasts one hour, followed by a refueling period of 15 days and a start-up of 10 hours (Grasso et al., 2013). In Figure 6, the axial profiles for AC and HC calculated by means of SERPENT are shown. Another option for the power history has been calculated by means of a Monte Carlo (MCNP) code at ENEA (Petrovich et al., 2012). This simulation gives a constant value also for the HC (averaged between the second and the third year), being less appropriate in describing the HC fuel performance.

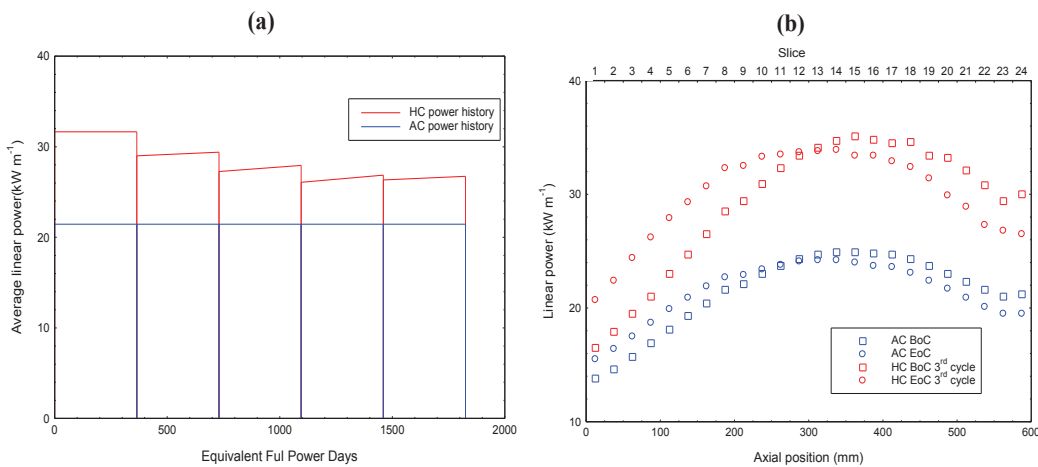


Figure 6: Power histories for ALFRED average and hot channel as a function of EFPD (a) and axial position (b).

2.2.3 Material properties

It is out of the scope of this work to present in detail the material properties available in the LFR-oriented version of TRANSURANUS. An extensive and careful review of the material properties



applied in this analysis can be found in Luzzi et al. (2014). For the modelling of the MOX fuel, reference correlations can also be found in Lassmann et al. (2013).



2.3 Reference case results

In this Section, the main results of the analysis of the reference case simulation are presented. AC and HC are here always analyzed in parallel, in order to properly point out peculiarities. These results are fundamental for the selection of the models on which the sensitivity analysis is performed. The discussion of the results is organized in order to progressively check the preliminary design limits suggested in literature for ALFRED. These preliminary limits are reported in Table 5.

All the limits reported have been found in literature. They have to be intended as preliminary indications, useful in the phase of ALFRED conceptual design. Final design limits may be different. As an example, the limit of 550°C for the peak cladding temperature, set against lead corrosion, depends on the coating material, which is still under development. The discussion of the results for the reference case is divided in four sub-sections: fuel and cladding temperature (2.3.1), fission gas release (2.3.2), gap dynamics (2.3.3), stresses and strains in the cladding (2.3.4).

Table 5: Preliminary design limits for ALFRED and LFRs.

Limited quantity	Proposed limit	Reference
Peak fuel temperature	< 2000°C	Grasso et al., 2013
Peak cladding temperature	< 550°C	Grasso et al., 2013
Plenum pressure	< 5 MPa	Grasso et al., 2013
Cladding $\Delta D/D$	< 3%	IAEA, 2012
Cladding swelling strain	< 5%	NEA, 2005
Thermal creep strain (1)	< 0.2%	IAEA, 2012
Thermal creep strain (2)	< 1%	NEA, 2005
Total creep strain	< 3%	NEA, 2005
Cumulative damage function*	< 0.2-0.3	IAEA, 2012
Cladding plastic strain	< 0.5%	Vettraino and Luzzi, 2001

*The Cumulative Damage Function (CDF) is a pin lifetime parameter that considers the linear accumulation of the fraction damage calculated as ratio between the short time interval and the time-to-rupture (Luzzi et al., 2014).



2.3.1 Fuel and cladding temperature

Figure 7 shows the fuel temperature evolution during the irradiation for both the average and the hot channel, together with the evolution of the gap conductance. The maximum fuel temperature is located just above the mid-plane of the active length. For the average channel it is well below the limit (2000°C), reaching 1800°C after the first irradiation year. On the other hand, for the HC the maximum temperature is close to 2200°C and located in the middle of the first year cycle (i.e., 1% at. burn-up).

As far as the cladding and the coolant temperatures are concerned, the maximum temperatures are reached at the beginning of the irradiation, at the outlet of the active length (Figure 8). In addition, the limit on the outer cladding temperature is respected, reaching 550°C only at the beginning of the irradiation.

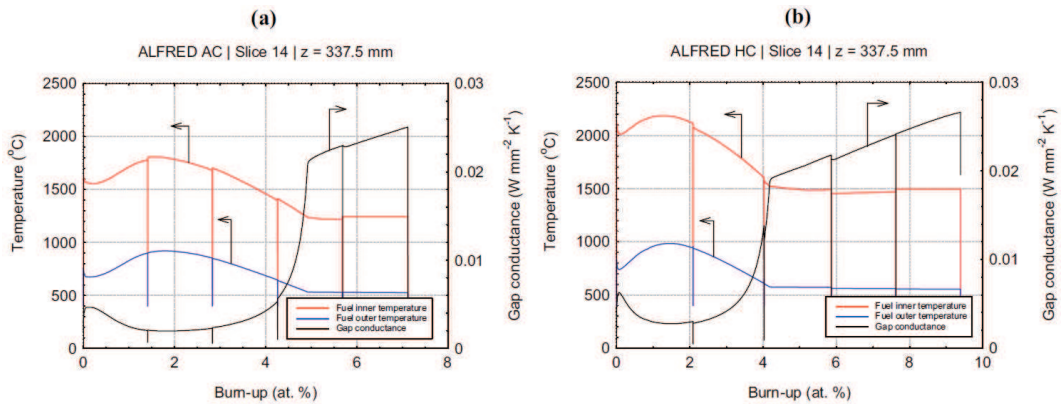


Figure 7: Inner and outer fuel temperature, and gap conductance evolution versus burn-up for (a) AC and (b) HC reference case.

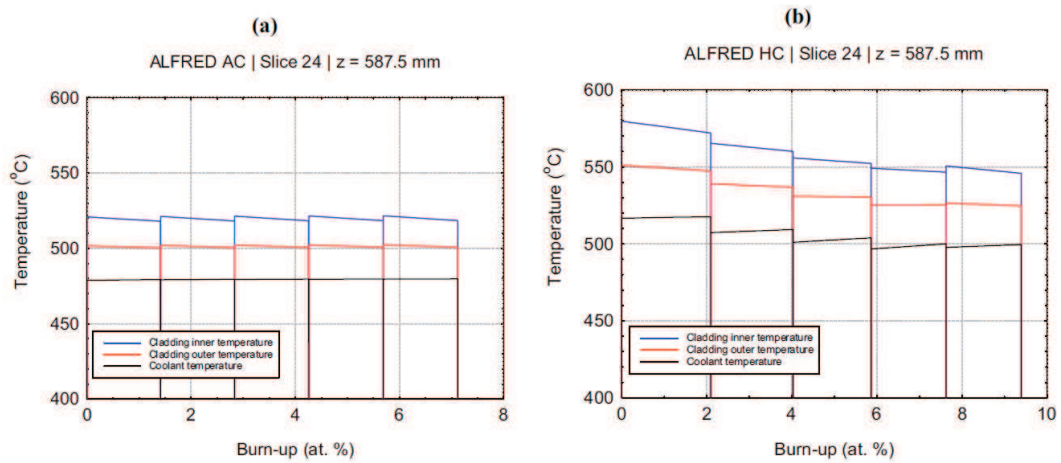


Figure 8: Coolant and cladding temperature evolution for (a) AC and (b) HC reference case.



2.3.2 Fission gas release

The integral Fission Gas Release (FGR) is of 32% for the AC and 32.4% for the HC. The fractional FGR along with the pin internal pressure is shown in Figure 9. The fractional FGR is the fraction of fission gas released with respect to the quantity produced, in each time step. Due to the fuel higher temperature, the fractional FGR in the hot channel is greater compared to the average channel, reaching 70% at 2% at. burn-up. Moreover, the peak in fractional FGR is in agreement with gap conductance evolution. The relative small amount of the fission gas released limits the value of the internal pressure, which remains below the preliminary limit of the 5 MPa (Grasso et al., 2013), both in the AC and the HC situation.

The relative low values reached by internal pressure suggest a potential increase of the design initial helium filling pressure (fixed at 0.1 MPa), with a beneficial effect on the fuel temperature. This increase will be discussed in detail in Section 4.

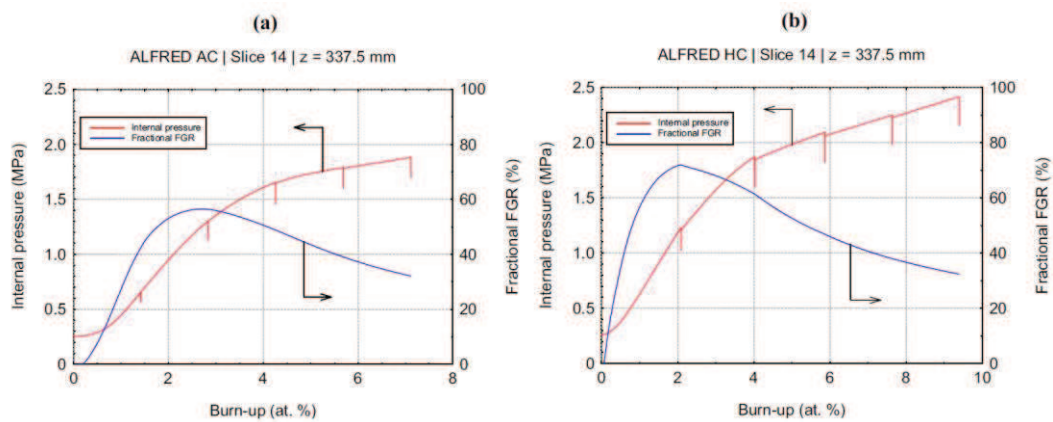


Figure 9: Fission gas release (FGR) and internal pressure as a function of burn-up for (a) AC and (b) HC reference case.



2.3.3 Gap dynamics

The evolution of the gap size, cladding and outer fuel radius are described for average and hot channel in Figure 10. The gap size dynamics is mostly driven by pellet deformation due to the progressive fuel swelling. In the average channel, the closure happens at a burn-up of 5 at. % (i.e., between the second and the third year of irradiation). On the other hand, the hot channel, which is subject to the higher linear heat rate, shows an anticipated gap closure at a burn-up of 4 at. % (i.e., at the end of the second year of irradiation). Consequently, a stronger Fuel Cladding Mechanical Interaction (FCMI) is observed in the hot channel, leading to the worsening of the clad performance (i.e., higher stress).

Being the gap dynamics basically driven by the fuel thermal expansion and fuel swelling strain, the models for fuel swelling and for fuel thermal conductivity assume a particular importance. Therefore, in Section 3, a sensitivity analysis will be performed focusing on these models.

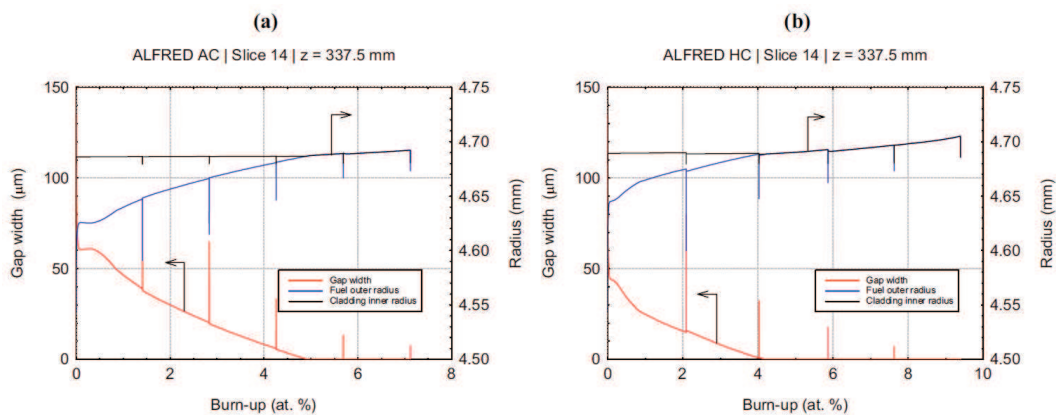


Figure 10: Cladding inner and fuel outer radius, and gap width evolution as a function of burn-up for (a) AC and (b) HC reference case.



2.3.4 Stress and strain in the cladding

The results of the mechanical analysis in terms of radially averaged cladding hoop stress during the irradiation are reported in Figure 11. No issues regarding the cladding stress are observed until the gap is open. In this situation, the only contributors are the internal pressure and the thermal stresses, which are both quite low. On the other hand, when the gap closes, the stress undergoes a sharp increase, reaching at the end of the irradiation 160 MPa and 430 MPa for the AC and the HC case, respectively. As expected, due to the anticipated gap closure, the cladding stress in the HC is much higher than the AC one, close to the yield strength. The stress relaxation due to thermal creep is not pronounced enough to completely avoid a little plastic strain, which is in any case very low. The high cladding stress is strictly related to the strain due to swelling and creep, occurring both in the fuel and in the cladding.

The main mechanical analysis result is that, in the hot channel, stress levels are high (whereas the average channel presents no issues). Particular attention has to be paid to this fact. Thermal creep strain, due to high stress induced by FCMI, could be a serious issue for the cladding. Therefore, it is necessary to perform a sensitivity analysis in order to find out the worst case and to give feedbacks on the design, trying to improve the safety limits of the fuel pin.

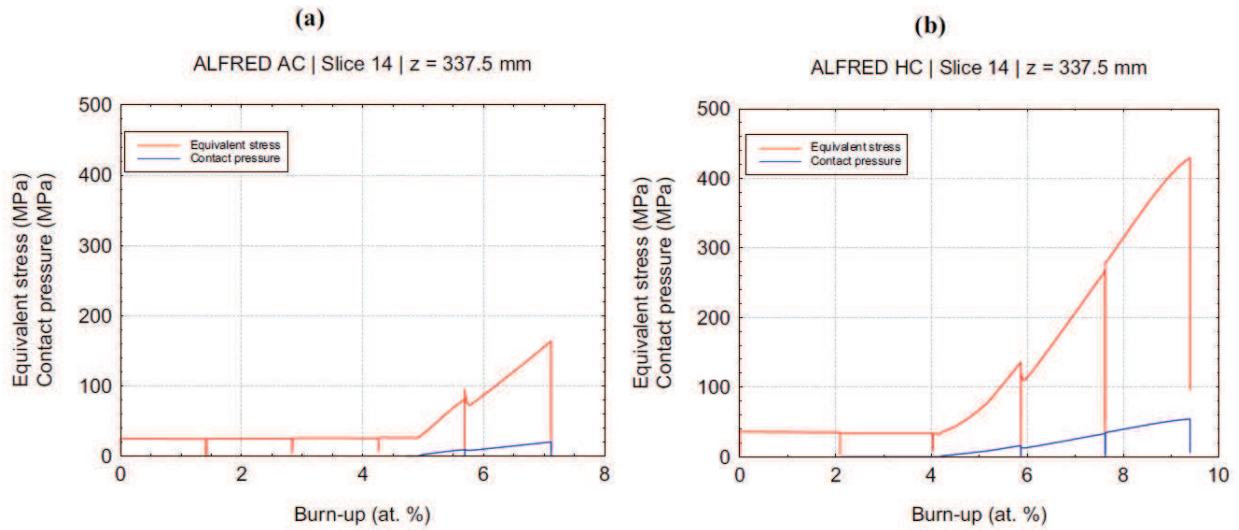


Figure 11: Contact pressure between fuel and cladding along with the radially averaged equivalent stress in the cladding for (a) AC and (b) HC reference case.



2.4 Closing remarks

The results of the simulation of ALFRED reference case present some peculiar aspects, which are summarized hereinafter. In Table 6, the main quantities of interest are shown. First of all, the temperature levels in the HC are not acceptable. The fuel inner temperature in the HC hot spot is 500°C below the melting point, but above the preliminary limit proposed of 2000°C (Grasso et al., 2013). Design-based ways to reduce the inner fuel temperature are proposed in Section 4. The cladding outer temperature is below the preliminary limit of 550°C (Grasso et al., 2013) set to contain lead corrosion of the cladding steel. Secondly, the gap closure dynamics is driven by the fuel pellet volume growth, due to swelling and thermal expansion. When the gap closes, the mechanical interaction between fuel and cladding increases the stress level in the cladding. In any case, the stress level in the cladding leads to strains well below the design limits. It is important to underline that the safety issues arise only in the HC. In fact, the AC fuel temperature is very low compared to the limit of 2000°C. Moreover, also the FCMI is weak in the AC, leading to low cladding strain.

Table 6: Summary of ALFRED reference case results at EoL.

	AC	HC
Fission gas released fraction (%)	32	32.4
Maximum burn-up (at. %)	8.04	11.2
Effective cladding swelling strain (%)	0.020	0.024
Effective cladding thermal creep strain (%)	1.8 10 ⁻⁵	0.086
Effective cladding irradiation creep strain (%)	5.05 10 ⁻⁴	8.84 10 ⁻⁴
Effective cladding plastic strain (%)	0	1.07 10 ⁻³
Maximum fuel temperature (°C)*	1810	2184
Maximum cladding temperature (°C)*	497	551
Inner gas pressure (MPa)	1.70	2.41
CDF (/)	0.000	0.047

*The maximum temperature occurs during the first batch (Figure 8).



(this page is intentionally left blank)



3. Sensitivity analysis

The uncertainties in some critical models defining the reference case for the ALFRED average and hot channel have to be handled by a sensitivity analysis. The goal of this analysis is the definition a worst case scenario, focusing on ALFRED hot channel conditions. On the basis of this worst case scenario, it is possible to suggest some feedbacks for the ALFRED fuel pin design.

3.1 Models considered

The main criticalities concerning ALFRED hot channel fuel pin are the high fuel temperature and the strong FCMI. Therefore, the models governing the gap dynamics and the fuel conductivity assume a particular importance in controlling the stress level both from the mechanical and thermal point of view. This fundamental statement comes directly from the discussion of the reference case results, which has been presented in the previous Section.

Among these models, three are affected by a significant uncertainty: fuel swelling, fuel thermal conductivity, and the cladding swelling. Brief details about each of these models are given in the following. One key parameter is also affected by great uncertainty, the fast neutron fluence. This parameter is fundamental because it affects the cladding swelling strain.

3.1.1 Fuel swelling model

The fuel swelling is the main responsible of the gap closure. There are two main models implemented in TRANSURANUS for the fuel swelling in MOX fuels. The one used in the reference case imposes 1.2% swelling strain per at. % burn-up, when the gap is open (Preusser and Lassmann, 1983). The other one, which is considered by the sensitivity analysis, imposes 2.0% swelling strain per at. % burn-up (Pesi et al., 1987). With closed gap, both the models impose a 0.065% swelling strain per at. % burn-up. It is important to notice that both these models are empirical, based on the results of experiments. They calculate the fuel swelling only as a function of atomic burn-up, not considering temperature and fluence dependences. This is a very important



point, because implies that the fuel swelling model is independent from the other models considered in this sensitivity analysis.

3.1.2 Fuel thermal conductivity model

The fuel thermal conductivity model is fundamental because it governs the fuel temperature level. This determines the fuel thermal expansion (which, together with the fuel swelling, governs the gap closure) and the fuel temperature margin towards the melting point. The two models implemented in TRANSURANUS for MOX fuel differ in quantifying the deterioration of the fuel thermal conductivity due to burn-up effects, such as fission gas accumulation. The one used in the reference case considers very slight burn-up worsening in the fuel conductivity (Philipponneau, 1992). The other one, used in this sensitivity, leads to lower thermal conductivity values at high burn-ups (Carbajo et al., 2001). For more details about the available models for MOX thermal conductivity, see Luzzi et al. (2014).

3.1.3 Cladding swelling model and fast neutron fluence

The cladding swelling models are discussed in detail in Luzzi et al. (2014). Briefly, there is a "AIM1" model based on the last cladding steel irradiated in PHENIX (i.e., AIM1), and a "15-15Ti" model considering an older cladding steel. It is important to highlight that these models strongly depend on the fast neutron fluence, for which two different energy thresholds between thermal and fast neutrons are considered, namely: 100 keV and 10 keV. In Table 7, a summary of the models considered in the reference case and in the sensitivity analysis is reported (the A and B notation is recalled in Figure 12).



Table 7: Models considered in the sensitivity analysis.

Model	Reference ("Option A")	Sensitivity ("Option B")
Fuel swelling	1.2% / at. % with gap open (Preusser and Lassmann, 1983)	2.0% / at. % with gap open (Pesi et al., 1987)
Fuel thermal conductivity	Philipponneau, 1992	Carbajo et al., 2001 (higher deterioration effects due to burn-up)
Cladding swelling	"AIM1"	"15-15Ti"
Fast neutron fraction	> 100 keV	> 10 keV

3.2 Worst case definition

The reference case representing ALFRED fuel pin has been defined always choosing the "best estimate" models. The goal of the sensitivity is the set-up of a worst case. The models and the parameters under discussion in this sensitivity analysis generate sixteen combinations. The groups introduced in the previous Section (fuel swelling, thermal conductivity, cladding swelling & fast neutron fluence) have the characteristic of being independent one from each other. The merit parameter chosen for this analysis is the Cumulative Damage Function (CDF) accounting for the cladding rupture time due to thermal creep. The choice of the CDF among the possible parameters can be justified reminding that the cladding is the first safety barrier of the pin and that the CDF is by definition a cumulate quantity, accounting for the entire power history. In Figure 12, the graph of the combinations of the sensitivity is reported, with the worst case highlighted. In Table 8, a summary of the models defining the worst case is reported.

Table 8: Models defining the worst case.

Model	Worst case choice
Fuel Swelling	Pesi et al., 1987 (B)
Fuel thermal conductivity	Carbajo et al., 2001 (B)
Cladding swelling	"AIM1" (A)
Fast neutron fraction	> 10 keV (B)

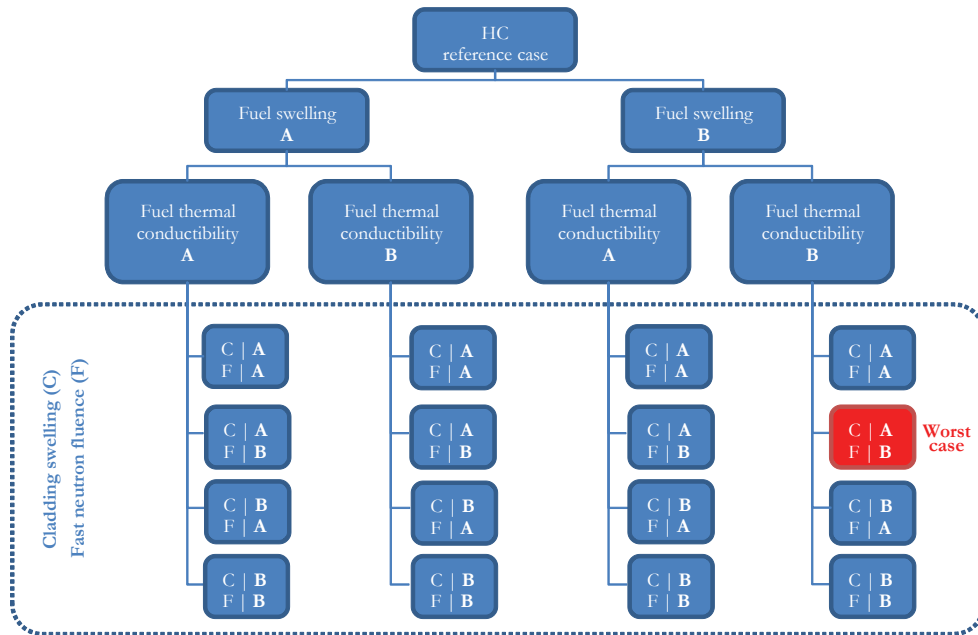


Figure 12: Graphical structure of the sensitivity analysis performed. The worst case corresponds to the fuel swelling model (option B) from Pesl et al. (1987), the fuel thermal conductivity model (option B) from Carbajo et al. (2001), the cladding swelling, C, model (option A) "AIM1" (Luzzi et al., 2014), and the fast neutron fluence, F, energy threshold (option B) >10 keV.



3.3 Worst case results

In this Section, we compare some quantities of interest for the fuel pin performance between the worst case (defined in the previous Section) and the HC reference case. The temperature in the fuel is a direct consequence of the thermal conductivity and the gap dynamics. From Figure 13 is clear that, when the gap is open, the temperature levels for the HC reference case are even higher than those achieved in the HC worst case. This is mainly due to the lower initial value of the fuel conductivity. The gap closure occurs earlier in the worst case, due to the enhanced swelling rate. The deterioration in the fuel thermal conductivity determines the higher temperature in the worst case after the gap closure. From roughly 3% of at. burn-up, the fuel inner temperature in the worst case is higher than in the reference case. At EoL (9.3% at.) the difference is of more than 500°C.

The stress in the cladding in the worst case is higher (Figure 14), due to anticipated and stronger FCMI. In the last batch, the thermal creep, with imposed strain, relaxes the stress level. The higher stress in the cladding is responsible of the higher thermal creep strain (Figure 15) (and CDF) in the worst case.



ALFRED HC | Slice 14 | z = 337.5 mm

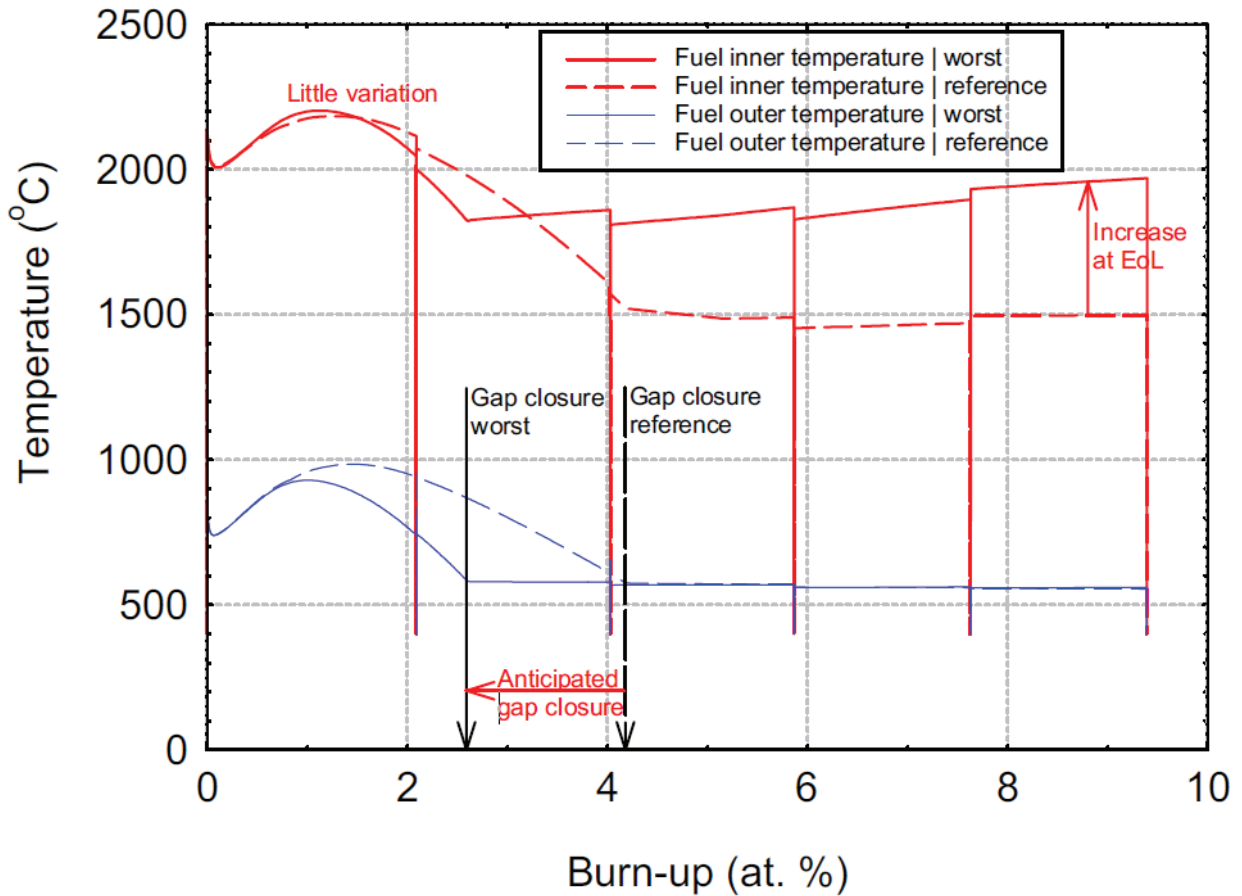


Figure 13: Comparison between ALFRED HC reference case and worst case: fuel temperature evolution.

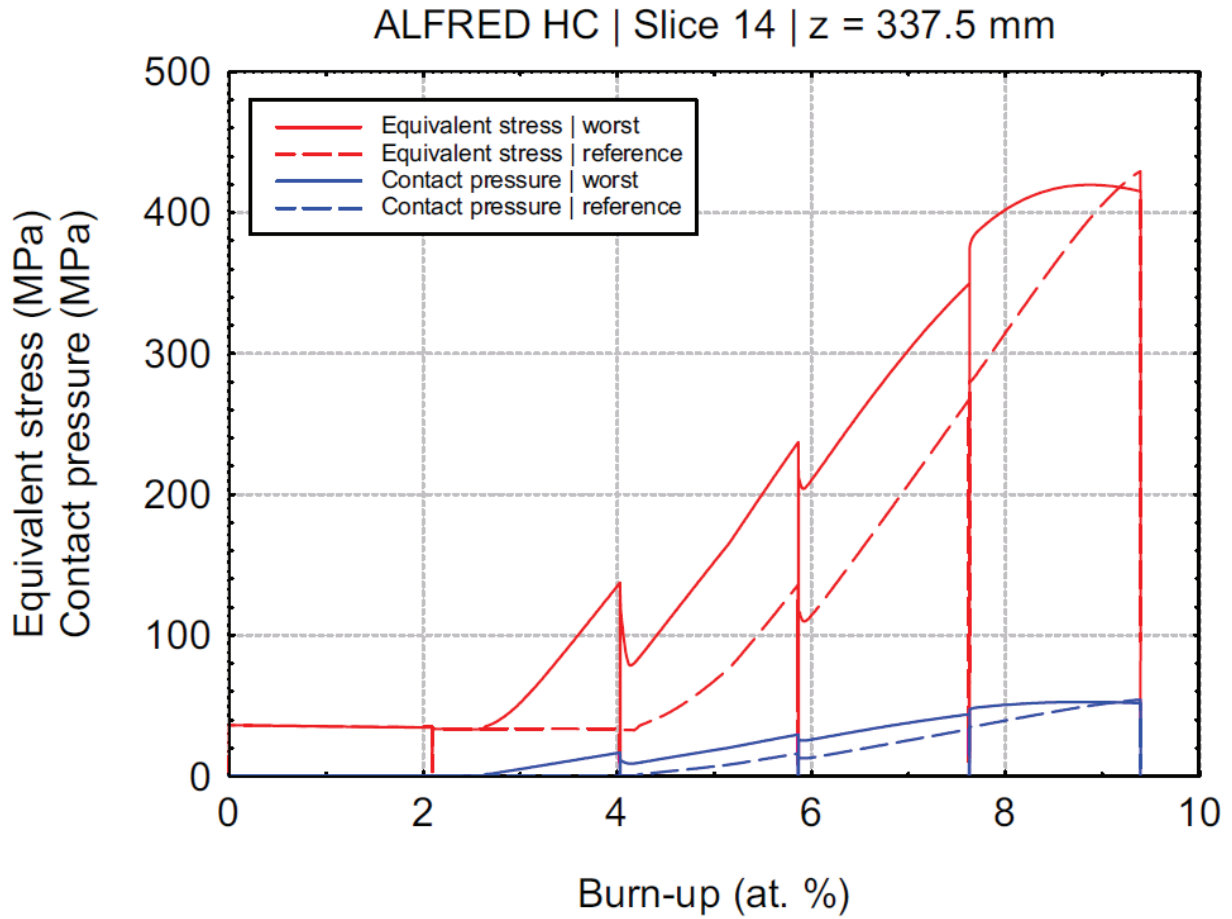


Figure 14: Comparison between ALFRED HC reference case and worst case: radially averaged equivalent stress in the cladding.

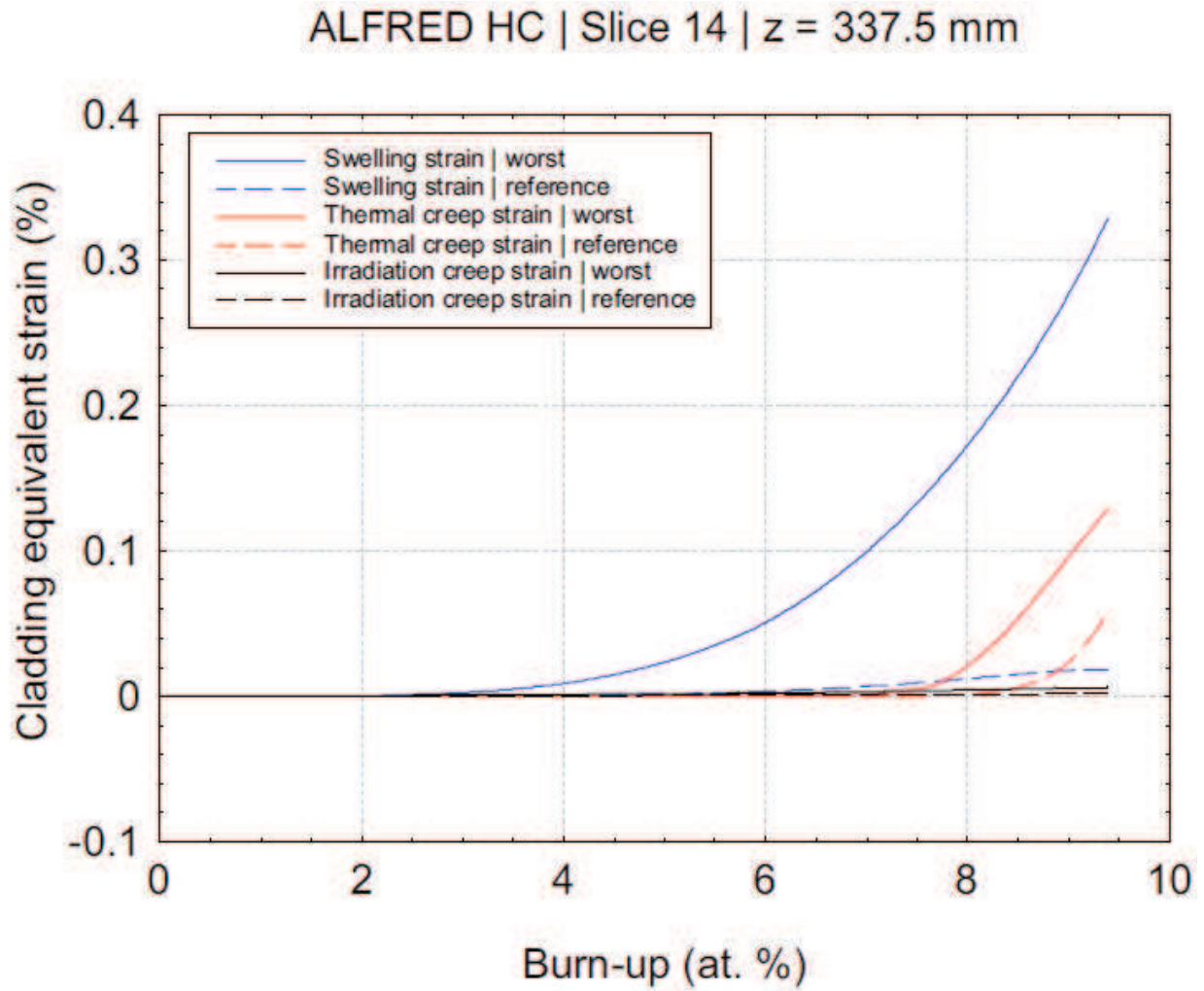


Figure 15: Comparison between ALFRED HC reference case and worst case: permanent strain components.



3.4 Closing remarks

In this Section, a sensitivity analysis on ALFRED HC has been carried out, focusing on the models governing the gap dynamics (i.e., fuel swelling, fuel thermal conductivity, cladding swelling and fast neutron flux). The result is the definition of a worst case for ALFRED fuel pin performance analysis. In Table 9, the main results of this scenario (for both AC and HC) are listed and compared with the HC reference case. The worst case presents both higher cladding strains (even if below the design limits) and higher fuel inner temperature (above 2200°C, with the limit fixed at 2000°C). In the following Section, changes to ALFRED fuel pin design are suggested, in order to reduce the HC fuel temperature to acceptable values.

Table 9: Summary of worst case and reference case numerical results at EoL.

	Worst case (AC)	Worst case (HC)	Reference case (HC)
Fission gas released fraction (%)	31	40.9	32.4
Maximum burn-up (at. %)	8.0	11.2	11.2
Effective cladding swelling strain (%)	0.26	0.35	0.024
Effective cladding thermal creep strain (%)	1.85 10 ⁻⁵	0.135	0.086
Effective cladding irradiation creep strain (%)	1.15 10 ⁻³	1.96 10 ⁻³	8.84 10 ⁻⁴
Effective cladding plastic strain (%)	0	2.62 10 ⁻²	1.07 10 ⁻²
Maximum fuel temperature (°C)*	1816	2201	2184
Maximum outer cladding temperature (°C)*	497	551	551
Inner gas pressure (MPa)	1.86	2.97	2.41
CDF (/)	0.000	0.081	0.047

* The maximum temperature occurs during the first batch.



(this page is intentionally left blank)



4. Feedbacks on ALFRED fuel pin design

In this Section, starting from the worst case results, preliminary design feedbacks are suggested. The aim of these feedbacks is to improve the fuel pin safety. In this work, only minor design changes have been considered, in order to not cause major changes in the current thermal-hydraulic and neutronic design. Therefore, three parameters of the fuel pin have been selected among the others: the initial gap width, the initial internal helium pressure, and the upper plenum height.

It is hard to predict the impact of a slight change in these parameters. Integral fuel rod performance analysis via TRANSURANUS is necessary. A set of configurations is simulated, combining different values of these design parameters. The results are condensed in a graphical way, in order to choose the best configuration, from a safety point of view. The limits considered in this analysis are the same preliminary design indications discussed in the Section 2.3 (Table 5).

4.1 Design variables

Three parameters have been selected in this analysis: the gap width, the initial internal helium pressure, and the upper plenum height (reported with their symbols in Table 10). The main advantage in these parameters is that the general thermal-hydraulic and neutronic design of the core is not altered by a slight variation of them.

In this Section, the rationale of the choice of these parameters is explained. The main issues in the ALFRED HC fuel pins are the high fuel temperature and the high stress in the cladding, when the gap is closed. In particular, the stress in the cladding is combined with a cladding temperature level that leads to considerable thermal creep rates. The creep mechanism with closed gap (therefore with imposed strain) is so that the stress in the cladding is actually relaxed by the thermal creep. To contain the stress in the cladding is fundamental to reduce the mechanical interaction between the fuel and the cladding. This can be achieved with a slight increase in the initial gap width. The result is a delay in the gap closure and an increase in the fuel temperature.



The increase in the fuel temperature, caused by the gap conductance decrease, can be contrasted by an increase in the helium filling pressure, which goes in the direction of increasing the gap conductance. Moreover, the pollution of the gap filling gas, due to the release from the fuel of gaseous fission products, and the internal pressure increase, can be limited by an increase in the upper plenum height.

A subset of the preliminary limits introduced in Table 5 are used in the following, in order to compare different configurations. These limits are summarized in Table 11. They have been selected among the others because of their consistency with the results of the reference case simulations. In order to properly compare different limits, normalized figures of merit are defined in Table 12.

Therefore, each configuration is represented by a set of three numbers (the values of the design parameters). A set of five numbers (the limit-normalized figures of merit) corresponds to every configuration. The configuration is considered acceptable if all the limit-normalized figures of merit are below unity (< 1). For example, a configuration Γ can be (according to the notation defined in Table 10 and Table 12):

$$\Gamma: [g_0; p_{int,0}; h_{up,0}] \rightarrow [\vartheta; \pi; \tau; \kappa; \delta] \quad (11)$$

In the following, different configurations are compared in a graphical way. The goal is to choose the configuration (i.e., the value of the design variables) that minimizes the limit-normalized quantities. Clearly, the main objective is the reduction of the fuel inner temperature, the only quantity of interest above the preliminary limits already in the HC reference case (Figure 7).



Table 10: ALFRED fuel pin design parameters considered.

Design parameter	Symbol	Unit
Initial gap width	g_0	(μm)
Initial internal filling pressure	$p_{int,0}$	(MPa)
Upper plenum height	$h_{up,0}$	(mm)

Table 11: Limits considered.

Fuel rod limits (maximum)	Symbol	Limit assumed
Fuel temperature	T_{lim}	2273 K (2000°C)
Internal pressure	p_{lim}	5 MPa
Thermal creep strain in the cladding	$\epsilon_{th,lim}$	0.2%
CDF in the cladding	CDF _{lim}	0.20
Plastic strain in the cladding	$\epsilon_{p,lim}$	0.5%

Table 12: Limit-normalized figures of merit.

Normalized quantity	Symbol	Definition
Fuel temperature	θ	T/T_{lim} (K K ⁻¹)
Internal pressure	π	p/p_{lim}
Thermal creep strain in the cladding	τ	$\epsilon_{th}/\epsilon_{th,lim}$
CDF in the cladding	κ	CDF/CDF _{lim}
Plastic strain in the cladding	δ	$\epsilon_p/\epsilon_{p,lim}$



4.2 Improved design case definition

In this Section, different configurations are compared. The results of each simulation are condensed in the values of five figures of merit, defined in Table 12. Kiviat's diagrams (also known as radar plot) are used in the following to represent the five-dimensional space of the limit-normalized figures of merit.

Eighteen configurations have been analyzed. The configuration are generated by the combination of the values assumed by the design variables. In Table 13, the range of variation of these parameters are reported.

The configuration [150; 120; 0.1] corresponds to the design values adopted in the fuel pin performance analysis of both the reference and the worst case, and is therefore called "standard design" configuration. The increase in the gap width is realized moving outward the cladding, without changing the cladding thickness and the fuel pellet geometry.

In Figure 16, the Kiviat's diagram for six configurations with gap equal to 150 micron (i.e., [150; h_{up} ; p_{int}]) is shown. Each configuration is represented by a polygon. The Kiviat's diagram allows visualizing graphically and quantitatively the consequence on the fuel pin safety caused by a change in the design parameters. From Figure 16, the influence of initial helium filling pressure and initial upper plenum height can be investigated.

Table 13: Range of variation of ALFRED fuel pin design parameters.

Design parameter	Range of variation
g_0 (μm)	{150; 175}
$h_{up,0}$ (mm)	{120; 180; 240}
$p_{int,0}$ (MPa)	{0.1; 0.3; 0.5}



On the one hand, it is clear that the most constraining limit is the inner fuel temperature. The design configuration is unacceptable for this limit, reaching a peak of 2200°C. The increase in the filling gas quantity and density, obtained increasing respectively the upper plenum height and the initial helium filling pressure, is quite efficient in reducing the fuel temperature. On the other hand, the quantitative analysis of the thermal creep in the cladding is encouraging. The CDF value is far from the limits suggested. The thermal creep strain is also well below the design limit.

An increase in the He filling pressure reduces the safety margin respect to each considered limit, except for the inner fuel temperature. The upper plenum height increase enhances the safety margins for both the mechanical properties of the cladding and for the inner fuel temperature.

In Figure 17, configurations with the same upper plenum height, but different initial gap width and internal filling pressure are compared. The emerging trend is that the initial gap width increase causes an increase in the inner fuel temperature and a decrease in the strains in the cladding. But, being the fuel temperature the limiting figure of merit, an increase in the gap width is not easy to pursue.

In the Figure 18, the "temperature optimum" configuration is shown. This configuration maximizes the safety margin with respect to inner fuel temperature keeping acceptable values with respect to the other limits considered in this work. To obtain this optimum configuration, it is enough to increase the initial helium filling pressure from 0.1 MPa to 0.5 MPa. Of course, this optimum configuration depends on the above discussed specific choices made both in terms of design variables and of figures of merit. The changes induced in both average and hot channel adopting these design configuration are discussed in the following Section.

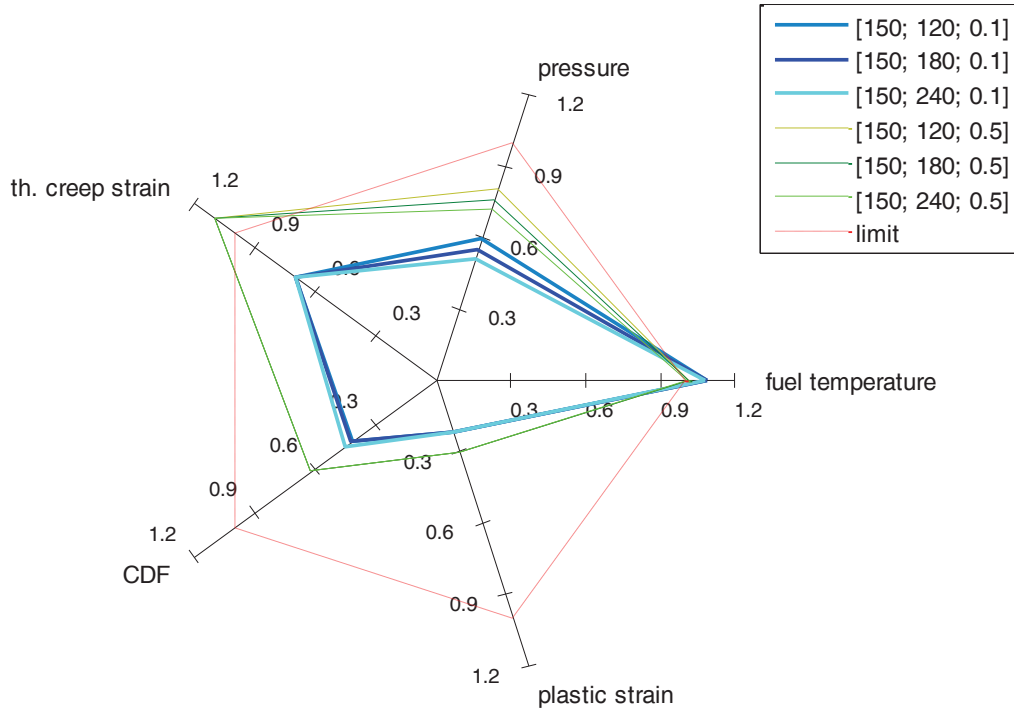


Figure 16: Kiviat's diagram comparing configurations with initial gap width of 150 micron. The comparison is based on the limit-normalized figures of merit important for a safety point of view (HC worst case models).

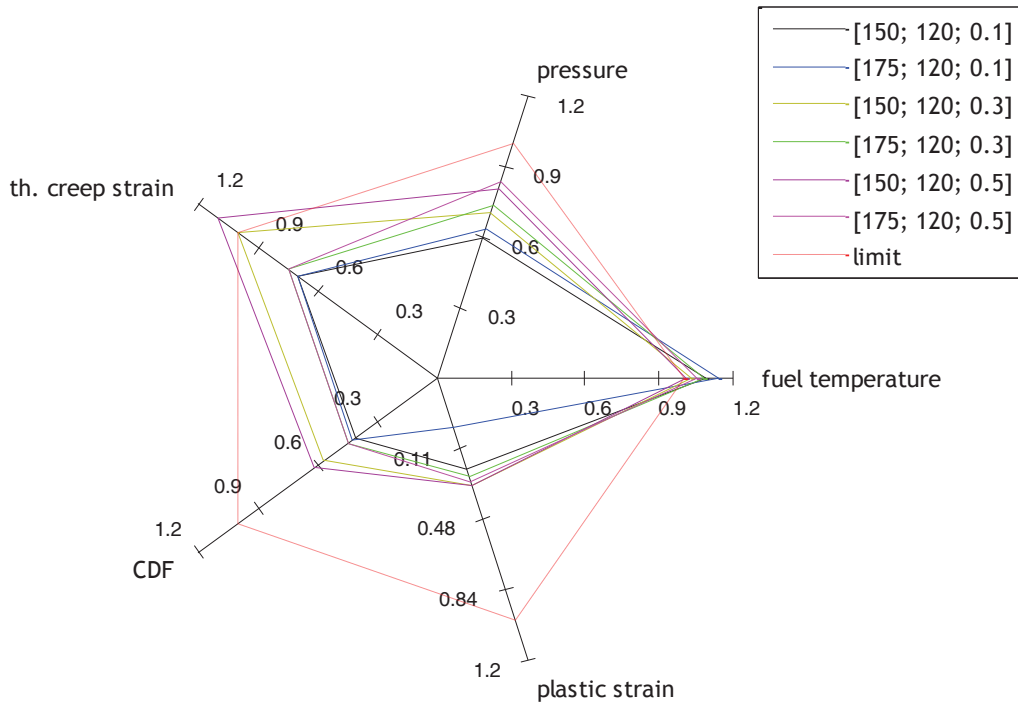


Figure 17: Kiviat's diagram showing initial gap width influence on ALFRED fuel pin performance, at different levels of initial internal pressure (HC worst case models).

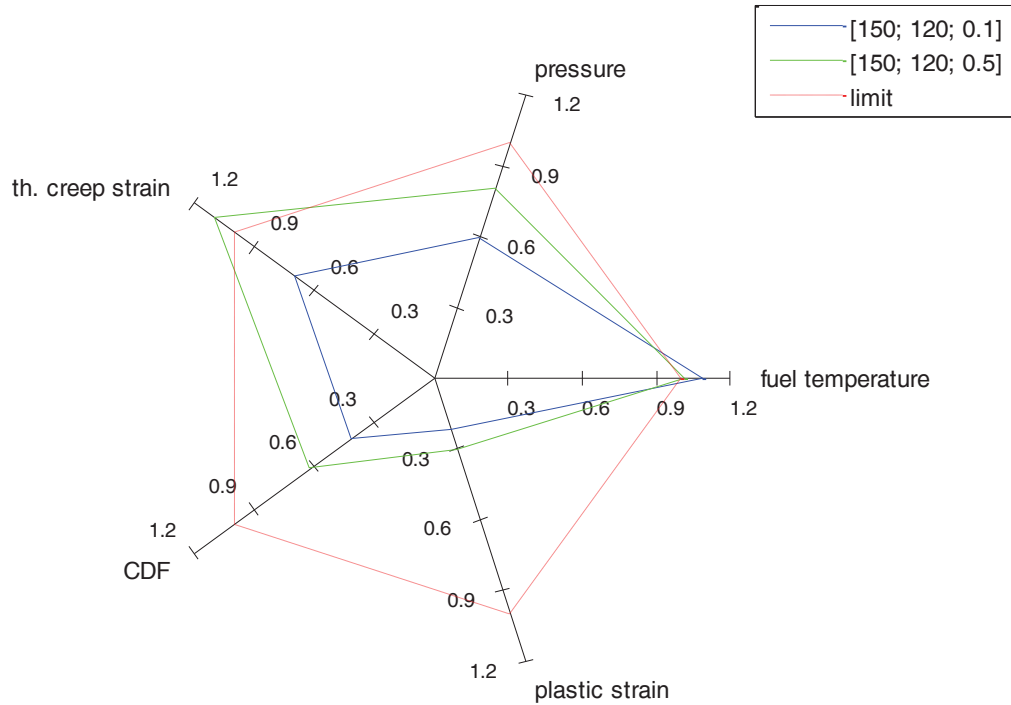


Figure 18: "Temperature optimum" configuration compared with the basic design configuration (HC worst case models).



4.3 Improved design case results

The "temperature optimum" configuration achievable through safety-oriented design is the one which minimizes the fuel inner temperature, respecting all the other limits (applying the models characterizing the reference case, both AC and HC). This objective is obtained with the combination of initial gap width, initial upper plenum height and initial helium filling pressure reported in Table 14. It is important to notice that only the initial filling pressure value changes from ALFRED reference design, causing only slight changes in the general design of the reactor.

In this Section, ALFRED reference and optimum design are compared. In Figure 19, the effect of an initial filling pressure increase on fuel temperature evolution is plotted, respectively for average and hot channel. The benefic effect on the fuel temperature is evident. It is also clear that this gain is not free of charge: the stress level in the cladding is increased and therefore, the thermal creep is more incisive. Nevertheless, the mechanical quantities are still well below the limits discussed in Section 2.

Table 14: ALFRED "temperature optimum" design configuration.

Design parameter	"Standard design"	"Temperature optimum"
Initial gap width (μm)	150	150
Initial plenum height (mm)	120	120
Initial filling pressure (MPa)	0.1	0.5

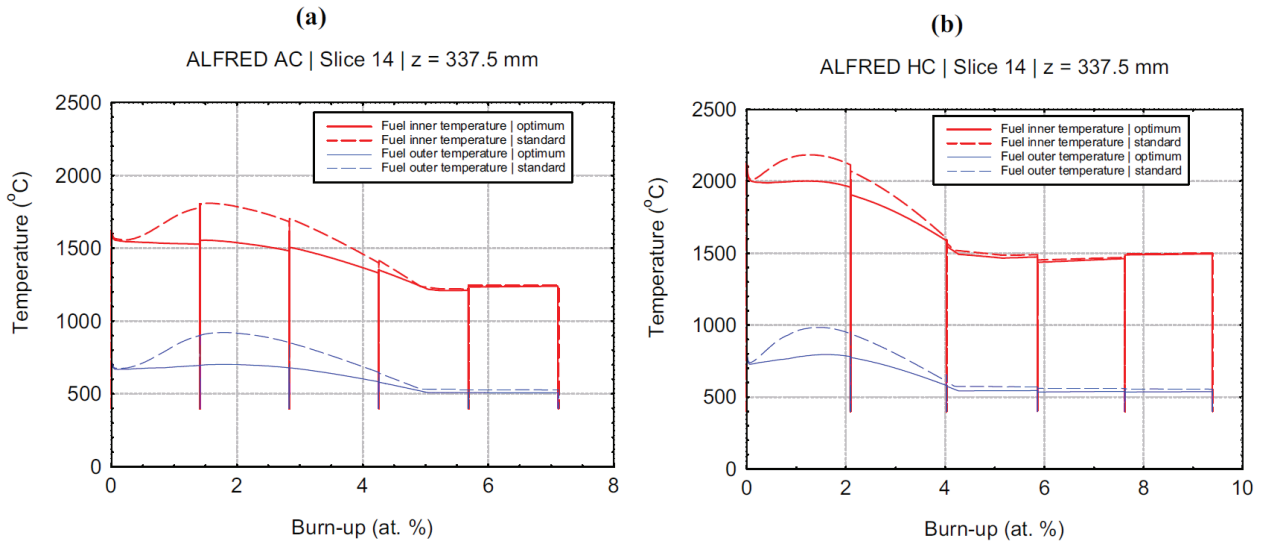


Figure 19: Inner and outer fuel temperature evolution versus burn-up: comparison between the reference and the optimum case for (a) AC and (b) HC reference case., an axial section of ALFRED fuel pin is sketched.

A 5-batches cycle without reshuffling with a five year fuel residence time is expected, i.e., 365 Equivalent Full Power Days (EFPD) per cycle for a total of 1825 EFPDs. The refueling time between two cycles is foreseen to last about 15 days (Grasso et al., 2013). In Table 1 and Table 2, the main fuel pin parameter are presented.

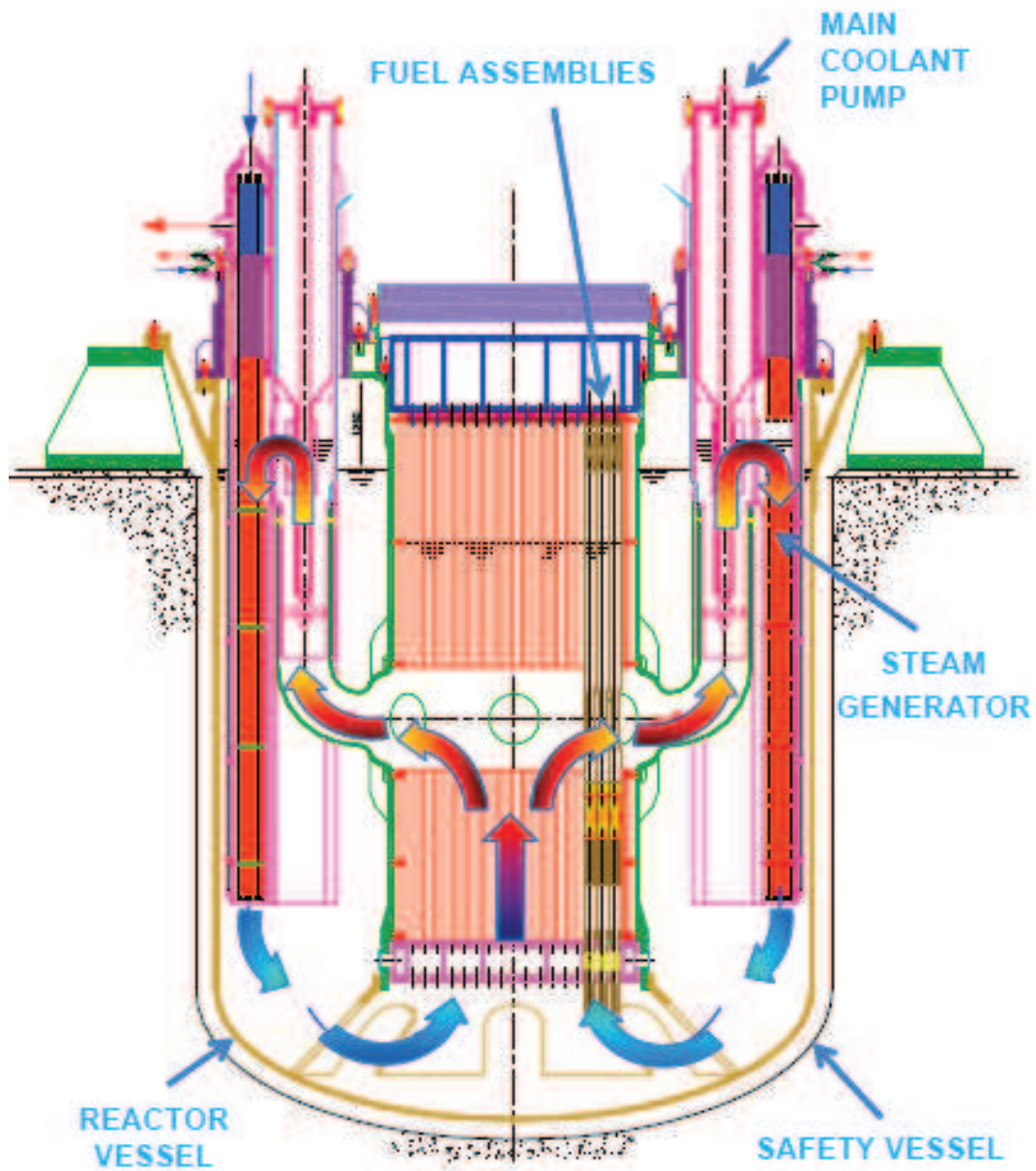


Figure 3: ALFRED reactor primary system.



Table 1: ALFRED reactor specifications.

Reactor specification	
Thermal power (MW)	300
Fuel residence time (years)	5
Coolant inlet temperature (°C)	400
Average coolant outlet temperature (°C)	480
Coolant mass flow rate (kg s ⁻¹)	≈ 25700
Average coolant velocity (m s ⁻¹)	≈ 1.4

Table 2: ALFRED fuel pin design parameters at Beginning of Life (BoL).

Fuel pin design specification	
Fuel type	MOX
Cladding	AIM1
Coolant	Lead
Enrichment as Pu/(Pu+U) (wt. %) (inner zone)	21.7
Enrichment as Pu/(Pu+U) (wt. %) (outer zone)	27.80
Fuel density (% theoretic density)	95
O/M (/)	1.97
Filling gas	He
Initial filling pressure (MPa)	0.1
Upper plenum volume (mm ³)	≈ 30000
Upper plenum length (mm)	120
Active length (mm)	600
Lower plenum length (mm)	550
Cladding outer diameter (mm)	10.5
Cladding inner diameter (mm)	9.3
Fuel pellet outer diameter (mm)	9
Fuel pellet inner diameter (mm)	2
Initial fuel-cladding gap width (µm)	150
Pin pitch (mm)	13.86

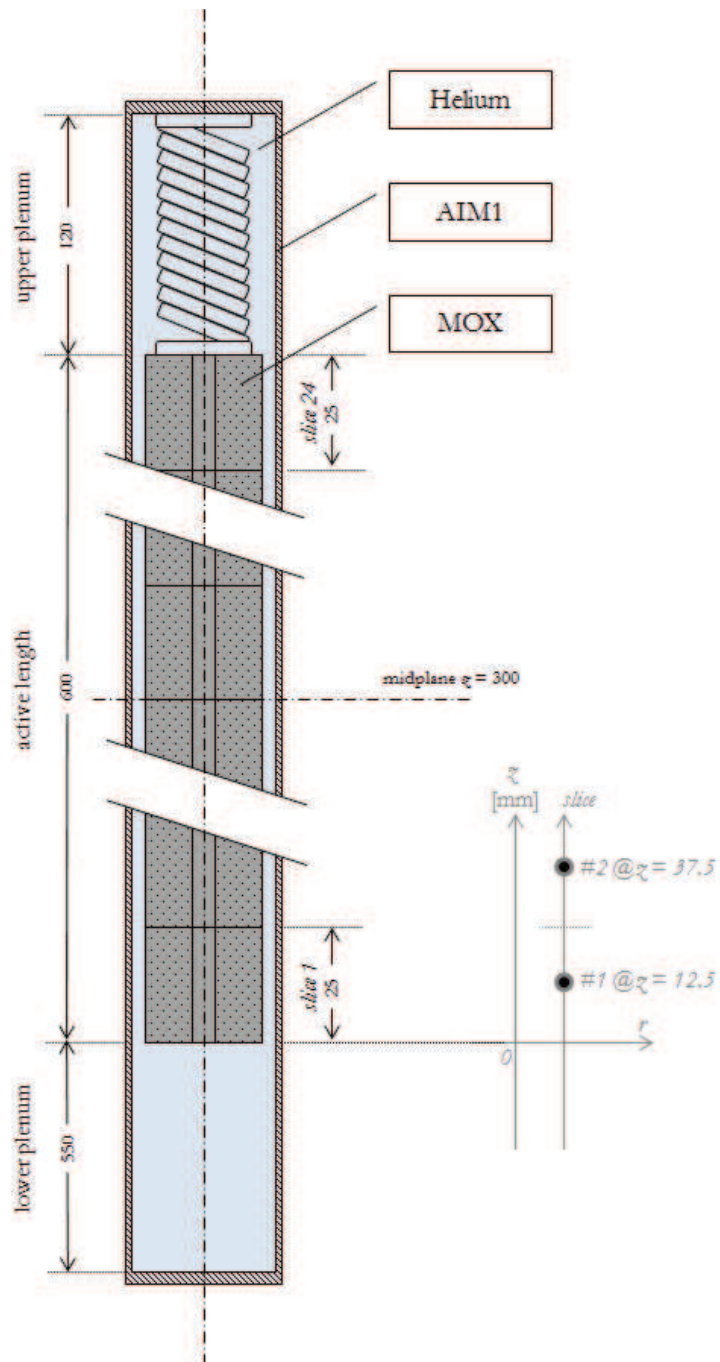


Figure 4: ALFRED fuel pin axial section (not in scale).

2.2 Reference case definition

The in-reactor life of a fuel pin is characterized by the interaction between many different phenomena. The properties of fuel and cladding, the position of the pin in the core, the power and irradiation history, all interact in determining the fuel pin general performance.

2.2.1 Selection of average and hot channel

We considered two different coolant channels of the ALFRED reactor, i.e., the Average Channel (AC) representative of the average conditions among the fuel pins, and the Hot Channel (HC) representative of the most critical conditions achieved in the core in terms of power history. These two channels are graphically represented in Figure 5.

The AC is defined as the triangular channel placed in a generic sub-assembly and it is characterized by a reactor average linear power, constant along the five irradiation years. The HC is a triangular channel as well, being the most close to the core center between the more enriched pins (outer zone). Actually, the corner channel is difficult to be modeled in TRANSURANUS, because the bypass flow between two FAs has not been determined already in the ALFRED design. Therefore, the immediately adjacent channel has been chosen. This channel is characterized by practically the highest linear power, which decreases from the Beginning of Life (BoL) to the End of Life (EoL).

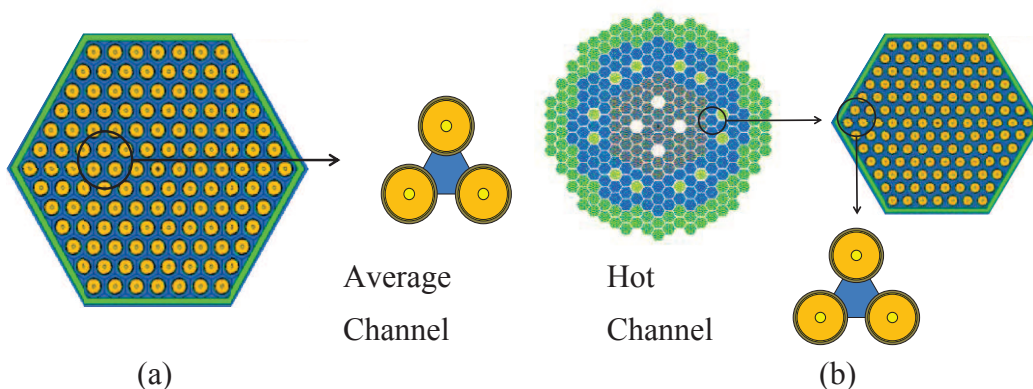


Figure 5: Graphical representation of the position of the AC (a) and the HC (b) within ALFRED core.



In Table 3 and Table 4, the main parameters of the AC and HC modelling are presented. Neutronic analysis of the ALFRED fuel pin has been carried out by means of the SERPENT code (Aufiero, 2013; SERPENT, 2011), which is able to calculate the one-group neutron cross sections and fast fluence to be provided to TRANSURANUS. In particular, the fast fraction of the neutron flux is crucial for the determination of the irradiation damage dose on the materials (e.g., related to swelling and irradiation creep). The flux changes over a batch, leading to different values at Beginning of Cycle (BoC) and at End of Cycle (EoC). These values are also affected by large discrepancies, namely: (i) the threshold above which neutrons are considered fast enough to produce damage; (ii) the conversion factor between fluence and displacement per atoms which is usually adopted in the correlations. These discrepancies will be taken into account in the sensitivity analysis.

Table 3: Main parameters of ALFRED AC and HC modeling.

	AC	HC
Pin power (kW)	12.9	17.7
Lead mass flow rate (kg s ⁻¹)	1.14	1.14
Burn-up (at. %)	7	9.5
Axial peak factor (BoC)	1.16	1.20
Axial peak factor (EoC)	1.13	1.13
Total flux (n cm ⁻² s ⁻¹)	1.53 10 ¹⁵	1.60 10 ¹⁵
Fast Flux (> 100 keV) (n cm ⁻² s ⁻¹)	0.47 10 ¹⁵	0.51 10 ¹⁵
Fast Flux (> 10 keV) (n cm ⁻² s ⁻¹)	0.93 10 ¹⁵	1.00 10 ¹⁵



Table 4: Summary of ALFRED main parameters for heat exchange. Every quantity is referred to the average channel AC at BoC.

ALFRED heat exchange parameters	
Lattice pitch, p (mm)	13.86
Rod outer radius, D/2 (mm)	5.25
p/D (/)	1.32
Mass flow per pin (kg s^{-1})	1.15
Linear power (kW m^{-1})	21.4
Lead velocity (m s^{-1})	1.37
Coolant area (mm^2)	79.77
Re	68269
Pr	0.0175
Pe	1192
Nu	16.72
Heat transfer coefficient ($\text{kW m}^{-2} \text{K}^{-1}$)	29.47



2.2.2 Power history and axial profile

The power history used in this work is based on a calculation performed by means of the deterministic ERANOS code. This power history is calculated simulating a five year cycle with five refueling phases. This leads to a decreasing power of the hot channel from one batch to the other, as is shown in Figure 6. For the average channel, a constant value along the five years is calculated. For both the channels, the shutdown lasts one hour, followed by a refueling period of 15 days and a start-up of 10 hours¹ (Grasso et al., 2013). In Figure 6, the axial profiles for AC and HC calculated by means of SERPENT are shown. Another option for the power history has been calculated by means of a Monte Carlo (MCNP) code at ENEA (Petrovich et al., 2012). This simulation gives a constant value also for the HC (averaged between the second and the third year), being less appropriate in describing the HC fuel performance.

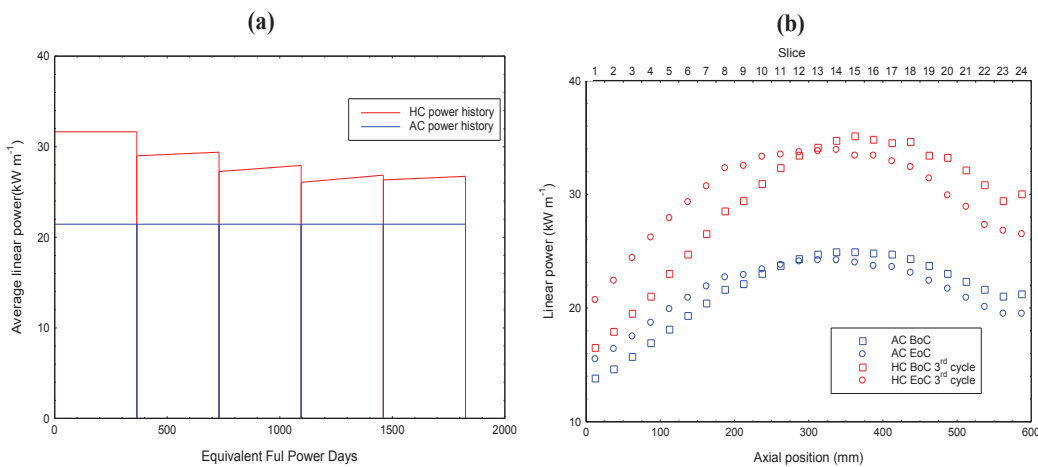


Figure 6: Power histories for ALFRED average and hot channel as a function of EFPD (a) and axial position (b).

¹ The time duration of shutdown and startup are set to limit temperature gradients in the materials. Of course, longer times can be chosen. In principle, fuel performance should depend also on these periods and a sensitivity on them can be a further development. Few preliminary analyses have been carried out in this direction, actually showing very limited impact on the fuel pin behavior.



2.2.3 Material properties

It is out of the scope of this work to present in detail the material properties available in the LFR-oriented version of TRANSURANUS. An extensive and careful review of the material properties applied in this analysis can be found in Luzzi et al. (2014). For the modelling of the MOX fuel, reference correlations can also be found in Lassmann et al. (2013).



2.3 Reference case results

In this Section, the main results of the analysis of the reference case simulation are presented. AC and HC are here always analyzed in parallel, in order to properly point out peculiarities. These results are fundamental for the selection of the models on which the sensitivity analysis is performed. The discussion of the results is organized in order to progressively check the preliminary design limits suggested in literature for ALFRED. These preliminary limits are reported in Table 5.

All the limits reported have been found in literature. They have to be intended as preliminary indications, useful in the phase of ALFRED conceptual design. Final design limits may be different. As an example, the limit of 550°C for the peak cladding temperature, set against lead corrosion, depends on the coating material, which is still under development. The discussion of the results for the reference case is divided in four sub-sections: fuel and cladding temperature (2.3.1), fission gas release (2.3.2), gap dynamics (2.3.3), stresses and strains in the cladding (2.3.4).

Table 5: Preliminary design limits for ALFRED and LFRs.

Limited quantity	Proposed limit	Reference
Peak fuel temperature	< 2000°C	Grasso et al., 2013
Peak cladding temperature	< 550°C	Grasso et al., 2013
Plenum pressure	< 5 MPa	Grasso et al., 2013
Cladding $\Delta D/D$	< 3%	IAEA, 2012
Cladding swelling strain	< 5%	NEA, 2005
Thermal creep strain (1)	< 0.2%	IAEA, 2012
Thermal creep strain (2)	< 1%	NEA, 2005
Total creep strain	< 3%	NEA, 2005
Cumulative damage function*	< 0.2-0.3	IAEA, 2012
Cladding plastic strain	< 0.5%	Vettraino and Luzzi, 2001

*The Cumulative Damage Function (CDF) is a pin lifetime parameter that considers the linear accumulation of the fraction damage calculated as ratio between the short time interval and the time-to-rupture (Luzzi et al., 2014).



2.3.1 Fuel and cladding temperature

Figure 7 shows the fuel temperature evolution during the irradiation for both the average and the hot channel, together with the evolution of the gap conductance. The maximum fuel temperature is located just above the mid-plane of the active length. For the average channel it is well below the limit (2000°C), reaching 1800°C after the first irradiation year. On the other hand, for the HC the maximum temperature is close to 2200°C and located in the middle of the first year cycle (i.e., 1% at. burn-up).

As far as the cladding and the coolant temperatures are concerned, the maximum temperatures are reached at the beginning of the irradiation, at the outlet of the active length (Figure 8). In addition, the limit on the outer cladding temperature is respected, reaching 550°C only at the beginning of the irradiation.

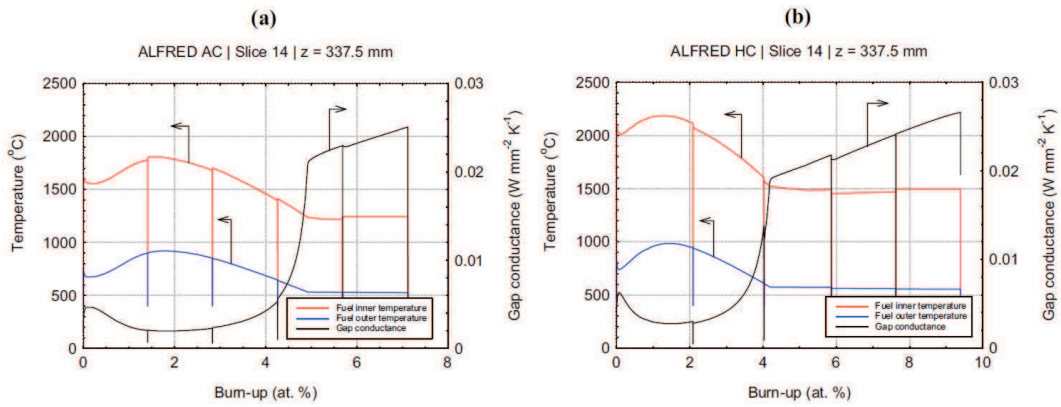


Figure 7: Inner and outer fuel temperature, and gap conductance evolution versus burn-up for (a) AC and (b) HC reference case.

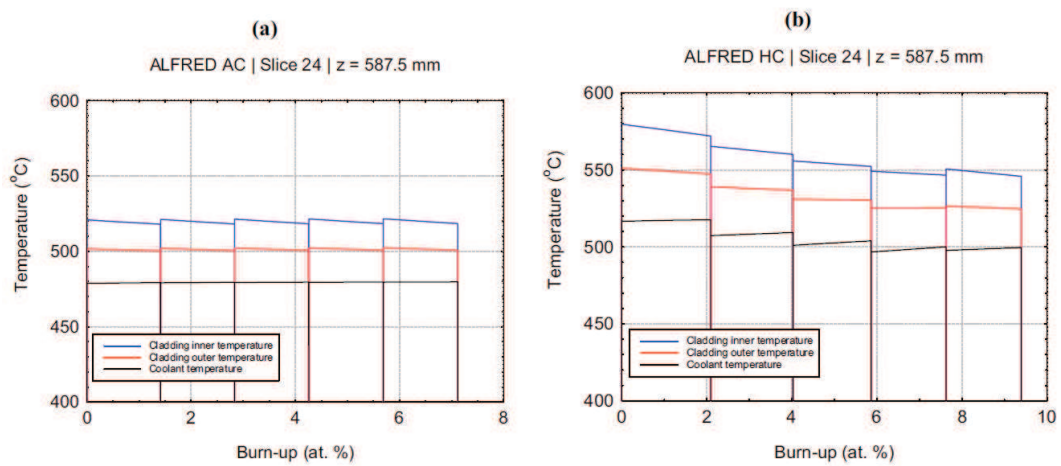


Figure 8: Coolant and cladding temperature evolution for (a) AC and (b) HC reference case.



2.3.2 Fission gas release

The integral Fission Gas Release (FGR) is of 32% for the AC and 32.4% for the HC. The fractional FGR along with the pin internal pressure is shown in Figure 9. The fractional FGR is the fraction of fission gas released with respect to the quantity produced, in each time step. Due to the fuel higher temperature, the fractional FGR in the hot channel is greater compared to the average channel, reaching 70% at 2% at. burn-up. Moreover, the peak in fractional FGR is in agreement with gap conductance evolution. The relative small amount of the fission gas released limits the value of the internal pressure, which remains below the preliminary limit of the 5 MPa (Grasso et al., 2013), both in the AC and the HC situation.

The relative low values reached by internal pressure suggest a potential increase of the design initial helium filling pressure (fixed at 0.1 MPa), with a beneficial effect on the fuel temperature. This increase will be discussed in detail in Section 4.

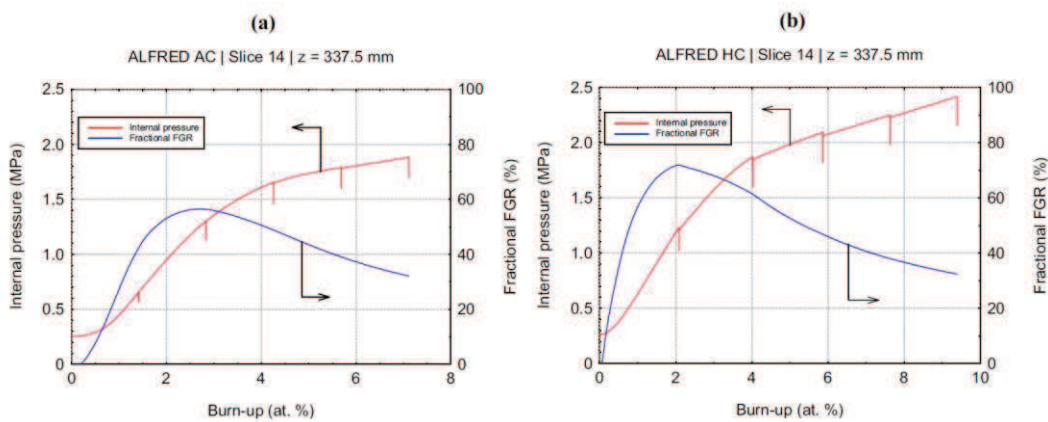


Figure 9: Fission gas release (FGR) and internal pressure as a function of burn-up for (a) AC and (b) HC reference case.



2.3.3 Gap dynamics

The evolution of the gap size, cladding and outer fuel radius are described for average and hot channel in Figure 10. The gap size dynamics is mostly driven by pellet deformation due to the progressive fuel swelling. In the average channel, the closure happens at a burn-up of 5 at. % (i.e., between the second and the third year of irradiation). On the other hand, the hot channel, which is subject to the higher linear heat rate, shows an anticipated gap closure at a burn-up of 4 at. % (i.e., at the end of the second year of irradiation). Consequently, a stronger Fuel Cladding Mechanical Interaction (FCMI) is observed in the hot channel, leading to the worsening of the clad performance (i.e., higher stress).

Being the gap dynamics basically driven by the fuel thermal expansion and fuel swelling strain, the models for fuel swelling and for fuel thermal conductivity assume a particular importance. Therefore, in Section 3, a sensitivity analysis will be performed focusing on these models.

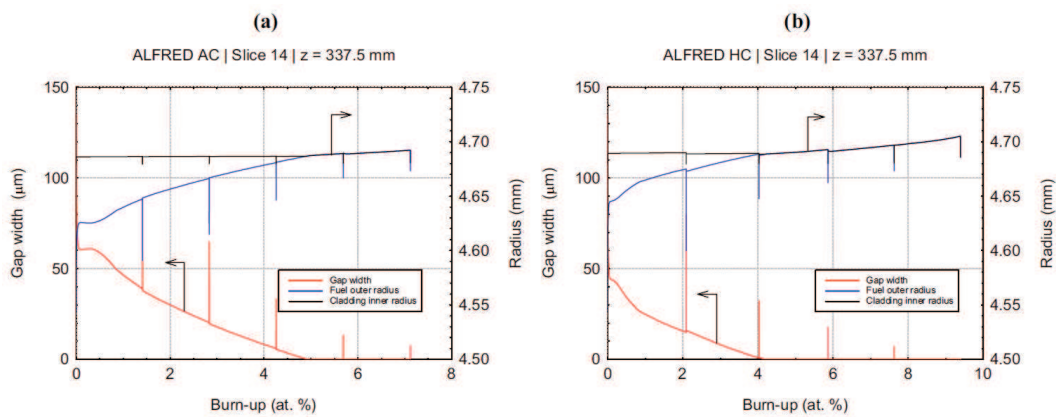


Figure 10: Cladding inner and fuel outer radius, and gap width evolution as a function of burn-up for (a) AC and (b) HC reference case.



2.3.4 Stress and strain in the cladding

The results of the mechanical analysis in terms of radially averaged cladding hoop stress during the irradiation are reported in Figure 11. No issues regarding the cladding stress are observed until the gap is open. In this situation, the only contributors are the internal pressure and the thermal stresses, which are both quite low. On the other hand, when the gap closes, the stress undergoes a sharp increase, reaching at the end of the irradiation 160 MPa and 430 MPa for the AC and the HC case, respectively. As expected, due to the anticipated gap closure, the cladding stress in the HC is much higher than the AC one, close to the yield strength. The stress relaxation due to thermal creep is not pronounced enough to completely avoid a little plastic strain, which is in any case very low. The high cladding stress is strictly related to the strain due to swelling and creep, occurring both in the fuel² and in the cladding.

The main mechanical analysis result is that, in the hot channel, stress levels are high (whereas the average channel presents no issues). Particular attention has to be paid to this fact. Thermal creep strain, due to high stress induced by FCMI, could be a serious issue for the cladding. Therefore, it is necessary to perform a sensitivity analysis in order to find out the worst case and to give feedbacks on the design, trying to improve the safety limits of the fuel pin.

² The fuel thermal creep model available in TRANSURANUS could present numerical convergence issues, probably requiring further development.

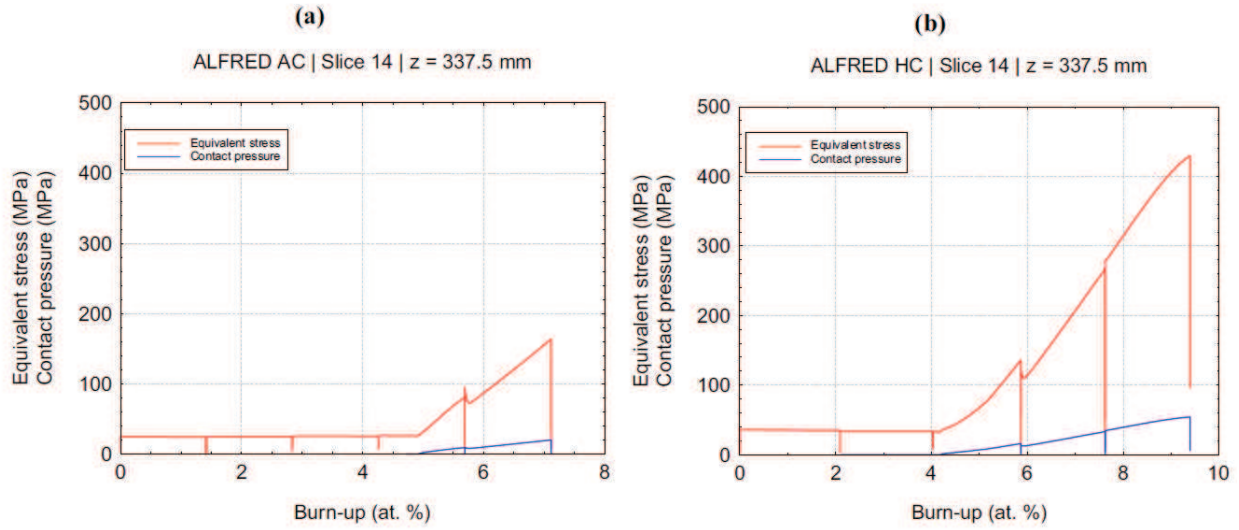


Figure 11: Contact pressure between fuel and cladding along with the radially averaged equivalent stress in the cladding for (a) AC and (b) HC reference case.



2.4 Closing remarks

The results of the simulation of ALFRED reference case present some peculiar aspects, which are summarized hereinafter. In Table 6, the main quantities of interest are shown. First of all, the temperature levels in the HC are not acceptable. The fuel inner temperature in the HC hot spot is 500°C below the melting point, but above the preliminary limit proposed of 2000°C (Grasso et al., 2013). Design-based ways to reduce the inner fuel temperature are proposed in Section 4. The cladding outer temperature is below the preliminary limit of 550°C (Grasso et al., 2013) set to contain lead corrosion of the cladding steel. Secondly, the gap closure dynamics is driven by the fuel pellet volume growth, due to swelling and thermal expansion. When the gap closes, the mechanical interaction between fuel and cladding increases the stress level in the cladding. In any case, the stress level in the cladding leads to strains well below the design limits. It is important to underline that the safety issues arise only in the HC. In fact, the AC fuel temperature is very low compared to the limit of 2000°C. Moreover, also the FCMI is weak in the AC, leading to low cladding strain.

Table 6: Summary of ALFRED reference case results at EoL.

	AC	HC
Fission gas released fraction (%)	32	32.4
Maximum burn-up (at. %)	8.04	11.2
Effective cladding swelling strain (%)	0.020	0.024
Effective cladding thermal creep strain (%)	$1.8 \cdot 10^{-5}$	0.086
Effective cladding irradiation creep strain (%)	$5.05 \cdot 10^{-4}$	$8.84 \cdot 10^{-4}$
Effective cladding plastic strain (%)	0	$1.07 \cdot 10^{-3}$
Maximum fuel temperature (°C)*	1810	2184
Maximum cladding temperature (°C)*	497	551
Inner gas pressure (MPa)	1.70	2.41
CDF (/)	0.000	0.047

*The maximum temperature occurs during the first batch (Figure 8).



(this page is intentionally left blank)



3. Sensitivity analysis

The uncertainties in some critical models defining the reference case for the ALFRED average and hot channel have to be handled by a sensitivity analysis. The goal of this analysis is the definition a worst case scenario, focusing on ALFRED hot channel conditions. On the basis of this worst case scenario, it is possible to suggest some feedbacks for the ALFRED fuel pin design.

3.1 Models considered

The main criticalities concerning ALFRED hot channel fuel pin are the high fuel temperature and the strong FCMI. Therefore, the models governing the gap dynamics and the fuel conductivity assume a particular importance in controlling the stress level both from the mechanical and thermal point of view. This fundamental statement comes directly from the discussion of the reference case results, which has been presented in the previous Section.

Among these models, three are affected by a significant uncertainty³: fuel swelling, fuel thermal conductivity, and the cladding swelling. Brief details about each of these models are given in the following. One key parameter is also affected by great uncertainty, the fast neutron fluence. This parameter is fundamental because it affects the cladding swelling strain.

3.1.1 Fuel swelling model

The fuel swelling is the main responsible of the gap closure. There are two main models implemented in TRANSURANUS for the fuel swelling in MOX fuels. The one used in the reference case imposes 1.2% swelling strain per at. % burn-up, when the gap is open (Preusser and Lassmann, 1983). The other one, which is considered by the sensitivity analysis, imposes 2.0% swelling strain per at. % burn-up (Pesi et al., 1987). With closed gap, both the models impose a

³ Also the models for thermal creep and FGR of MOX fuel are affected by uncertainty, but a complete review of this phenomenon is out of the scope of this work.



0.065% swelling strain per at. % burn-up. It is important to notice that both these models are empirical, based on the results of experiments. They calculate the fuel swelling only as a function of atomic burn-up, not considering temperature and fluence dependences. This is a very important point, because implies that the fuel swelling model is independent from the other models considered in this sensitivity analysis.

3.1.2 Fuel thermal conductivity model

The fuel thermal conductivity model is fundamental because it governs the fuel temperature level. This determines the fuel thermal expansion (which, together with the fuel swelling, governs the gap closure) and the fuel temperature margin towards the melting point. The two models implemented in TRANSURANUS for MOX fuel differ in quantifying the deterioration of the fuel thermal conductivity due to burn-up effects, such as fission gas accumulation. The one used in the reference case considers very slight burn-up worsening in the fuel conductivity (Philipponneau, 1992). The other one, used in this sensitivity, leads to lower thermal conductivity values at high burn-ups (Carbajo et al., 2001). For more details about the available models for MOX thermal conductivity, see Luzzi et al. (2014).

3.1.3 Cladding swelling model and fast neutron fluence

The cladding swelling models are discussed in detail in Luzzi et al. (2014). Briefly, there is a "AIM1" model based on the last cladding steel irradiated in PHENIX (i.e., AIM1), and a "15-15Ti" model considering an older cladding steel. It is important to highlight that these models strongly depend on the fast neutron fluence, for which two different energy thresholds between thermal and fast neutrons are considered, namely: 100 keV and 10 keV. In Table 7, a summary of the models considered in the reference case and in the sensitivity analysis is reported (the A and B notation is recalled in Figure 12).



Table 7: Models considered in the sensitivity analysis.

Model	Reference ("Option A")	Sensitivity ("Option B")
Fuel swelling	1.2% / at. % with gap open (Preusser and Lassmann, 1983)	2.0% / at. % with gap open (Pesi et al., 1987)
Fuel thermal conductivity	Philipponneau, 1992	Carbajo et al., 2001 (higher deterioration effects due to burn-up)
Cladding swelling	"AIM1"	"15-15Ti"
Fast neutron fraction	> 100 keV	> 10 keV

3.2 Worst case definition

The reference case representing ALFRED fuel pin has been defined always choosing the "best estimate" models. The goal of the sensitivity is the set-up of a worst case. The models and the parameters under discussion in this sensitivity analysis generate sixteen combinations. The groups introduced in the previous Section (fuel swelling, thermal conductivity, cladding swelling & fast neutron fluence) have the characteristic of being independent one from each other. The merit parameter chosen for this analysis is the Cumulative Damage Function (CDF) accounting for the cladding rupture time due to thermal creep. The choice of the CDF among the possible parameters can be justified reminding that the cladding is the first safety barrier of the pin and that the CDF is by definition a cumulate quantity, accounting for the entire power history. In Figure 12, the graph of the combinations of the sensitivity is reported, with the worst case highlighted. In Table 8, a summary of the models defining the worst case is reported.

Table 8: Models defining the worst case.

Model	Worst case choice
Fuel Swelling	Pesi et al., 1987 (B)
Fuel thermal conductivity	Carbajo et al., 2001 (B)
Cladding swelling	"AIM1" (A)
Fast neutron fraction	> 10 keV (B)



3.3 Worst case results

In this Section, we compare some quantities of interest for the fuel pin performance between the worst case (defined in the previous Section) and the HC reference case. The temperature in the fuel is a direct consequence of the thermal conductivity and the gap dynamics. From Figure 13 is clear that, when the gap is open, the temperature levels for the HC reference case are even higher than those achieved in the HC worst case. This is mainly due to the lower initial value of the fuel conductivity. The gap closure occurs earlier in the worst case, due to the enhanced swelling rate. The deterioration in the fuel thermal conductivity determines the higher temperature in the worst case after the gap closure. From roughly 3% of at. burn-up, the fuel inner temperature in the worst case is higher than in the reference case. At EoL (9.3% at.) the difference is of more than 500°C.

The stress in the cladding in the worst case is higher (Figure 14), due to anticipated and stronger FCMI. In the last batch, the thermal creep, with imposed strain, relaxes the stress level. The higher stress in the cladding is responsible of the higher thermal creep strain (Figure 15) (and CDF) in the worst case.



ALFRED HC | Slice 14 | z = 337.5 mm

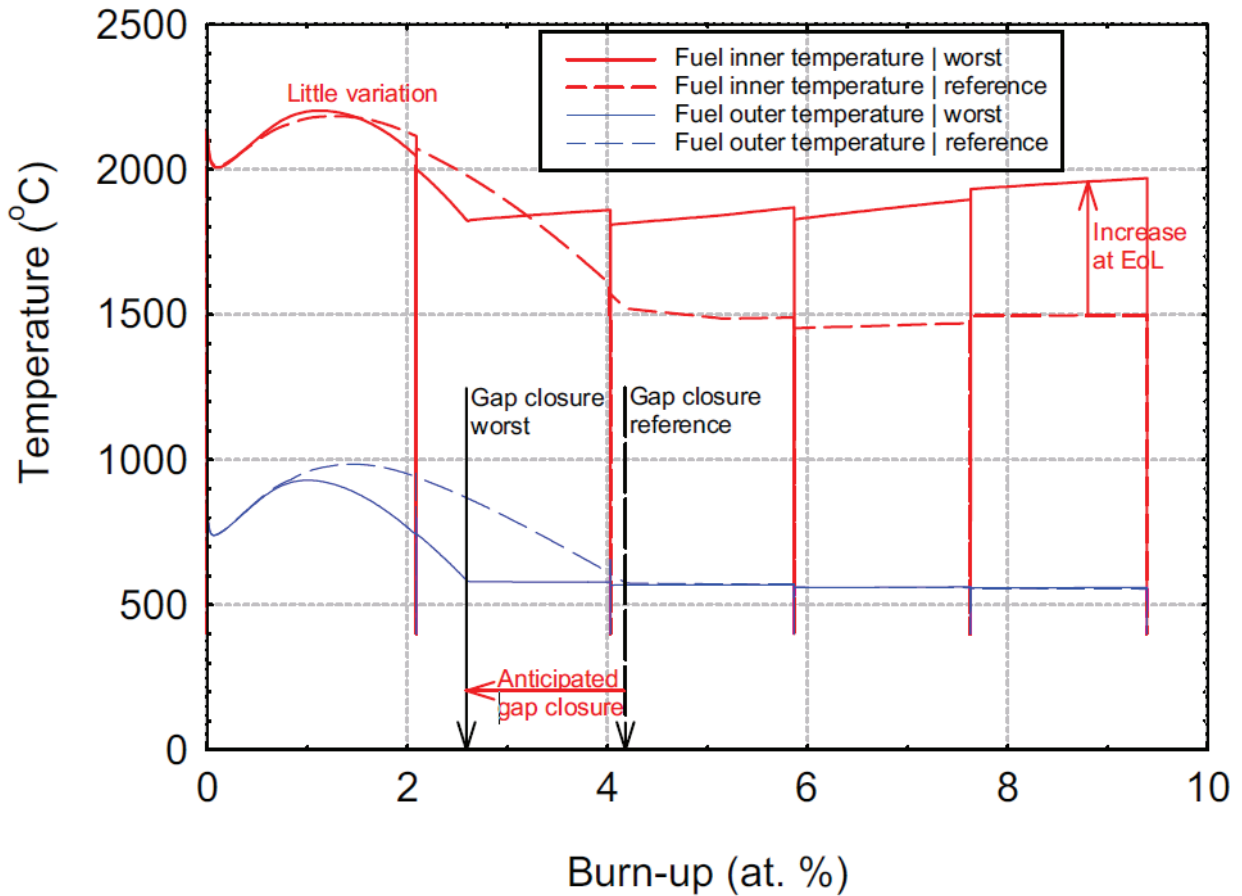


Figure 13: Comparison between ALFRED HC reference case and worst case: fuel temperature evolution.

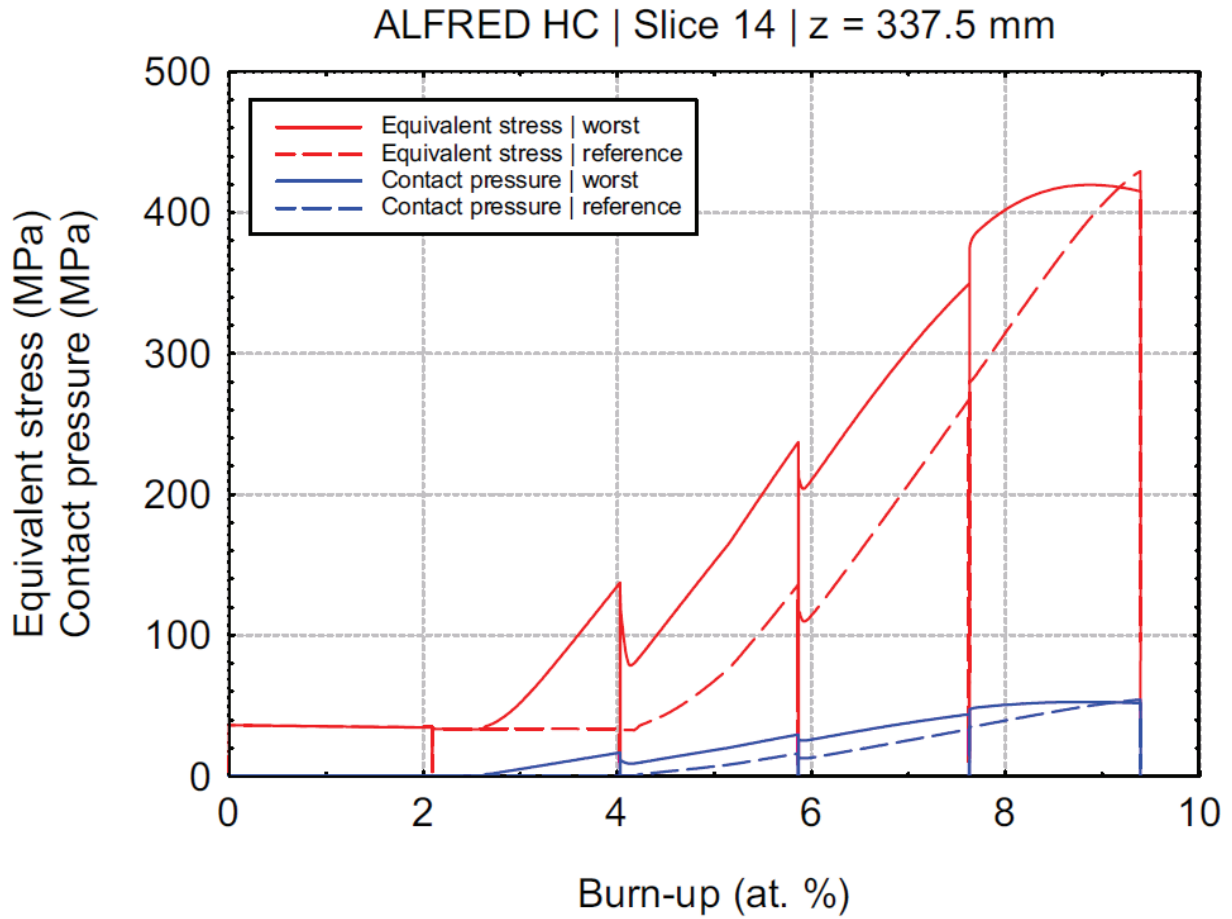


Figure 14: Comparison between ALFRED HC reference case and worst case: radially averaged equivalent stress in the cladding.

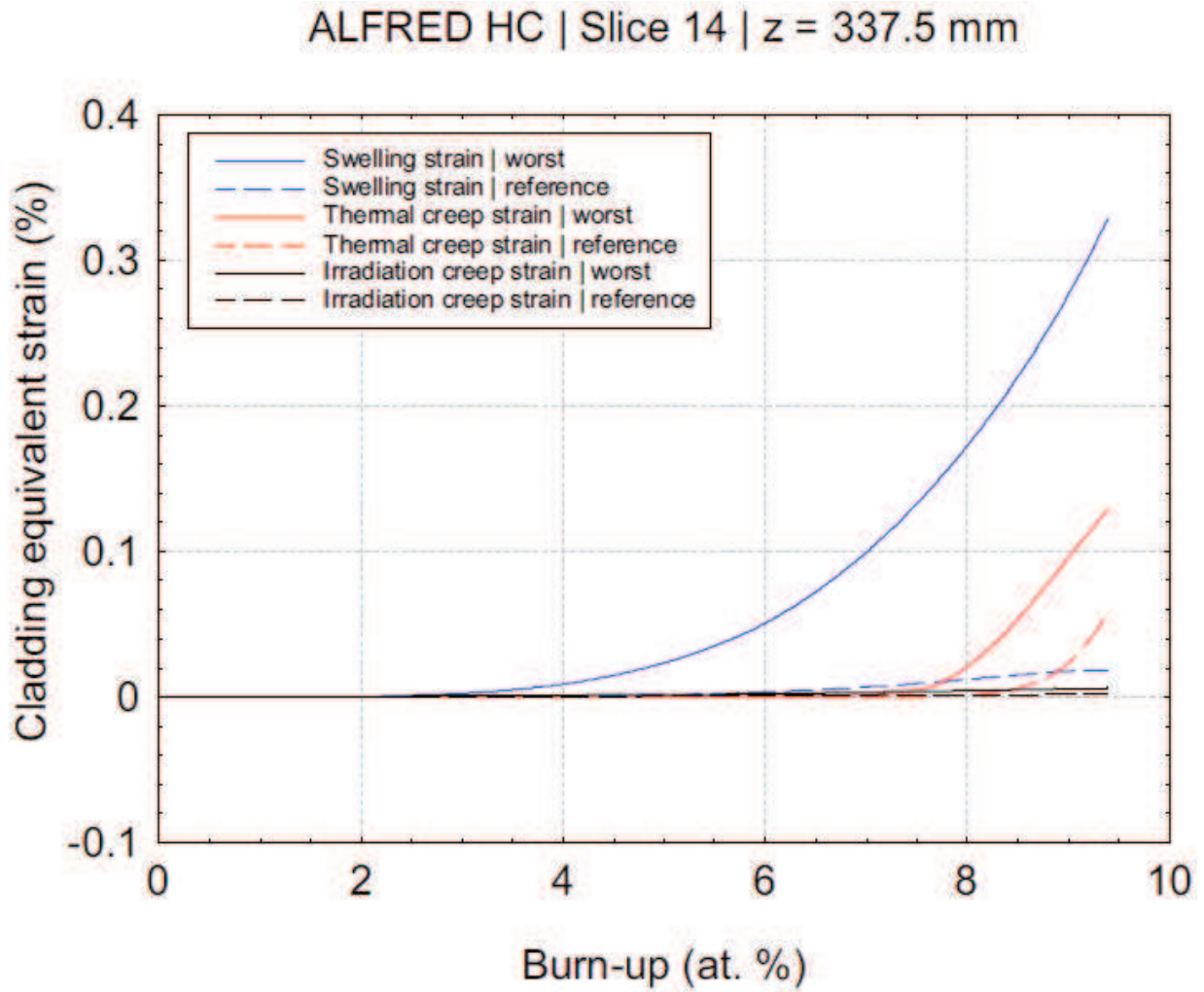


Figure 15: Comparison between ALFRED HC reference case and worst case: permanent strain components.



3.4 Closing remarks

In this Section, a sensitivity analysis on ALFRED HC has been carried out, focusing on the models governing the gap dynamics (i.e., fuel swelling, fuel thermal conductivity, cladding swelling and fast neutron flux). The result is the definition of a worst case for ALFRED fuel pin performance analysis. In Table 9, the main results of this scenario (for both AC and HC) are listed and compared with the HC reference case. The worst case presents both higher cladding strains (even if below the design limits) and higher fuel inner temperature (above 2200°C, with the limit fixed at 2000°C). In the following Section, changes to ALFRED fuel pin design are suggested, in order to reduce the HC fuel temperature to acceptable values.

Table 9: Summary of worst case and reference case numerical results at EoL.

	Worst case (AC)	Worst case (HC)	Reference case (HC)
Fission gas released fraction (%)	31	40.9	32.4
Maximum burn-up (at. %)	8.0	11.2	11.2
Effective cladding swelling strain (%)	0.26	0.35	0.024
Effective cladding thermal creep strain (%)	$1.85 \cdot 10^{-5}$	0.135	0.086
Effective cladding irradiation creep strain (%)	$1.15 \cdot 10^{-3}$	$1.96 \cdot 10^{-3}$	$8.84 \cdot 10^{-4}$
Effective cladding plastic strain (%)	0	$2.62 \cdot 10^{-2}$	$1.07 \cdot 10^{-2}$
Maximum fuel temperature (°C)*	1816	2201	2184
Maximum outer cladding temperature (°C)*	497	551	551
Inner gas pressure (MPa)	1.86	2.97	2.41
CDF (/)	0.000	0.081	0.047

* The maximum temperature occurs during the first batch.



(this page is intentionally left blank)



4. Feedbacks on ALFRED fuel pin design

In this Section, starting from the worst case results, preliminary design feedbacks are suggested. The aim of these feedbacks is to improve the fuel pin safety. In this work, only minor design changes have been considered, in order to not cause major changes in the current thermal-hydraulic and neutronic design. Therefore, three parameters of the fuel pin have been selected among the others: the initial gap width, the initial internal helium pressure, and the upper plenum height.

It is hard to predict the impact of a slight change in these parameters. Integral fuel rod performance analysis via TRANSURANUS is necessary. A set of configurations is simulated, combining different values of these design parameters. The results are condensed in a graphical way, in order to choose the best configuration, from a safety point of view. The limits considered in this analysis are the same preliminary design indications discussed in the Section 2.3 (Table 5).

4.1 Design variables

Three parameters have been selected in this analysis: the gap width, the initial internal helium pressure, and the upper plenum height (reported with their symbols in Table 10). The main advantage in these parameters is that the general thermal-hydraulic and neutronic design of the core is not altered by a slight variation of them.

In this Section, the rationale of the choice of these parameters is explained. The main issues in the ALFRED HC fuel pins are the high fuel temperature and the high stress in the cladding, when the gap is closed. In particular, the stress in the cladding is combined with a cladding temperature level that leads to considerable thermal creep rates. The creep mechanism with closed gap (therefore with imposed strain) is so that the stress in the cladding is actually relaxed by the thermal creep. To contain the stress in the cladding is fundamental to reduce the mechanical interaction between the fuel and the cladding. This can be achieved with a slight increase in the initial gap width. The result is a delay in the gap closure and an increase in the fuel temperature.



The increase in the fuel temperature, caused by the gap conductance decrease, can be contrasted by an increase in the helium filling pressure, which goes in the direction of increasing the gap conductance. Moreover, the pollution of the gap filling gas, due to the release from the fuel of gaseous fission products, and the internal pressure increase, can be limited by an increase in the upper plenum height.

A subset of the preliminary limits introduced in Table 5 are used in the following, in order to compare different configurations. These limits are summarized in Table 11. They have been selected among the others because of their consistency with the results of the reference case simulations. In order to properly compare different limits, normalized figures of merit are defined in Table 12.

Therefore, each configuration is represented by a set of three numbers (the values of the design parameters). A set of five numbers (the limit-normalized figures of merit) corresponds to every configuration. The configuration is considered acceptable if all the limit-normalized figures of merit are below unity (< 1). For example, a configuration Γ can be (according to the notation defined in Table 10 and Table 12):

$$\Gamma: [g_0; p_{int,0}; h_{up,0}] \rightarrow [\vartheta; \pi; \tau; \kappa; \delta] \quad (11)$$

In the following, different configurations are compared in a graphical way. The goal is to choose the configuration (i.e., the value of the design variables) that minimizes the limit-normalized quantities. Clearly, the main objective is the reduction of the fuel inner temperature, the only quantity of interest above the preliminary limits already in the HC reference case (Figure 7).



Table 10: ALFRED fuel pin design parameters considered.

Design parameter	Symbol	Unit
Initial gap width	g_0	(μm)
Initial internal filling pressure	$p_{\text{int},0}$	(MPa)
Upper plenum height	$h_{\text{up},0}$	(mm)

Table 11: Limits considered.

Fuel rod limits (maximum)	Symbol	Limit assumed
Fuel temperature	T_{lim}	2273 K (2000°C)
Internal pressure	p_{lim}	5 MPa
Thermal creep strain in the cladding	$\varepsilon_{\text{th,lim}}$	0.2%
CDF in the cladding	CDF_{lim}	0.20
Plastic strain in the cladding	$\varepsilon_{\text{p,lim}}$	0.5%

Table 12: Limit-normalized figures of merit.

Normalized quantity	Symbol	Definition
Fuel temperature	θ	T/T_{lim} (K K^{-1})
Internal pressure	π	p/p_{lim}
Thermal creep strain in the cladding	τ	$\varepsilon_{\text{th}}/\varepsilon_{\text{th,lim}}$
CDF in the cladding	κ	$\text{CDF}/\text{CDF}_{\text{lim}}$
Plastic strain in the cladding	δ	$\varepsilon_{\text{p}}/\varepsilon_{\text{p,lim}}$



4.2 Improved design case definition

In this Section, different configurations are compared. The results of each simulation are condensed in the values of five figures of merit, defined in Table 12. Kiviat's diagrams (also known as radar plot) are used in the following to represent the five-dimensional space of the limit-normalized figures of merit.

Eighteen configurations have been analyzed. The configuration are generated by the combination of the values assumed by the design variables. In Table 13, the range of variation of these parameters are reported.

The configuration [150;120;0.1] corresponds to the design values adopted in the fuel pin performance analysis of both the reference and the worst case, and is therefore called "standard design" configuration. The increase in the gap width is realized moving outward the cladding, without changing the cladding thickness and the fuel pellet geometry.

In Figure 16, the Kiviat's diagram for six configurations with gap equal to 150 micron (i.e., [150; h_{up} ; p_{int}]) is shown. Each configuration is represented by a polygon. The Kiviat's diagram allows visualizing graphically and quantitatively the consequence on the fuel pin safety caused by a change in the design parameters. From Figure 16, the influence of initial helium filling pressure and initial upper plenum height can be investigated.

Table 13: Range of variation of ALFRED fuel pin design parameters.

Design parameter	Range of variation
g_0 (μm)	{150; 175}
$h_{up,0}$ (mm)	{120; 180; 240}
$p_{int,0}$ (MPa)	{0.1; 0.3; 0.5}



On the one hand, it is clear that the most constraining limit is the inner fuel temperature. The design configuration is unacceptable for this limit, reaching a peak of 2200°C. The increase in the filling gas quantity and density, obtained increasing respectively the upper plenum height and the initial helium filling pressure, is quite efficient in reducing the fuel temperature. On the other hand, the quantitative analysis of the thermal creep in the cladding is encouraging. The CDF value is far from the limits suggested. The thermal creep strain is also well below the design limit.

An increase in the He filling pressure reduces the safety margin respect to each considered limit, except for the inner fuel temperature. The upper plenum height increase enhances the safety margins for both the mechanical properties of the cladding and for the inner fuel temperature.

In Figure 17, configurations with the same upper plenum height, but different initial gap width and internal filling pressure are compared. The emerging trend is that the initial gap width increase causes an increase in the inner fuel temperature and a decrease in the strains in the cladding. But, being the fuel temperature the limiting figure of merit, an increase in the gap width is not easy to pursue.

In the Figure 18, the "temperature optimum" configuration is shown. This configuration maximizes the safety margin with respect to inner fuel temperature keeping acceptable values with respect to the other limits considered in this work. To obtain this optimum configuration, it is enough to increase the initial helium filling pressure from 0.1 MPa to 0.5 MPa. Of course, this optimum configuration depends on the above discussed specific choices made both in terms of design variables and of figures of merit. The changes induced in both average and hot channel adopting these design configuration are discussed in the following Section.

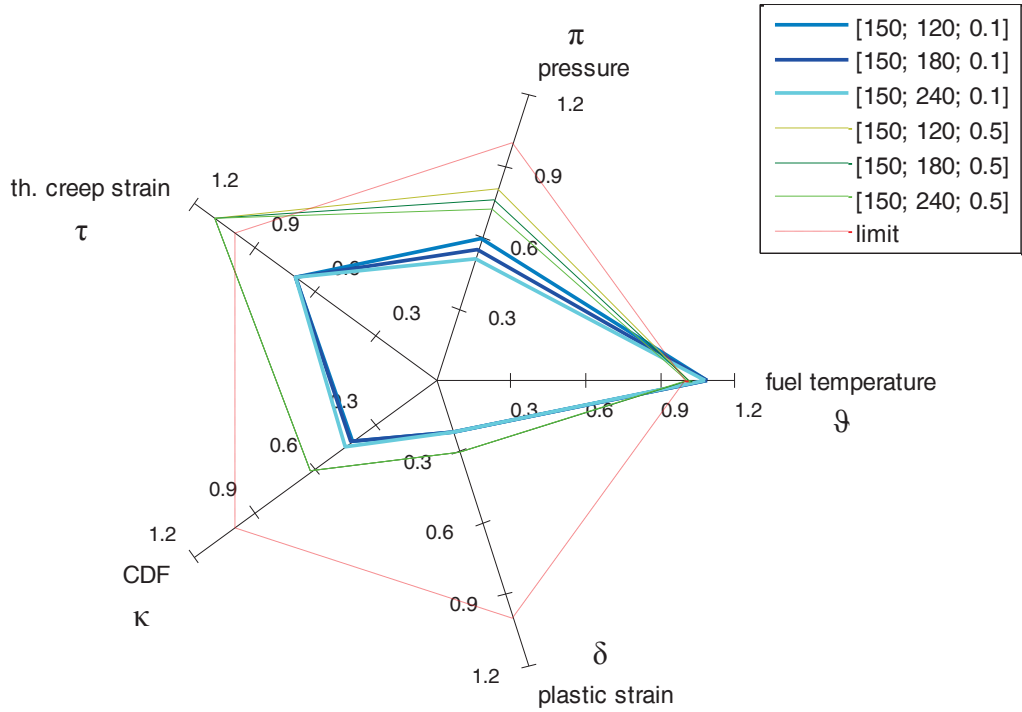


Figure 16: Kiviat's diagram comparing configurations with initial gap width of 150 micron. The comparison is based on the limit-normalized figures of merit important for a safety point of view (HC worst case models).

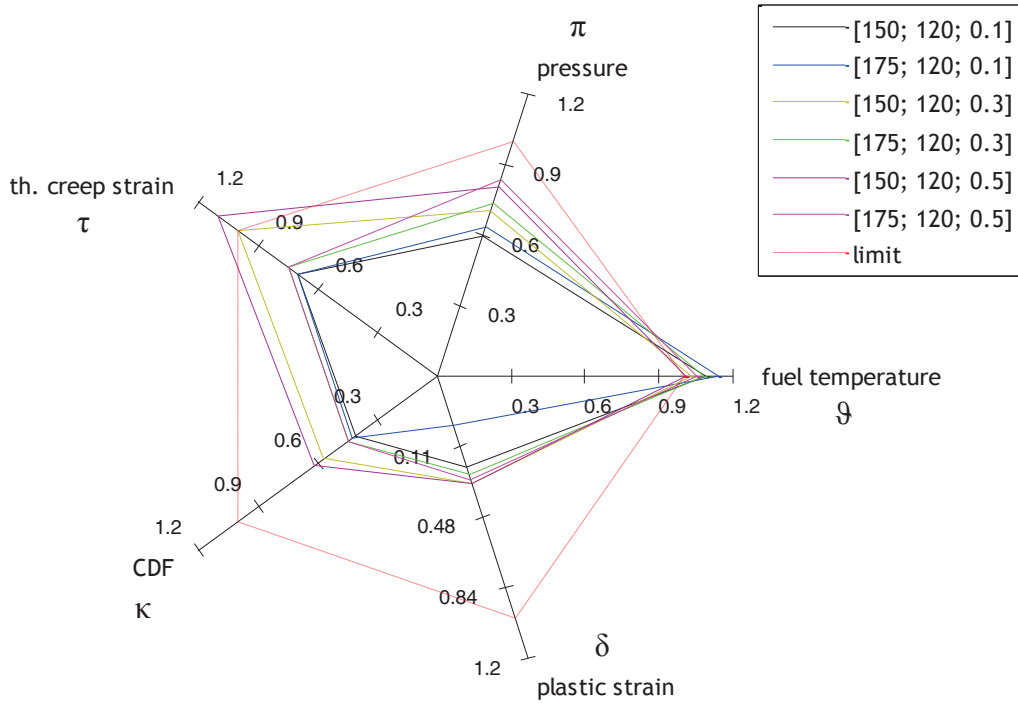


Figure 17: Kiviat's diagram showing initial gap width influence on ALFRED fuel pin performance, at different levels of initial internal pressure (HC worst case models).

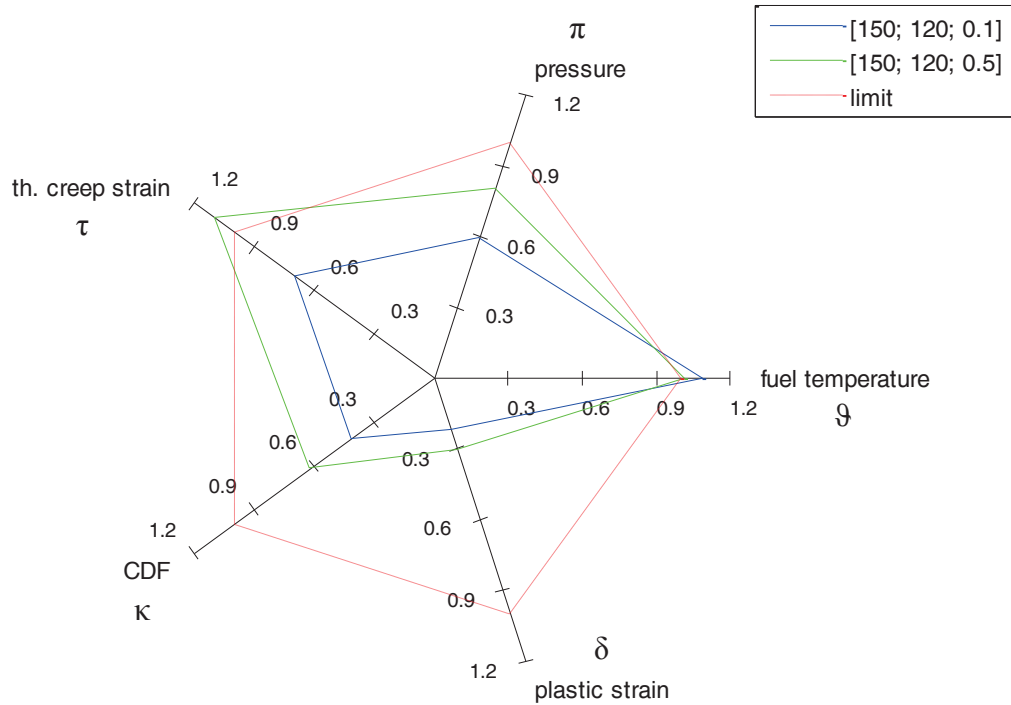


Figure 18: "Temperature optimum" configuration compared with the basic design configuration (HC worst case models).



4.3 Improved design case results

The "temperature optimum" configuration achievable through safety-oriented design is the one which minimizes the fuel inner temperature, respecting all the other limits (applying the models characterizing the reference case, both AC and HC). This objective is obtained with the combination of initial gap width, initial upper plenum height and initial helium filling pressure reported in Table 14. It is important to notice that only the initial filling pressure value changes from ALFRED reference design, causing only slight changes in the general design of the reactor⁴.

In this Section, ALFRED reference and optimum design are compared. In Figure 19, the effect of an initial filling pressure increase on fuel temperature evolution is plotted, respectively for average and hot channel. The benefic effect on the fuel temperature is evident. It is also clear that this gain is not free of charge: the stress level in the cladding is increased and therefore, the thermal creep is more incisive. Nevertheless, the mechanical quantities are still well below the limits discussed in Section 2.

Table 14: ALFRED "temperature optimum" design configuration.

Design parameter	"Standard design"	"Temperature optimum"
Initial gap width (μm)	150	150
Initial plenum height (mm)	120	120
Initial filling pressure (MPa)	0.1	0.5

⁴ In steady state, no changes at all should arise in the neutronic and thermo-hydraulic design from the suggested increase in the helium filling pressure. In transient conditions (i.e., ULOF, Unprotected Loss Of Flow), the internal pressure plays an important role and the effect of its increase has to be considered in further detail.

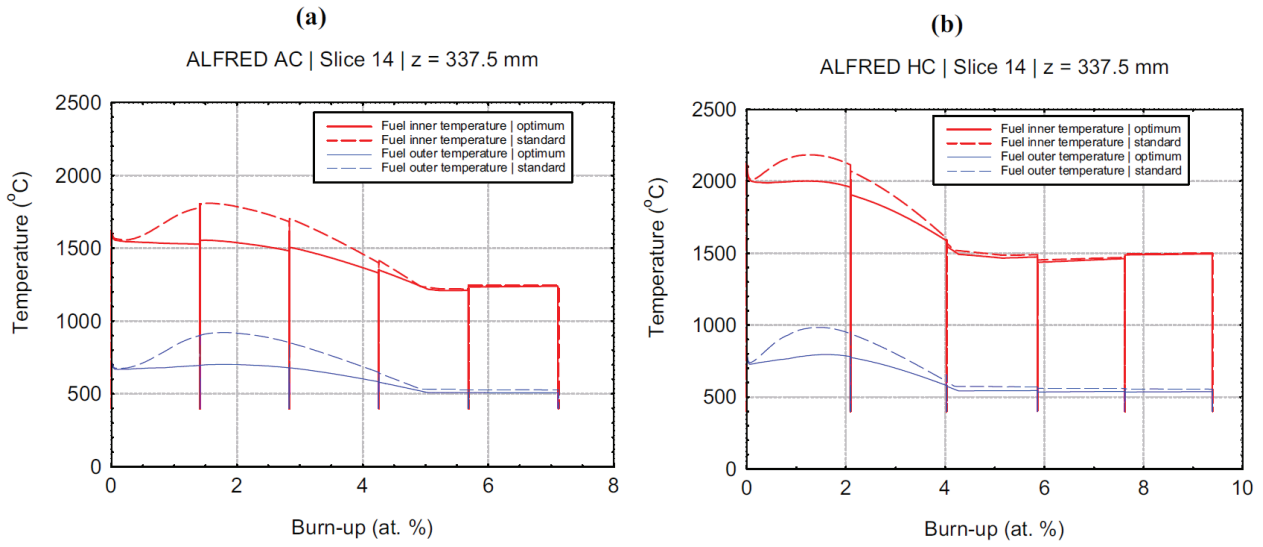


Figure 19: Inner and outer fuel temperature evolution versus burn-up: comparison between the reference and the optimum case for (a) AC and (b) HC reference case.



4.4 Closing remarks

In this Section, the optimization process of ALFRED fuel pin has been carried out. The attention has been focused on reducing the HC inner fuel temperature, because the AC presents no critical issues. The LFR-oriented version of TRANSURANUS has been useful to give design feedbacks, leading to a "temperature optimum" configuration achievable with an increase of the internal pre-pressurization of the pin (from 0.1 MPa to 0.5 MPa). The application of this design change to the reference case modelling set (Section 2) leads to the results summarized in Table 15. The maximum fuel temperature is reduced by 200°C, in both AC and HC. Moreover, the cladding strain is well-below the preliminary limits. To reduce the strains in the cladding and the cumulative damage function, it is not sufficient to alter slightly some pin design parameters. Actually, significant changes in the neutronic design of the core will be required (e.g., focusing on a reduction of the radial power peak factor, in the light of the satisfactory results obtained for the average channel).

Table 15: Comparison between the results of "temperature optimum" and "standard design" configurations at EoL, applying reference models.

	AC		HC	
	Standard	Optimum	Standard	Optimum
Fission gas released fraction (%)	32	18	32.4	26
Maximum burn-up (at. %)	8.04	8.04	11.2	11.2
Effective cladding swelling strain (%)	0.020	0.020	0.024	0.024
Effective cladding thermal creep strain (%)	$1.8 \cdot 10^{-5}$	$1.8 \cdot 10^{-5}$	0.086	0.15
Effective cladding irradiation creep strain (%)	$5.05 \cdot 10^{-4}$	$4.71 \cdot 10^{-4}$	$8.84 \cdot 10^{-4}$	$7.9 \cdot 10^{-3}$
Effective cladding plastic strain (%)	0	0	$1.07 \cdot 10^{-3}$	$5.54 \cdot 10^{-2}$
Maximum fuel temperature (°C)*	1810	1620	2184	1994
Maximum cladding outer temperature (°C)*	497	497	551	551
Inner gas pressure (MPa)	1.70	2.32	2.41	3.15
CDF (/)	0.000	0.000	0.047	0.085

* The maximum temperature occurs during the first batch.



(this page is intentionally left blank)



Conclusions

In this work, a version of the TRANSURANUS code dedicated to LFR fuel pin performance has been used to carry out the fuel pin performance analysis of the ALFRED reactor. A *reference case* representative of the Average Channel (AC) and Hot Channel (HC) conditions, and based on "best estimate" models has been defined and analyzed. The main result of these simulations is the high value of the inner fuel temperature in the HC ($\approx 2180^{\circ}\text{C}$), which is above the proposed design limit of 2000°C . Moreover, strong Fuel Cladding Mechanical Interaction (FCMI) leads to high stress in the cladding, which can be an issue for the cladding performance. On the other hand, the situation in the AC is absolutely not problematic.

Starting from these results, a sensitivity analysis has been performed, considering the models and parameters with a major influence on the fuel temperature and the FCMI (which is governed by the gap dynamics). The result of this analysis is the definition of a *worst case* for the ALFRED HC fuel pin (the strong difference between AC and HC is due to the high value of the radial peak factor), characterized by an even higher inner fuel temperature ($\approx 2200^{\circ}\text{C}$). Therefore, an "optimization" process oriented to a reduction of the fuel temperature has been performed. It is important to underline that this optimization process is not feasible without a tool like TRANSURANUS, because of the strong interaction between the phenomena governing the fuel pin behavior.

A major result of the "optimization" process is that an increase of the internal helium filling pressure (from 0.1 MPa to 0.5 MPa) is enough to reduce the inner fuel temperature below the safety limits ($\approx 1990^{\circ}\text{C}$ in the HC). The internal pressure increase causes a slight increase in the stress level in the cladding, but the strains (effective thermal creep strain and effective permanent strain) remain well below the design limits. To obtain a reduction of the FCMI, the initial gap width can be increased, but this leads to unacceptable fuel temperatures.

Some aspects require further investigation, since they could actually have an influence on LFR fuel pin performance. First of all, given the strong FCMI, chemical effects between fuel and cladding have to be somehow considered (e.g., introducing a "fuel adjacency coefficient" in the CDF definition). Secondly, the TRANSURANUS thermal creep modeling of the fuel (which plays a



major role in determining the stress intensity in the cladding) should be carefully considered for fast reactors. Moreover, more accurate models for material properties (especially fuel and cladding swelling, cladding thermal creep and irradiation creep) are needed to enhance the confidence in fuel pin performance analysis results.

The main methodological output of this work is that ALFRED conceptual design can be improved from a safety point of view by taking advantage of the indications that a fuel pin performance code can provide. In this regard, TRANSURANUS revealed a useful tool: (i) for supporting the fuel pin design, according to the procedure adopted in this work; and (ii) for giving important feedback to the reactor designers. As to the item (i), the capabilities of the TRANSURANUS integral performance code have been exploited to evaluate the synergy of the phenomena occurring in the fuel pin and their impact on the fuel pin design improvement, on the basis of operational power history simulations. Accidental simulations were beyond the scope of this work. Such analysis, along with additional investigation on the modelling uncertainties and model improvements (e.g., the dependence of the cladding swelling on the stress and the coupling with the creep phenomenon; the chemical fuel–cladding interaction; the JOG formation; the cesium migration; and, in general, the FCMI modelling), will be the object of future work. As to the item (ii), to achieve the double objective of decreasing the maximum fuel temperature and decreasing FCMI, major changes in the neutronic design of ALFRED have to be made, focusing on the optimization of the radial power peak factor of the reactor core, given the satisfactory results obtained for the average channel.



Acknowledgements

The authors wish to thank Dr. Giacomo Grasso and Dr. Carlo Petrovich (ENEA, Italy) for the technical information on the ALFRED reactor, as well as Manuele Aufiero (Politecnico di Milano) for the neutronic analysis. A special thank is due to Dr. Valentino Di Marcello (KIT, Germany), Dr. Giovanni Pastore (INL, USA) and Mr. Stefano Lorenzi (Politecnico di Milano) for their valuable advice and scientific support.



(this page is intentionally left blank)



References

- Aufiero M., 2013. *ALFRED neutronic evaluation*. Private communication.
- Alemberti A. Frogheri M., Mansani L., 2013. *The Lead Fast Reactor: Demonstrator (ALFRED) and ELFR Design*. In: Proceedings of the IAEA International Conference on Fast Reactors and Related Fuel Cycles: Safe Technologies and Sustainable Scenarios (FR13), Paris, France, March 3–4.
- Baker C., and Killeen J.C., 1987. *Fission gas release during post irradiation annealing of UO₂*. Materials for nuclear reactor core applications, BNES, London.
- Bober M., and Schumacher G., 1973. *Material transport in the temperature gradient of nuclear fuel elements*. Journal of Nuclear Materials, 75, 193–200.
- Cacuci D.G., 2010. *Lead-Cooled Fast Reactor (LFR) Design: Safety, Neutronics, Thermal Hydraulics, Structural Mechanics, Fuel, Core, and Plant Design*. Handbook of Nuclear Engineering, vol. 4. (chapter 23), Springer, Boston.
- Carbajo J.J., Yoder G.L., Popov S.G., Ivanok V.K., 2001. *A review of the thermophysical properties of MOX and UO₂ fuels*. Journal of Nuclear Materials, 299, 181–198.
- Carroll R.M., Morgan J.G., Perez R.B., and Sisman O., 1969. *Fission density, burnup, and temperature effects on fission-gas release from UO₂*. Nuclear Science and Engineering, 38, 143–155.
- Di Marcello V., Schubert A., van de Laar J., Van Uffelen P., 2012. *Extension of the TRANSURANUS plutonium redistribution for fast reactor performance analysis*. Nuclear Engineering and Design, 248, 149–155.
- Di Marcello V., Rondinella V., Schubert A., van de Laar J., Van Uffelen P., 2014. *Modelling actinide redistribution in mixed oxide fuel for sodium fast reactors*. Progress in Nuclear Engineering, 72, 83–90.



- Ducros G., Pontillon Y., and Malgouyres P.P., 2013. *Synthesis of the VERCORS experimental program: separate-effect experiments on fission product release, in support of the PHEBUS-FP programme*. *Annals of Nuclear Energy*, 61, 75–87.
- GIF, 2002. *A Technology Roadmap for Generation IV Nuclear Energy Systems*. Technical Report GIF-002-00.
- Glessner-Leme D., and Matzke H.J. 1982. *Interdiffusion and chemical diffusion in the UO_2 -(U,Pu) O_2 system*. *Journal of Nuclear Materials*, 106, 211–220.
- Grasso G., Petrovich C., Mikityuk K., Mattioli D., Manni F., Gugiu D., 2013. *Demonstrating the effectiveness of the European LFR concept: the ALFRED core design*. In: *Proceeding of the IAEA International Conference on Fast Reactors and Related Fuel Cycles: Safe Technologies and Sustainable Scenarios (FR13)*, Paris, French, March 3–4.
- Hasting I.J., Smith A.D., Fehrenbach P.J., and Carter T.J. , 1986. *Fission gas release from power-ramped UO_2 fuel*. *Journal of Nuclear Materials*, 139, 531–543.
- Hering W., 1982. *The KWU fission gas release model for LWR fuel rods*. *Journal of Nuclear Materials*, 114, 41–49.
- IAEA, 2012. *Structural Materials for Liquid Metal Cooled Fast Reactor Fuel Assemblies – Operational Behaviour*. IAEA Nuclear Energy Series No. NF-T-4.3.
- Lackey W.J. et al., 1972. *Porosity and actinide redistribution during irradiation of (U,Pu) O_2* . *Nuclear Technology*, 16, 120–142
- Lassmann K., 1992. *TRANSURANUS: a fuel rod analysis code ready for use*. *Journal of Nuclear Materials*, 188, 295–302.
- Lassmann K. et al., 2013. *TRANSURANUS Handbook*. Copyright© 1975–2013. European Commission.
- Luzzi L., Lorenzi S., Pizzocri D., Rozzia D., Aly A., Del Nevo A., 2014. *Modeling and Analysis of Nuclear Fuel Pin Behavior for Innovative Lead Cooled FBR*. Technical Report ADPFISS-LP2-054.



- Nakamura J., Suzuki M., and Uestsuka H., 1999. *Re-irradiation tests of LWR spent fuel at JMTR*. Enlarged Halden Programme Group Meeting, Loen, Norway, May 24-29.
- NEA, 2005. *Fuels and Materials for Transmutation*. OECD NEA No 5419.
- Notley M.J.F., and MacEwan J.R., 1966. *Stepwise release of fission gas from UO₂ fuel*. Nuclear Applications, 2, 477.
- Olander D.R., 1976. *Fundamental Aspects of Nuclear Reactor Fuel Elements*. TID-26711-P1.
- Pastore G., Luzzi L., Di Marcello V., and Van Uffelen P., 2013. *Physics-based modelling of fission gas swelling and release in UO₂ applied to integral fuel rod analysis*. Nuclear Engineering and Design, 256, 75–86.
- Pastore G., Pizzocri D., Hales J.D., Novascone S.R., Perez D.M., Spencer B.W., Williamson R.L., Van Uffelen P., and Luzzi L., 2014. *Modelling of transient fission gas behaviour in oxide fuel and application to the BISON code*. Enlarged Halden Programme Group Meeting, Røros, Norway, September 7–12.
- Pesl R., Freund D., Gärtner H., Steine K., 1987. *SATURN-S, Ein Programm-system zur Beschreibung des thermomechanischen Verhaltens von Kernreaktorbrennstäben unter Bestrahlung*. Technischer Bericht, KFK 4272.
- Petrovich C. et al., 2012. D07 – *Definition of the ETDR core and neutronic characterization*. ENEA, Seventh Framework Program.
- Philipponneau, Y., 1992. *Thermal conductivity of (U,Pu)O_{2-x} Mixed Oxide Fuel*. Journal of Nuclear Materials, 188, 194-197.
- Pizzocri D., Pastore G., Barani T., Bruschi E., Luzzi L., and Van Uffelen P., 2015. *Modelling of burst release in oxide fuel and application to the TRANSURANUS code*. Accepted for the 11th International Conference on WWER Fuel Performance, Modelling and Experimental Support, Varna, Bulgaria, September 26–October 3.



Preusser T., and Lassmann K., 1983. *Current status of the transient integral fuel element performance code URANUS*. In: International Conference on Structural Mechanics in Reactor Technology (SMiRT), paper C 4/3, Chicago, USA, August 22–26.

Rothwell E., 1962. *The release of Kr^{85} from irradiated uranium dioxide on post-irradiation annealing*. Journal of Nuclear Materials, 5, 241–249.

SERPENT, 2011. PSG2/Serpent Monte Carlo Reactor Physics Burnup Calculation Code, <http://montecarlo.vtt.fi>.

Small G.J., 1988. *Fission gas release and bubble development in UO_2 during high temperature transients*. Technical Report IWGFPT/32, Preston.

Une K., and Kashibe S., 1990. *Fission gas release during post irradiation annealing of BWR fuels*. Journal of Nuclear Science and Technology, 27, 1002–1016.

Van Uffelen P., Schubert A., Van de Laar J., Györi C., Elenkov D., Boneva S., Georgieva M., Georgiev S., Hózer Z., Märten D., Spykman G., Hellwig C., Nordstrøm Á., Luzzi L., Di Marcello V., Ott L., 2007. *The verification of the TRANSURANUS fuel performance code - an overview*. In: Proceedings of 7th International Conference on WWER Fuel Performance, Modelling and Experimental Support, Albena, Bulgaria, 17-21 September.

Vettrano F., Luzzi L., 2001. *ADS-demo Fuel Rod Analysis Report*. ENEA-DT-SBD.00033 Technical Report, pp. 1-93.

Walker C.T., Knappik P., Mogensen M., 1988. *Concerning the development of grain face bubbles and fission gas release in UO_2 fuel*. Journal of Nuclear Materials, 161, 10–23.

White R.J., Corcoran R.C., and Barnes P.J., 2006. *A summary of swelling data obtained from the AGR/Halden Ramp Test Programme*. Technical Report R&T/NG/EXT/REP/ 0206/02.



Short scientific curriculum

Lelio Luzzi graduated from the Politecnico di Milano (POLIMI, Italy) in Nuclear Engineering. He obtained his Ph.D. in Science and Technology in Nuclear Plants at POLIMI (1999). From 1999 to 2001, he worked as POLIMI post-doctoral researcher. During that period, he was detached for 2 years at the Materials Research Unit of JRC-ITU, within the TRANSURANUS Developers Team. Since 2001, he is permanent researcher of Nuclear Plants at POLIMI, where currently is associate professor of Nuclear Engineering and teaches Nuclear Design and Technology for the MSc in Nuclear Engineering. He belongs to the POLIMI Department of Energy, Nuclear Engineering Division - CeSNEF (Nuclear Reactors Group, <http://www.nuclearenergy.polimi.it>) and to the Faculty of the Doctorate School in Energy and Nuclear Science and Technology. He is Italian representative of the IAEA-CRP-FUMEX-III, of the IAEA-CRP-FUMAC and of the OECD/NEA International Fuel Performance Experiments database. His research activities in Italy and abroad include nuclear fuel pin modeling and thermo-mechanics, as well as the development of multi-physics simulation tools. In the framework of a lasting collaboration with JRC-ITU, he was involved in MSc. and Ph.D. projects, aimed at the development of TRANSURANUS fuel performance code and mainly focusing on analysis of fuel pin irradiation experiments and fission product behavior modeling. He is author of more than 100 peer-reviewed scientific publications.

Davide Pizzocri graduated in Nuclear Engineering (2013) at POLIMI, with a thesis on the "Extension and application of a fuel pin performance code in the conceptual design of a Lead-cooled Fast Reactor". He also obtained the Alta Scuola Politecnica (double degree program of POLIMI and POLITO) diploma with a thesis on the environmental impact of space activities. In the frame of a collaboration research between INL, POLIMI and JRC-ITU, he worked at INL as an international technical specialist (February 1 - August 7, 2014) to the development and assessment of the INL fuel performance code BISON, focusing on the modeling of the behavior of fission gases in LWR fuel during both normal operating and accidental reactor conditions. These R&D activities are the subject of his PhD at POLIMI, where he got (July 2014) a fellowship for the Doctoral Program in "Energy and Nuclear Science and Technology".